Dottorato di Ricerca in Scienza per la Conservazione dei Beni Culturali - XXV ciclo

INVESTIGATIONS ON THE USE OF TITANIUM DIOXIDE AND SILVER NANOPARTICLES TO INHIBIT BIODETERIORATION OF STONE MATERIALS

Francesca Bellissima

Chemistry Department - University of Florence

UNIVERSITÀ
DEGLI STUDI
FIRENZE

DOTTORATO DI RICERCA IN
SCIENZA PER LA CONSERVAZIONE DEI BENI CULTURALI

CICLO XXV

COORDINATORE Prof. Baglioni Piero

Investigations on the use of titanium dioxide and silver nanoparticles to inhibit biodeterioration of stone materials

Settore Scientifico Disciplinare CHIM/02

Dottoranda
Dott.ssa Bellissima Francesca

Tutore
Prof. Baglioni Piero

Co-tutore
Dott.ssa Perito Brunella

Coordinatore
Prof. Baglioni Piero

Anni 2010/2013

Table of contents

Chapter 1.
Introduction: conservation science, biodeterioration and nanotechnology

1.1 Outline

This thesis is the result of a work that has the purpose to find innovative long-term solutions to biodeterioration problems of stone artworks, *i.e.* to damages caused by microorganisms on lithic Works of Art.

Since the floods that devastated Florence and Venice in 1966, conservation science has been based on the paradigm that good results can be obtained only if an appropriate analytical characterization of both the artistic object and the proposed remedy is performed, in order to conceive adequate solutions in terms of durability and compatibility with the materials (Giorgi *et al*., 2010).

In this scenario, nanotechnology offers a new reliable way to restore and preserve artworks, as it enables to specifically tailor proper remedies to each case study. In particular, certain nanoparticles (NPs) are known to constitute very interesting antimicrobials to be used in several fields, including the preservation of different surfaces to the attack of degrading microorganisms (Ruffolo *et al*., 2010; Ditaranto *et al*., 2011; Wang *et al*., 2013). The outstanding potentials shown by NPs are due to their high surface-to-volume ratio with respect to the bulk material, which confers them very particular physico-chemical characteristics.

Step by step, in this thesis work it has been studied the potentials of two typologies of NPs as antimicrobial agents. First, the NPs were synthesized and characterized; second, the NPs were surface modified with a linker able to graft them to the lithic substrate; third, the antimicrobial activity was assessed through microbiological tests.

Among the metal oxides or metallic NPs featuring antimicrobial behavior, in this dissertation the attention was focused on titanium dioxide and silver nanoparticles (TiO_2 NPs and AgNPs, respectively), whose general characteristics and

antimicrobial mode of action are widely discussed in Chapter 2. The same chapter also deals with the chemistry of alkoxysilanes, as it was taken advantage of their reactivity to surface modify the NPs in order to be grafted to the rocky surface.

The efficacy of the proposed nanosystems toward the inhibition of microbial viability was evaluated mainly toward a common biodeteriogen of stone surfaces, *Bacillus subtilis*, using both classical and specifically tailored microbiological methods. Serena stone was chosen as reference lithic substrate, being commonly used for artistic expression in Tuscany. Brief discussion about *B. subtilis* (and some other microorganisms used) and Serena stone is also presented in Chapter 2.

Chapter 3 reports about the chemical synthetic procedures and experimental methods used to characterize the proposed nanosystems. A specific subsection is associated with microbiological cultural techniques and with the test typologies performed to assess the NP antimicrobial activity.

Chapter 4 is divided in two main sections that widely discuss the results obtained using either titanium dioxide or silver nanosystems. In each section, the first part deals with chemical synthesis and characterization results, the second part describes microbiological results.

Conclusions and future perspectives are summarized in Chapter 5.

The Annex is devoted to introduce the fundamentals of the main characterization techniques used along this thesis work.

The following paragraphs (Chapter 1) deal with general description of biodeterioration processes and address common and innovative approaches to conservation science. It is in fact introduced the breakthrough of nanotechnology in science of conservation of cultural heritage.

Information about the approach followed to study the proposed nanoremedies are given in the last paragraph of Chapter 1, where the aim of the project is discussed.

1.2 Science of cultural heritage conservation

During the last decades, scientific community have become seriously aware of the need to preserve our huge cultural heritage, as its conservation is fundamental for conveying to future generations our culture and traditions.

This thesis work is part of a project that has the aim to find adequate long-term remedies to the biological degradation of stone artifacts. Such conservation treatments can be conceived only if the degradation mechanisms and the characteristics of the proposed remedy are fully understood. That is the only way to develop appropriate and compatible restoration methodologies and achieve the goal to transfer to future generations the world cultural heritage that we have inherited from the past.

What is generally referred to as "conservation treatments" are all the interventions aimed at cleaning, restoring and protecting cultural artifacts. The scientific approach to that subject characterizes modern conservation science, originated from the emergency situation that followed Florence and Venice floods in 1966. In that contingency, the research for new conservation methods resulted dramatically stimulated. Since that time, the research activity in conservation science has been based on the paradigm that the most important prerequisites to obtain excellent results are the reversibility of the treatment, its durability and the compatibility of all the materials (Baglioni *et al*. 2009; Giorgi *et al.*, 2010).

Science of cultural heritage conservation is a discipline in its very infancy and represents an interesting scientific challenge, requiring the collaborative efforts between experts of different fields, ranging from chemists, microbiologists, physicists or material scientists. Given the complexity of the subject, it is not sufficient that scientists are aware of the conservation problems, but it is conversely very important to sensitize general public, policy makers, private or public institutions and funding agencies that massive efforts have to be undertaken in order to limit damages to relevant parts of our history.

Historic monuments, paintings, manuscripts, textiles, archeological woods and stone artifacts are some examples of the objects that need to be preserved from

deterioration. Natural aging and human related events act in synergy to put cultural heritage at risk. With its multiple activities, mankind contribute to degradation problems inducing air pollution (SO_2, NO_x, VOC), acid rains and, more directly, carrying out incorrect conservation treatments. On the other hand, natural aging of the artifacts is caused by the balance of weathering agents and environmental conditions, such as wind, sunlight, temperature, rain, marine aerosols, dust and biological deterioration (Papida *et al.*, 2000). The problem that makes so hard to find adequate and durable conservation treatments lies in the fact that degradation processes and mechanisms are not precisely known.

1.3 Biodeterioration

Biodeterioration is referred to as the damages and changes in material characteristics caused by microorganisms (Guiamet *et al.*, 2013). The term "biodeterioration" was first defined by Hueck (1965) as "any undesirable change in the properties of a material caused by the vital activities of living organisms". Microbial deterioration, either of a common surface or of a cultural heritage object, occurs through several steps. A single species or a community of species establish on a surface and, under favorable conditions, they undergo cellular division and create cell-to-cell communications that eventually lead to the formation of a "biofilm", a complex community of microorganisms, dead or alive, embedded in their secreted metabolic products and attached to the surface. That process is referred to as "biocolonization", and is generally initiated by bacteria, the first organisms to foul exposed surfaces through adhesion, cell growth and biofilm formation. The biofilm formation represents a natural stationary phase of bacterial growth in which bacterial cells physiology is changed by increasing the production of secondary metabolites (Lopez *et al.*, 2010). Bacteria adhesion to solid surfaces is governed by nonspecific interactions, such as electrostatic, van der Waals and Lewis acid-base interactions. The initial adhesion phase is affected both by the metabolites produced by bacteria and by surface properties, such as roughness, porosity, chemical structure, hydrophobicity and surface charge (Faille *et al.*, 2002; Li and Logan, 2005). It is the

subsequent irreversible adhesion process that leads to the biofilm formation, through the synthesis of extracellular polymeric substances (EPS). EPS are responsible not only for cell cohesion and their surface adhesion, but also play the key role to enclose and shield the community from desiccation and erosion, and serve as a reservoir of nutrients and energy storage. Biofilms also have the role to balance moisture changes and protect microorganisms from extreme environments (UV radiation, pH shifts, osmotic shock) and toxic impact of salts and heavy metals (Belie, 2010). Because of all the benefits that microbial communities obtain from biofilm formation, it is simple to understand why biofilms are ubiquitous: about 90% of all the microorganisms in natural environment occur attached to surfaces (Belie, 2010). Once established, biofilms are extremely difficult to be eradicated (Costerton, 1995; Urzi and Realini, 1998; Tommaselli, 2003) and they impact on human life in many ways, inducing detrimental effects on materials like medical devices, food-processing equipments, industrial settings, buildings and cultural heritage objects.

As long as biofilm growth causes enormous economic damages, it is very advantageous and challenging to minimize bacterial attachment to the surfaces and prevent the early stages of biofilm formation (Li and Logan, 2005). This thesis work has the aim to contribute in this direction.

1.3.1 Deterioration of stone materials

The use of stones as media for artistic expression has ranged from the construction of ancient monuments and historic buildings to statues and little objects. Stone artifacts are exposed to the action of physical, chemical and biological factors, along with the exposure to mankind-related activities that also contribute to their decay (Fig. 1). The resulting deterioration is associated with a consortium of weathering mechanisms that are greater than the actual sum of the individual action of each parameter (Papida *et al.*, 2000). The relative impact of each factor varies according to the environmental conditions, the stone type and the preservation state of the object. As long as natural stones exhibit a wide range of mineral composition, texture and structure, also their ability to resist weathering is widely differentiate. The location of the artifact plays a crucial role in degradation as well, since outdoor

exposed objects degrade faster than the indoors due to rain, solar irradiation, thermal variations and wind. Indoor located artifacts are conversely mainly degraded by microorganisms carried in from outdoor through ventilation and visitors.

Conservation interventions aimed at reducing microbial colonization involve cleaning actions and the application of biocides hopefully able to prevent, inhibit or slow down the occurrence of biodegradation in the future.

Figure 1. Maya pyramids in the archeological site of Calakmul. It is evident the state of physico-chemical and biological degradation of the stone constituting the monuments.

Physico-chemical degradation. The major physical degradation problems that affect stone matrix stability are related with the loss of mechanical resistance, fissuration, formation of salt efflorescences (crusts), deformations (thermal expansion-contraction of the minerals) and erosion. Chemical degradation is conversely associated with the detrimental effects of all the reagents that can attack rock mineral constituents, causing chemical corrosion, oxidation/dehydratation reactions or the dissolution of some mineral elements (Guiamet *et al.*, 2013). For example, alkalies degrade silicate minerals, especially granitic rocks; acid solutions, on the contrary, react with carbonates and dissolve this way the primary constituents of calcite and dolomite rocks.

Biodeterioration. When the substrates colonized by microorganisms are cultural heritage materials, biodeterioration becomes not only an economic but also a social and cultural problem. One of the degradation consequences is in fact the loss of the original message of the object, *i.e.* of its cultural and artistic value. It was estimated that ~30% of the visible alteration on building materials is due to microbial impact, responsible for aesthetic, biogeophysical and biogeochemical decay (Sand, 2001).

Lots of investigations were oriented to elucidate the essential role played by microorganisms in the deterioration of different kind of artworks, either paintings, woods, papers, textiles or stones, and it emerged that their degradative capability is related with metabolic characteristics and with the ability to form biofilms (Palmer *et al.*, 1991). Moreover, the degree of colonization depends on the "bioreceptivity" of the lithic substrata, defined as the intrinsic properties of the material (surface roughness, porosity and chemical composition) that affect the initial adhesion of microorganisms to the surface (Miller *et al.*, 2012). For example, rough surfaces are usually colonized more quickly than smooth surfaces, since the irregularities constitute anchoring sites for microorganisms. The detrimental effects associated with the accumulation of biological deposit is referred to as "biofouling", strongly dependent on environmental conditions.

The consequences of microbial impact on the deterioration of porous inorganic material that constitute cultural artifacts have been widely acknowledged and reviewed (Warscheid and Braams, 2000). Microbial communities interact with mineral materials from the cleavages and fissures present on the surface, and the biodeterioration process that follows strongly depends on the surface-invading microorganisms and the lithotype.

Microbial colonization induce alterations that range from aesthetic and chromatic changes (*i.e.* pigmentation, discoloration, black crust or patina formation, stains and pitting) to the variation of physical properties (*i.e.* changes in water circulation and diffusivity, changes in thermohygric behavior, weakening of the mineral structure, disaggregation, detachments of materials, corrosion, powdering, cracks formation, exfoliation) (Gaylarde *et al.*, 2003; Scherrer *et al.*, 2009).

Two types of biodeterioration can be considered: biogeophysical and biogeochemical. The former is defined as the mechanical damage caused by the

pressure exerted during biological growth and it is mostly regulated by the porosity of the rocks; it can result in surface detachments and increased porosity. The latter is caused by metabolic processes of the organisms on the substratum. It involves the release of organic agents (acids such as lactic, pyruvic, oxalic, succinic, acetic, glycolic, citric, formic, fumaric) and the consequences are determined by the chemistry of the minerals composing the stone artifact (Griffin, 1991; Warscheid and Braams, 2000; Macedo *et al.*, 2009).

Microorganisms involved in biodeterioration processes. Potentially, all types of microorganisms can be involved in biodeterioration processes, and nearly all naturally occurring substrates can be degraded (Belie 2010). Biodeterioration is not a process in which only one group of microorganisms is involved, and rarely a single species can be pointed out as entirely responsible of the biodecay. Opposite, close interactions between several groups can be found. The microorganisms most frequently implicated in biodeterioration events are bacteria, cyanobacteria, algae, fungi and lichens. They can either induce assimilative or non-assimilative decay: the former is promoted by microorganisms that use stone material as nutrient, the latter is originated by metabolites produced by microorganisms (Gaylarde *et al.*, 2003). In the following paragraphs it is given a brief introduction to each category of microorganisms and their detrimental effects on stone surface.

Bacteria can be primarily categorized as Gram-positive (Gram+) and Gram negative (Gram–) on the basis of their cell-wall structure. Cell wall is designed to provide strength, rigidity and shape, and to protect cells from osmotic rupture and mechanical damages (Hajipour *et al*., 2012). Gram+ cell wall contains a thick layer of peptidoglycan, consisting of linear chains of polysaccharides cross-linked to form a three-dimensional rigid structure, very difficult to be penetrated. Gram– cell wall is quite more complex, and comprises an external layer of lipopolysaccharide and a thin peptidoglycan layer between two membranes (outer and plasma membrane). The outer membrane is composed of a complex layer of lipids, lipopolysaccharides and proteins. Lipopolysaccharides are not as rigid as peptidoglycan and are negatively charged. Bacteria responsibility in degradation of stoneworks is related to the ability

to oxidize inorganic compounds (chemolithoautotrophic bacteria) and to the release of acids and metabolites (Lewis *et al.*, 1987).

Cyanobacteria and algae are photolithoautotrophic microorganisms. They use sunlight as energy source and release oxygen through the photosynthesis. The photosynthetic communities are very common on stone cultural heritage materials (generally evidenced by green to black stains) and are considered the pioneering inhabitants in stone colonization, as they can develop even when no organic matter is present. They also have an active role in supporting the growth of heterotrophic microorganisms, conditioning the surfaces and excreting nutrients (McNamara and Mitchell, 2005). The detrimental effects induced by cyanobacteria range from surface discoloration produced by their pigments to excretion of erosive metabolites (Gaylarde *et al*., 2012).

Fungi are chemoorganotrophic organisms and they use organic substrates as energy source. Their detrimental effects are due to the release of organic acids or the oxidation of metal cations of the mineral lattice of the lithic substratum. In addition, fungal hyphae can penetrate beneath the stone surface and cause deterioration through their shrinking and swelling. They can also provide an entry for water, promoting its dangerous freeze and thaw cycles (McNamara and Mitchell, 2005).

Lichens are symbiotic association of fungi (that in this association feed upon the nutrients produced by the algae) and algae or cyanobacteria (which gain minerals leached from the stone by fungal acids).

The predominant role of photosynthetic microorganism (such as microalgae, cyanobacteria and lichens) in the deterioration of stone surfaces have been extensively studied by Miller and coworkers (Miller *et al.*, 2009 and citations within). They reproduced in laboratory conditions the photosynthetic colonization of stones, studying the primary bioreceptivity of different lithotypes.

Even though the microbial colonization commonly starts with phototrophic organisms, the establishment of heterotrophic microorganisms on the rocks is possible even without the pioneering participation of phototrophic organisms (Warscheid and Braams, 2000).

1.4 Nanotechnology and nanoparticles

The first concept of nanotechnology was given by professor Feynman in his lecture "There's plenty of room at the bottom" (Feynman, 1959), but the actual term "nanotechnology" was coined by Professor Taniguchi of Tokyo Science University in the year 1974 (Taniguchi, 1974) and describes the manufacturing of new materials at the nanoscale level (10^{-9} m).

Nanostructured materials are attracting a great deal of attention because, especially if shape and size are controlled, they can achieve specific characteristics and reaction selectivity. As the dimensions decrease down to the nanoscale, materials present particular physical, chemical, electronic, mechanical, magnetic, thermal, optical and biological properties that differ pronouncedly from the bulk material. These properties are due to the large surface-to-volume ratio, the large surface energy, the spatial confinement and the reduced imperfections.

The synthetic strategies to obtain nanosized material can be grouped in two main categories: "top-down" and "bottom-up" methods. In the top-down approach, bulk material is gradually broken down to nanodimensions using externally controlled microfabrication methods and specific tools to cut, mill and shape materials into the desired assembly. The top-down process to prepare, for example, inorganic particles consists in breaking down bulk solids into fine particles, either by mechanical approach or by thermal decomposition (mainly for ceramics manufacturing). This method suffers of the contamination of the particle surface with atmospheric gases or materials used for the mill, and cannot produce particles with size below a few microns, because of their tendency to re-aggregate (Baglioni and Giorgi, 2006).

Bottom-up approaches, conversely, refer to the buildup of a material from the bottom, atom-by-atom, molecule-by-molecule or cluster-by-cluster, to assemble molecular structures in the nanometer range of dimensions. That requires controlled growth conditions that allow the regulation of the nanomaterial characteristics. This kind of approach is commonly used for chemical and biological synthesis of nanoparticles.

Among the nanosystems, nanoparticles (NPs) have a primary role. They are gaining an ever increasing importance in several fields due to the fact that, being constituted by clusters of a few thousands atoms, they show extraordinary intermediate properties between the molecular state and the bulk material. Particle size, morphology and composition can be manipulated to obtain end products with different and specifically controlled properties (if a bottom-up approach is used).

A common synthetic pathway to obtain inorganic particles of oxides, hydroxides, metals or sulfides with nanodimensions is from water-in-oil microemulsion or reverse micelles. Micelles are used as nanoreactors capable to exchange the content of different droplets. This methods enables the reduction or precipitation *in situ* of the nanoparticles, whose final dimensions are dependent on the concentration of the reagents, the nature of the reducing agent as well as the relationship between the content of water and the surfactant of the microemulsion. In this case the final nanoparticles are stabilized by the surfactant and do not have the tendency to re-aggregate (Baglioni and Giorgi, 2006).

Another common method to synthesize size- and shape-controlled inorganic nanoparticles is the sol-gel technique, that involves the phase transition from a liquid colloidal *sol* into a solid *gel* phase, usually starting from inorganic metal salts or metal-organic compounds, such as metal alkoxides. The sol-gel process transforms the precursor through hydrolysis and polymerization reactions to form a colloidal suspension (*sol*). The increase in viscosity of the suspension leads to the formation of a network (*gel*) by polycondensation and polyesterification reactions. By aging, gel is transformed into a solid mass, through the expulsion of the solvent from the pores. The gel is then converted into a polycrystalline powder or a dry gel through further drying and heat-treatment (Schmidt *et al.*, 1994).

Another common way to obtain inorganic NPs is through a solvothermal process. It requires a sealed vessel in which the solvents can be brought to temperatures above their boiling points, thanks to the increase in pressure. If water is the solvent, the process is referred to as hydrothermal. This process is useful to take advantage of the increased solubility and reactivity of metal salts and complexes at high temperatures and pressures. Solvothermal processing allows many inorganic materials to be prepared at temperatures substantially below those required by traditional solid-state reactions. Unlike the cases of co-precipitation and sol-gel

methods, the products obtained by solvothermal reactions are usually crystalline and do not require post-annealing treatments.

More recently it has been developed an innovative thermal treatment to obtain metallic or oxide nanoclusters, the flame-spraying. Using this method, nanoparticles synthesized from inverted micelles or microemulsions are introduced as aerosol onto a flame produced by a flame spraying system. In this step they lose the surfactant that initially stabilized them and can be deposited to be collected as powders (Bonini *et al.*, 2002).

However, the most simple and cheapest way to obtain NPs is probably through a precipitation reaction from a liquid phase. By changing the reaction conditions, such as temperature, reagent concentrations or aging time, it is possible to adjust size, shape, structure and composition of the particles (Baglioni and Giorgi, 2006).

Nanoparticles have been successfully used in several fields by our research group: as agents for the delivery of therapeutic molecules (Bellissima *et al.,* 2013 b), for DNA transfection for therapeutic purposes (Montis *et al.*, 2012), for biosensors nanostructuring (Mariani *et al.,* 2013), for the development of antimicrobic fabrics (Falletta *et al.*, 2008), for innovative extrusion processes of cementitious materials (Ridi *et al.*, 2013) or for conservation science purposes (Bonini *et al.,* 2007; Domingues *et al.*, 2013).

1.4.1 Nanoparticles as antimicrobials

Nanoparticles can be exploited as antimicrobials in many different fields, ranging from water and air disinfection to conservation of cultural heritage materials. The reason lies in the fact that whilst bacteria can be able to develop resistant strains toward metal ions and antibiotics, it is quite difficult that they get resistant to NPs (Gong *et al.*, 2007). Among the antibacterial NPs can be cited some metal oxides as TiO_2, ZnO, MgO, CuO as well as metal hydroxides (such as $Ca(OH)_2$ and $Mg(OH)_2$) and metallic nanoparticles (AgNPs, CuNPs) (Dong *et al.*, 2011).

The cytotoxic properties of each nanomaterial towards bacteria is dependent both on the type of NPs and on the bacterial strain. Regarding the typology of NPs, for example, the antibacterial effect of AgNPs is higher than CuNPs both against *E.*

coli (–) and *S. aureus* (+). Among common oxide NPs such as CuO, NiO, ZnO, and Sb_2O_3 used against *E. coli* or *B. subtilis*, CuO NPs have the highest toxicity, followed by ZnO, NiO and Sb_2O_3 NPs. As far as bacterial strain is concerned, *E. coli* (–) is more susceptible to CuO NPs then *B. subtilis* (+), and conversely *S. aureus* (+) and *B. subtilis* (+) are more susceptible than *E. coli* (–) to NiO and ZnO NPs (Hajipour *et al*., 2012).

Nanoparticles exert their antimicrobial effect through lots of different routes, depending on their composition, surface characteristics and bacterial species. It is important to highlight that enteric bacteria are 1-3 μm in length, and hundreds of NPs can accumulate on the bacterial cell surface.

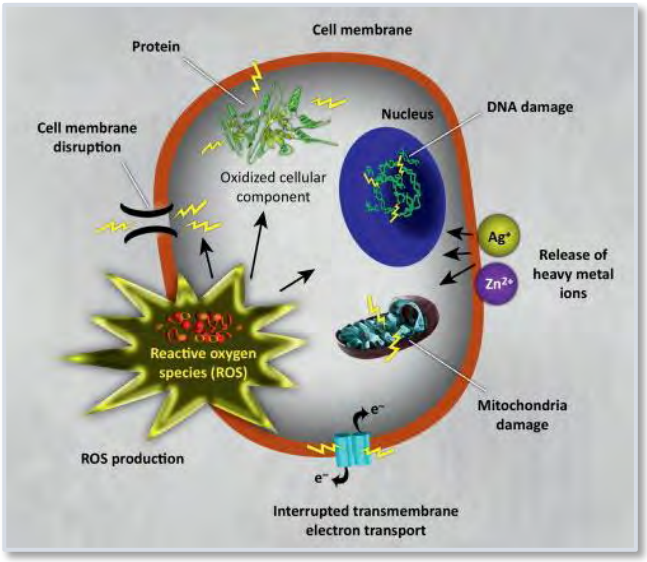

Figure 2. Mechanisms of toxicity of NPs against bacteria (Hajipour *et al*., 2012).

NPs can attach by electrostatic interaction to the cell membrane and disrupt its integrity by direct contact. They can also interfere with electron transport mechanisms or induce nanotoxicity by generation of reactive oxygen species; the oxidative stress induced by free radicals damage essential proteins and DNA. Moreover, NP effect depends also on the toxic properties of the heavy metals by which the NP is composed. Some examples of heavy metals toxic to bacteria can be Cu and Zn, and their use resulted effective in the prevention of recolonization on clean surfaces (Wessel, 2003; Henriques *et al.*, 2007). Another possibility of NP toxicity is the nitric-oxide-release, whose behavior relies on the delivery of NO to the

target (Hajipour *et al*., 2012). All the possible mechanisms of action of NPs toward bacteria are summarized in Figure 2.

1.5 Traditional approaches in Conservation Science of stone artifacts

Traditionally, conservation treatments on stone materials include interventions aimed at cleaning (transient intervention), restoring and protecting cultural artifacts (durable interventions). Very often though, even the use of consolidated procedures for a specific problem do not produce the desired result in the long period. For example, some drawbacks can arise *i*) when the treatment applied ages, *ii*) when the remedy is not durable enough or *iii*) when it amplifies the occurrence of other related deteriorations. In the following sub-sections some traditional approaches to different kinds of stone degradation (either chemical, physical or biological) are briefly described.

1.5.1 Chemical and physical degradation

As far as chemical and physical degradation is concerned, well established procedures can be applied. For example, to remove spots and other alterations it is commonly used the application of oxalic acid, sand blasting or oxygenated water. For the treatment of chips and cracks, it is common the fulfilling with plastic mass or white cement mixed with powder of the damaged rock.

An interesting approach to consolidate carbonate lithotypes takes advantage of bioremediation. Microbial hydrolysis of urea (degraded to carbonate and ammonium) produces high amounts of carbonate within a short period of time; in presence of calcium ions, that results in calcium carbonate precipitation that acts as consolidant once a certain level of supersaturation is reached (Belie 2010). However, the most common practice for preserving stones is the application of polymeric consolidants, designed to penetrate beneath the stone surface and re-establish the cohesion between the deteriorated grains. Up to recent years, this kind of restoration consisted in the

application of different classes of synthetic polymers, especially acrylic and vinylic, as it was generally accepted that these substances could be removed at any time with no drawbacks. That assumption revealed not to be true, and nowadays the use of such polymers is subject to frequent controversies due to their non-reversible application and their performance limited in time. Afterwards, silicon-based products have been introduced as consolidants (Favaro *et al.*, 2007**)**, being able to restore the natural binder lost during the weathering processes and to increase the material mechanical strength. But also their use has some drawbacks, due to *i*) the enhanced hydrophobicity of the consolidated material, *ii*) poor effectiveness in carbonate stones, *iii*) significant cracking during shrinkage and drying (Mosquera *et al.*, 2008; Sandrolini *et al*., 2012).

The progressive deterioration of building materials treated with polymers have led to the new approach of performing comprehensive studies on the chemical deterioration of the proposed remedy prior to its application, in order to develop consolidation systems tailored to the nature of the stone to be treated. Moreover, if a stone artwork experiences also biodeterioration problems associated with loss of cohesion of its constituting material, the risk using polymeric organic consolidants is that they can be degraded by microbial community that, as a result, is stimulated in its growth and accelerates stone decay (Cappitelli *et al.*, 2004).

1.5.2 Biological degradation

Conservators and restorers are coming to realize that also biodeterioration is a fundamental parameter to be controlled in order to preserve our cultural treasures. To do so, it is required an interdisciplinary approach aimed at understanding the environmental factors and the material properties implicated in the process of biogenic damage.

Traditionally, the very first intervention facing with biodeteriorated materials is the mechanical cleaning (Tretiach *et al.*, 2007). The second step relies on the synergic use of water repellents and the application of biocidal products. One of the critical factors that influence biocolonization of stones is in fact the water absorption, dependent on surface roughness, porosity and the presence of cavities. The use of

water repellents helps in the direction of reducing bioreceptivity, and the application of biocidal products is conversely intended to inhibit biological activity.

Among the biocides, we can mention various inorganic and organic compounds, such as organosilicon, organotitanium, or phenolic, quaternary ammonium, copper, zinc, magnesium, tin, and boron compounds (Khamova *et al.*, 2012). Biocide carriers are often based on epoxies or alkoxysilanes, traditional compounds used for stone consolidation (Khamova *et al.*, 2012). Benzalkonium chloride is a quaternary ammonium salt very commonly used as a biocide for its cationic character. To enhance its activity, it is useful to take advantage of permeabilizers such as EDTA, polyethylenimine (PEI) or succimer (meso-2,3-dimercaptosuccinic), able to change the structure and permeability of target biological membranes (Alakomi *et al.*, 2006). It has been reported that the use of quaternary ammonium salts as biocides may lower the water-repellent properties of the products applied, so that it would be important to develop single step applications of both water-repellent and biocide (Magoldi *et al.*, 2000).

The main problem related to the use of chemical biocides is their limited long-term benefits. The rapid re-grow of microorganisms could be ascribed both to the development of resistance to common biocides and to the rain water washing. In addition, bactericides are generally not targeted to specific classes of microorganisms and they may represent a risk for environment and human health.

1.6 Nanotechnology revolution in Conservation Science

The real revolution in conservation field comes from nanoscience and nanotechnology. In the last decades, nanoscale materials have emerged in cultural heritage conservation scenario and have appeared as excellent durable remedies to solve many conservation debates that, up to their advent in this field, did not find any satisfactory solution. Nanotechnologies are usually considered to be involved only in miniaturization of systems or electronics, but that is far from being true. On the contrary, they contribute to lots of different fields such as chemistry, biology, physics, medicine and material science. Due to the exploitation of these new

technologies, also conservation science is maturing and it is getting lots of benefits. Borrowing methodological tools from scientific field makes possible the development of new generation of control strategies, respecting the physico-chemical characteristics of the material to be restored. This new approach is eventually intended to counteract or even revert the deterioration processes that threaten cultural heritage preservation.

More specifically, it is colloid science that is playing the dominant role in providing new palettes of tools for conservation treatments. The application of nanotechnologies offers new reliable ways to restore and preserve artworks through the synthesis of systems specifically tailored to each case study, and may offer the possibility to solve conservation issues with long-term and substrate-compatible responses.

1.6.1 General conservation issues

Some of the most advanced applications of nanotechnology to conservation science are related to cleaning procedures. They are oriented not only to remove natural dirt and accidental contaminants from artworks, but also to remove the synthetic polymers applied during past restorations that have undergone loss of solubility and yellowing (Carretti*, et al.*, 2007; Baglioni *et al.*, 2009). These cleaning methods take advantage of micelles and swollen micelles dispersed in aqueous medium that work as nanocontainers of organic solvents able to dissolve polymers up to their complete removal from the work of art. The detergency capability mainly depends on the very large surface area of micelles and nanodroplets available for specific interaction with the polymeric coating. If the aqueous medium is not suited for the substrate to be cleaned, it is preferred to use oil-in-water microemulsions and micellar solution confined into gel network, with the possibility to make the gels responsive to external stimuli (Giorgi *et al*., 2010). Another innovative cleaning approach consists of magnetic particles associated with a permanent hydrogel that can be loaded with oil-in-water microemulsions to form a magnetically responsive system tailored for specific applications (Bonini *et al*., 2007).

An additional common conservation issue is represented by the deacidification of cellulosic materials, whose degradation, consisting in the chemical disruption of the cellulose polymer, is catalyzed by acidification processes. Innovative tools have been successfully used also in this field, getting rid of the traditional approach with alkaline aqueous solution that may cause the swelling of cellulose fibers and the leaching of associated compounds, such as inks. Conversely, the application of alkaline nanosized particles (such as $Mg(OH)_2$ and $Ca(OH)_2$) from non-aqueous dispersions (alcoholic solvents) have found to be particularly efficient for the preservation of cellulose-based materials (Baglioni and Giorgi, 2006). Another step forward in the direction of paper deacidification consists in the use of nanocomposite of $Mg(OH)_2$–TiO_2–hydroxyethylcellulose that, due to the intervention of the antimicrobial activity of TiO_2 particles, increases the durability of paper by imparting fungal growth resistance, moderate alkalinity, mechanical reinforcement and UV protection (Wang *et al.*, 2013).

The powdering of the surface also constitutes a pervasive conservation issue that requires consolidation intervention. Through the use of new technologies, it has been implemented the application of alkaline-earth inorganic metal hydroxide NPs such as $Ca(OH)_2$ and $Ba(OH)_2$ (Giorgi *et al.*, 2005; Poggi *et al.*, 2010; Chelazzi *et al.*, 2013) in place of classical consolidants that involve the use of silanes, acrylics or epoxy resins. Another alternative approach to the common consolidation treatments has been proposed by Mosquera *et al.* (2008) that synthesized particle-modified silica consolidant using a range of colloidal oxide particles with different colors in order to achieve the ability to tailor remedies whose color matches each stone under consideration.

1.6.2 Biodeterioration issue

The research of novel materials for the protection of artworks from the action of microbial communities may follow two main directions: the first is to develop techniques capable of preventing and inhibiting biodeterioration, the second is to improve the biocides to be used once the biodeterioration has occurred.

A successful approach for the prevention of biocolonization on stone surfaces is the research for suitable non-toxic active natural compounds to be incorporated in antimicrobial coatings (Villa *et al.*, 2009). It was recently developed a mild biocide based on epoxy siloxane sol modified with a nanostructured biocide additive (nanoparticulate carbon denominated detonation nanodiamond). This remedy demonstrated to be environmentally safe and to produce biologically stable protective coating (Khamova *et al.*, 2012).

In a recent study it was analyzed an anatase treatment for preventing biodeterioration of mortars caused by phototrophic microorganisms (cyanobacteria). The result was satisfactory, as the anatase modified mortars displayed reduced cyanobacteria growth with respect to mortars treated with conventional biocide (Fonseca *et al*., 2010).

Also the use of copper NPs provides new concepts for the lithic cultural heritage preservation. It was in fact recently reported (Ditaranto *et al.*, 2010) on the role of copper-based nanocoatings as agents capable of acting both as a remedy and as a prevention tool against microbial proliferation. CuNPs mixed with a silicon-based product (commonly used as water repellent) and a consolidant formed a bioactive system to be applied on stone substrates. Similar results were obtained using nano-Cu particles mixed with consolidants and water repellents for the prevention of biological growth on substrates with either low or high bioreceptivity. These mixtures hold promise for preventing re-colonization of stones after a conservation treatment (Pinna *et al.*, 2012).

Also the problem of microbial contamination of museums and archives has been recently dealt with the use of nanoparticles, in particular AgNPs. It was shown that AgNPs can be used as disinfectant for the surface of historical objects and archival documents (Gutarowska *et al.*, 2012).

It has been explored also the possibility to use photocatalytic semiconductor nanoparticles to obtain biocidal and protective coating for different surfaces. If the photocatalytic particles (ZnO, TiO_2, CdS, Fe_2O_3, Bi_2O_3,) are in direct contact with microbes, once they are irradiated the microbial surface becomes the primary target of the initial oxidative attack, resulting in a decrease of cell respiratory activity and cell death. In a recent study (Ruffolo *et al.*, 2010), ZnO and $ZnTiO_3$ oxides were dispersed in a polymeric matrix (either acrylic or fluorinated, commonly used as

protective coatings for stone materials), and the growth inhibition of *Aspergillus niger* was assessed. It was obtained a novel coating technology, with hydrophobic and biocidal properties suitable for the restoration of stone materials.

The exploitation of tools borrowed from nanoscience in the field of conservation science is still in its infancy, but it is growing really fast. The results obtained so far are really encouraging, as they are safe, durable and compatible with the substrates analyzed.

1.7 Aim of the work

In this thesis work we were interested in studying the potential use of different kinds of nanosystems to be applied on stone materials to inhibit their biodeterioration. The design of a surface coating able to prevent long term microbial colonization on stone artifacts is in fact still challenging and of great interest. Biocolonization has a relevant impact on the conservation of stone-based artworks, with consequences ranging from esthetic changes to physical and chemical deterioration. Our research was oriented to the use of nanoremedies physico-chemically compatible with the substrate to be protected, in view of a non-invasive application and a long-lasting effect. We studied two kinds of inorganic nanoparticles, titanium dioxide (TiO_2 NPs) and silver nanoparticles (AgNPs), whose antimicrobial activity, although exerted through different mechanisms, is well recognized. Briefly, TiO_2 NPs need to be photoactivated to exert their antimicrobial activity, based on oxidative stress, whilst AgNPs do not need any activation and their biocidal activity is based on many different synergic routes.

Bacteria are extensively involved in biodeterioration of lithic materials. Among them, even heterotrophic bacteria can establish on stones as primary colonizers without the pioneering participation of autotrophic organisms (Warscheid and Braams, 2000). Gram+ bacteria, in particular, are the most frequently found on stone materials. Among them, organisms of the very common *Bacillus* and *Bacillus*-related genera (spore forming chemoorganotrophic bacteria) have been frequently identified on monumental stones and their potential degrading activity was demonstrated also

through laboratory experiments (Stassi *et al*, 1998; Scheerer *et al*., 2009). For this reason, *B. subtilis* was the main bacterial strain used along this thesis work to test the efficacy of the proposed nano-remedies in inhibiting bacteria viability.

We synthesized TiO_2 and AgNPs in the desired crystallographic form and shape, respectively, and we evaluated, through microbiological assays, their potential use as antimicrobials. The NPs were surface modified in order to make them able to be grafted to a stone surface and not to be washed off by rain. Briefly, the aim of the work was to alter the bioreceptivity of the lithic surface by treating it with a nanostructured antimicrobial agent.

As grafting agents (*i.e.* linkers between the NPs and the rocky surface), it was taken advantage of the well known reactivity of alkoxysilanes toward lithic materials. The reference lithotype used was Serena stone, an ornamental sandstone very diffused especially in Florentine buildings.

This dissertation is divided in two main sections, the former concerning TiO_2 NPs and the latter regarding AgNPs. Each of these sections is further divided in a chemical and a microbiological part.

TiO_2 NPs. The first part of the work was focused on the synthesis and characterization of anatase NPs (this crystallographic phase is the most photochemically active), either pristine or alkoxysilanes-functionalized. The photoactivation of the NPs was preliminary tested toward the degradation of an organic dye, with the aim to find out if the surface functionalization badly affects the NP photo-characteristics. The final step was to assess bacteria photokilling capabilities of the NPs through microbiological tests, either on solid nutrient support, in solution or on lithic substratum.

AgNPs. In the second part of this dissertation the attention was focused on the synthesis of triangular silver nanoprisms, assessed to have enhanced antimicrobial activity (Pal *et al.*, 2007). AgNPs were functionalized by means of an alkoxysilane and it was verified if such a triangular shape was retained after surface modification. The actual antimicrobial activity was tested through several classical and specifically tailored techniques, both on pristine and surface-modified NPs. Microbiological assays were preliminary focused on the antimicrobial activity in nutrient media (solid

or liquid), whilst in the last section of this work the attention was oriented to the antimicrobial characteristics of the NPs grafted to the stone surface.

Chapter 2.
Materials and fundamentals

The escalation of bacterial resistance to conventional antibiotics is subject of paramount concern worldwide, and that justifies the ever increasing attention on the research for novel and innovative antimicrobial agents. Some answers to the challenging problem of bacteria proliferation may come from the emerging nanoscale materials, which have proved to have great potentials as antimicrobials. This chapter has the aim to give some backgrounds on the materials used along this thesis work, from the nanoparticles (TiO_2 or Ag NPs), the grafting agents, the microorganisms to the lithic support. Within this same chapter it is also remarked the state of the art of these materials in the cultural heritage field.

2.1 Titanium dioxide nanoparticles

Semiconductor photocatalysts have gained great attention in the last decades due to its use for many technological purposes. Titanium dioxide (TiO_2) is a naturally occurring semiconductor and it is being employed for a wide range of applications for its outstanding optical and electronic properties and for its chemical stability (Chen and Mao, 2007; Hu *et al*., 2010). TiO_2 can occur in crystalline form as well as in amorphous state. The crystalline forms present in Nature in three phases: anatase, brookite and rutile. Even if rutile is the thermodynamically stable form, it is anatase that is reported to have the highest photocatalytic activity and the strongest oxidizing power, when illuminated by UV light of proper wavelength (Kato *et al.*, 1994; Kakinoki *et al.*, 2004). Anatase is a metastable phase and it has the highest octahedral condensation and the lowest density. The photocatalytic characteristics of titanium dioxide rely not only on the crystallinity degree, but also depend on morphology, particle size and specific surface area (Cozzoli *et al.*, 2003).

Common uses. Taking advantage of its potent oxidizing effect when exposed to UV radiation, the pioneering use of TiO_2 as a photocatalyst was in the field of organic compounds removal from polluted water and air; TiO_2 is able to break down volatile organic carbon species, nitrous oxides and other pollutants into less harmful species.

TiO_2 is non-toxic and has been approved by the American Food and Drug Administration (FDA) to be used in human food, drugs, cosmetics and food contact materials. Its current uses range from white pigment in paint, toothpaste, sunscreen, cosmetics and food coloring to self-cleaning materials and photoluminescent and photochromic devices (Iuchi *et al.*, 2004; Zhao *et al.*, 2004; Fujishima and Zhang, 2005). Strong efforts have being devoted to the development of TiO_2-based environmental applications. Up to date, titanium dioxide is the most important semiconductor for photocatalytic degradation of air and water pollutants (Tian *et al.*, 2009; Paz, 2010), it is employed in energy efficient windows, in anti-fogging glasses (Allen *et al.*, 2010), in dye-sensitized solar cells (Hagfeldt *et al.*, 2010), gas sensors (Lin *et al.*, 2007; Faia *et al.*, 2004; Chaudhari *et al.*, 2006) and antibacterial systems (Fu *et al.*, 2005; Karunakaran *et al.*, 2010).

Synthesis. The precipitation of oxides, from both aqueous and non-aqueous solutions, is less straightforward than the precipitation of metals. The reaction pathways for the synthesis of oxides fall into two categories: those that directly produce an oxide and those that produce a precursor that must be further processed (drying, calcination).

Several efforts have been made toward the synthesis of titanium dioxide nanoparticles in anatase metastable phase from the hydrolysis of different precursors, as titanium chlorides ($TiCl_4$, $TiCl_3$), titanium alkoxides ($Ti(O^iPr)_4$, $Ti(O^nBu)_4$) or titanium sulfate ($Ti(SO_4)_2$). Lots of different synthetic strategies for the preparation of anatase crystal form have been developed over the years (Chae *et al*., 2003; Chen and Mao, 2007; Yu *et al.*, 2007; Hagfeldt *et al*., 2010). Some examples are the reverse micelle methods in nonpolar solvent, chemical precipitation, microemulsion-based synthesis (calcination or thermal annealing is required to induce crystallization), hydrolytic or not hydrolytic sol-gel synthesis, hydrothermal or solvothermal synthesis, sonochemical methods, microwave deposition techniques,

direct oxidation, chemical or physical vapor deposition. The properties of the resulting nanocrystals are strongly dependent on the reaction conditions. Several studies have been made with the attempt to tailor morphology and dimension of nanocrystals by varying the hydrolysis conditions or controlling the hydrothermal treatment (Cheseddine and Morits, 1999). In a recent paper, for example, Liao *et al.* (2009) studied the effects of different water/alcohol mixtures on size, morphology and crystallinity of TiO_2 nanostructures obtained through a solvothermal approach. They showed that only some solvents produce crystalline NPs and that their sizes range from few to few tens of nanometers, depending on the synthetic conditions.

Just as for metal NPs, oxide NPs frequently require a capping ligand or a stabilizer either to prevent agglomeration of the primary particles or to enhance the compatibility with other materials. The most used surface-modifiers are carboxylates, phosphonates and silanes (Neouze and Schubert, 2008).

Photocatalytic activity: mode of action. TiO_2 semiconductor is activated by the absorption of photons of UV radiation whose energy matches or exceeds TiO_2 band gap energy: electrons are excited from the valence band (VB) to the conduction band (CB), photo-creating positive holes (h^+) in the VB and electrons (e^-) in the CB. These reactive species participate in oxidation and reduction processes either within TiO_2 itself (electron-hole recombination) or with adsorbates at the surface. Any wavelength shorter than 385 nm induces this photoexcitation (Fig. 3). The migration of the electron-hole pairs to the nanoparticle surface catalyze reactions between electron donors and acceptors adsorbed on the surface. For instance, the photogenerated hole may react with moisture water adsorbed on the catalyst surface to produce $OH^{\cdot}$ radicals; photogenerated free electrons may be transferred to adsorbed molecular oxygen generating superoxide radicals ($^{\cdot}O_2^-$ $^{\cdot}O_2H$). The irradiation of a semiconductor results therefore in the catalytic production of reactive oxygen species (ROS) such as $^{\cdot}OH$, $HO_2^{\cdot}$, H_2O_2, and $O_2^{\cdot -}$ (Cozzoli *et al.*, 2003; Chen and Mao, 2007; Karunakaran *et al.*, 2010). Because of their high non-selective reactivity, ROS species are also very short lived and, in the absence of O_2 or a suitable electron acceptor, no photocatalytic reactions occur due to the electron-hole recombination.

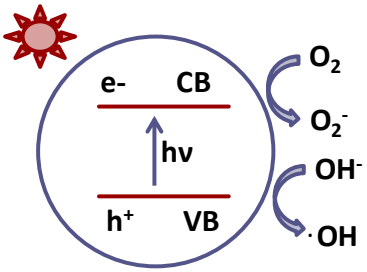

Figure 3. Schematic illustration of the photoexcitation of TiO_2 semiconductor and the subsequent generation of an electron (e-) and a hole (h+), respectively in the conduction band (CB) and in the valence band (VB). The electron and the hole are trapped by the surface-adsorbed oxidant (O_2) and the surface-bound reductant (OH-), respectively.

Scheme 1 summarizes the reactions that take place when the semiconductor is irradiated with a proper wavelength (Sunada *et al.*, 1998; Rincon and Pulgarin, 2003; Zacarias *et al.*, 2010).

Scheme 1. Redox and recombination reactions taking place when TiO_2 is irradiated by UV light of a proper wavelength.

$$\mathbf{TiO_2 + h\upsilon \rightarrow TiO_2\ (e^- + h^+)}$$

$TiO_2\ (e^-) + O_2 \rightarrow TiO_2 + O_2{\cdot}^-$	$TiO_2\ (h^+) + {}^aRX_{ad} \rightarrow TiO_2 + RX_{ad}{\cdot}^+$
$O_2{\cdot}^- + H^+ \rightarrow HO_2{\cdot}$	$TiO_2\ (h^+) + H_2O_{ad} \rightarrow TiO_2 + {\cdot}OH_{ad} + H^+$
$O_2{\cdot}^- + HO_2{\cdot} \rightarrow {\cdot}OH + O_2 + H_2O_2$	$TiO_2\ (h^+) + {}^-OH_{ad} \rightarrow TiO_2 + {\cdot}OH_{ad}$
$2\ HO_2{\cdot} \rightarrow O_2 + H_2O_2$	${\cdot}OH + {\cdot}OH \rightarrow H_2O_2$
$TiO_2\ (e^-) + H_2O_2 \rightarrow TiO_2 + OH^- + {\cdot}OH$	

[a] RX, organic substance; [ad], adsorbed

The effectiveness of TiO_2 as a photocatalyst is dependent upon the rate of production of reactive oxygen species at its surface, and that is in turn dependent upon other factors as the energy of the light illuminating the surface, the competition between electron–hole recombination and the redox processes occurring at the surface.

Antimicrobial activity. Because of the widespread use of antibiotics and the emergence of more resistant strains of microorganisms, nowadays we are facing the need to develop alternative technologies against bacteria proliferation. TiO_2 photocatalytic process is a conceptually simple and promising technology. The ROS

species produced as a consequence of UV irradiation are not only useful in the oxidation of organic substances, but can also cause various damages to living microorganisms, as long as they consist of abundant organic compounds.

The first application of TiO_2 photocatalysis for microbiocidal purposes was reported by Matsunaga *et al.* (1985). They implemented the novel concept of photokilling *E. coli* cells in water by contact with TiO_2, illuminated by UV light. Since then, much research work on the bactericidal effect of TiO_2 photocatalyst has been reported, and TiO_2 activity has been proved to be very effective toward a wide spectrum of microorganisms. Besides from water and air disinfection, TiO_2 photocatalytic technology has been extensively employed also for anti-bacterial activity on a variety of surfaces (Huang *et al*., 2000), ranging from surgical instruments (Haenle *et al.*, 2011) to innovative building materials, with self-cleaning and self-sterilizing characteristics (Chen and Poon, 2009).

Even though lots of the hypothesis have been proposed and validated, TiO_2 bactericidal mode of action is not fully understood. In his first work, Matsunaga (Matsunaga *et al*, 1985) proposed that the direct photooxidation of intracellular coenzyme A (CoA) to its dimeric form was the root cause of the decrease in respiratory activities that lead TiO_2-treated cells to die. Another proposed explanation is that the ROS generated at the photocatalyst surface attack the cytoplasmatic membrane of the microorganisms and oxidize the polyunsaturated phospholipid component of the cell membrane. This process would eventually lead to a membrane breaching that results in the leakage of intracellular components and in the promotion of cell respiration disruption (Fujishima, 1999; Maness *et al*., 1999; Huang *et al.*, 2000; Saito *et al.*, 1992; Page *et al.*, 2007). When a microbial cell is close to an irradiated TiO_2 particle, microbial surface (cell wall and cytoplasmatic membrane) is the primary target of the initial oxidative attack and all the functionalities that rely on an intact membrane structure are expected to change, *i.e.* semipermeability, respiration and oxidative phosphorylation reaction (Maness *et al.*, 1999). Moreover, once the integrity of the cell envelopes are damaged, TiO_2 can diffuse into cells and directly attack enzyme targets and DNA.

The different morphologies of Gram+ and Gram− cell envelopes hinder by different extent the passage of ROS species. For Gram+ bacteria, the barrier to the cytoplasmic membrane is constituted by the thick peptidoglycan layer; in Gram–

bacteria, the passage of ROS species to the cytoplasmic membrane is protected by a thin layer of peptidoglycan and by an outer membrane, this one being the real barrier. Although the outer membrane is semi-permeable, many radicals react with the lipid constituents of the membrane but, once the membrane is breached, there are no further significant obstacles blocking radicals from approaching the cytoplasmic membrane, destroying it and inducing cell death (Page *et al.*, 2007). Also cellular self-repair mechanisms (usually activated after irradiation) are inhibited by the action of TiO_2 (Rincon and Pulgarin, 2003).

Even the more resistant spore-forming bacteria (such as *B. subtilis*) were detected to be vulnerable to photocatalytic attack, as the mechanisms based on the action of photogenerated ROS are able to progressively oxidize spore coat together with spore core (Zacarias *et al.*, 2010; Barnes *et al.*, 2013).

Cultural Heritage Applications. From the conservation point of view, it is important to find environment-friendly technologies for biodeterioration control. TiO_2 is non toxic to human beings, quite inexpensive, sustainable for the environment and chemically stable. Given this background, the use of surface immobilized TiO_2 NPs seem a good strategy to counteract microorganisms growth with respect to conventional biocides.

In a recent study it was analyzed the possibility to use anatase TiO_2 particles for preventing biodeterioration of mortars (artificial stones), in comparison with conventional biocides. Mortar slabs were treated with anatase (applied as a coating or mixed within the mortar when it is prepared), inoculated with cyanobacteria and incubated over months. From chlorophyll quantification it resulted that anatase was a better agent for preventing biodeterioration than the conventional biocides (Fonseca *et al.*, 2010).

2.2 Silver nanoparticles

Silver-based materials present excellent properties such as thermal and chemical stability, low volatility, health and environmental safety and low toxicity to human cells. Because of all these features, silver-based compounds are suitable for a variety of applications and are very attractive as antimicrobial agents (Rai *et al.*, 2009). Silver ions are in fact acknowledged as one of the most toxic forms of heavy metals to microorganisms, and have a relevant activity against a broad range of bacteria, fungi and viruses (Morones *et al.*, 2005; Kim *et al.*, 2007).

Silver compounds: uses. The use of bulk silver as antimicrobial dates back to ancient times, when water and wine were stored in silver vessels to prevent spoilage. As early as 1000 B.C., silver was used to make water potable and Greeks used it for its antibacterial activity. Unintentionally, also the use of silver nanoparticles dates back to Romans, as they used AgNPs to color the glass of the famous Licurgus cup. In the 17th century, diluted solution of silver salts were used to heal ulcers and chronic wounds. In the 19th century silver was further used in the treatment of burns and wounds and in the prophylactic treatment of newborn eye infections (Silver *et al*., 2006; Rai *et al.*, 2009); this last practice on eyes was abandoned at the beginning of 20th century, when it was recognized as caustic.

Nowadays, silver compounds (and silver nanoparticles among them) are largely exploited both in medical and non-medical fields. As antimicrobial agents, they are applied in textile fabrics, home water filtration, cosmetics, electronic devices and food packaging. In medical field, AgNPs are used to prevent bacteria colonization on protheses, catheters, dental materials or stainless steel materials (Panacek *et al.*, 2006; Xu *et al*, 2006; Duran *et al.*, 2007, Falletta *et al.*, 2008; Chaloupka *et al.*, 2010; Knetsch and Koole, 2011; Gutarowska *et al.*, 2012; Mariani *et al*, 2013). Besides its antimicrobial characteristics, nanosilver exhibits strong optical features that make it suitable for biological sensing and imaging (Mariani *et al.*, 2013). The high conductivity of silver nanocompounds also allows to use them for conductive inks in a range of electronic devices. In addition, silver nanoparticles can be used as catalysts of several chemical reactions.

Synthesis. Silver NPs can be synthesized by several physical, chemical and biological pathways. The most common chemical method implies the liquid-phase synthesis through metal precipitation from aqueous or non-aqueous solution. Three main components are required in this chemical synthesis (Fig. 3A): a silver salt (usually $AgNO_3$), a reducing agent and a stabilizer or capping agent (to control nanoparticle growth and avoid aggregation). The most common reducing agents are gaseous H_2, solvated sodium or potassium borohydride ($NaBH_4$ or KBH_4), hydrazine hydrate ($N_2H_4 \cdot H_2O$) and hydrazine dihydrochloride ($N_2H_4 \cdot 2HCl$).

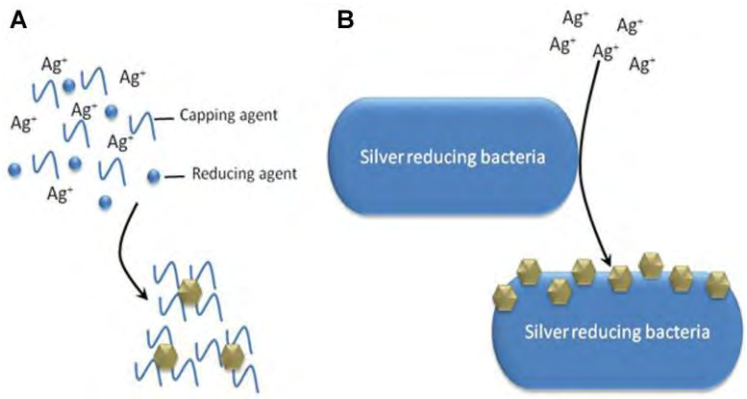

Figure 3. Chemical (A) versus biological (B) synthesis of AgNPs. In the case of chemical synthesis, Ag^+ from the silver salt is reduced by means of a chemical reducing agent. The first nucleus that is formed grows controlled by a capping agent, which also prevents aggregation by steric hindrance or electrostatic repulsion. In the case of biological synthesis, the reducing and the capping agents are both provided by the microorganism, for example a functional group on the bacteria cell wall (Sintubin *et al.*, 2012).

Some other chemical and physical synthetic methods include: microemulsions, supercritical liquids, high-temperature reductions, vapor-phase condensation, laser ablation, photoreduction, electrolysis or irradiation of Ag^+ solutions with visible light, ultraviolet rays, microwaves or ultrasounds (Reicha *et al*., 2012).

Nanobiotechnology offers further possibilities to synthesize AgNPs using environment-friendly procedures, where both the reducing agent and the stabilizer are provided by molecules produced by a living microorganism (Fig. 3B). The reduction may be enzymatic or non-enzymatic, and the stabilizer (or the capping agent) is usually represented by a protein (Sintubin *et al*., 2012). Microbes produce the inorganic particles either intra- or extracellularly (in the cell supernatant),

depending on the localization of the reductive components of the cell, but either way the NPs are collected by a post-production extraction and purification (Narayanan and Sakthivel, 2010). With the help of genetically engineered microbes that overexpress specific reducing agents, it is possible to control size and shape of biological NPs, that result in exquisite morphologies.

Antibacterial activity. Even if the mode of action of silver compounds towards microorganisms is still not fully understood, some multidirectional mechanisms have been proposed and accepted.

In its metallic state silver is inert, but it can get ionized through reaction with moisture or other fluids, hence it can get highly reactive.

Silver ions (Ag^+) are able to penetrate inside bacterial cells and to make DNA molecules turn from relaxed state into condensed form, making them to lose their replication ability that leads to cell death. They also interfere with membrane permeability to protons and phosphate, and interact with proteins inducing their inactivation. Additionally, when Ag^+ binds to respiratory enzymes, it uncouples respiratory electron transport from oxidative phosphorylation and induce the inhibition of respiratory chain (Schreurs and Rosenberg, 1982; Feng *et al.*, 2000).

Silver nanoparticles show enhanced antimicrobial properties compared to silver salts, due to their physicochemical characteristics and their large surface area-to-volume ratio that provides better contact with microorganisms. It is generally believed that three different mechanisms determine the antimicrobial activity of AgNPs: *i*) the direct physical contact between NPs and microbes, that causes structural damages (Kim *et al*., 2007; Sondi and Salopek-Sondi, 2004); *ii*) the generation of reactive oxygen species (ROS), that damage the membrane (Kim *et al*., 2007; Choi and Hu, 2008); *iii*) the slow release of silver ions, which interferes with DNA replication and inhibits enzymes and proteins (Feng *et al*., 2000; Morones *et al*., 2005; Lok *et al.*, 2006; Rai *et al*., 2009). In a recent study it was suggested a shape-dependent interaction between AgNPs and bacterial cells: it was demonstrated an activity-shape correlation toward *E. coli* cells, and truncated triangular silver nanoplates resulted the most effective biocidal nanostructures, compared to spherical and rod-shaped NPs and to silver ions (Pal *et al.,* 2007; Sharma *et al.*, 2009). The fact that NPs are positively charged and microorganism cell membrane is negatively

charged, makes the electrostatic force an additional cause of interaction between NPs and bacteria (Morones *et al*., 2005). Also the cell membrane morphology plays a crucial role: Gram+ bacteria are in fact more difficult to be penetrated as their external layer of rigid and cross-linked peptidoglycan offers few anchoring sites for NPs.

AgNP antimicrobial activity can be summarized as follows (Fig. 4): AgNPs get attached to the cell membrane and penetrate inside the cell causing changes of membrane permeability, perforation and eventually membrane disintegration (Sondi and Solopek-Sondi, 2004); once penetrated, AgNP accumulation in the cytoplasm constitutes an important source of cytotoxic activity, also mediated through the induced oxidative stress and the release of silver ions (Duran *et al.*, 2010).

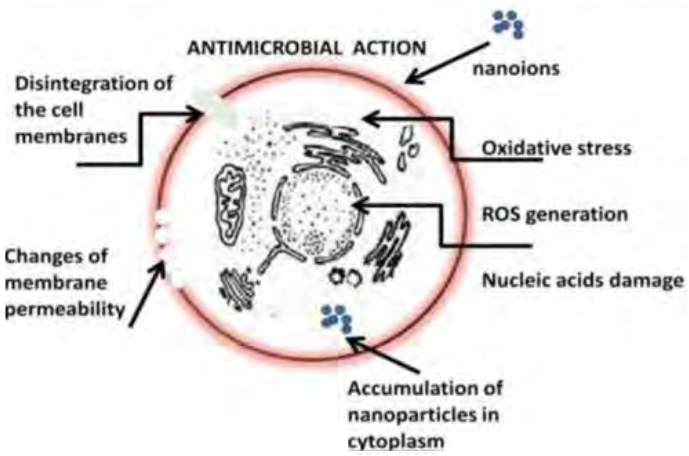

Figure 4. Mechanism of action of silver nanoparticles. AgNPs inhibit the replication of DNA; disturb the electrical potential changing membrane permeability; alter the functioning of cytoplasmatic membranes; cause perforation of the membrane that lead to the outflow of metabolites from the cell; cause loss of bioactivity; disrupt respiratory processes; induce oxidative stress due to the generation of ROS.

In contrast with conventional narrow-target antibiotics, that attack one or few centers in the cell, AgNP multiple and synergic mechanisms of cytotoxic activity make very unlikely for the microorganisms to develop resistance against silver containing compounds (Silver, 2003); it would be necessary that all the mutations required for their protection develop simultaneously.

A possible explanation to the fact that, opposite to microorganisms, human cells are not affected by silver ions might rely on the fact that mammalian cells do not have exterior sulphidryl groups. Ag^+ ions find therefore an external barrier and do not manage to permeate through mammalian cell membranes to react with the interior -SH groups. This fact makes low silver concentrations relatively non-toxic to humans and animals (Shah *et al.*, 2008).

Cultural heritage applications. Nowadays it is possible to engineer synthesis, characterization, surface-modification and functionalization of nanosized silver compounds that would constitute bactericidal materials with enhanced activity for a variety of applications. Even though the protection of cultural heritage materials may constitute one of these applications, from the top of our knowledge only one example of silver nano-compound use in this field have been discussed. Le *et al.* (2010) reported on silver-silica core shell nanoparticles for marine antimicrobial corrosion coating with controlled release. They reasonably envisioned that Ag metal cores would release Ag^+ slowly through the outer porous silica shell, so that Ag leaching would result more efficiently controlled. In their study, they proved that Ag/SiO_2 core-shell composites maintain the excellent antimicrobial effects of the not covered nanoparticles.

2.3 Silane functionalization

The functionalization is the surface modification of the nanoparticles with organic or inorganic ligands, performed to add attractive features to the NPs. Functionalization can improve nanoparticle stability and compatibility with other substrates.

To the purposes of this work, both TiO_2 NPs and AgNPs need to be surface functionalized in order to be grafted to the stone substratum. It is therefore important to think of a proper surface modification for these NPs, basing on the paradigm that compatibility between the conservation treatment materials and the substrate is a fundamental pre-requisite for a good result.

Alkoxysilanes have been selected as the surface modifying agents of choice, and in the following paragraphs it is presented a brief excursus of the reasons why they have been considered adequate reagents for our purposes.

Why alkoxysilanes. The principal conservation practice on deteriorated stones, after accurate cleaning, is the application of consolidation products. Consolidating agents have to meet several criteria: they should be stable, penetrate to sufficient depth, improve stone mechanical properties and avoid changes in the material appearance (Brus and Kotlik, 1996). The agents most often used as stone preservatives are organosilicone compounds, acrylic polymers or epoxy resins (Brus and Kotlik, 1996). Also mixtures of these components should be employed, as the Bologna Cocktail composed of acrylic polymers and silicone (Favaro *et al*., 2007). Polymeric resins though, do not satisfy the requisites of good consolidating agents, as they are not stable enough and degrade rapidly in open air both due to microorganism attack and to thermal- and photo-aging (Yang *et al.*, 2012). In addition, synthetic organic resins are not compatible with the rocky inorganic substrate. Eventually, organosilicone compounds are the most successfully applied in sandstone consolidation. They have high stability and confer good physical and mechanical properties to the material; they also contribute to make the stone surface more hydrophobic, and that is advantageous because the reduced water availability lowers microorganism proliferation (El-Midany *et al*., 2011). It has been calculated

that about 50% of non-functionalized silicon compounds are employed for architectural coatings and mineral consolidation (Zarraga *et al.*, 2002).

Among the organosilicons, alkoxysilanes are the most diffuse consolidant agents, with very good compatibility characteristics with sandstones (inorganic in nature) with respect to polymeric resins (Yang *et al.*, 2012).

Alkoxysilane consolidation is obtained through the sol-gel process of polymerization within the pores of the stone upon contact with environmental moisture. That allows for the formation of a stable silicon-oxygen backbone that strengthen the stone material (Mosquera *et al.*, 2008). The hydrolysis and polycondensation of alkoxysilanes take place following the reaction Schemes 2 and 3. Once penetrated into the material pores, the consolidant undergoes hydrolysis by means of a classic sol-gel process, forming silanol groups (Si-OH) and alcohol, which evaporates (Scheme 2).

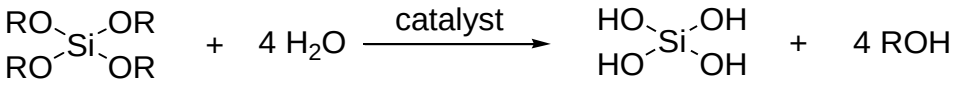

Scheme 2.Hydrolysis reaction of alkoxysilanes: formation of silanol groups and alcohol.

Afterwards, silica gel precipitates inside the porous microstructure by dehydratation/condensation process. In stones composed of silicate phases (*i.e.* sandstones), silica gels can react with the hydroxyl groups present onto the pore surface, forming chemical bounds (Si−O−Si) to the siliceous minerals (Scheme 3) (Sandrolini *et al.*, 2012).

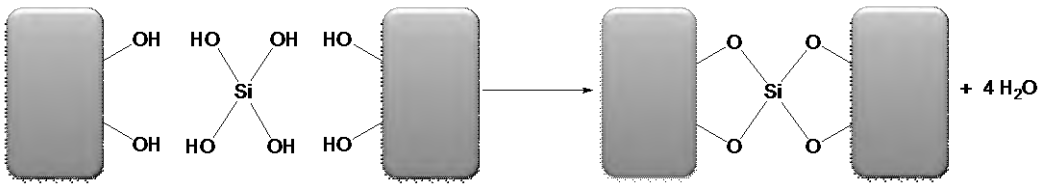

Scheme 3. Condensation reaction between silanol groups and surface hydroxyl groups of the siliceous minerals of the stone.

In the case of carbonatic stones, such as marble, the condensation reaction of the alkoxysilanes takes place with the carbonatic group forming Si−O−C bonds.

The widespread use of alkoxysilanes is therefore justified by their chemical formulation that, unlike many other polymeric consolidants, guarantees stability and provides compatibility with the substrate, because of the inorganic nature of silica (the final reaction product) and volatile by-products (alcohols).

The alkoxysilane characteristics that have been described in the case of stone consolidation also constitute the reason why we chose this class of reagents to surface-modify the NPs. An example of application of these products in the field of protection from biodeterioration is presented in a research work by Nascimbene and Salvadori (2008). They studied lichen recolonization of limestone statues and detected a correlation between the consolidant and the water repellent used and the durability of the treatment. They found that the best performance over time was associated with silicate-based products.

Alkoxysilanes used in this work. Along this thesis work, three kinds of alkoxysilanes were used to surface modify the NPs (either TiO_2 NPs or AgNPs) with the aim to anchor them to the stone surface. Scheme 4 shows their structural formula.

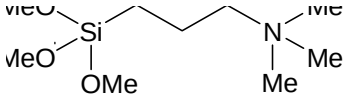

TSPMC

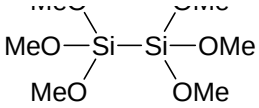

TMDS

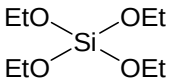

TEOS

Scheme 4. Structural formula of the alkoxysilanes used in this thesis work. TSPMC (N-trimethoxysilylpropyl-N,N,N-trimethylammonium) is a quaternary ammonium silane. TMDS (hexamethoxydisilane) is a disilane. TEOS (hexamethoxydisilane) is the most common alkoxysilane used in conservation science toward lithic materials.

Each one of these alkoxysilanes eventually lead to the formation of the backbone structure indicated in Scheme 5, were the silane acts as the linker between the stone and the nanoparticles. Due to the geometry of each silane, it is not possible that all the alkoxyl group of a single molecule react at once onto a single NP, and unreacted alkoxyl groups expose out of NPs still having the ability to react with the hydroxyl groups present on the stone surface.

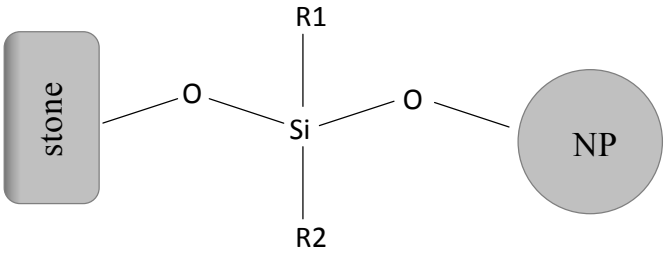

Scheme 5. Schematic representation of the final result obtained after NP functionalization with alkoxysilanes. R1 and R2 are the functional groups, different for each silane used. The silane is grafted to the stone surface through Si−O−Si (silicatic stones) or C−O−Si (carbonatic stones) bonds, and it is linked to the NP through Si−O−Ti (TiO_2 NPs) or Si−O−Ag (AgNPs) bonds.

The following paragraphs briefly present the main characteristics of each of the alkoxysilanes used.

TSPMC. N-trimethoxysilylpropyl-N,N,N-trimethylammonium chloride ($(CH_3O)_3Si\text{-}(CH_2)_3\text{-}N^+(CH_3)_3\ Cl^-$) has been employed to surface functionalize TiO_2 NPs. It is a quaternized aminosilane, able to cross-link on the surface of TiO_2 NPs forming Ti−O−Si bonds through the methoxysilane ends. The silane layer that is formed consequently is able to react with the rocky surface, either silicatic or carbonatic. At the same time, also TSPMC positively-charged end can interact, electrostatically, with the surface of TiO_2 NPs. This approach leaves the methoxysilane ends able to react with the lithic material surface.

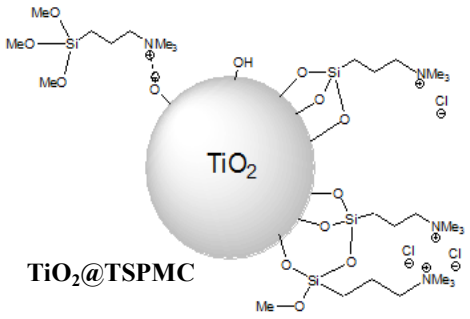

TiO_2@TSPMC

This aminosilane is commonly related in literature to the synthesis of mesoporous silica using an anionic-surfactant template route, where TSPMC works as a co-structure-directing agent. Briefly, mesoporous material syntheses rely on surfactant micelles as templates for the assembly and condensation of inorganic precursors. The alkoxysilane end of TSPMC can co-condense with the silica precursor to form the silica framework, and the ammonium site can interact electrostatically with the negatively charged head group of the surfactant (Che *et al*., 2003; Beaudet *et al*, 2009).

TMDS. Hexamethoxydisilane ($(CH_3O)_3Si\text{-}Si(OCH_3)_3$) is a different methoxysilane used along this thesis work to functionalize TiO_2 NP surface. The use of an alkoxy disilane would guarantee for an higher number of hydrolysable alkoxy groups and therefore an higher probability of NP grafting to the lithic material.

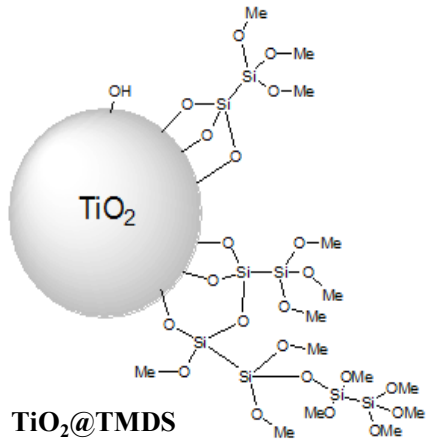

TiO_2@TMDS

The hydrolyzed alkoxy ends react with TiO_2 NP surface through the formation of Ti−O−Si bonds. The resultant alkoxysilane shell that modifies the NP surface is in turn able to react with the rocky substrate, either if it is silicatic or carbonatic.

Silicon alkoxy disilanes with the generic silane monomer type $(OR)_3Si{-}Si(OR)_3$, where −OR group is a hydrolysable alkoxy, have been used before to synthesized bulk-silica based luminescent material (Rodrıguez *et al*., 2012).

TEOS. Tetraethoxysilane ($Si(OCH_2CH_3)_4$) is the alkoxysilane with the most widespread use. We took advantage of its high reactivity to surface functionalize AgNPs in order to create a silane layer over the particle able to react with the rocky substrate.

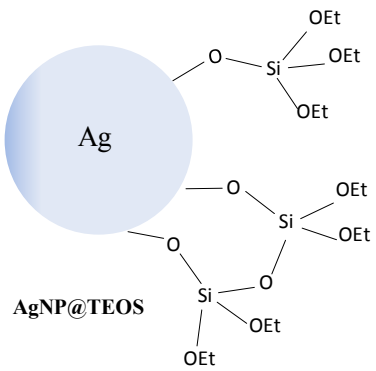

AgNP@TEOS

TEOS is particularly used for ancient building conservation (consolidation) as it proved to be more reactive than other alkylsiloxanes, to have the best re-aggregating effects and to have the deepest penetration into porous substrates due to its low viscosity (Zendri *et al*., 2007). TEOS polymerization occurs when a catalyst is added to the monomer, that otherwise tends to evaporate long before it can react with atmospheric moisture to polymerize (Wheeler *et al.*, 1992). Moreover, the polymerization process is more efficient when an alcohol is added, due to the immediate miscibility between the alkoxysilane and the alcohol (Zarraga *et al*., 2002).

2.4 *Bacillus subtilis* and *Aspergillus versicolor*

Bacillus subtilis has been chosen as the reference bacterium to test the antimicrobial activity of the synthesized NPs both in nutrient medium (either solid or liquid) and on stone material.

A study based on the analysis of a single species is obviously not representative of the real natural occurrence, as microorganisms develop on stones in complex communities formed by different species. Nevertheless, it is a starting point to verify if the synthesized NPs have antibacterial properties and if this property is retained once functionalized and applied on lithic support; interesting information can be derived therefore also from these preliminary studies.

Bacillus subtilis is a rod-shaped, Gram+ bacterium that is naturally found in soil and vegetation. *B. subtilis* has evolved the strategy to form stress-resistant endospores that allow survival under adverse conditions. When the nutrients required for the bacterium to grow are abundant, *B. subtilis* exhibits metabolic activity; when conversely carbon-, nitrogen- and phosphorus-nutrient levels fall below an optimal threshold, it produces spores, slows down its metabolism and remains vital for long time without any nutrient or water requirement (Fajardo-Cavazos and Nicholson, 2006). Endospores are easily spreadable and highly resistant, not only to extreme environmental conditions but also to antibiotics and many other chemical substances. Among genus *Bacillus*, *B. subtilis* was found to be more resistant to disinfection (Gutarowska *et al.*, 2012).

B. subtilis is not only commonly considered as a model organism to study endospore formation in bacteria, but also as a model for biofilm formation. Different *B. subtilis* strains are able to secrete two distinct polymers: polysaccharide EPS and poly-d-glutamate (Lopez *et al*., 2010). These polymers participate in the biofilm formation process by different extent, depending on the strain and the surrounding conditions. *B. subtilis* expresses a single major protein associated with the extracellular matrix, named TasA; it has been shown to form extracellular filaments with amyloid-like properties, thought to play a key structural role in the extracellular matrix (Romero *et al*., 2010).

Bacillus related bacteria have been frequently identified on cultural heritage stones (Mc Namara, *et al.*, 2005; Scheerer *et al.*, 2009; Gutarowska *et al.,* 2012). It acts as a stone deteriogen both through organic acid production and mechanical action, similarly to many other heterotrophic microorganisms that coexist in the biofilm biomass.

A different bacterial strain that has been employed in some experiments along this thesis work is *Escherichia coli*, the most widely used bacterium in laboratory research and the most thoroughly studied life form. It is a Gram− bacterium, and we used it as a counterpart of the Gram+ *B. subtilis*. *E. coli* is a rod-shaped bacterium propelled by long, rapidly rotating flagella, and it normally inhabits the intestinal tracts of animals. For this reason it can be found in soil and water.

Fungi are nonetheless important components of microbial communities, colonizing different types of building stones in environments ranging from temperate to tropical settings (Scheerer *et al.*, 2009). Among them, we performed some studies on *Aspergillus versicolor*. It is an ubiquitous air-borne fungus widely distributed in nature, mostly on substrates exposed to humid conditions, and it is toxic and pathogenic both for humans and animals. *A. versicolor* is highly aerobic and is therefore found in almost all oxygen-rich environments, where it commonly grows as molds over the surfaces. It is one of the most common microfungi isolated from mineral substrates, and it is able to produce acid metabolites (gluconic, oxalic, acetic, butyric, lactic), oxidize minerals, chelate metallic cations and produce exogenous pigments, causing green staining. In addition, the ability of fungal hyphae to attack and penetrate mineral substrates creates defects in the structure of the materials, *i.e.* micro- and macroscopic cracks, deformations, roughness, stains and crusts. As a result, the porous material loses its original character (Simonovicova *et al*, 2004; Guiamet *et al*, 2013).

Occurrence in cultural heritage field. The following paragraphs present some examples of research works in which *Bacillus* and *Aspergillus* genera were encountered on monumental stones.

Bacteria from genus *Bacillus* were detected on the biofilms originated on the salted ceiling of a tunnel at the Mayan site of Edzna, Mexico (Ortega-Morales *et al.*, 2005). Another example of *Bacillus* genus on cultural heritage material is constituted

by the sandstone monuments in Akgkor Wat temples, Cambodia, where *Bacillus* was identified in the microbial biofilms on monument surfaces (Gaylarde *et al*., 2012). *Bacillus* genus was also found in the biofilms covering the surface of paleolithic caves in Zuheros, Spain (Urzì *et al*., 2010). In that habitat, chemoorganotrophic bacteria (90% prevalence of Gram+ bacteria) were closely associated to phototrophic microorganisms. *Bacillus* was identified as the main bacterial strain associated with mineral precipitates of white fluffy biofilm covering deteriorated surfaces of caves and catacombs. In a recent study, *Bacillus* was shown to actively participate in the precipitation of mineral phases (De Leo *et al.*, 2012). From microbiological sampling and identification on funeral sculptures in Argentina (Guiamet *et al.*, 2013), *Bacillus* and *Pseudomonas* were the most commonly isolated bacteria genera. In the same sites, the fungal genera most commonly represented were *Aspergillus*, *Alternaria* and *Penicillium*.

Bacillus genus was also found as an indoor biodeteriogen at the museum archive of La Plata, Argentina (Guiamet *et al*., 2011); the complex enzyme system of the proteolytic activity of *Bacillus* species was found to be able to degrade fibrous and non-fibrous components of paper. Among the fungal genera, in the same archive *Aspergillus* was the prevailing fungus on photographs and maps (Guiamet *et al*., 2011). *Aspergillus* genus was isolated from the mycobial survey of the ancient Temple group of Satmahla (India) as one of the dominant fungal type responsible for biodeterioration. Its proliferation was contrasted in that situation through regular cleaning and the use of fumigants (Sharma and Verna, 2011). *Aspergillus* and *Bacillus* genera were encountered in the biofouling occurred in the valuable crypts of La Plata cemetery in Argentina. The appearance of biofilms and fungal colonies was particularly serious as it resulted not only in aesthetic deterioration but also in the loss of historical information, since it has become impossible to read some of the inscriptions engraved in the stones (Guiamet *et al.*, 2012).

2.5 Serena stone

Serena stone is a gray colored clastic sedimentary rock composed mainly of sand-sized minerals or rock grains. It is a sandstone (arenite) ascribable to feldspathic greywacke with an abundant clay matrix and poor cement.

It is a very compact and tough material but it is porous as well, with 5-10% open porosity (Dei *et al*. 1999). Nowadays it is principally caved form Firenzuola quarry, Italy (Fig. 5).

Figure 5. Firenzuola quarry. Serena stones are principally caved from that site.

This kind of rock has been cited in literature since mid XVI century, and maybe also Dante Alighieri cited it. Even if Etruscans used Serena stone for fortification walls, it is in Renaissance period that this lithotype found its maximum expression and application in stone-based constructions, especially in Florence. Some admirable architectural examples in which Serena stone has been used are “Ospedale degli Innocenti”, “Medicea Laurenziana library” or “Uffizi” museum (Fig. 6a).

Besides for architectural purposes, Serena stone has been used also for architectural decoration and sculptures, such as "Annunciazione Cavalcanti" (Fig. 6b).

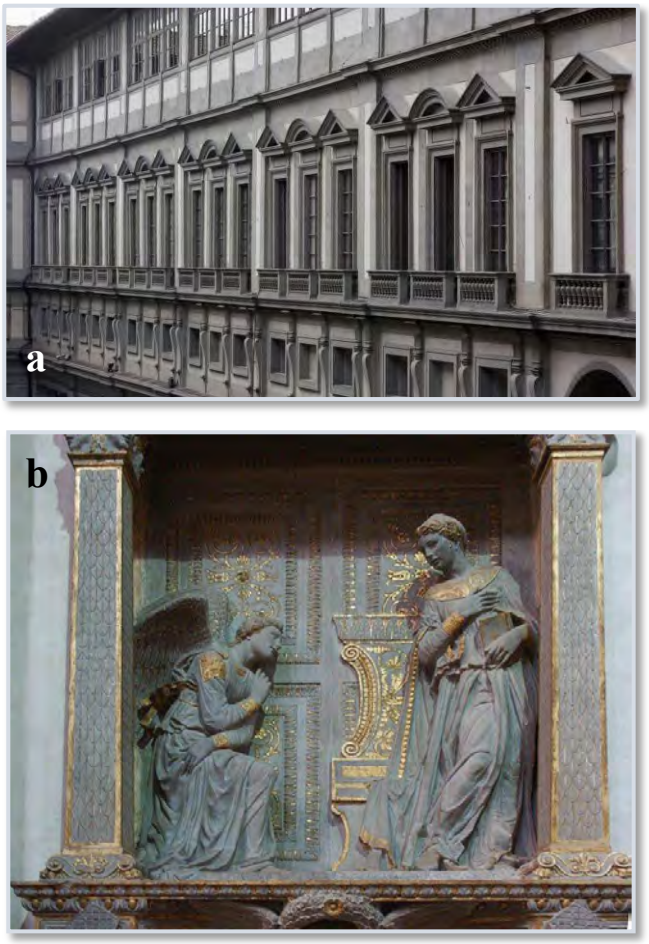

Figure 6. a) Uffizi, the main Florence museum and one of the most important worldwide for the exposed collections. It is made of Serena stone. **b)** Annunciazione Cavalcanti (Donatello, 1435, Santa Croce, Florence). It is engraved in Serena stone.

Because it is a very resistant material, Serena stone was also used for paving entire cities, such as Florence, Siena or Arezzo (Tuscany).

When Serena stone is used in cultural heritage objects, it is subjected to be weathered and eroded by the same physical, chemical and biological agents as the rocks in natural environments. In particular, microbial biofilm formation is relevant on this lithotype because it is quite porous. On the other hand, because quartz minerals (SiO_2) that compose sandstones are rather insoluble at pH 3-9, the acidification produced by microbial colonization plays a minor role in weathering

Serena stone (Palmer *et al*., 1991). However, sandstones are composed of other substances besides quartz, as the clay minerals that constitute the binders; the organic acids anions produced by microorganisms as metabolites (citrate, pyruvate, malate, succinate, lactate, formate, fumarate, oxalate) are known to chelate mineral cations and dissolve minerals themselves (Palmer *et al*, 1991). That aspect has a relevant impact on the physicochemical weathering process of Serena stone, more than the actual acidification of the substrate.

Chapter 3.
Experimental: synthesis and characterization methods

In the following section we are going to describe the analytical methods used to characterize TiO_2 NPs and AgNPs both from chemical and microbiological point of view. The synthetic procedures and the experimental conditions are fully explained, along with the reagents used and the instrumental setups. Insights of the more complex techniques used during this thesis can be found in the Annex, where explanations of the concepts underlying these techniques and their basic theoretical background are discussed.

3.1 Chemical analysis - TiO_2

This subsection is devoted to summarize the synthetic pathways used to obtain pristine and functionalized TiO_2 NPs and the analytical chemical techniques and instrumental conditions used to characterize the nanosystems and the stone surface.

3.1.1 Synthetic procedure

Reagents. All chemicals were used as received, without any further purification.

Titanium (IV) sulfate aqueous solution ($Ti(SO_4)_2$, 15% w/v) was supplied by Fisher Scientific. Aqueous ammonia solution (NH_4OH, 33%), ethanol (C_2H_5OH, > 99%), methanol (CH_3OH, > 99%), 2-propanol (≥ 99.8%), tetramethylammonium hydroxide (TMAOH, 25% wt.), hydrogen peroxide (H_2O_2, 30%) and chloroform ($CHCl_3$, ≥ 99%) were purchased from Sigma Aldrich. Methylene blue (MB, 98.5%) and chloroform (> 99.8%) were provided from Carlo Erba.

N-trimethoxysilylpropyl-N,N,N-trimethylammonium chloride solution in methanol (TSPMC, $(CH_3O)_3Si\text{-}(CH_2)_3\text{-}N^+(CH_3)_3\ Cl^-$, 50% in methanol) and hexamethoxydisilane (TMDS, $(CH_3O)_3Si\text{-}Si(OCH_3)_3$, 90%) were supplied from ABCR. MilliQ water (18.2 MΩ/cm) was used throughout all the synthetic steps.

Nanoparticles synthesis. TiO_2 colloidal dispersions were prepared following a solvothermal approach (Liao *et al.*, 2009). Briefly, 40 ml of $Ti(SO_4)_2$ 15% w/v were diluted with MilliQ water to obtain a 0.2 M titanium (IV) sulfate solution.
The pH value was adjusted to 8 slowly adding aqueous ammonia under stirring. A white precipitate immediately formed. The mixture was aged for 20 h at room temperature and the precipitate was collected by filtration and washed until the electric conductivity of washing waters was below 100 μs/cm. The filtrate was dispersed in 200 ml of water/alcohol mixtures (the alcohol being either ethanol or methanol, see Table 1).

Table1. Sample names of the colloidal dispersions obtained performing a solvothermal synthesis with different reaction mixtures. E = ethanol, W = water, M = methanol. A representative picture of the resultant dispersion of TiO2 NPs is dispayed on the right of the table.

TiO_2 sample names	**$V_{water}/V_{alcohol}$**
S_E	0:1
$S_{WE0.25}$	1:4
S_{WE1}	1:1
S_{WE4}	4:1
S_W	1:0
$S_{WM0.25}$	1:4
S_{WM1}	1:1
S_{WM4}	4:1
S_M	0:1

The dispersion was placed in an ice-water bath and 2.5 ml of H_2O_2 30% were added dropwise under continuous stirring. The resulting yellow mixture was refluxed at 78 ˚C for 4 h and then transferred to an autoclave were it was kept at 120 ˚C for 15 h. The nanoparticles were collected by centrifuge (1 h at 10800 g) and then re-dispersed in 200 ml of MilliQ water (Fig. 7).

Figure 7. A representative batch of TiO_2 pristine nanoparticles.

Surface functionalization. The surface modification has the aim to enable the nanomaterial to be grafted to the stone surface. The reaction was performed using TiO_2 powders collected by freeze-drying the colloidal dispersions (from each different synthetic solvent combination). The surface functionalization process was carried out using two different alkoxysilanes: N-trimethoxysilylpropyl-N,N,N-trimethylammonium chloride (TSPMC) and hexamethoxydisilane (TMDS). The surface modified NPs are referred to as TiO_2@TSPMC or TiO_2@TMDS.

In a typical synthesis, 20 mg of TiO_2 powder were dispersed in 4 ml of methanol, adjusting the pH to 8 by adding NH_4OH. The effectiveness of the surface modification process was studied as a function of temperature and reaction time, and the best results were obtained at 50 ˚C for 17 h, respectively. Functionalized nanoparticles were collected by centrifuge and washed twice with 2 ml chloroform to remove the unreacted alkoxysilane. Different amounts of alkoxysilane were then added to the dispersion to reach the desired percentage of surface coverage.

3.1.2 Characterization techniques

SAXS and WAXD. Small angle X-Ray scattering (SAXS) was used to determine size and polydispersity of the TiO_2 nanoparticles in the as-prepared colloidal dispersions, whilst wide angle X-ray diffraction (WAXD) was used to preliminarily detect their crystallographic phase. Simultaneous SAXS/WAXD measurements were carried out with a HECUS SWAX-camera (Kratky) equipped

with a position-sensitive detector (OED 50M) containing 1024 channels of 54 μm width. Cu K_α radiation of wavelength λ = 1.542 Å was provided by a Seifert ID-3003 X-ray generator (sealed-tube type), operating at a maximum power of 2 kW. A 10 μm thick Ni-filter was used to remove the Cu K_β radiation. The sample-to-detector distance was 275 mm. The volume between the sample and the detector was kept under vacuum (P < 1 mbar) during the measurements to minimize the scattering from air. The Kratky camera was calibrated in the small angle region using silver behenate (d = 58.38 Å) (Huang *et al*., 1993) and in the wide angle region using the two strongest reflections (110 and 200) of isotropic high density polyethylene, HDPE (Lupolene) (Rueda *et al*, 2006). Scattering curves were obtained in the Q-range, $Q=(4\pi/\lambda)\sin 2\theta$, between 0.01 and 0.54 $Å^{-1}$, Q being the scattering vector, and 2θ the scattering angle, while WAXD angular range spanned from about 18 to 28° in 2θ. Liquid samples were filled into a 1 mm glass capillary and sealed with an epoxy glue, while powdered samples were filled into a 1 mm demountable cells having Kapton films as windows. All samples were monitored at 25 °C, temperature being controlled by a Peltier element (accuracy ± 0.1 °C). All scattering curves were corrected for the background contribution. Additionally, SAXS patterns were iteratively desmeared using the procedure reported by Lake (Lake, 1967). Error bars for each intensity point were calculated as the square root of the absolute intensity (I) value. Some theoretical background of these techniques is reported in the Annex.

SAXS profiles were fitted using the unified model, developed by Beaucage (Beaucage, 1995; Beaucage, 1996; Beaucage *et al*., 2004). The unified equation describes complex nanostructured systems in terms of consecutive structural levels. Each level corresponds to a Guinier regime (Guinier *et al.*, 1995) combined with a power law function associated to the Porod regime of that structural level or to the fractal scaling law of the greater structural level. The global unified scattering function is (Beaucage, 1995; Beaucage, 1996):

$$I(q) = bkg + \sum_{i=1}^{N} G_i \exp\left(\frac{-q^2 Rg_i^2}{3}\right) + B_i \exp\left(\frac{-q^2 Rg_{i-1}^2}{3}\right)\left(q^*\right)^{-P_i}, \quad q^* = \frac{q}{\left[erf\left(kqRg_i/\sqrt{6}\right)\right]^3}$$

where *bkg* is an instrumental background, *N* is the number of single polydisperse structural levels present in the investigated system, *G* is the Guinier prefactor, R_g the radius of gyration, *B* is a prefactor specific to the type of power-law scattering, *P* is the power-law exponent and *erf( )* is the error function. If the higher level is not associated with the previous smaller size level, Rg_{i-1} is set to zero. In general $k = 1$, while in the case of mass fractal behavior *k* is set to 1.06.

In the Unified approach, the polydispersity is directly obtained from a dimensionless parameter associated with the fitting results (Beaucage *et al.*, 2004). In particular, the ratio BR_g^4/G is indicative of the polydispersity index (PDI) of the nanoparticle distribution. This value can thus be obtained from *B* and *G* even if the SAXS intensity is in arbitrary units as their ratio cancels out the undetermined prefactor.

The fitting was performed by using the Irena analysis package (Ilavsky and Jemian, 2009), version 2.40, running on IGOR pro 6.2. The unified approach has been limited only to two levels of complexity: the aggregates (Level 2) and the sub-units (Level 1). In all cases P_1 is equal to 4 as expected for smooth particles (Porod regime), while P_2 varies from 3 to 4. G_2 and R_{g2} cannot be extracted due to the limited Q range associated with the SAXS experiment and consequently the P_2 value does not have any physical meaning.

HRTEM. The nanoparticle morphologies were studied by means of high resolution transmission electron microscopy (HRTEM). The images were recorded on JEM 3010 (JEOL) electron microscope operating at 300 kV. In order to keep the specimen stable under such an energetic beam, a cryogenic holder was used (cooled with liquid nitrogen). The lens parameters were Cs = 0.6 mm, Cc = 1.3 mm, giving a point resolution of 0.17 nm at Scherzer defocus. A few milligrams of the specimen were sonicated for 5 min in order to disrupt possible agglomerates. A 5 mL droplet of suspension was transferred onto an amorphous carbon film, coating a 200 mesh copper grid, dried at room temperature, and then put into the microscope.

Moreover, the diffraction pattern that was originated from a selected area of the specimen was enlarged, displayed and recorded to obtain average crystallographic information (**SAED**, selected area electron diffraction analysis). Insights of these techniques are given in the Annex.

XRD. X-ray powder diffractograms were recorded to assess crystallographic phases and crystallite sizes of the nanoparticles under study. Measures were performed at 295 K, with a step size of 0.05°, on a 20–50° 2θ angular range using Philips X'Pert vertical goniometer connected to a highly stabilized generator, Cu Kα Ni-filtered radiation, a graphite monochromator, and a proportional counter with a pulseheight discriminator. The background of this technique is summarized in the Annex.

ATR-FTIR. Fourier Transformed Infrared Spectroscopy operating in Attenuated Total Reflectance mode (Nexus 870 spectrophotometer equipped with a MCT-A detector, Thermo Nicolet, Paris, France) was performed to study the functionalization extent of the nanoparticle surface. Spectra of the as-prepared and of the surface-modified powders were collected using 64 scans at 4 cm^{-1} resolution in the 650-4000 cm^{-1} range.

TGA. Thermal degradation of both pristine and functionalized nanoparticles was studied by means of thermogravimetric analysis (TGA) on a SDT Q600 apparatus (TA instrument, Milan, Italy). The powders were first isothermally equilibrated at 100 ˚C for 10 min in order to remove physisorbed water and then heated up to 750 ˚C under nitrogen atmosphere at a heating rate of 10 ˚C/min.

Arc lamp and UV-Visible spectrophotometry. The photocatalytic activity of the nanoparticles was studied by UV-irradiating a 2-propanol dispersion of TiO_2 nanoparticles (TiO_2 0.005% w/v) and methylene blue (MB, 0.01 mM). The samples, contained in 10 mm path length quartz cells (Hellma), were irradiated with an Oriel Arc Lamp Source equipped with a Hg(Xe) lamp operating at 130 W. The UV source was equipped with a 35 mm water filter and focused to irradiate the sample. The evolution of MB concentration was measured by UV-visible spectrophotometry in the 450 - 750 nm range (Cary 100 Bio Varian spectrophotometer), the spectra being recorder at different time points up to 150 s from the beginning of sample irradiation.

This arc lamp, filtered at 365 nm, was used also to irradiate stone samples treated with TiO_2 NPs and their corresponding negative controls.

Pen lamp. Spectroline 36-380 ultraviolet quartz pencil lamp is a mercury-vapor (Hg(Ar)) discharge lamp which uses mercury line spectrum. It is accessorized with a short pass filter that absorbs the visible lines and a long pass filter that converts short-wave radiation to long wave radiation, due to the coating with conversion phosphors that absorb the 254 nm line converting this energy into a band peaking at 365 nm. Its average intensity is 1 mW/cm^2 at 2.54 cm distance. UVA intensity in sunny daylight is about 4.0 mW/cm^2, and decreases to 0.4 mW/cm^2 in cloudy condition (Kangwansupamonkon *et al.*, 2009). This irradiation source was used in most microbiological assays to photoactivate TiO_2 NPs (with the exception of tests performed on stone surface).

SEM. Scanning electron microscopy (SEM) experiments were carried out with a Stereoscan 360, Cambridge (detector SE). The energy dispersive X-ray microanalysis (EDS) to detect the elemental composition of the material was performed using an INCA 300 X-sight, Oxford. Stone samples were functionalized with 0.4 mg/cm^2 nanoparticles ($TiO_2(S_M)$@TMDS). Theoretical background of this technique is given in the Annex.

AFM. Atomic force microscopy (AFM) images were collected using a Park XE-100 microscope in non-contact mode (SSS-NCHR probes, nominal resonant frequency 330 kHz, radius of curvature < 5 nm). Stone specimens treated with silane-modified TiO_2 nanodispersions were analyzed before and after a washing treatment. Stone samples were functionalized with 0.4 mg/cm^2 nanoparticles ($TiO_2(S_M)$@TMDS). Insights of this technique are summarized in the Annex.

3.2 Chemical analysis - AgNPs

This subsection is devoted to the description of the reaction conditions used to obtain pristine and functionalized AgNPs and to the overview of the chemical techniques used to characterize the surface of AgNP-treated stone samples.

3.2.1 Synthetic procedure

Reagents. All chemicals were used as received, without any further purification. Silver nitrate ($AgNO_3$, > 99%), poly(sodium styrenesulphonate) (PSSS, 1000 KDa), sodium borohydride ($NaBH_4$, > 99%), ascorbic acid, trisodium citrate, tetraethylorthosilicate (TEOS) (> 99%) were supplied by Sigma-Aldrich. Ammonium hydroxide (30%) and 2-propanol were purchased from Panreac. All solutions were prepared in MilliQ water (18.2 MΩ/cm).

Nanoparticles synthesis. Silver nanoparticles were synthesized according to a seed-based procedure that results in the formation of triangular nanoprisms (Aherne *et al*., 2008).

Figure 8. Pictures taken at different stages of nanoparticle growth, from seeds (light yellow solution) to the final nanoprisms (blue solution).

Silver seeds were prepared combining 5 mL of aqueous trisodium citrate (2.5 mM), 0.250 mL aqueous poly(sodium styrenesulphonate) (500 mg/L), 0.3 mL of aqueous sodium borohydride (freshly prepared, 10 mM), followed by addition of 5 mL of aqueous silver nitrate (0.5 mM, added at a rate of 2 mL/min under stirring). Nanoprism growth was achieved by combining 150 mL of water, 2.25 mL of aqueous ascorbic acid (10 mM) and 3.6 mL of seed solution, followed by the addition of 90 mL aqueous silver nitrate solution (0.5 mM) at a rate of 1 mL/min under stirring. Figure 8 shows the AgNP dispersions at different stages of the synthesis, during the addition of increasing amounts of $AgNO_3$ 0.5 mM.

After the synthesis, 15 mL of aqueous trisodium citrate (25 mM) were added to stabilize the dispersion and avoid aggregation or precipitation of the nanoprisms. The solution obtained is referred to as pristine nanodispersion or naked nanoparticle dispersion.

Surface functionalization. The surface modification with an alkoxysilane derivative has the aim to graft the nanosystem to the lithic material, in order to make the nanoremedy able to resist to stressing conditions such as rain water washing. Pristine nanoprisms were functionalized using a modified procedure inspired to a known literature approach (Niitsoo *et al*., 2011). The grafting agent used was a layer of tetraethyl orthosilicate (TEOS), ideally thick as one alkoxysilane molecule (AgNP:TEOS 20:1 w/w). The desired amount of pristine aqueous AgNPs was concentrated up to the volume of < 200 μL using centrifugal concentrators (Vivaspin 20, Sartorius Vivascience MWCO 3,000 Da, 20 mL; Amicon 500, Merck Millipore, Amicon Ultra 0.5 mL) and diluted to the final reaction volume with 2-propanol (4:1 V/V, 2-propanol:aqueous solution of AgNPs). A TEOS solution diluted in 2-propanol (i-PrOH) was added to the AgNP dispersion while stirring. Immediately after, the growth of the silica coating was initiated by the rapid injection of an aqueous dimethylamine solution (DMA, final concentration 0.4 M) into the AgNP/TEOS colloidal dispersion (Kobayashi *et al*., 2005*;* Niitsoo *et al*., 2011). The amine was used as the catalyst for TEOS hydrolysis and its condensation into SiO_2. The mixture was stirred for 30 min at room temperature and concentrated to the

desired volume by N_2 insufflation. The functionalized nanoparticle dispersions (AgNP@TEOS) were resuspended by sonication before using.

3.2.2 Characterization techniques

SEM. Scanning electron microscopy (SEM) experiments were carried out with a field emission gun (FEG)-SEM, mod. ΣIGMA by Carl Zeiss, working at 8 kV of acceleration potential. Images were acquired by collecting back-scattered electrons (BSE) to highlight the differences in lightness of high atomic weight atoms (silver) with respect to lighter elements (calcium) and by collecting secondary electrons with an in-lens detector, when working at higher magnifications. Stone samples (1.5 X 1.5 X 0.3 cm) were functionalized with 30 μg/sample pristine or functionalized nanoparticles. Theoretical background of this technique is given in the Annex.

AFM. Atomic force microscopy (AFM) images were collected using a Park XE-100 microscope in non-contact mode (SSS-NCHR probes, nominal resonant frequency 330 kHz, radius of curvature < 5 nm). Stone samples (1.5 X 1.5 X 0.3 cm) were functionalized with 30 μg/sample pristine or functionalized nanoparticles. Stone control samples were treated only with TEOS solution (TEOS being in the same concentration as for the corresponding AgNP@TEOS-treated samples). Insights of this technique are summarized in the Annex.

Colorimetric measurements. Color changes induced by the presence of AgNPs were evaluated by means of colorimetric measurements. The light reflected by the sample (1 mm^2 spot) was collected with of a fiber-optic cable (FRP series) and recorded with a high sensitivity CCD camera. Colorimetric data were collected using standard illuminant C and standard observer CIE 1931 (2°) in a λ range 400-700 nm and with a 0°/0° geometry, operating conditions being derived from UNI NORMAL 43/93 recommendations (Raccomandazioni NorMal, 1993). The specimens were analyzed in two different stone regions, three measurements being taken for each region. The colorimetric coordinates L^* (lightness), a^* (red-green coordinate), b^* (yellow-blue coordinate) were averaged out to obtain a single value for each

specimen. The resultant chromatic change (ΔE) was determined through the following equation:

$$\sqrt{L^2 \quad a^2 \quad b^2}$$

Δ indicating the difference between the coordinates of the treated and untreated samples.

3.3 Microbiological analysis

This section is focused on the description of the experimental conditions used to grow bacterial and fungal strains.

Reagents. All the reagents used in microbiological assays were sterilized before use. The sterilization was performed either by autoclave humid heat method (Vapormatic), keeping reagents and materials for 15 min at 120 °C, or by dry heat method, using a dry heather at 160 °C for 3 h. The autoclave method was principally used to sterilize culture media (liquid or solid), saline solution, water and plastic materials (*i.e.* Gilson tips, Eppendorf tubes), whilst the dry method was principally used to sterilize glass materials, such as flasks or glass beads.

Luria-Bertani broth (LB, NaCl 10g/L (Merck), Yeast Extract 5 g/L (OXOID), bacto-triptone 10 g/L (DIFCO laboratories)) and Nutrient Broth (NB, OXOID, 13 g/L) were used as liquid growth medium for bacteria, while Sabouraud Dextrose (OXOID, 30 g/L) was used for fungal growth. Nutrient Agar (NA, OXOID, 28 g/L) and LB-agar (1.5 % w/v agar) were used as solid growth medium for *B. subtilis* and *E. coli,* respectively. Malt Extract Agar (MEA, OXOID, 50 g/L) was used as solid medium for fungal growth. Saline solution was prepared with 0.85% w/v NaCl (Merck) in distilled water.

Microorganisms and growth conditions. The microorganisms used in this thesis work were grown by classical microbiological culture techniques.

Bacterial cultures of *B. subtilis* strain 168 (genotype: *trp C2,* Fig. 9a) (Anagnostopoulos and Spizizen, 1961) were prepared in 100 mL flasks by inoculating a single bacterial colony into NB medium.

Cultures of *E. coli* strain DH5α (Fig. 10a) were prepared in LB medium. Bacterial cultures were aerobically incubated on a rotary shaker at 30 °C and 120 rpm for 18 h.

To determine the culture viable count, the microbial suspension was serially 10-fold diluted in saline solution and 100 μL of dilutions were spread on NA plates (*B. subtilis*, Fig. 9b) or LB-Agar plates (*E. coli*, Fig. 10b). Colony formant units (CFU) were counted after 24 h incubation at 37 °C. In such growth conditions, the viable count of the overnight culture was about 10^8 CFU/mL for *B. subtilis* and 10^9 CFU/mL for *E. coli*.

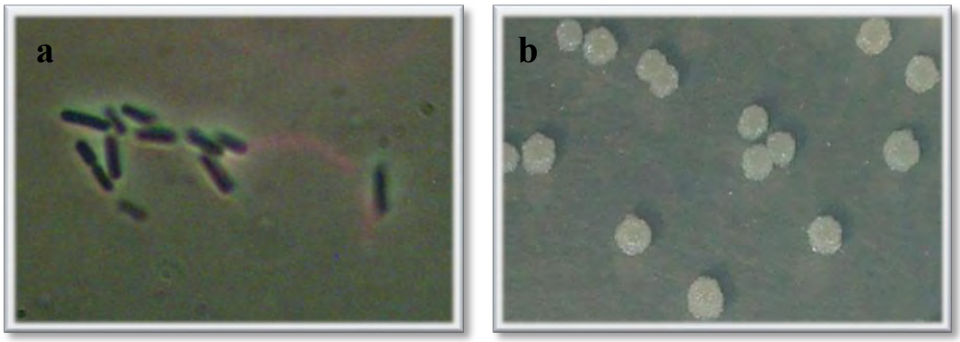

Figure 9. a) Optical microscopy (Nikon SMZ-1, 1000X) image of *B. subtilis* cells. Bacteria present the typical rod shape. **b**) Stereomicroscope (Nikon ALPHAPHOT-YS, 10X) morphology observation of *B. subtilis* colonies on NA solid medium.

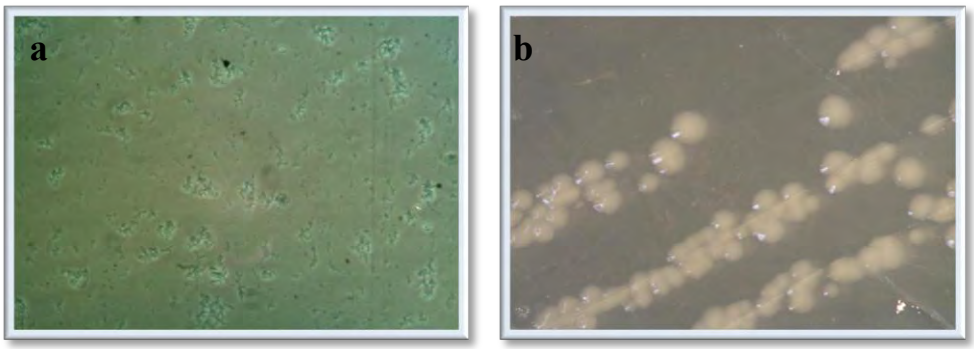

Figure 10. a) Optical microscopy (Nikon SMZ-1, 400X) image of *E. coli* cells. **b)** Stereomicroscope (Nikon ALPHAPHOT-YS, 8X) morphology observation of *E. coli* colonies on LB-agar medium.

Aspergillus versicolor, strain M2 (Figg. 11 a, b) and *Sarcinomyces petricola*, strain M4 (Figg. 11 c, d) were isolated from the statue "Il ratto delle sabine" from Giambologna (1580), Piazza della Signoria, Firenze. They were allowed to grow in Saboraud Dextrose liquid medium and on MEA solid medium.

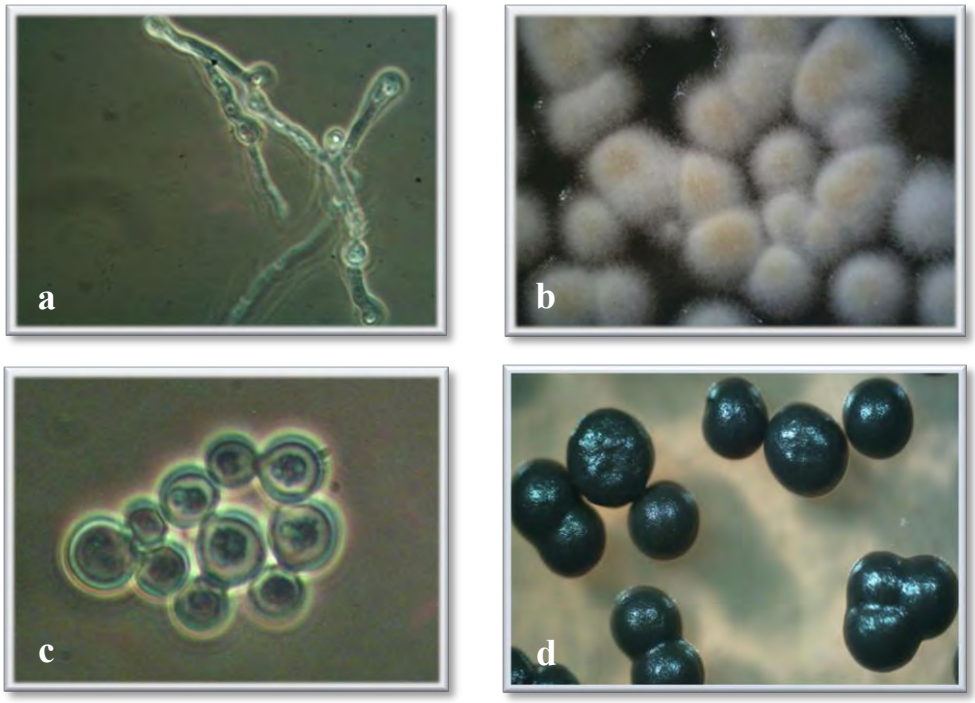

Figure 11. a, c) Optical microscopy (Nikon SMZ-1, 1000X) image of *A. versicolor* fungal hyphae and *S. petricola* cells, respectively. **b, d)** Stereomicroscope (Nikon ALPHAPHOT-YS, 30X) morphology observation of *A. versicolor* and *S. petricola* colonies, respectively, on MEA solid nutrient medium.

3.4 Microbiological methods – TiO_2

This section regards the description of microbiological methods used to assess the microbiocidal effect of TiO_2 NPs, either surface modified or not. The tests were performed both on nutrient medium and directly on stone surface.

Antibiogram. The antibiogram method was performed with different concentrations of TiO_2 NPs, either laboratory synthesized or purchased (Sigma Aldrich anatase TiO_2 NPs) (Fu *et al*., 2005). 0.1 mL of 10^7 CFU/mL of *E. coli* or *B.*

subtilis suspension were plated on LB-Agar or NA dishes, respectively, and allowed to dry for 10 min. The experiment was performed in duplicate. 10 μL spots of TiO_2 NP solution ($TiO_2(S_M)$) at different concentration (125 mM, 12.5 mM, 1.25 mM, 0.125 mM) were dropped on the plated bacteria along with 10 μl spot of water and 5 μl spot of Ampicillin (5 mg/ml) used as negative and positive controls, respectively. The test dishes were irradiated for different time periods (20 min, 1 h, 5 h) with a black-light lamp (Pen-lamp, see section 3.1.2) peaking at 365 nm, whilst the control dishes were kept in dark conditions. All the samples were incubated at 37 °C overnight and the results visually determined.

Antibacterial activity in solution. Besides the antibiogram method, another common test to evaluate TiO_2 NP capability of killing bacteria is to UV-irradiate TiO_2-bacteria slurries and plate sample aliquots withdrawn at different irradiation times (Huang *et al*., 2000; Swetha *et al*., 2010).

Overnight culture of *B. subtilis* or *E. coli* were harvested by centrifugation (5 min, 11000 rpm, 4 °C), washed several times with sterile water and re-suspended in 10 mL sterile water. The bacterial viable counts of these suspensions were about 10^7 CFU/mL (*B. subtilis*) and 10^8 CFU/mL (*E. coli*).

1 ml of the bacterial water suspension, 1 mL of TiO_2 NPs (TiO_2 $S_{(M)}$ or TiO_2 $S_{(M)}$@TMDS 125 mM) and 6 mL sterile water were added in a sterile glass Petri dish (test dish). This slurry was UV irradiated for different time periods (10 min, 15 min, 30 min, 1 h, 1 h 30 min, 2 h, 3 h, 5 h) while stirring. Another glass Petri dish (control dish) with 1 mL bacterial suspension and 7 mL water was used as negative control under the same irradiation conditions. The irradiation source was a Pen Lamp (see 3.1.2 section) peaking at 365 nm placed at such a distance to have a light intensity reaching the solution of 1 mW/cm^2. After the desired irradiation time interval, 100 μL suspensions from each Petri dish were serially diluted (up to 10^{-4} dilution) and plated. Cell viability was determined by colony counting after 24 h incubation. The initial microbial count (before any irradiation treatment) was evaluated withdrawing 100 μL suspension from one of the dishes not containing NPs and plating 10^{-3} and 10^{-4} dilutions. The plates were visually counted after overnight incubation. The effect of the UV irradiation by itself was evaluated by keeping a test

dish (supplied with NPs) and a control dish (with no NPs) in dark conditions for the same time periods as the irradiated dispersions.

The experimental setup is schematically shown in Scheme 6.

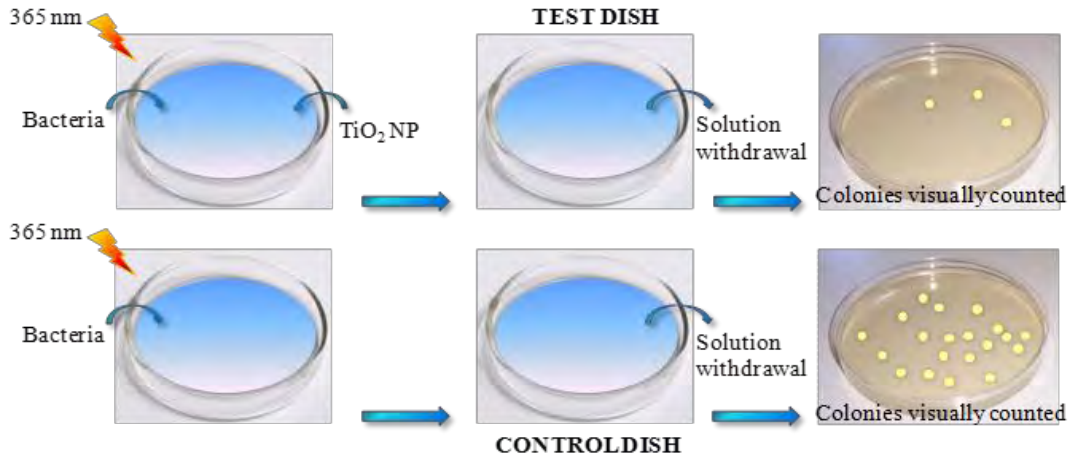

Scheme 6. Schematic representation of the experimental setup used to test the antimicrobial activity of TiO_2 NPs in solution.

Antibacterial activity on stone support: cell deposition and recovery in solution. Serena stone samples (1.5 X 1.5 X 0.3 cm) were treated either with the test nanoparticle dispersion ($TiO_2(S_M)$@TDMS, test specimens), or with the corresponding amount of the alkoxysilane (TMDS, blank specimens), without the addition of NPs. The final NP concentration over Serena stone surface was 0.4 mg/cm^2.

50 µl of bacterial suspension (*B. subtilis*) from overnight culture were pipetted on one of the largest surface of Serena stone specimen and allowed to dry for 20 min. All the samples were exposed to arc lamp UVA light irradiation (peaking at 365 nm, 3.1.2 section) for 20, 30 or 40 min. After the desired irradiation time period, the stone specimens were placed in a Petri dish (5 cm ∅) supplied with 10 mL saline solution (0.85% NaCl) and shaken for 30 min, turning the stone samples upside-down after 15 min. 1 mL of this "washing solution" was withdrawn (twice for each sample) and diluted 10 and 100 times with saline solution. 0.1 mL of undiluted and diluted samples were plated, incubated at 37 °C for 24 h and colonies visually counted. In order to evaluate the effect of the UV irradiation alone, control samples either supplied with NPs or only with TMDS were subjected to the same treatment

conditions as the test and blank specimens, except for the fact that they were not exposed to irradiation but kept in dark conditions.

3.5 Microbiological methods – AgNPs

The microbiological tests described in this section were performed in order to evaluate the antimicrobial characteristics of silver NPs, functionalized or not, in different conditions. The first step involved liquid nutrient medium tests, then solid nutrient medium ones and eventually experiments with silver treated stone surface. Some of the tests were specifically tailored for the nanosystems under study. In all the tests the amount of the AgNPs added is described in μg units: that accounts for the Ag content, *i.e.* the weight of the NPs.

Antibiogram. Preliminary tests to assess the antibacterial characteristics of pristine AgNPs were performed toward *E. coli*. 0.1 mL of either 10^6, 10^5, 10^4, CFU/mL *E. coli* suspension were plated on LB-Agar dishes and allowed to dry for 10 minutes. 10 μL spots of pristine AgNPs at different concentration (500 μg/ml, 100 μg/ml, 20 μg/ml, 4 μg/ml, 0.8 μg/ml) were dropped on plated bacteria. 10 μL water spot and 5 μl Ampicillin spot (5 mg/mL) were used as negative and positive controls, respectively. The experiment was performed in duplicate. Growth inhibition zones were visually evaluated after overnight incubation at 37 °C.

MIC and MBC. Minimum inhibitory concentration (MIC) test was performed in plastic tubes containing LB as growth medium. The tubes were inoculated either with about 10^5 CFU/mL *E. coli* or about 10^4 CFU/mL *B. subtilis* from overnight cultures and supplemented with different concentrations of AgNPs (functionalized or not). The final volume was set at 1 mL, composed of 900 μl LB broth, 50 μl bacteria suspensions and 50 μl AgNPs (whose final concentration varied from 0.05 μg/mL to 11 μg/mL). Positive control tubes were composed of 900 μl LB, 50 μl bacteria inoculum and 50 μl sterile water. Negative control tubes contained 950 μl LB broth and 50 μl sterile water. The tubes were incubated on the rotary shaker at 100 rpm and

30 °C for 24 h. Turbidity was visually evaluated. The lowest AgNP concentration corresponding to a non-turbid tube was indicated as the minimum inhibitory concentration (MIC).

0.1 mL aliquots from non-turbid tubes were spread on NA (*B. subtilis*) or LB (*E. coli*) plates, incubated at 37 °C for 24 h and colonies visually counted to evaluate the minimum bactericidal concentration (MBC), *i.e.* the lowest concentration of the antimicrobial agent required to achieve irreversible inhibition of bacterial growth.

Spot on spot. Antibacterial activity of AgNPs (functionalized or not) toward *B. subtilis* was qualitatively assessed on solid medium by determining the presence of growth inhibition zones. This test was used instead of the classical antibiogram method to overcome the problems associated with the fact that functionalized NPs (AgNP@TEOS) are dispersed in 2-propanol/water medium. The alcoholic dispersing mixture in fact inhibits bacteria growth by itself, once spotted over an inoculated plate. Using the spot on spot method, 10 µl of nanoparticle dispersions were spotted on NA plates and allowed to dry under the aspiration hood. Afterwards, 20 µl spots containing about 10^3 cells were laid onto the previous spot, so that the area covered by the cells was larger than the NP spot. Plates were incubated for 24 h at 37 °C and the inhibition activity was visually evaluated.

Cell deposition and recovery in solution. To assess the antimicrobial activity of NP-treated Serena stones, test pieces (1.5 X 1.5 X 0.3 cm) were treated with 50 µL of AgNP@TEOS dispersions at different concentrations (from 6 to 110 µg/sample) and allowed to dry overnight.

Each test sample was placed in a Petri dish (∅ 5 cm) and supplemented with 50 µL of 10^{-1} dilution of an overnight *B. subtilis* culture spread on one of the largest surface. After 30 min from bacteria deposition (that is the time necessary to dry off the stone surface), 10 mL saline solution (0.85% NaCl) were added and the Petri dish was shaken for 30 min (the stone sample was turned upside-down after 15 min). 1 mL of this "washing solution" was withdrawn (twice for each sample) and diluted 10 and 100 times with saline solution. To enumerate the viable bacteria recovered from the stone samples, 0.1 mL of undiluted and diluted solutions were plated on NA solid

medium, incubated at 37 °C for 24 h and visually counted (Scheme 7). Stone samples treated with the corresponding amount of TEOS solution (instead of NP dispersions) were used as blank and treated in the same way. Two replicates with at least three repetitions each were performed for each concentration of AgNPs and the corresponding blanks.

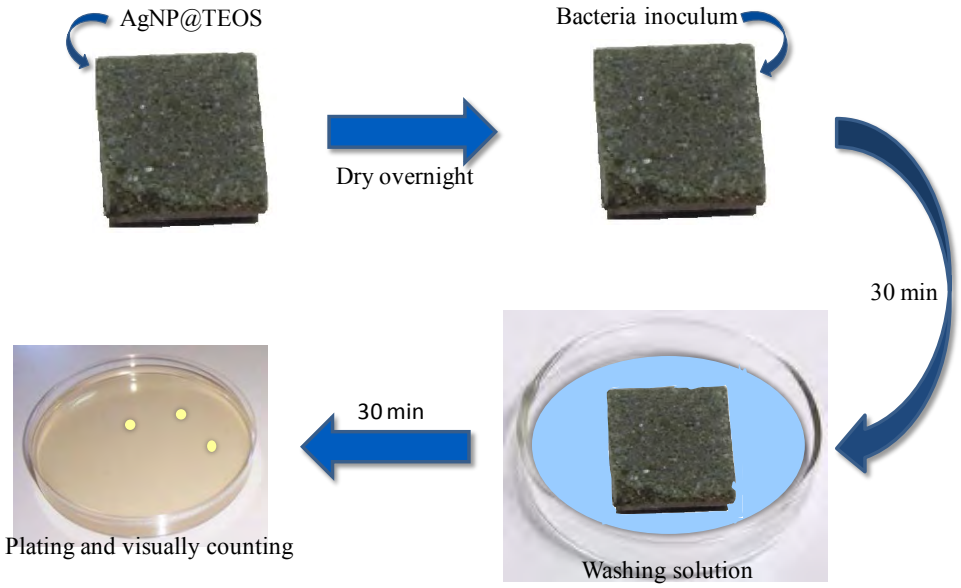

Scheme 7. Schematic representation of the different steps of the "cell deposition and recovery in solution assay".

The reduction in cell viability achieved due to NP antimicrobial effect was evaluated comparing final microbial counts (FMC) of AgNP@TEOS-treated and TEOS-treated samples. The initial microbial count was normalized at the same value for all the test pieces (Page *et al.*, 2007; Ozy *et al.*, 2010):

$$\text{Antimicrobial effect} \quad \frac{\text{MC(untreated)} \quad \text{MC(treated)}}{\text{MC(untreated)}} \quad 100$$

Cell deposition and recovery by contact plates. The antimicrobial activity of silver NPs grafted to Serena stone was also evaluated by the use of contact plates. Selected areas (∅ 5 cm) on the surface of Serena stone specimens (10 X 10 X 2 cm) were uniformly spread either with 27 μg/cm^2 AgNP@TEOS (test samples) or with

the corresponding amount of TEOS (blank samples), allowed to dry overnight and inoculated with 100 μl *B. subtilis* (about 10^4 CFU/sample). After 30 min from their deposition, bacteria cells were sampled using NA contact plates (∅ 5 cm) and the viable count was performed after 24 h incubation at 37°C.

Fungal growth on stone. Serena stone samples (1.5 X 1.5 X 0.3 cm) were inoculated with different quantities of fungal spores or cells (about 10^4, 10^3 or 10^2 spores/sample) of *Aspergillus versicolor* or *Sarcinomyces petricola* strains, respectively. To make fungal spores to grow on stone samples, the inoculated specimens were placed in a Petri dish (∅ 5 cm) which in turn was placed in a bigger Petri dish (∅ 9 cm) filled with water, to maintain high humidity level. Each stone sample was supplemented with 25 μl Sabouraud liquid nutrient medium and incubated at 30 °C in the described humid conditions up to 60 days. The extent of growth was periodically observed with the help of stereomicroscopy.

Chapter 4.
Results and discussion

In the following chapter we are going to present and discuss the principal results obtained in this thesis work. This chapter is divided in two main sections, the first regarding TiO_2 NPs and the second devoted to AgNPs. Each of these sections is in turn divided in other subsections, as chemical and biological results are discussed separately.

4.1 Titanium dioxide nanoparticles (TiO_2 NPs)

The first aim of this thesis work was to obtain highly crystalline titanium dioxide nanoparticles to be grafted to a stone surface in order to confer it durable antibacterial properties. Several intermediate steps were pursued to achieve this final goal. First, TiO_2 NPs were synthesized and characterized (size and crystallinity degree). Next, TiO_2 NPs were surface modified with two different alkoxysilane derivatives able to chemically interact with a lithic substrate. Then, the antibacterial properties were evaluated. As long as TiO_2 NPs require photoactivation to exert their toxicity toward bacteria, it was first assessed the actual photoactivity of pristine and functionalized NPs toward the degradation of an organic dye prior to test the synthesized nanoremedies toward bacteria.

4.1.1 Chemical synthesis and characterization

Anatase phase synthesis. Anatase is one of the three crystalline forms of titanium dioxide in Nature. Even though it is a metastable phase, it is the form with the highest photocatalytic activity, very important characteristic to our scopes. TiO_2 nanoparticles have been prepared from a peroxotitanate complex solution by a solvothermal process in water/alcohol media. This synthetic method was developed

by Liao *et al.* (2009) using $Ti(SO_4)_2$ and H_2O_2 as precursors. In their work, the authors demonstrated that different relative proportions of the crystallization solvents greatly influenced size and shapes of the final nanocrystals. Their investigations included the use of pure *n*-propanol, pure *n*-butanol and ethanol/water mixture as solvents. As far as pure *n*-propanol and *n*-butanol systems resulted in amorphous floccus-like structures, our study started from the synthesis of TiO_2 nanoparticles using both ethanol/water and methanol/water mixtures for the solvothermal synthesis, in order to study if the NPs obtained differ in size or in crystallinity degree. Methanol/water mixtures were investigated because in their work Liao *et al*. (2009) suggested that long carbon chains badly affect the crystallinity and the growth rate of anatase crystals. Our study was aimed at verifying if the very short methanol chain gives rise to anatase phase crystallization even at higher extent than in ethanol or ethanol/water solutions.

The NPs were obtained from solvothermal solvent mixtures varying from 100% water (S_W), 4:1 V/V water/ethanol (S_{WE4}), 1:1 V/V water/ethanol (S_{WE1}), 1:4 V/V ($S_{WE0.25}$) water/ethanol, 100% ethanol (S_E), 100 % methanol (S_M), 4:1 V/V water/methanol (S_{WM4}), 1:1 V/V water/methanol (S_{WM1}), 1:4 V/V water/methanol ($S_{WM0.25}$) (see Table 1, section 3.1.1). All the sample batches resulted in well dispersed milky-white colloidal systems that tend to settle down over time, but promptly re-disperse if gently shaken (Fig. 7, section 3.1.1).

SAXS and WAXD investigations. TiO_2 nanoparticles obtained from all the combinations of synthetic solvents were first investigated by means of small and wide angle X-ray scattering techniques, SAXS and WAXD respectively. These measurements provide insights in dimension and crystallinity of the NPs and, compared to microscopy techniques, are well-suited for preliminary investigations. SAXS analysis can in fact be performed directly on the dispersions, without the need of any time consuming sample preparation. Moreover, they reflect the real characteristics of the systems under study, as they provide the dimensions of the particles in solution, without the risk of introducing artifacts in the evaluation of the sizes due to the use of dried specimens. Furthermore, SAXS results include the overall averaged information coming from all the nanoparticles present in the dispersion that is lightened by the X-ray beam, providing this way a very good

statistic over the whole sample. In addition, WAXD investigations are particularly useful dealing with titanium dioxide samples as the two most common titania polymorphs (anatase and rutile) can be easily discerned based on their most intense diffraction peaks. The narrow angular range (18-28°) analyzed by the WAXD setup allows in fact to recognize anatase and rutile diagnostic peaks, that fall respectively at 25°, (1 0 1) plane, and 27°, (1 1 0) plane. A clear advantage as a preliminary investigation tool of WAXD technique over X-ray powder diffraction (XRD) is the use of as-prepared colloidal dispersions, without the need to freeze-dry the samples to obtain adequate amounts of powdered material.

SAXS curves were collected for each sample batch prepared from different solvent mixtures. They were fitted according to the Unified model (Beaucage *et al.*, 2004) by using two structural levels: one for the primary particles (Level 1) and the other for the aggregates of primary particles (Level 2). The results are shown in Figure 12 and the parameters obtained from the fitting model are summarized in Table 2.

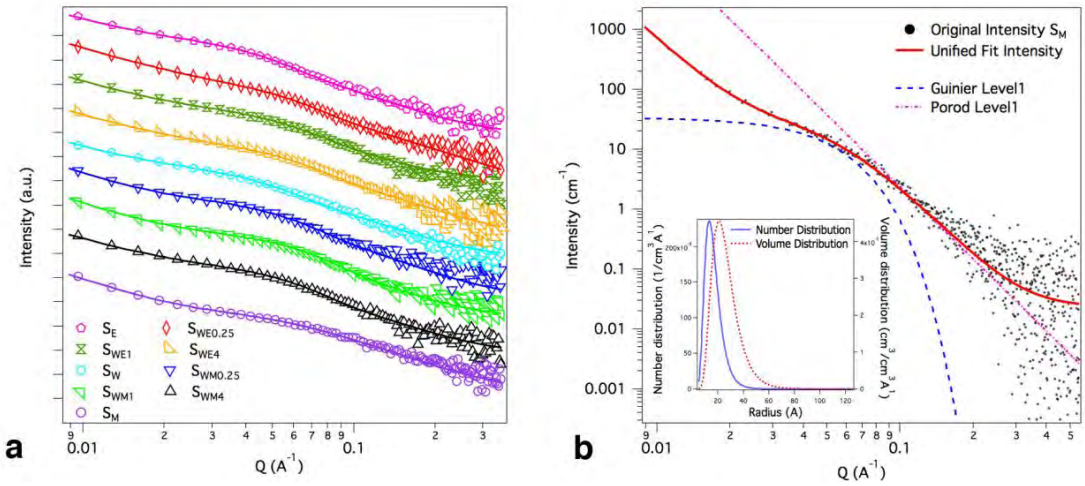

Figure 12. Panel **a** displays SAXS intensity distributions for all the investigated TiO_2 nanoparticle dispersions. The continuous lines represent the Unified fit. Panel **b** shows an example of the Unified fit on sample S_M. The fit consists of two levels: *i*) the high-*q* level is divided in a Guinier-fit and a Porod-power-law fit, *ii*) the low-*q* level displays only the Porod-power-law fit. The inset represents the size distribution corresponding to the Unified fit.

Figure 12a shows the *log-log* representation of SAXS intensity distributions versus *Q* (the scattering vector) obtained for all the investigated samples. One

example of the Unified fit is reported in Figure 12b (sample S_M) along with the structural level corresponding to the nanoparticles. The agreement between the experimental data and the fitting was excellent in all the sample batches. The *log-log* plot of the scattering intensities displayed a knee-like shape in the transition region between Porod regime of the aggregates (Level 2) and Guinier regime of the primary particles (Level 1). Usually, the presence of this feature is characteristic of nanoparticles with a low-polydispersity (see Table 2).

Table 2 summarizes the results obtained from SAXS curves and their relative fit in terms of size of the primary nanoparticles and polydispersity. Opposite to what was found by Liao and coworkers (2009), the solvent mixtures used during the synthesis did not appear to affect by a great extent the final nanocrystal dimensions or the crystalline phase. Only minor differences were detectable between all the synthesized batches. The NPs obtained from pure methanol were the smallest among all the others, while the NPs synthesized from pure ethanol and pure water were the largest, being quite similar the ones to the others. Conversely, all the colloidal dispersions obtained from water/alcohol solvent mixtures were very similar in terms of primary particle dimensions, either if the alcohol was methanol or ethanol.

It is therefore possible to assess that these preliminary SAXS studies on the colloidal dispersions did not show any particular trend in the nanoparticle sizes.

The next WAXD investigation was oriented to find out if different synthetic solvent mixtures affect the crystallinity degree of the colloidal nanodispersions. WAXD patterns evidence in all the samples the presence of the anatase phase, whose diagnostic diffraction peak falls at 25° (Fig. 13). One exception to the purity of anatase phase is represented by sample $S_{WM0.25}$, which displays a tiny shoulder around 27° that can be ascribed to the presence of small amounts of rutile. Another particularity to be further investigated is represented by sample S_M, whose crystallinity degree appears less evident.

Also WAXD measurements did not show any particular variation between the samples prepared from different solvothermal reaction mixtures.

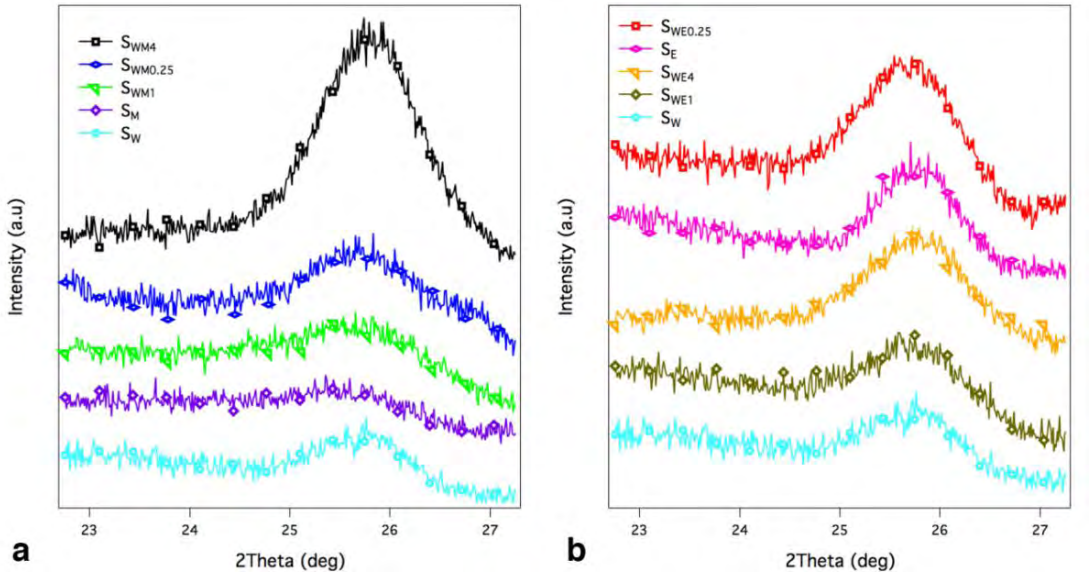

Figure 13. WAXD pattern for all the synthesized TiO_2 samples. Panel **a** displays the samples synthesized from pure water, pure methanol or from their mixtures; panel **b** displays the samples synthesized from pure water, pure ethanol or their mixtures. The peak at about 25° is the diagnostic reflection for the anatase phase. It is slightly shifted to higher 2Theta values (0.3-0.4°) with respect to XRD pattern (Fig. 18) as a result of the fact that Lupolene has been used as a secondary calibrant. Sample $S_{WM0.25}$ displays a tiny shoulder around 27°, that may be due to a small amount of rutile phase.

The next step in the characterization of TiO_2 NPs was aimed at gaining further insights about the size and morphology of the synthesized nanostructures by using different specific techniques.

HRTEM-SAED. Complementary results on the size of the NPs with respect to SAXS ones were obtained by means of high resolution transmission electron microscopy (HRTEM). Opposite to what happens with SAXS measurements, this technique does not provide particle dimensions in solution, but gives information on the sizes of the dried specimens.

Images displayed in Figure 14 are representative for each synthetic condition used. The size of the nanoparticles was estimated through the analysis of several HRTEM images by the evaluation of the size of the NPs in each picture. The average dimensions, derived from a log-normal fitting process of all the data points (Fig. 15), are summarized in Table 2 and are in good agreement with SAXS results.

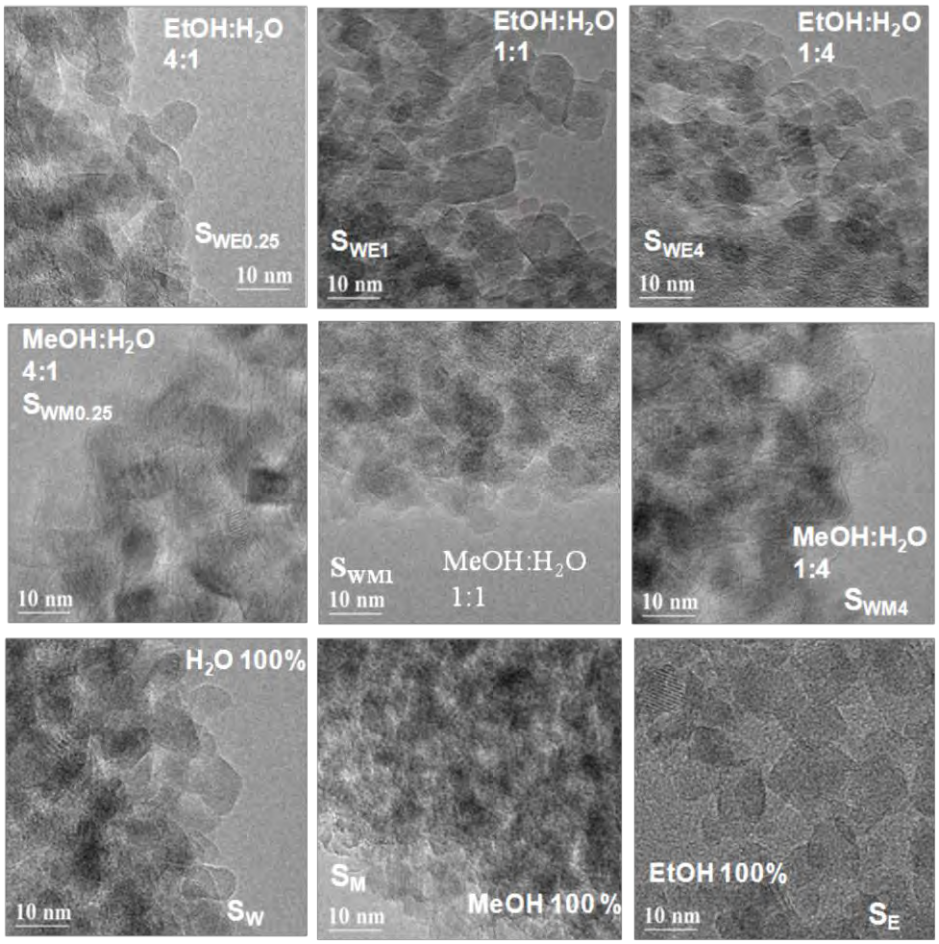

Figure 14. HRTEM images (300 K magnification) of all the samples originated from solvothermal synthetic pathway using different reaction solvent mixtures.

From the images taken at higher magnification (Fig. 16) it is evident that all the nanoparticles display a faceted shape, highlighting their crystalline structure. Moreover, when the size of the nanoparticles exceeds about 10 nm, the growth seems to take place preferentially along one direction, as shown by the elongated shape of greater particles (see the arrow in Fig. 16a).

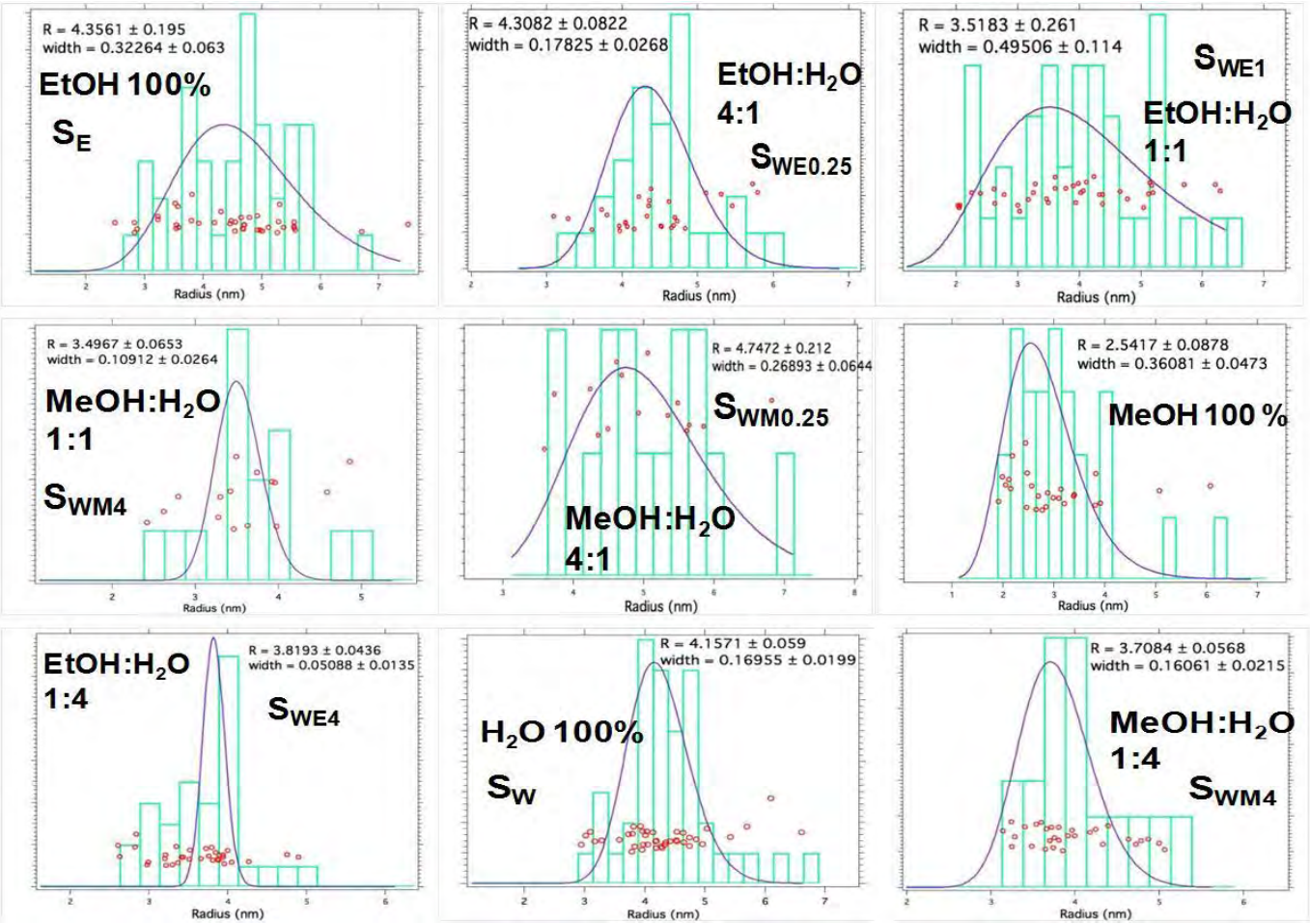

Figure 15. Log-normal fittings of the NP dimensions derived from the HRTEM images of each sample.

The nanoparticle crystallinity in selected specimen regions was studied by means of SAED analysis (selected area electron diffraction). Diffraction rings (see the insets in Fig. 16) are indicative of anatase crystallographic phase.

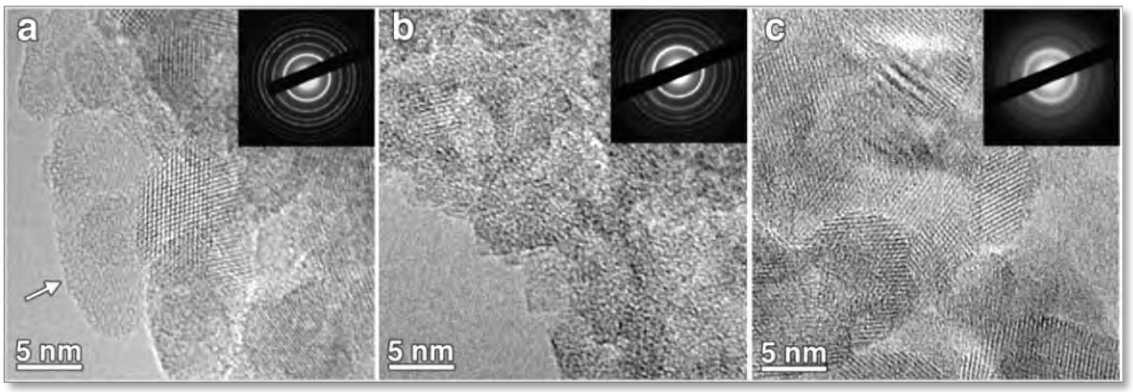

Figure 16. HRTEM images of samples S_W (**a**), S_M (**b**), S_E (**c**) at 600 K magnification. The insets display the SAED analysis on selected specimen regions (60 K magnification). The diffraction rings are typical of pure anatase phase. The arrow in panel **a** indicates the preferential growth direction of the crystalline nanoparticles.

SAED analysis do not detect any amorphous halos or other crystalline phases in any sample, with the exception of batch S_{WE1} which reveal the co-presence of a much weaker second diffraction ring typical of brookite phase, as indicated by the arrow in the inset of Figure 17. As a matter of fact, the lack of brookite characteristic diffraction ring in all the samples other than S_{WE1} can be due to the very limited area investigated in a SAED measurement. It is also important to stress out that brookite diagnostic diffraction signal appears around 30˚, *i.e.* outside the angular region examined through WAXD measurements. The result obtained in the case of our sample S_{WE1} is similar to what was found by some other researchers (Chae *et al.,* 2003) that synthesized TiO_2 NPs using an hydrothermal reaction in ethanol rich conditions. Their NPs were mainly in the anatase phase, but with actual impurities of brookite or rutile phases.

XRD. Since WAXD measurements presented some points to be clarified and SAED results were affected from a poor statistical relevance (the investigated area is very small), X-ray diffraction (XRD) on the nanoparticle powders was performed.

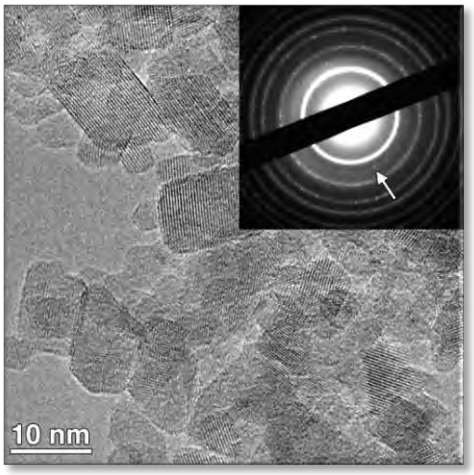

Figure 17. HRTEM image (300 K magnification) of sample S_{WE1}. The biggest nanoparticles are in anatase phase, the smallest ones are in brookite phase. The brookite phase is represented by the weak colored diffraction ring indicated by the arrow in the SAED inset.

These measurements had several aims: *i*) to actually prove that brookite phase is present in significant amount only in sample S_{WE1}, *ii*) to verify whether sample $S_{WM0.25}$ is also composed of a little percentage of rutile phase or not and *iii*) to ensure that sample S_M consists of crystalline nanoparticles.

XRD results of the powdered samples S_E, S_W, S_M, S_{WE1} and $S_{WM0.25}$ are shown in Figure 18.

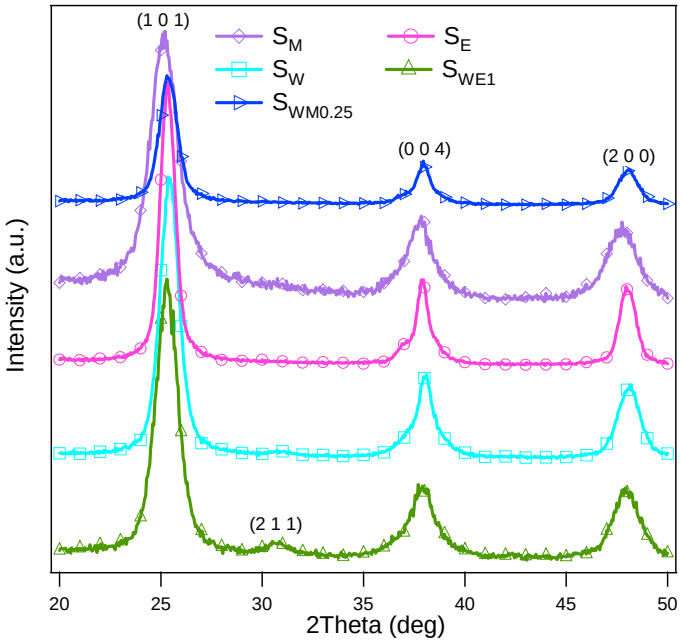

Figure 18. XRD diffraction patterns corresponding to samples S_M, S_W, S_E, $S_{WM0.25}$, S_{WE1}.

These measurements actually confirmed SAED findings and clarified the doubts raised from WAXD measurements. The brookite phase is in fact detectable only in sample S_{WE1}, through the diagnostic diffraction peak at 30.8°, plane (2 1 1), but even in this powdered sample it constitutes a minority phase with respect to the anatase one. Moreover, XRD results proved that the weak shoulder in the WAXD spectrum of the sample $S_{WM0.25}$ was not due to the presence of rutile phase in significant amounts. It was also confirmed that sample S_M is crystalline indeed and in the anatase form.

The analysis of XRD data allowed also to extract the average crystallite sizes. According to the Warren-Averbach method (Warren, 1969), which takes into account the whole information contained in the XRD peak profile and not only its half width at half maximum as in the Scherrer method, the crystallite size diameters are: S_W = 8.6 nm, S_E = 10.9 nm, S_M = 5.4 nm S_{WE1} = 7.1 nm, S_M = 8.3 nm. The fact that these dimensions nearly match those obtained from SAXS and HRTEM measurements, indicate that the nanoparticles are actually monocrystalline.

Table 2. For each synthesized batch of TiO_2 NPs, the table summarizes: the size of primary nanoparticles by means of different characterization techniques (SAXS and HRTEM), the polidispersity index (PDI, from SAXS curve fitting model) and the crystallographic phase (from WAXD, HRTEM-SAED and XRD measurements).

	$V_{water}/V_{alcohol}$	R_{SAXS} (nm)	PDI	R_{HRTEM}[a] (nm)	Crystalline phase
S_E	***0:1***	5.54 ± 0.17	*0.26*	4.3 ± 0.3	anatase
$S_{WE0.25}$	*1:4*	4.40 ± 0.25	*0.25*	4.3 ± 0.2	anatase
S_{WE1}	*1:1*	4.36 ± 0.30	*0.28*	3.5 ± 0.5	anatase, brookite
S_{WE4}	*4:1*	4.27 ± 0.22	*0.25*	3.8 ± 0.2	anatase
S_W	***1:0***	5.27 ± 0.23	*0.29*	4.2 ± 0.2	anatase
$S_{WM0.25}$	*1:4*	4.50 ± 0.23	*0.26*	4.7 ± 0.3	anatase
S_{WM1}	*1:1*	3.90 ± 0.16	*0.22*	3.5 ± 0.1	anatase
S_{WM4}	*4:1*	4.27 ± 0.18	*0.22*	3.7 ± 0.2	anatase
S_M	***0:1***	3.45 ± 0.30	*0.39*	2.5 ± 0.3	anatase

[a] Results obtained by measuring 20-50 distinct particle dimensions from several HRTEM images. Average sizes and errors were obtained from a log-normal distribution.

Basing on all the results obtained, it is possible to extrapolate some conclusions on the effects of changing the solvent reaction mixture on particle size and crystallinity. Both scattering and microscopy results suggest that, no matter which is the reaction solvent mixture (water/(ethanol or methanol) in different proportions), the nanoparticles obtained are highly monocrystalline and in the anatase form. Even though the dimensions do not vary by a great extent in dependence of the synthetic solvent combination, the NPs synthesized from pure methanol (S_M) are the smallest, particularly in comparison with the ones obtained from the other pure solvents (water (S_W) and ethanol (S_E)).

Surface functionalization. Once obtained titanium dioxide nanoparticles in anatase form, the next step of the work was to make them able to be grafted to a rocky substrate, fundamental requisite to allow the NPs to exert *in situ* antimicrobial activity. Since TiO_2 nanoparticles have reactive hydroxyl groups on their surface, the NPs were surface modified taking advantage of the reaction of these −OH functionalities with proper end-functional molecules, such as alkoxysilanes.

Because of the very similar characteristics in terms of crystallinity degree and sizes of the primary particles of all the different NP batches, it was decided to surface modify only samples S_W and S_M. These samples were chosen on the basis of their dimensions; S_W is in fact composed of NPs whose size is among the largest, and S_M is composed of the smallest NPs. The as-prepared TiO_2 nanodispersions were surface functionalized by means of two different methoxysilanes, TSPMC ($(CH_3O)_3Si-(CH_2)_3\text{-}N^+(CH_3)_3Cl^-$) and TMDS ($(CH_3O)_3Si-Si(OCH_3)_3$).

TSPMC was selected as it should be able to bind to the nanoparticles both through chemical bonds, using its siloxane end, and through electrostatic interactions (reverse attachment) using its quaternary ammonium end, as documented in literature (Scheme 8) (Ukaji *et al*., 2007; Song *et al*., 2010). TMDS, on the other hand, can only be chemically bound to the surface and it was selected as it is an alkoxy-disilane; the presence of six siloxane ends should simplify the condensation reactions to form Ti−O−Si bonds with the NPs (Scheme 8) and Si−O−Si or Si−O−C bonds with the lithic material, respectively if the stone is silicatic or carbonatic (Scheme 5, section 2.3).

The process of methoxysilane grafting to TiO_2 surface can be described by the following equations:

$$TiO^- + {}^+N(Me)_3(CH_2)_3{-}Si(OMe)_3 \rightarrow Ti{-}O{-}Si{-}(CH_2)_3{-}{}^+N(Me)_3 + 3\ MeOH$$

$$Ti\text{-}O^- + {}^+N(Me)_3{-}(CH_2)_3{-}Si(OMe)_3 \rightarrow Si(OMe)_3{-}(CH_2)\ {-}{}^+N(Me)_3{\cdots}{}^-O{-}Ti$$

$$Ti\text{-}O^- + Si(OMe)_3{-}Si(OMe)_3 \rightarrow Ti{-}O{-}Si{-}(OMe)_3 + 3\ MeOH$$

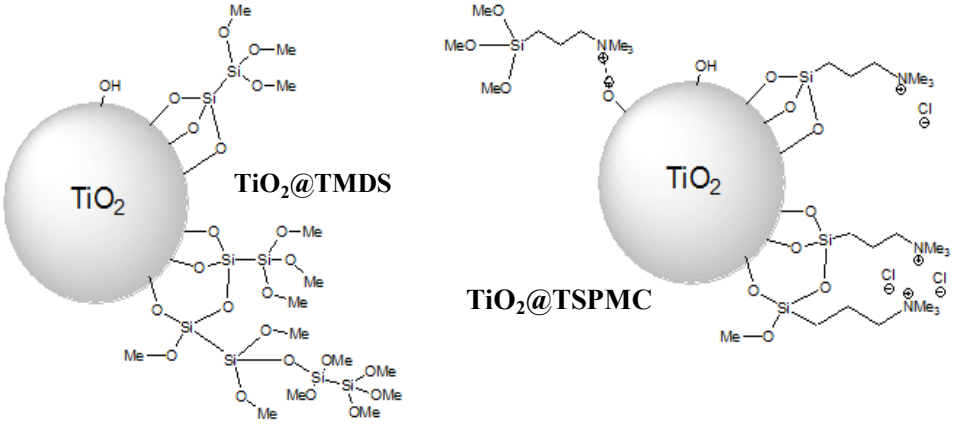

Scheme 8. Simplified schematic representation of the surface modification of the TiO_2 NPs by means of two methoxysilanes. TMDS is an alkoxydisilane, TSPMC is a quaternized aminoalkoxysilane.

FTIR. The functionalization reaction between TiO_2 NPs and methoxysilanes was monitored by infrared spectroscopy (ATR-FTIR) and studied as a function of temperature, reaction time and silane concentration.

As for the temperature, either room temperature conditions or 50 °C were examined; the reaction status was monitored after 2 h, 17 h or 3 days in stirring conditions. The best results were obtained setting the temperature at 50 °C and the reaction time at 17 h.

The methoxysilane amount to be added was decided in order to reach the desired percentage of NP surface coverage, either 84, 100 or 130 %. The theoretical NP surface area and the coverage were calculated referring to the ideal assumption of spherically-shaped monodisperse nanoparticles (according to SAXS dimensions), with the silane evenly distributed on the surface.

Figure 19 displays selected regions of the ATR-FTIR spectra of the functionalized and pristine NPs (samples S_M or S_W), together with the spectra of pure alkoxysilanes (TSPMS or TMDS).

The spectra of the TiO_2 NPs synthesized from pure water (S_W) or from pure methanol (S_M) are basically identical. In the high frequency region a broad band is present, which can be ascribed to the hydroxyl groups on TiO_2 NPs (Ti-OH) and to the water complexes strongly bound to their surfaces (Xu *et al*., 2008). A sharp peak, characteristic of the scissor-bending mode of physisorbed water (Xu *et al*., 2008), is detected around 1630 cm^{-1}. A much weaker signal is detected around 1440 cm^{-1}, which could be due to the adsorption of CO_2 onto the surface of the NPs (Xu *et al*., 2008; Vayssieres, 2009). The region at low IR frequencies does not feature any significant characteristic, with the only exception of the shoulder around 900 cm^{-1} that indicates the presence of peroxo groups on the surface of TiO_2 particles, as previously reported for nanostructured systems where H_2O_2 is used during the synthesis (Coates, 2000; Gao *et al*., 2004; Sawicka *et al*., 2006).

In the case of pure TMDS, a group of peaks is present between 3000 and 2800 cm^{-1}, which is due to the –CH stretching vibrations of methoxy groups (Coates, 2000). In the mid region, the spectrum of pure TMDS features a peak slightly above 1450 cm^{-1}, which can be ascribed to $–CH_3$ bendings (Coates, 2000; Sawicka *et al*., 2006). These peaks reported for the pure TMDS spectrum are always present when the NPs are coated with TMDS and, as expected, their intensities grow as a function of the coverage percentage.

The presence of TMDS onto TiO_2 NPs is further confirmed by the broadening of peak at 1450 cm^{-1}, due to the appearance of a shoulder between 1450 and 1400 cm^{-1} that can be ascribed to Si–O–C groups in silane-based coatings on TiO_2 NPs (Sabzi *et al.*, 2009). As for the previously discussed signals, the intensity increases according to the amount of the grafting agent. This is especially evident in the case of the highest coverage spectrum (130%), where a further shoulder emerges at about 1550 cm^{-1}, also diagnostic of Si–O–C groups (Sabzi *et al.*, 2009).

In the low energy part of the TMDS spectrum, two strong peaks are present: one around 1200 cm^{-1}, which can be assigned to $–CH_3$ rocking vibration (Murphy *et al.*, 1993; Lien *et al.*, 2005), and the other around 1050 cm^{-1}, characteristic of Si–O–C vibrations (Coates, 2000). The spectra of modified NPs show the presence of the very same peaks, providing further evidence of the successful grafting. Furthermore, the shape of the peak around 1050 cm^{-1} is much less defined than in pure TMDS, likely due to the overlapping of the signals due to Si–O–Si groups eventually

forming during the condensation of the silane on NPs, typically appearing slightly below 1100 cm^{-1} (Zeitler and Brown, 1957; Cheng *et al.*, 2006; Finocchio *et al.*, 2007; Ukaji *et al.*, 2007; Sabzi *et al.*, 2009). Finally, the formation of Ti–O–Si groups is highlighted by the appearance of a shoulder around 950 cm^{-1}, slightly above the signal due to peroxo groups in naked particles.

FTIR results of TSPMC-coated NPs almost entirely follow those of TMDS-coated NPs, apart from the different chemical structure of the grafting agent and the consequent IR absorptions. All the signals discussed in the case of TMDS are present in TSPMC as well, with the addition of new peaks arising from the $-N(CH_3)_3$ and $-CH_2$ functional groups. Therefore we discuss here only the new absorptions related to those functions.

In the high energy region, a slight broadening of the –CH stretching peaks is visible in the spectra of pure TSPMC and TiO_2@TSPMC, reasonably due to the overlapping –CH stretching vibrations of methylene groups in the TSPMC alkyl chain and methyl groups from the quaternary ammonium end. The presence of the N–C–H peak is clearly detected in the mid region between 1500 and 1400 cm^{-1} (Sawicka *et al.*, 2006), also in the spectra of the modified NPs, which overlaps those from Si–O–C groups.

In the low energy part of the spectra, in addition to the rocking $–CH_3$ signal around 1200 cm^{-1} and the second peak from the Si–O–C group appearing slightly below 1100 cm^{-1}, the peak of quaternary N–C group is clearly visible in all the samples around 1040 cm^{-1} (Murphy *et al.*, 1993; Lien *et al.*, 2005).

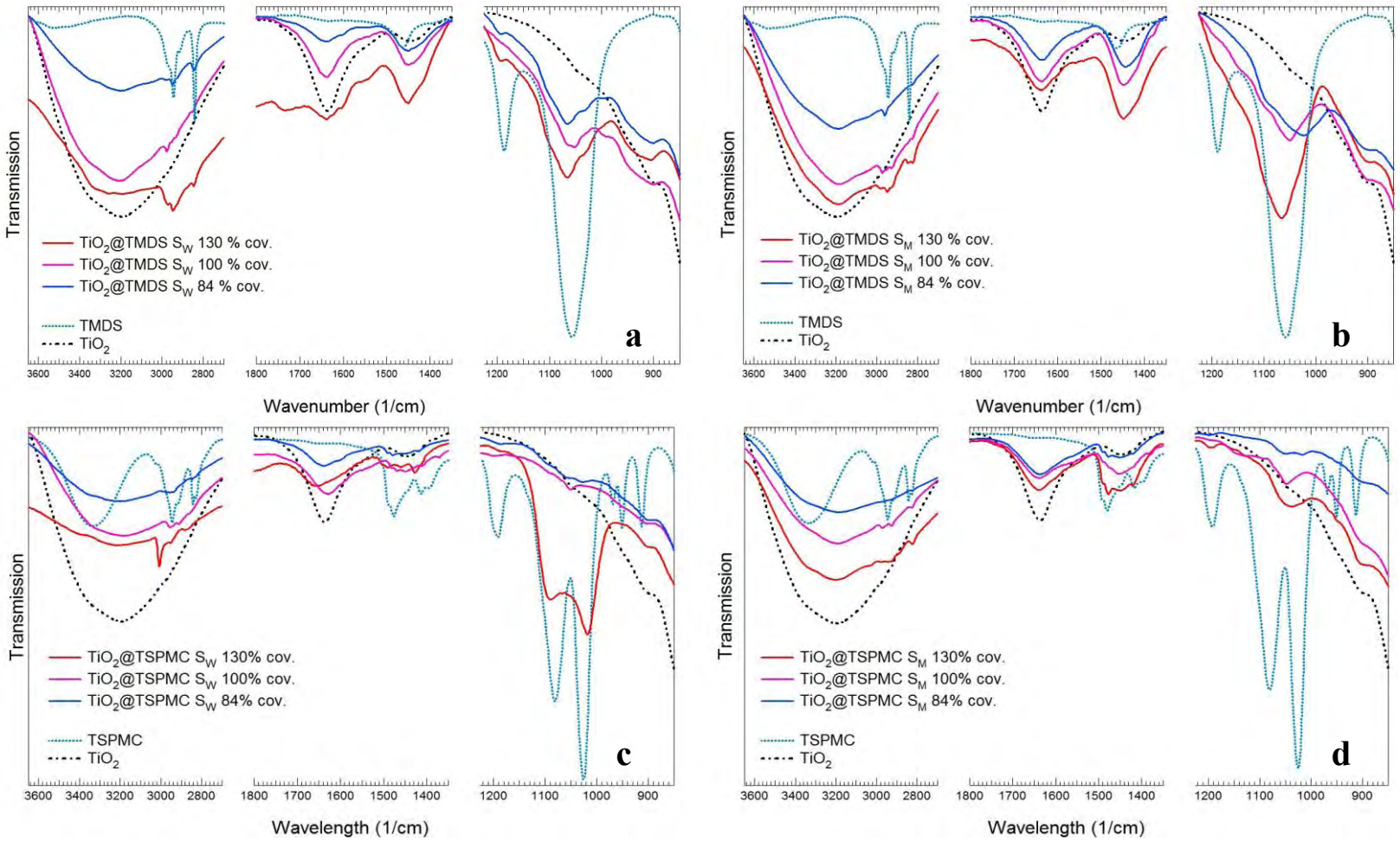

Figure 19. ATR-FTIR spectra of the TiO_2@TMDS (**a**, **b**) and TiO_2@TSPMC samples (**c**, **d**). Surface functionalization was performed on samples S_W and S_M. Please note that TSPMC spectrum refer to an alcoholic solution of it, this being the reason of the characteristic –OH stretching band around 3400-3300 cm^{-1}.

TGA. The successful grafting of the methoxysilanes on the surface of TiO_2 NPs was also monitored through thermogravimetric analysis (TGA). Thermal degradation of both pristine and functionalized nanoparticles was studied in order to device potential differences before and after the NP surface modifications. The powders were first isothermally equilibrated at 100˚ for 10 min in order to remove physisorbed water and then heated up to 750 ˚C under nitrogen atmosphere at a heating rate of 10 ˚C/min.

Figure 20 displays the weight loss curves of naked NPs prepared from water (S_W) and methanol (S_M), together with the curves associated with NPs functionalized with an excess (130% coverage) of alkoxysilane, either TMDS or TSPMC. The weight loss profiles are normalized to 100% after the isothermal step to get rid of the water contribution to the curves. All the samples show a similar trend. At temperatures slightly higher than 100˚C, the weight loss percentage in naked NPs is larger than in functionalized ones, likely due to a larger amount of water strongly bound to the surface. As the temperature increases, the pyrolysis of the organic content in the silanes causes a larger weight loss percentage in surface-functionalized NPs. Despite the low molecular weight of the silane molecules and their very small contribution to the total weight, pyrolytic processes can be detected in the weight loss derivative curves (Fig. 21).

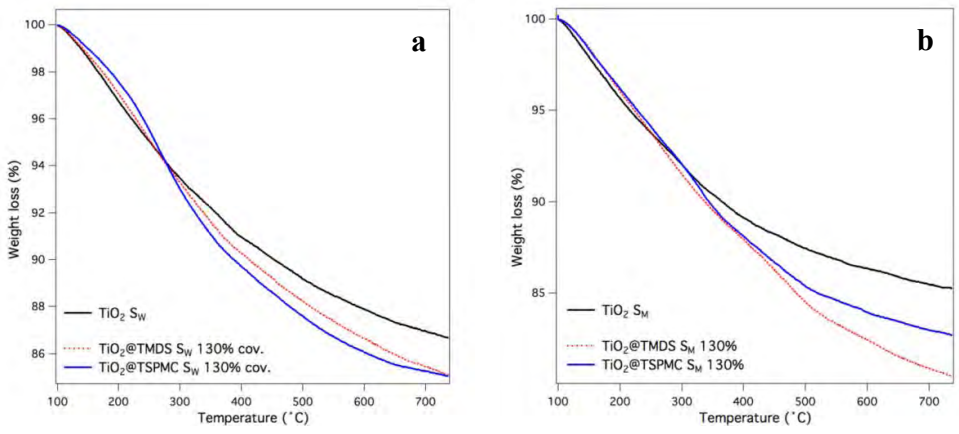

Figure 20. Weight loss curves for naked and silane functionalized samples (the grafting agent being either TMDS or TSPMC in excess). Samples in panel **a** are obtained from S_W; samples in panel **b** are obtained from S_M.

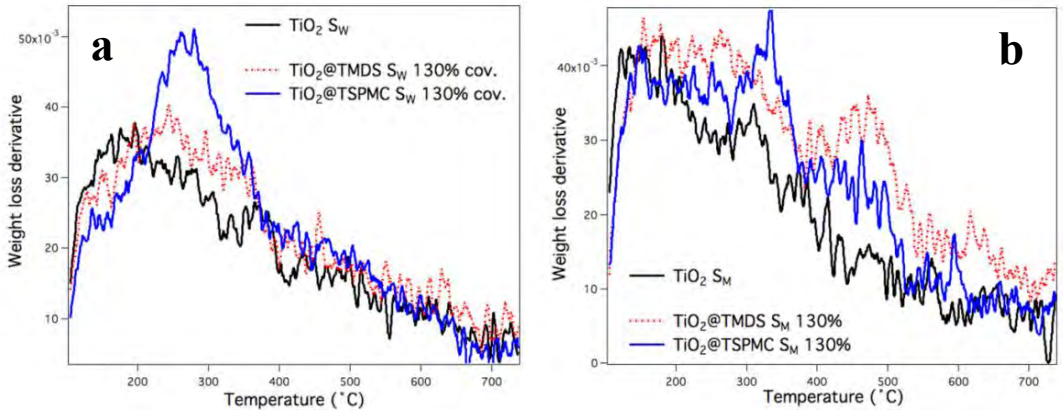

Figure 21. Weight loss derivative curves for the pristine S_W (**a**) or S_M (**b**) NPs and for the S_W (**a**) or S_M (**b**) samples functionalized with an excess of the grafting agent (130% coverage with TMDS or TSPMC).

HRTEM. The surface modification of TiO_2 nanoparticles with a silane derivative was also evident by means of high resolution TEM measurements. A representative image is shown in Figure 22, where the crystalline TiO_2 core appears uniformly covered by an amorphous layer of silane (~ 1 nm thick), obtained from the reaction of pristine NP (S_M) with TMDS in the case of 130% surface coverage.

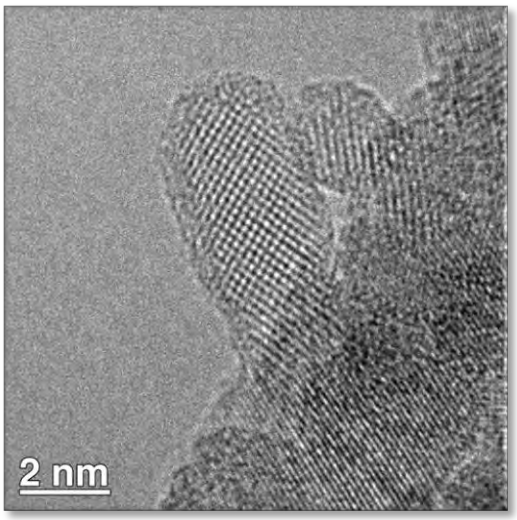

Figure 22. HRTEM image of S_M TiO_2@TMDS at 800 K magnification. Crystalline cores are uniformly covered by an amorphous layer of silane.

From the synergic use of different investigation techniques it was therefore possible to make sure that the synthetic procedure used was effective in yielding anatase nanocrystals surface-functionalized with alkoxysilane molecules.

TiO_2 grafting to the stone surface. Before testing the NP killing properties toward bacteria, it was necessary to perform a preliminary study in order to test the grafting efficiency of the nanoparticles to the stone surface. Two different lithic substrata were chosen: marble and Serena stone.

Microscopic techniques were used to evaluate the potential differences between the untreated stone surface and the functionalized one. The specimens were also subjected to a water flow that simulates an heavy rain condition (7 mL/s for 30 min), with the aim to test the resistance of the grafting agent.

AFM images of marble surface (Fig. 23) were collected before and after functionalization with the NPs (S_M TiO_2@TMDS where chosen, the ones with the highest photocatalytic activity).

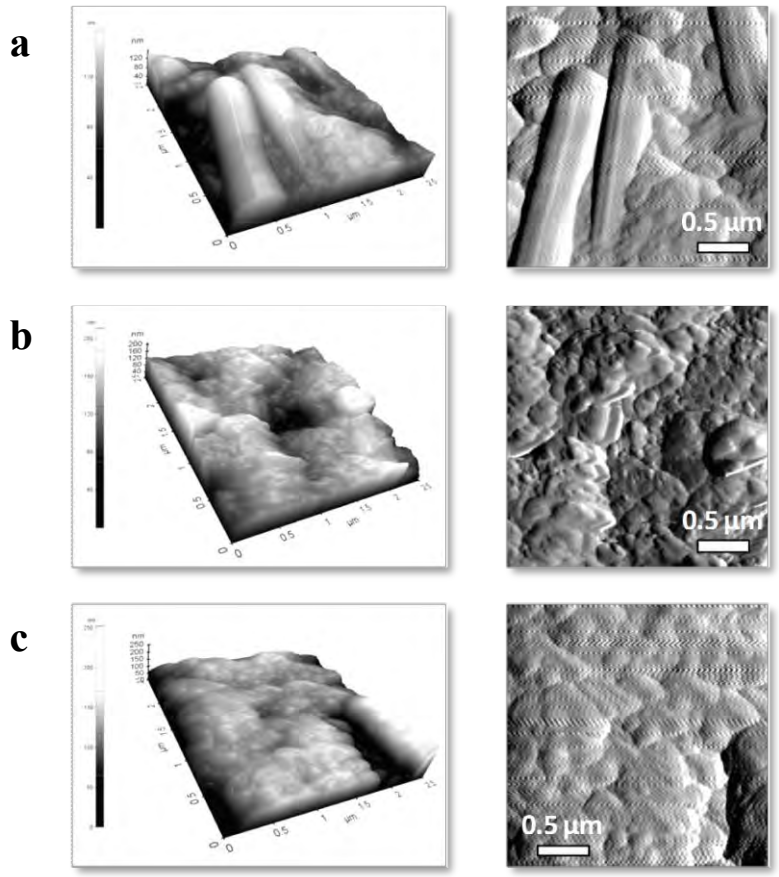

Figure 23. AFM 3D topography (left images) and corresponding error images (right images) of (**a**) untreated marble surface and of marble surface functionalized with S_M TiO_2@TMDS before (**b**) and after (**c**) the washing treatment.

Figure 23 displays some representative images, and no significant differences can be appreciated between the samples. That is due to the fact that the NPs are too small to be visualized on such a rough surface.

The same specimens were then analyzed by means of SEM technique (Fig. 24).

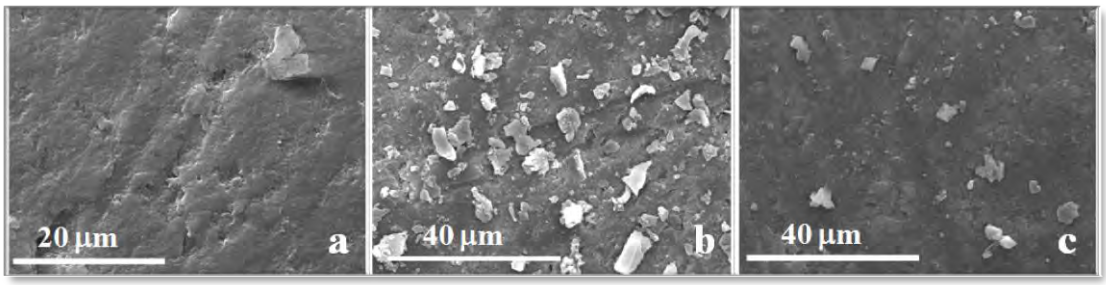

Figure 24. **a)** Neat marble surface (2500 K magnification). **b**) and **c**) images show S_M TiO_2@TMDS grafted to marble surface before and after washing treatment, respectively (1500 K magnification).

The images evidence that the NP grafting to marble surface is not efficient, as after the exposition to the water jet a significant percentage of the nanoparticles is diluted.

It was therefore changed the stone substrate from marble to Serena stone, and SEM images (Fig. 25) show a better performance of the grafting agent, as the functionalized NPs resist well to the washing treatment, and their loss after washing is by far less evident than in the case of marble surface.

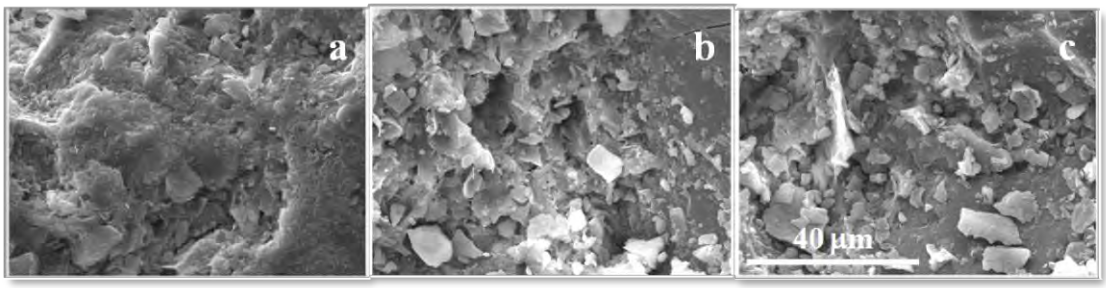

Figure 25. Serena stone surface **(a)** and its functionalization with $TiO_2(S_M)$@TMDS before **(b)** and after **(c)** the washing treatment (1500 K magnification).

AFM images were not collected on Serena stone treated surface, as we did already know that TiO_2 NPs are too small to be visualized on such rough surfaces.

From these results, Serena stone was preferred over marble and it was used as the reference lithotype along this thesis work.

The next step of our study was to investigate the response of the surface modified nanoparticles to UV irradiation. The suggestion to use anatase NPs as bio-nanoremedies lies in their capability to exert photoinduced antimicrobial activity. Briefly, when the radiation wavelength matches the semiconductor (TiO_2) band gap, at its surface takes place the generation of highly oxidizing species (ROS), proved to be active toward the degradation of organic compounds (Fujishima, 1999; Vohra *et al.*, 2009). We tested if synthesized pristine NPs exhibit such photocatalytic activity and if surface-modified NPs also retain such photobehavior. Some literature data, in fact, report on a reduction of photocatalytic activity of TiO_2 NPs once they are surface modified by means of a silane coupling agent (Siddiquey *et al*., 2007; Ukaji *et al*., 2007).

Photocatalytic chemical degradation. Before testing the actual capability of TiO_2 NPs to photodisinfect microorganisms, it was assayed NP photocatalytic efficiency toward the degradation of an organic dye. It was carried out a model photoreaction based on the UV irradiation of methylen blue (MB), since its photobleaching sensitized by TiO_2 has been widely investigated (Mills and Wang, 1999). Briefly, once the organic molecule physically adsorbs on the NP surface and absorbs a proper photon energy, the electrons from the excited dye molecule could inject into TiO_2 conduction band (CB) and be trapped by electron scavengers (*i.e.* O_2), forming transient radical species that break down the organic dye. This degradation mechanisms is summarized by the following reactions (Yu *et al.*, 2007):

$$\text{Dye } (h\upsilon) \rightarrow \text{Dye}^*$$

$$\text{Dye}^* + TiO_2 + O_2 \rightarrow TiO_2 + O_2^{\cdot -} + \text{Dye}^{+\cdot}$$

$$O_2^{\cdot -} + 2\ H_2O \rightarrow 2\ OH^- + 2OH^{\cdot} + O_2$$

$$O_2^{\cdot -}(OH^{\cdot}) + \text{Dye}^{+\cdot} \rightarrow \text{(Cleavaged Dye)}$$

The nanometer sized particles are able to enhance photocatalytic efficiency due to their high surface area that can promote the contact between TiO_2 and the organic

molecules. Moreover, the large amount of hydroxyl groups present at the surface of nanosized particles constitute an important parameter in the photodegradation mechanism, as they can accept the positive holes generated by the irradiation to form hydroxyl radicals and prevent electron recombination (Yu *et al.*, 2007).

In Figure 26a it is displayed the UV-visible spectrum of MB in iso-propanol; it shows a sharp absorption band centered at λ_{max} = 657 nm. The UV-vis spectrum of TiO_2 NPs (Fig. 26b) does not show any significant absorption over 400 nm, featuring only a broad absorption at wavelengths shorter than 400 nm, due to an intrinsic band-band transition (Xu *et al.*, 2008).

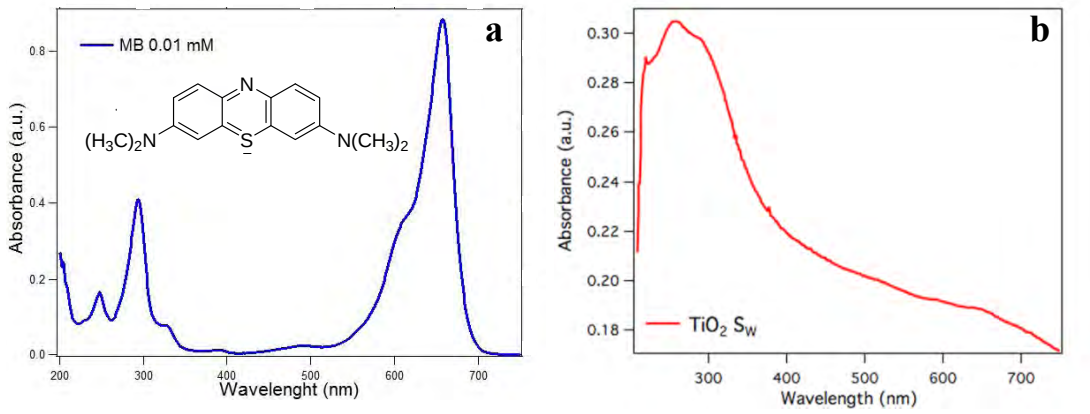

Figure 26. UV-visible absorption spectra of **a)** MB (0.01 mM in iso-propanol) and **b)** TiO_2 anatase (S_W 0.005% w/v in iso-propanol).

It was possible to follow the absorbance variation (due to the dye deterioration) of MB/TiO_2 mixtures monitoring the MB peak at 657 nm as a function of the irradiation time.

Figure 27 shows the spectra collection obtained irradiating a representative dye/NP mixture, in particular MB/(S_M TiO_2@TMDS). The variations in absorbance of the test sample (MB/(S_M TiO_2@TMDS) were compared with a blank, *i.e.* a MB solution where no TiO_2 NPs were added. The test sample exhibits higher rate of absorbance decrease upon irradiation with respect to the blank, indicating the action as photosensitizer performed by the NPs.

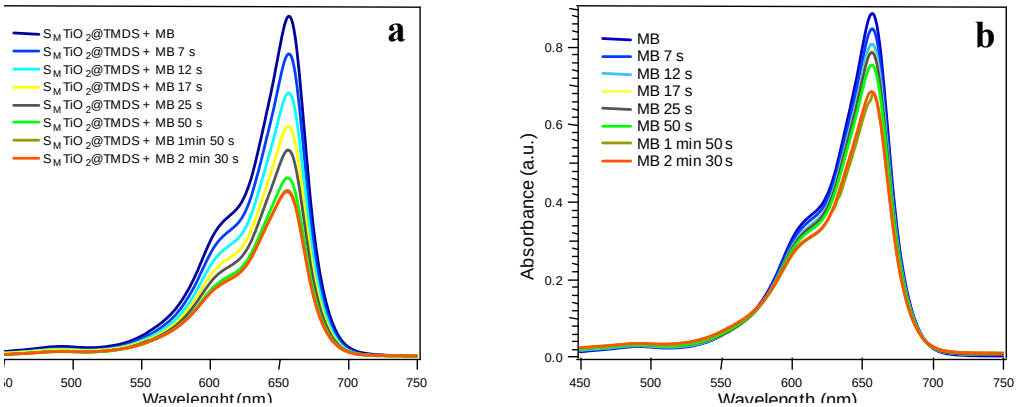

Figure 27. Variations in the UV-vis absorption spectra of (**a**) the test sample (MB + S_M TiO_2@TMDS) and (**b**) of the blank (MB) as irradiation time increases.

The same experiment and spectra collection was performed with several representative pristine or functionalized samples. In representation of pristine NPs the ones synthesized from pure methanol (S_M), pure ethanol (S_E) and pure water (S_W) were chosen, in addition to the NPs obtained from water/ethanol 1/1 mixture, since S_{WE1} is the only sample that displays brookite phase. In representation of functionalized NPs, S_W or S_M samples either surface modified with TMDS or with TSPMC were tested.

All the results recorded over the irradiation time are summarized in Figure 28.

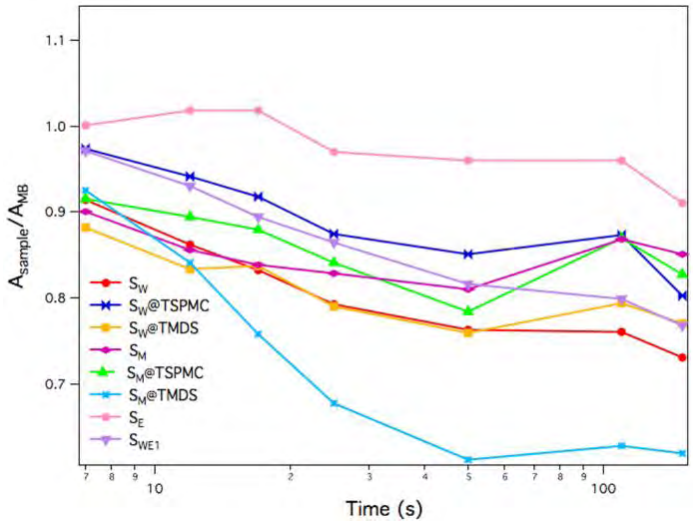

Figure 28. Absorbance of the test samples (MB + TiO_2) normalized for the absorbance of MB at λ_{max} = 657 nm as function of the irradiation time.

Instead of displaying all the absorption curves of the test samples and the blank, the absorbance results were corrected for the non-catalytic contribution to photodegradation of MB (photochemical degradation), *i.e.* MB/TiO_2 curves were normalized using the absorbances from the blank solution.

Sample S_M TiO_2@TMDS shows the highest photocatalytic activity, whilst sample S_E seems not to act as a photosensitizer toward the degradation of the organic dye. Anyhow, it was not observed a specific trend in the photocatalytic performance neither in dependence of the surface characteristics of the NPs (*i.e.* if they are functionalized or not) nor in dependence of the solvent mixture used during the synthetic procedure. It was previously reported that anatase powders with a small fraction of brookite phase display enhanced photocatalytic activity as compared to pure anatase, due to the electron-hole transfer between the two phases (Ozawa *et al*., 2005). That was not corroborated by our experiments; sample S_{WE1}, the one that contains a small amount of brookite phase according to HRTEM-SAED and XRD investigations, did not show any significant improvement in the photocatalytic performance with respect to pure anatase NPs.

Anyway, the results of these experiments with MB prove that TiO_2 NPs can be surface modified with alkoxysilanes without losing the photocatalytic properties of the naked ones. At the same time, it is difficult to extrapolate a clear correlation between the NP surface composition and the photoactivity, as the use of different samples did not incisively affect the photocatalytic results. The results were therefore encouraging to proceed with microbiological testing of the synthesized NPs.

4.1.2 Microbiological assays

Biological deterioration of lithic materials is associated with the alteration of the physico-chemical structure of the rocky substratum along with its appearance (Ortega-Morales *et al*., 2000; Fonseca *et al*., 2010). Current procedures for the treatment of biodeteriorated lithic materials involve the use of biocides but they fail in the long term protection of the surfaces and may also present problems related to their toxicity (Nascimbene and Salvadori, 2008). Conversely, the use of nanostructured TiO_2 NPs as preservative treatment against microbial colonization of

inorganic substrata potentially constitute a compatible method of intervention that would not interfere with material characteristics. Moreover, this kind of treatment would also confer the material a long lasting anti-microbial effect with no harm for the environment and human health.

The preliminary results obtained using the synthesized NPs for the photodegradation of the organic dye (MB) were promising and stimulated further investigations oriented to use TiO_2 NPs as UV-activated antimicrobials. It is important to highlight that photocatalytic bacteria disinfection is different from that of organic molecules. The reason lies in the fact that the organic molecule size is less than 1 nm, and that makes them to adsorb on the photocatalytic NPs; contrariwise, bacteria have micrometer size and it is the semiconductor NPs that wraps the microorganisms (Karunakaran *et al.*, 2010). Another factor to be considered is that, depending on the bacterium under study, sensitivity to UV-light exposure may be different, and also relatively low energy radiation can damage cells through oxidative stress (Barnes *et al.*, 2013).

In this thesis work, the photokilling capabilities of synthesized TiO_2 NPs against bacteria were investigated in suspension and on surface-grafted conditions, using an UVA light peaking at 365 nm as energy source.

Antibiogram method. The very first attempt to verify the antimicrobial properties of synthesized TiO_2 NPs was performed through the antibiogram test, a very common microbiological method. Petri dishes were inoculated with bacteria (*E. coli* or *B. subtilis*), spotted with different concentrations of NPs and with positive and negative controls (ampicillin and water, respectively), UV-irradiated for the desired time period and then incubated overnight. The test was conceived only for pristine NPs in the first place (also purchased TiO_2 NPs, Degussa P25, were tested). Bacteria growth was evident on TiO_2 and negative control spots of the Petri dishes irradiated for 20 min, and it was conversely totally inhibited on the ampicillin spot. On the other hand, 1 h or 5 h irradiation resulted in a total inhibition of bacteria growth all over the Petri dishes, indicating a microbiocidal effect of the radiation. Control dishes (not UV-irradiated) showed conversely homogenous growth all over the plate, TiO_2 spots included. These results were quite unexpected, as on the basis of literature data 365 nm radiation was not supposed to have such germicidal effect toward

bacteria (Huang *et al.*, 2000; Lu *et al.*, 2003; Rincon and Pulgarin, 2003; Fu *et al.*, 2005; Swetha *et al.*, 2010; Zacarias *et al.*, 2010; Polo *et al.*, 2011), even though genus *Bacillus* was indicated as particularly sensitive to UV irradiation (Barnes *et al.*, 2013; Lin and Li, 2013).

Photodisinfection in solution. Since the antibiogram test evidenced that the direct irradiation of Petri dishes expose bacteria to UV-related damages, we tried to decrease the detrimental effects of this exposure by irradiating bacteria and NPs in solution. The experiments were carried out by exposing the sample dishes (TiO_2-cells slurry) and the control dishes (cells slurry) to the UVA energy source (λ_{max}= 365 nm). Aliquots from the irradiated test samples were withdrawn after different periods of UV-exposure (30 min, 1 h, 2 h, 3 h and 5 h), properly diluted, plated and visually counted (Scheme 6, section 3.4). Additional control dishes, either with or without NPs, were subjected to dark conditions. The use of controls is essential to determine whether the action of NPs by themselves, UV exposure by itself, or the combination of these two contributes results in the final antibacterial effect (Page *et al.*, 2007).

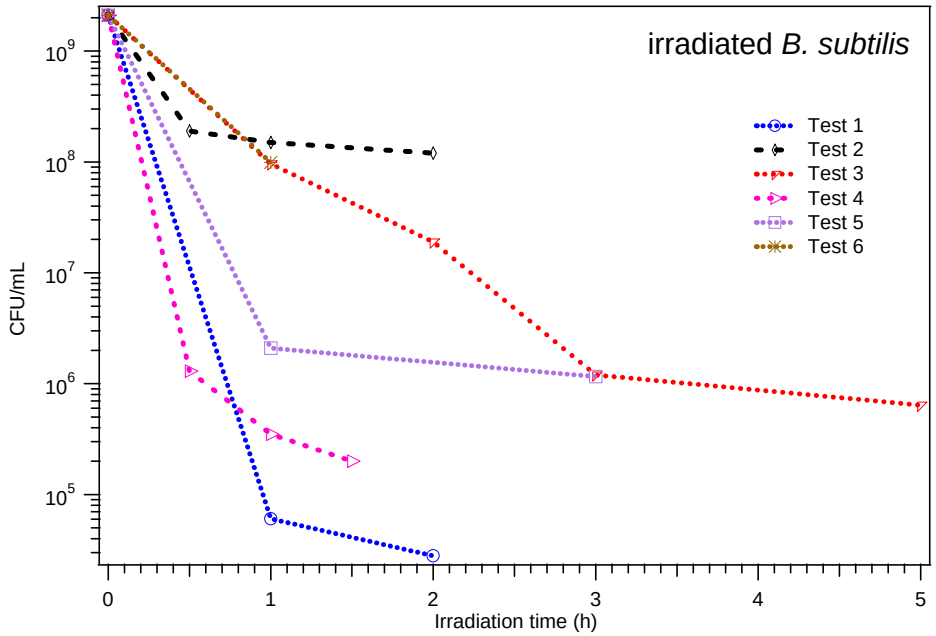

Figure 29. Results of cell viability counts (CFU/mL) from six different irradiation experiments of the control dishes (*B. subtilis* cells slurries without NPs). The samples were irradiated for different time intervals, and then aliquots of the slurries were plated and incubated overnight.

No differences were encountered between the samples incubated with or without NPs in dark conditions. These dark controls ruled out the possibility of a photodisinfection based on the action of NPs by themselves, without the UV-mediation. On the other hand, the results of the experiments performed UV-irradiating the cell slurries suffered from the variable viability results of bacterial cells after irradiation. Figure 29 displays data of *B. subtilis* cell survival (CFU/mL) in the irradiated control dishes (*i.e.* only containing cells dispersed in water without the addition of the NPs) from independent experiments.

Two main observation can be derived from these results. The first is that the UV irradiation at 365 nm may result in a relevant bactericidal action, from 1 to more than 4 order of magnitude decrease of cell viability. Literature data report of about 1 order of magnitude reduction in cell viability for the same bacterial strain, *B. subtilis* (Page *et al.*, 2007; Yeung *et al.*, 2009; Zacarias *et al.*, 2010; Barnes *et al.*, 2013; Lin and Li, 2013). The second observation is that from the application of the same experimental setup and irradiation conditions were not obtained reproducible results, which spanned over 4 order of magnitude. The reason why cellular response varied to such an extent from one experiment to the other was not well understood and constitutes a lack in the reliability of the tests performed.

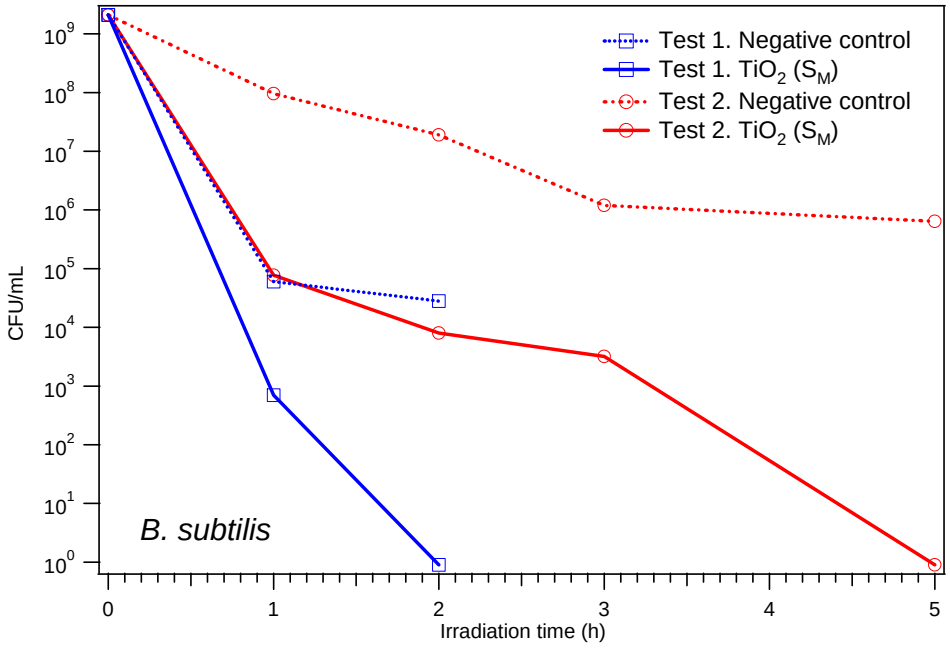

Figure 30. Viable cells counts expressed as CFU/mL obtained from the irradiation of TiO_2 (S_M)-*B. subtilis* cells slurry and the corresponding negative control (only containing bacterial cells).

Each of the tests summarized in Figure 29 have the counterpart performed irradiating NP-containing Petri dishes, but the differences in terms of viability loss between the NP-containing and the NP-free dishes were evident in few cases (Figg. 30 and 31). Nevertheless, these particular cases are still very interesting, since the pronounced differences in the results from NP-containing and NP-free irradiated dishes are ascribable only to the additional oxidative stress induced by the NPs.

When *B. subtilis* was exposed to UV-light in TiO_2 containing slurry (Fig. 30) its viability decreased significantly, and the extent of bacteria inactivation increased for longer irradiation periods. After 1 h irradiation, the loss of cell viability in Test 1 was of 6 order of magnitude, whilst it was of 4 order of magnitude in Test 2. In the same time interval, the extent of *B. subtilis* inactivation in the negative control dishes was either of 4 order of magnitude (Test 1) or 1 order of magnitude (Test 2). That means that the NPs incremented bacteria inactivation by two or three orders of magnitude (Test 1 and 2, respectively) with respect to the corresponding control dish. Moreover, after 2 h (Test 1) or 5 h (Test 2) exposure of TiO_2-cells slurries to UVA-irradiation, the number of viable cells was lower than the quantification limit of this plating method.

Despite the variability in cellular response to UV-light encountered also in NP-containing dishes (CFU/irradiation time curves obtained from the two tests are far from being superimposable), these results still stress out the contribute to cell disinfection of the photoactivated NPs, as none of the NP-free experiments (Fig. 29) led to similar bacteria inactivation.

Similar results have been reported both for *E. coli* (Rincon and Pulgarin, 2003; Lu *et al.*, 2003) and *B. subtilis* (Zacarias *et al.*, 2010; Barnes *et al.*, 2013), and several order of magnitude of cellular viability reduction were observed in presence of TiO_2 NPs. It was also reported that TiO_2 NPs are able to kill approximately all bacteria after 60 min UV illumination (Hajipour *et al.*, 2012). It is interesting to report that Rincon and Pulgarin (2003) found that after 2 h and 20 min irradiation, bacterial cells (*E. coli*) were totally killed even without the help of the photocatalyst. That evidences the oxidative stress to which bacteria are subjected by the simple exposure to irradiation.

The same experimental setup and bacterial strain (*B. subtilis*) were used to test the antimicrobial performance of functionalized nanoparticles. $TiO_2(S_M)$@TMDS

were chosen as their photoactivity was the highest toward the organic dye. In the NP-containing slurry it was detected a cellular killing efficiency of about 40% superior than the negative control dish, but that difference is not so significant given the experimental variability of the test.

The experiments with the Gram+ *B. subtilis* were compared with the results obtained from the most universally studied Gram− bacterium, *E. coli*. In this case, after 2 h irradiation the difference in cell viability between NP-photoactivated and NP-free slurry was about 1 order of magnitude, with a loss of viability 94% higher when the irradiated dish contained NPs (Fig. 31). Similar results were obtained by Huang *et al.* (2000), as after 30 min illumination 96% cells lost their viability.

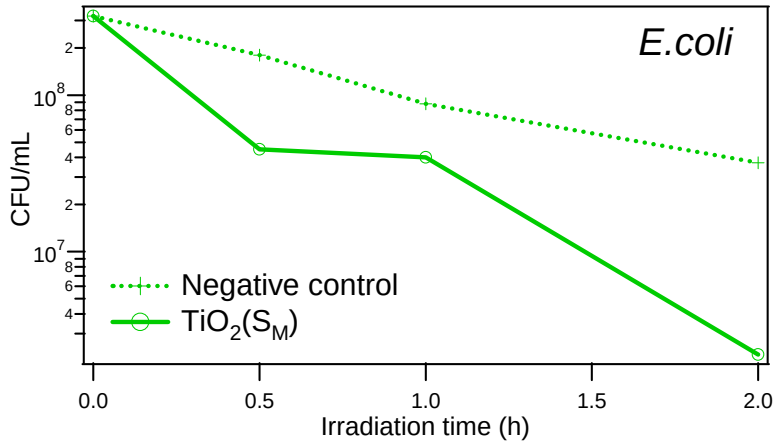

Figure 31. Cell viability counts (CFU/mL) after irradiation of *E. coli*-TiO_2 (S_M) dish and of the TiO_2-free control.

In conclusion, despite the variability of cellular response to UV irradiation and NP effect, some good results were obtained from these experiments performed in solution. They in fact indicated that the synthesized NPs behave as photocatalysts in the reduction of cell viability.

It was therefore prosecuted the research work by testing the antimicrobial effect of functionalized NPs directly on stone treated surfaces.

Antimicrobial activity on stone surface. From the preliminary studies performed to understand the grafting efficiency of TiO_2 functionalized NPs, Serena stone was chosen over marble as the candidate lithotype for the antibacterial tests. It

was designed an *ad hoc* experimental setup in which the stone sample is first functionalized with the NPs and inoculated with bacteria, then it is UV-irradiated for the desired period of time and eventually washed in shaking conditions with saline solution (30 min). Aliquots from the washing solution are plated and visually counted after incubation (section 3.4).

The stone specimens were treated with a NP concentration of 0.4 mg/cm^2. In a recent study, 0.032 mg/cm^2 PEG functionalized TiO_2 NPs were spread over an aluminum surface to test their antimicrobial activity against lots of microorganisms strains, including *B. subtilis* (Yao and Yeung, 2011). We used an higher concentration of NPs as our substratum was not as even as aluminum but rough and porous instead, and that potentially results in less efficient NP-to-microorganism interactions.

Two stone specimens were surface functionalized with $TiO_2(S_M)$@TMDS NPs (test samples), and two other specimens were treated only with the corresponding amount of the grafting agent, TMDS (blank samples, negative controls). One test sample and one control were UV-irradiated, whilst the other pair of stone specimens were kept in dark conditions. The test setup was optimized (as described in section 4.2.2 – preliminary tests on stone sample) in order to know the number of cells to be inoculated on the stone surface and the lag time before recollecting viable cells by washing.

UV-irradiated stone specimens (test sample and negative control) gave the same CFU counts as the specimens kept in dark condition, and no relevant differences were encountered between the $TiO_2(S_M)$@TMDS treated samples and the blanks (TMDS) (~ 10^5 CFU/sample, with an inoculum of ~ 10^7 CFU/sample).

On the basis of the results obtained from the antibiogram method and from the experiments in solution, we expected to obtain a bactericidal effect of UV light by itself. The lack of this effect was surprising and could be attributed to a protective effect of the stone surface against UV and/or to a different UV susceptibility of bacteria cells in different surroundings. Regarding the additional lack of NP effect on cell viability with respect to the tests performed in solution, a first explanation could be based on the fact that in TiO_2-cell slurries bacteria are surrounded by NPs, whilst in the case of the NPs immobilized on the stone surface the contact between microorganisms and TiO_2 is restricted to the exposed TiO_2 surface. Moreover, TiO_2

particles on the stone surface may be more agglomerated than in solution, and that could be a factor that badly affects the photocatalyst behavior, as bacteria can only get in contact with the surface of the agglomerates rather than with all the NP.

Checking in literature, lots of different results were encountered on the microorganism disinfection capability of TiO_2 NPs. In a recent study (Polo *et al*., 2011) it was exploited the ability of titanium dioxide as an agent for biofilm control. Two *Pseudomonas* strains and a *Bacillus* strain isolated from environmental biofilms were used as planktonic cells. Photoactivated TiO_2 resulted effective in decreasing cells viability of planktonic cultures, but it did not have any effect toward biofilm cells. The same result was encountered by Gage *et al.* (2005) working with planktonic and biofilm cells of *P. aeruginosa*. Pinna *et al*. (2009) did not experience any benefit against colonization by cyanobacteria, green algae and lichens by treating ceramic materials surface with TiO_2. Ramirez and De Belie (2009) conversely evidenced the reduction of the algal growth on outdoor concrete surface treated with TiO_2. Rajagopal and coworkers (2006) obtained very good results observing a 4-log reduction in microorganism viability in 10 min irradiation of a natural biofilm due to TiO_2 photocatalysis. A similar result was reported in a study where TiO_2-coated package film decreased cells viability up to 3-log (CFU/mL) after 3 h illumination, whilst the result was only of 1-log decrease for the uncoated film (Chawengkijwanich and Hayata, 2008).

In conclusion, in this section we presented the first part of the results obtained during this thesis work, the ones regarding the research performed on titanium dioxide nanoparticles with the final aim to use them as remedies to inhibit bacteria proliferation on stone surfaces. Synthesis, surface-modification and characterization of TiO_2 NPs were successfully performed, whilst microbiological assays were biased by the variability of cellular response to irradiation. Even though we encountered some difficulties dealing with the microbiological tests, interesting results were nonetheless obtained. From the photodisinfection in solution assays we observed in fact the role of photoactivated NPs in the reduction of bacterial viability.

4.2 Silver nanoparticles (AgNPs)

In the second part of the thesis work it was investigated the potential of a different nanosystem to be used as protecting agent against microbial proliferation on stone artworks; a nanoremedy that, contrariwise to TiO_2, does not need to be photoactivated to exert bacterial disinfection. Silver nanoparticles (AgNPs) have been used for centuries for their antibacterial properties against a broad range of microorganisms and lots of studies have been made to develop medical and non-medical applications for these NPs. To our knowledge, any attempts have been made therefore to use AgNPs on lithic materials to prevent surface biocolonization.

Our investigation and contribution in this field followed three main steps. First, silver nanoparticles were synthesized and functionalized with a proper ligand to be efficiently bound to the stone surface. Then the grafting efficiency to the stone substratum was tested through microscopy techniques, and eventually the antimicrobial capabilities were assayed.

4.2.1 Chemical results

Synthesis and functionalization. The nanoparticle synthesis was aimed to obtain triangular nanoprisms, as it was reported that this shape is the most efficient in terms of antimicrobial activity with respect to any other nanostructure (Pal *et al*., 2007). Prism-shaped NPs were obtained using a seed-based procedure (section 3.2.1) in water and at room temperature (Aherne *et al.*, 2008); these conditions would make easy a scale up to produce at reasonable costs the necessary amounts of nanoparticles to treat large stone artifacts. The shape and size of the NPs were assessed by the field emission scanning electron microscopy technique (FEG-SEM), and a representative image is displayed in Figure 32.

The synthesized pristine NPs were surface modified using a common alkoxysilane derivative, TEOS (tetraethyl orthosilicate). This agent would have the dual role of grafting the nanomaterial to the lithic specimen (its chemical reactivity toward stones is well known) and to protect Ag cores from being oxidized (Xu *et al*., 2009).

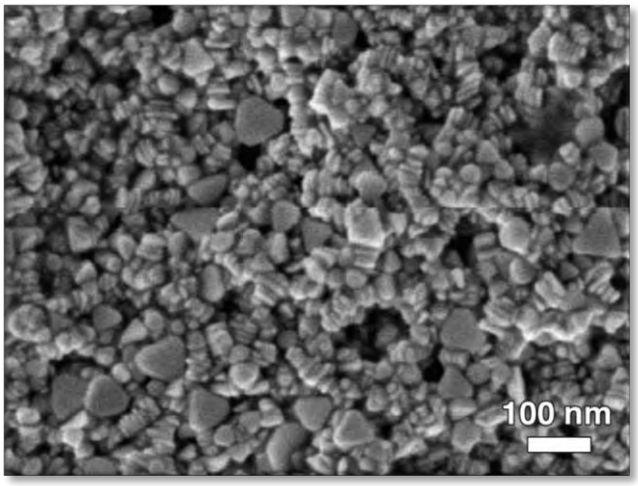

Figure 32. FEG-SEM micrograph of AgNPs. It is clearly shown the prism shape of the particles, whose edge length is about 70 nm and thickness about 5 nm.

These functionalized NPs (referred to as AgNP@TEOS along this dissertation) are usually prepared by modifications of the Stöber process (Stöber *et al.*, 1968) or by reverse microemulsion method, and ammonia (NH_3) is usually chosen as the catalyst of the reaction. The functionalization procedure that was adopted in this work took advantage, conversely, of the use of dimethyl ammonium (DMA) as catalyst, basing on the suggestions of some recent works (Kabayashi *et al*., 2005; Niitsoo and Couzis, 2011). According to these papers, the use of DMA in place of NH_3 allows a higher reproducibility of the shell synthesis because DMA vapor pressure is an order of magnitude lower than the NH_3 one. It was also proposed to use 2-propanol (iPrOH) as reaction solvent in place of ethanol (EtOH). In iPrOH medium, the hydrolyzed TEOS molecules are allowed to reach Ag surface before condensing, minimizing this way the formation of multicore or coreless NPs and promoting a better degree of functionalization of all the NPs.

Stone surface characterization

Colorimetric results. Preliminary colorimetric measurements were performed on Serena stone specimens in order to assess the potential chromatic changes induced by the NPs grafted to the stone surface. As a result, no significant color changes were detected between the NP-treated and untreated samples (Fig. 33), even using the

highest concentration of AgNP@TEOS tested in the stone-surface microbiological assays. Colorimetric change (ΔE) was 0.5 for the stone specimen treated with 110 μg/sample (48.9 μg/cm^2) AgNP@TEOS, below the limit value of ΔE = 2 above which the human eye can appreciate a chromatic difference.

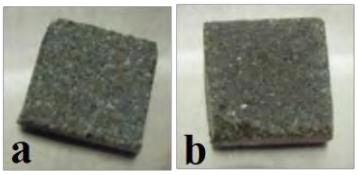

Figure 33. Serena stone specimens **(a)** not treated with NPs and (**b**) treated with AgNP@TEOS, 48.9 μg/cm^2 (Bellissima *et al.*, 2013 a).

The material surface characteristics were evaluated through microscopic techniques before and after the NP grafting. Serena stone specimens were treated with pristine or with functionalized AgNPs and it was studied their disposition over the surface, along with their resistance to a stressing washing treatment. These preliminary considerations were aimed at evaluating if the proposed combination of NPs and surface-modifying agent were suitable (in terms of grafting efficiency) for the next steps of this study, *i.e.* the use of the nanoremedy for antimicrobial assays.

SEM. Scanning electron microscopy analysis (SEM) provided insights about how the nanoparticles were distributed and how strongly they were bound to the stone surface. The strength of nanoparticle grafting was assayed subjecting the stone samples to a 7 mL/s water jet for 30 min (Yao and Yeung, 2011).

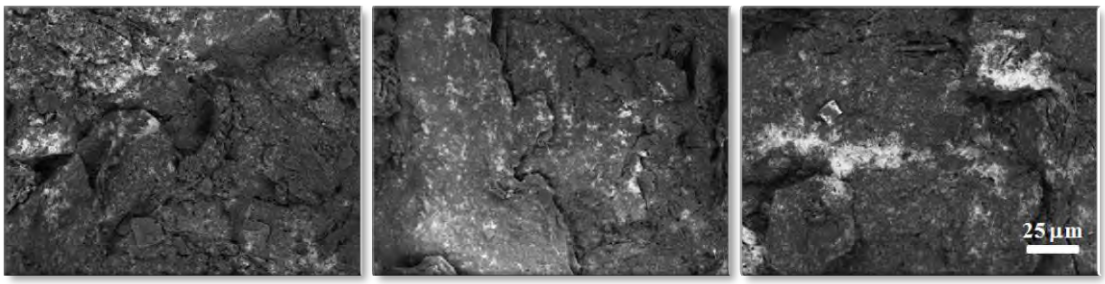

Figure 34. SEM images of the Serena stone surface treated with pristine AgNPs (1.5 kX magnification, BSE mode of acquisition).

Images in Figures 34 and 35 display representative regions of the surface treated with pristine NPs before and after the washing procedure, respectively (Bellissima *et al.*, 2013 a).

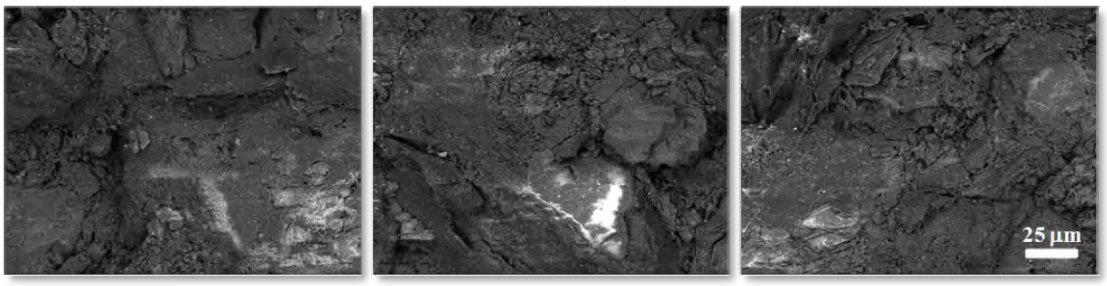

Figure 35. SEM images of the Serena stone surface treated with pristine AgNPs and subjected to a water jet of 7 mL/s for 30 min (1.5 kX magnification, BSE mode of acquisition).

Even though pristine nanoparticles did spread all over the surface of the stone quite uniformly (Fig. 34), their concentration was strongly affected by the washing treatment (Fig. 35). The great percentage of NPs that was lost in the flowing water was indicative of the poor adhesion of pristine AgNPs to the stone surface.

The same investigation was performed on AgNP@TEOS treated stone specimens, and representative SEM images are displayed in Figures 36 and 37 (Bellissima *et al.*, 2013 a).

AgNPs@TEOS treated surfaces (Fig. 36) clearly displayed the formation of large agglomerates of primary nanometer-sized particles, so that the functionalized NPs resulted in an uneven coating on the stone surface with micrometer-sized clusters. Through the analysis of several SEM images (about 50) acquired moving frame by frame along parallel lines, can be estimated an average AgNP@TEOS cluster-to-cluster distance of about 150 µm. These results suggest that the clusters are formed during the functionalization of AgNPs, as their amount is clearly higher in the functionalized sample.

Conversely to what observed with pristine NPs, the washing process of the stone specimens treated with AgNPs@TEOS did not significantly affect the NP concentration over the surface (Fig. 37). This result highlights the successful chemical reaction between the stone surface and the functionalized NPs, and suggests that TEOS is a good grafting agent for the purposes of this work.

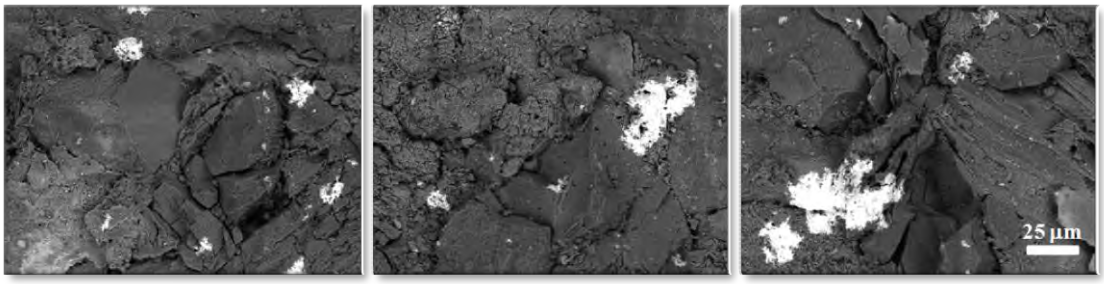

Figure 36. SEM images of the Serena stone surface treated with AgNP@TEOS (1.5 kX magnification, BSE mode of acquisition).

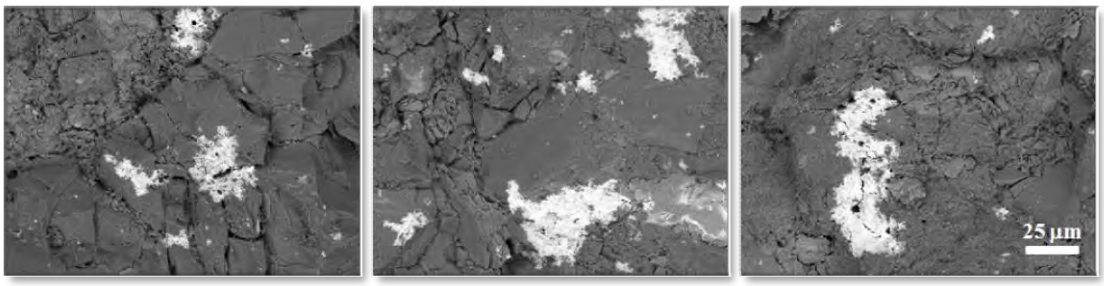

Figure 37. SEM images of the Serena stone surface treated with AgNP@TEOS and subjected to a water jet of 7 mL/s for 30 min (1.5 kX magnification, BSE mode of acquisition).

SEM images taken with higher magnification (Fig. 38) better show the disposition of the NPs (pristine or functionalized) over the surface.

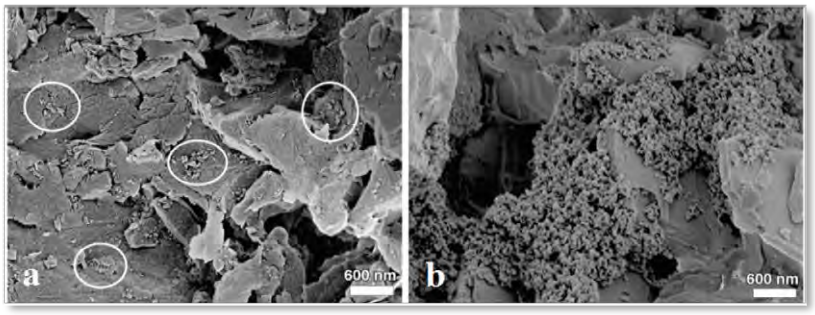

Figure 38. SEM images of pristine (**a**) and functionalized NPs (**b**) on Serena stone surface (50 kX magnification). Circles in picture **a** highlight groups of pristine nanoparticles.

In Figure 38a (white circles) it is well recognizable that pristine NPs do not form any kind of clusters and conversely appear as single self-standing nanostructures spread over the surface. On the contrary, Figure 38b clearly evidences that AgNPs@TEOS tend to aggregate forming clusters intimately bound to the stone surface (Bellissima *et al.*, 2013 a).

AFM. The stone surface was also analyzed by means of atomic force microscopy (AFM). The presence of cracks and voids on Serena stone surface did not allow the analysis of the whole surface. The images were acquired over selected regions where no micrometric irregularities were detected with the aid of the optical microscope equipping the AFM (Fig. 39).

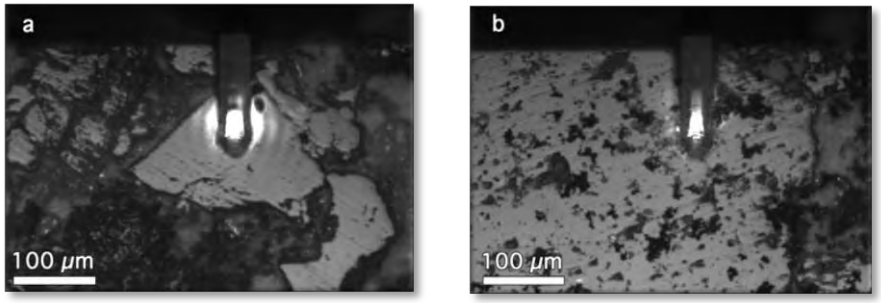

Figure 39. Optical images of the AFM tip positioning over smooth regions during the investigation of the blank stone sample (only treated with TEOS) (**a**) and of the AgNP@TEOS treated sample (**b**).

A representative AFM image of the blank sample (*i.e.* treated with TEOS but without AgNPs) is shown in Figure 40 *a* and *c*. The surface displays the typical aspect of a freshly cut stone slab, and no evidence of silica structure resulting from TEOS condensation can be detected, suggesting that the amount of TEOS added (which is the same present in the case of AgNPs@TEOS) is not sufficient to cover the surface and that the application conditions do not take to the formation of silica nanospheres. It is reasonable to presume therefore that in our conditions TEOS diffuse within the pores. Figure 40 *b* and *d*, conversely, show the aspect of the Serena stone surface functionalized with AgNP@TEOS after the washing treatment. AFM results are consistent with SEM findings, as they show the NP tendency to form clusters over the surface. That could be due to the fact that the hydrolysis of TEOS functions is not confined to the formation of Si−O−Si bridges between one NP and the stone surface, but can also take place between two NPs. Even though in this study AFM is complementary to SEM technique, the results obtained allow to demonstrate that AgNPs retain their triangular shape also after functionalization and that no spherical particles (that would suggest the formation of silica nanospheres) are

present, not even on the surface treated with functionalized NPs (Bellissima *et al.*, 2013 a).

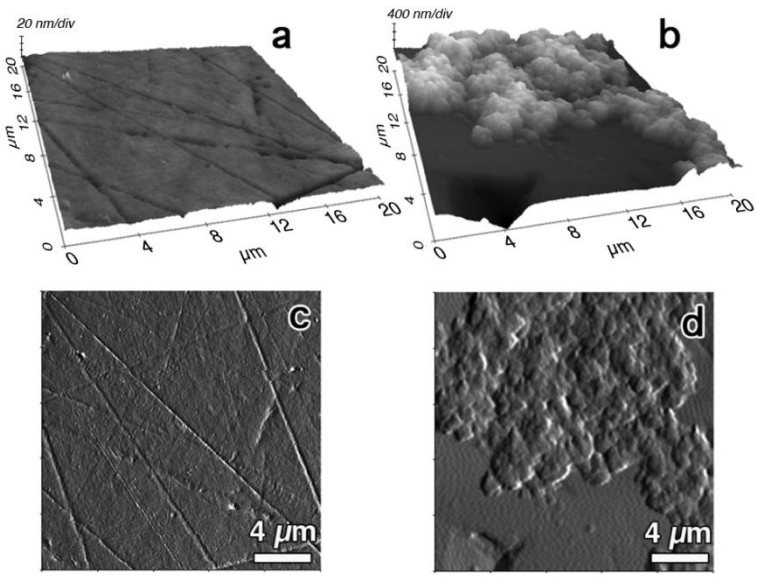

Figure 40. AFM 3D topography and corresponding error images of Serena stone surfaces treated only with TEOS (**a**, **c**) or with AgNP@TEOS (**b**, **d**).

In conclusion, silver nanoparticles with triangular shape were synthesized and surface functionalized with an alkoxysilane derivative, and this surface modification did not lead to variation on the nanoparticle shape. Moreover, the grafting agent used proved to be suitable to our purposes as it is able to bind the NPs to the stone surface quite tightly, conferring the nanoremedy the ability not be leached after a stressing washing treatment. SEM and AFM images show that functionalized NPs tend to aggregate and dispose as clusters on the stone surface.

In the following section, the main microbiological tests performed to elucidate if the nanoremedy proposed is effective as antimicrobial agent are described.

4.2.2 Microbiological results

Before testing the microbial viability inhibition characteristics of the treated stone samples, microbiological studies were performed on naked and surface modified NPs in liquid and in solid nutrient medium, by the use of classical methods. Our interest was particularly oriented in finding out if AgNP surface

functionalization constitutes a significant obstacle to the antibacterial activity. After these preliminary investigations it was assayed the actual antibacterial performance of AgNPs grafted on Serena stone surface. That goal was fulfilled by developing particular experimental setups to test the microbiocidal activity toward *B. subtilis* (bacterium) and *A. versicolor* (fungus).

The procedure to obtain AgNPs in the final useful concentration from the as-prepared nanodispersions implied the use of centrifugal concentrators, that invariably entrapped part of the NPs in the filter meshes. Inductively coupled plasma–optical emission spectrometry measurements (ICP-OES, VARIAN 720 OES) were performed to quantify the material loss during the concentration process, and it resulted an actual AgNP concentration ranging from 1.6 to 8.2 times lower than the nominal value. For this reason, the numeric results from microbiological assays are intended as indicative and not strictly quantitative.

Antibiogram on pristine AgNPs. Pristine AgNPs were first analyzed with the common antibiogram method. 10 μL NP solution were spotted directly on the inoculate plates because AgNPs did not manage to diffuse from discs to medium in the common agar diffusion test.

Table 3. Pristine AgNP antibiogram results. This test was performed on LB Petri dishes inoculated with 0.1 mL of an *E. coli* suspension at different concentrations (10^6, 10^5 or 10^4 CFU/mL). Each plate was composed of several spots at different concentration of AgNPs (μg/mL). Ampicillin (mg/mL) and water were used as positive and negative controls, respectively. +, indicates bacteria growth; –, indicates complete growth inhibition.

CFU/mL	AgNP (μg/mL)[a]				Ampicillin (mg/mL)		H_2O
	500	100	20	4	0.8	2.5	
10^6	–	–	±	+	+	–	+
10^5	–	–	–	±	+	–	+
10^4	–	–	–	–	+	–	+

[a] Calculated as the total Ag content

This preliminary test was conducted on *E. coli* (Gram–), as it is supposed to be less resistant than *B. subtilis* (Gram+) to the antimicrobial activity. The results are summarized in Table 3. Total inhibition of bacterial growth was obtained at 100, 20 or 4 μg/ml AgNP concentration in the plates inoculated with 10^6, 10^5 or 10^4 CFU/mL respectively (Fig. 41).

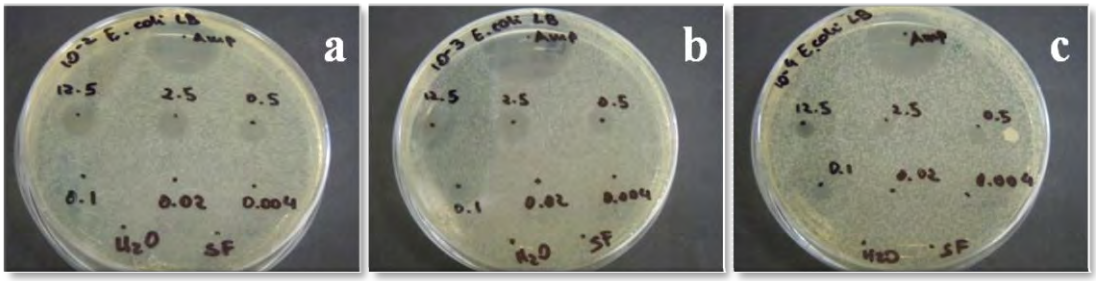

Figure 41. LB Petri dishes inoculated with different dilutions of *E. coli* (**a** 10^6, **b** 10^5 and **c** 10^4 CFU/mL) and different concentrations of AgNPs. 500, 100, 20, 4, 0.8 and 0.16 μg/mL are respectively indicated as 12.5, 2.5, 0.5, 0.1, 0.02 and 0.004 in the picture. The two negative control spots are indicated as H_2O and SF (saline solution); the positive control spot is indicated as Amp (Ampicillin 2.5 mg/mL).

MIC and MBC on pristine AgNPs. The indications obtained from the antibiogram (solid nutrient support) were useful to assay the minimum inhibitory concentration in solution (MIC, Fig. 42).

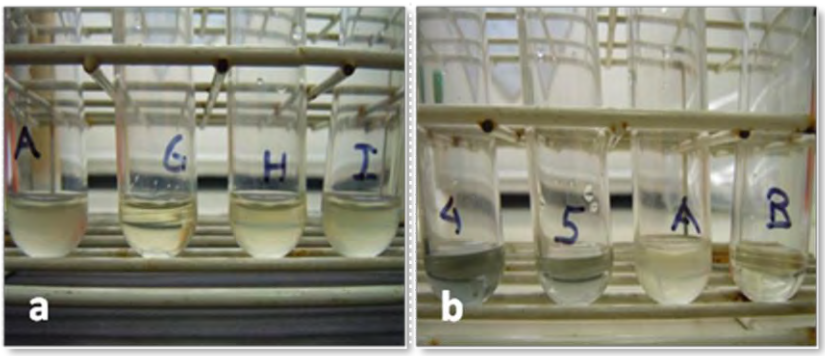

Figure 42. MIC test tubes. **a) *A.*** Positive control, *E. coli* (10^5 CFU/mL), LB and sterile water, ***G.*** *E. coli* (10^5 CFU/mL), LB and AgNPs 0.2 μg/mL, ***H.*** *E. coli* (10^5 CFU/mL), LB and AgNPs 0.1 μg/mL, ***I***. *E. coli* (10^5 CFU/mL), LB and AgNPs 0.05 μg/mL. **b) *A.*** Positive control, *B. subtilis* (10^4 CFU/mL), LB and sterile water, ***B.*** Negative control, LB and sterile water, ***4.*** *B. subtilis* (10^4 CFU/mL), LB and AgNPs 8 μg/mL, ***5.*** *B. subtilis* (10^4 CFU/mL), LB and AgNPs 4 μg/mL.

The results obtained from MIC test define the lowest concentration of silver additive that inhibits the visible growth of microorganisms. Both *E. coli* (Gram–) and *B. subtilis* (Gram+) were assayed. Plastic test tubes were inoculated either with about 10^5 (*E. coli*) CFU/mL or with about 10^4 (*B. subtilis*) CFU/mL in LB liquid medium.

No visual turbidity of the growth medium was detected by the addition of pristine AgNPs at the concentration of 0.2 μg/mL (*E. coli* tubes, Fig. 42a) or 4 μg/mL (*B. subtilis* tubes, Fig. 42b).

These results are comparable with MIC values of commercial antibiotics (Martinez-Gutierres *et al.*, 2010) and are promising if compared with previous studies on *E. coli* and *B. subtilis*. Martinez-Gutierres and coworkers (2010) found MIC values in the range 0.4-1.7 μg/mL for several bacterial strain (*E. coli* and *B. subtilis* included); Martínez-Castañón and coworkers (2008) reported MIC concentration of 13 μg/mL for *E. coli*; MIC values in the range 1.7-13 μg/mL (*E. coli*) were found by Panacek *et al*. (2006); AgNPs were reported to be citotoxic to *E. coli* at concentration of 8 μg/mL (Baker *et al.*, 2005); Sondi and Solopek-Sondi (2004) indicated the MIC value at 10 μg/mL AgNPs (*E. coli*), whilst Morones and coworkers (2006) found that only above 75 μg/mL no significant Gram– bacteria growth took place. Moreover, a recent study (Gutarowska *et al.*, 2012) evidenced differences in nanosilver sensitivity in diverse *Bacillus* strains *(B. megaterium*, *B. pumilus*, *B. licheniformis* and *B. subtilis*), noticing that *B. subtilis* was the more resistant to the disinfection (MIC and MBC values in the range from 22 to 45 μg/mL).

The minimal bactericidal concentration (MBC), *i.e.* the minimum concentration of the antimicrobial agent required to achieve irreversible inhibition of bacterial growth, was determined for both *E. coli* and *B. subtilis* by surface plating 0.1 mL aliquots from the non-turbid tubes. After the incubation (24 h at 37˚C) the MBC was devised at AgNP concentration of 16 μg/mL for *E. coli* and 65 μg/mL for *B. subtilis*. As expected, *B. subtilis* was less susceptible to AgNP bactericidal action than *E. coli*, maybe due to the thicker layer of protection of its Gram+ cells. Despite the uncertainty on the actual numeric results, MIC and MBC are still representative of an effective antimicrobial activity of the synthesized nanosystems.

These preliminary tests performed on pristine NPs were encouraging to proceed with similar tests on functionalized nanoparticles (AgNP@TEOS), in order to understand if functionalization represents a limit to the antibacterial activity. *B. subtilis* was the target bacterial strain.

Spot on spot method. The spot on spot method on solid nutrient medium was performed in place of the traditional antibiogram to find out the threshold concentration of AgNPs@TEOS required to inhibit bacterial growth. This alternative method allowed to overcome a problem met when classical antibiogram method was used; 2-propanol, one of the dispersing solvents of AgNPs@TEOS, inhibits in fact by itself the growth of *B. subtilis* vegetative cells or spores. This method did not involve NP spot application on inoculated dishes, but on the contrary the application of bacterial inoculum on pre-dried NP spots.

Spots with different concentration of AgNPs were tested, as indicated in Table 4. Figure 43 shows the plates inoculated with AgNPs@TEOS.

Table 4. Spot on spot method performed on AgNPs and AgNPs@TEOS. Chloramphenicol (Cmf) and TEOS solution were used as positive and negative control, respectively. +, indicates bacteria growth; -, indicates complete growth inhibition. NP quantity is calculated as total Ag content.

	Cmf (μg)	**TEOS**	**AgNPs (μg)**			**AgNP@TEOS(μg)**		
Sample	5	[a]	5	35	70	5	35	70
Growth	−	+	+	±	−	+	±	−

[a] The quantity of TEOS used was the same of the 70 μg AgNP@TEOS sample.

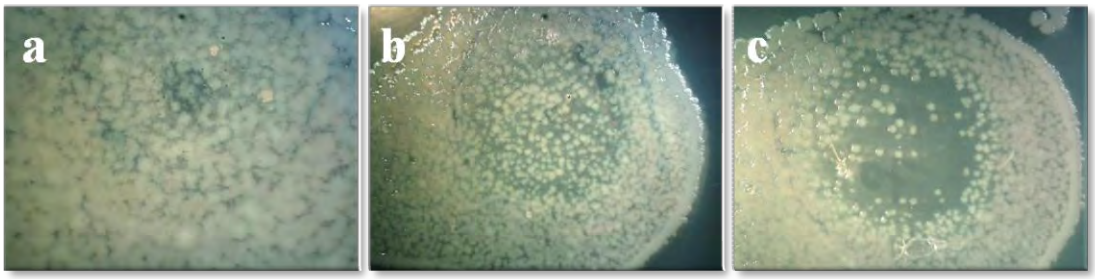

Figure 43. Stereomicroscope images (15 X magnification) of the inhibition zones obtained from the spot on spot method. The concentration of AgNPs@TEOS used are the following: **a**) 5μg, **b**) 35 μg, **c**) 70 μg.

Results show that 5 μg spot does not inhibit bacterial growth, 35 μg are only partially effective, whilst 70 μg fully inhibit bacterial growth (Bellissima *et al.*, 2013 a). There is no difference in antimicrobial activity between pristine and functionalized nanoparticles, indicating that functionalization does not affect nanoparticle toxicity (similar conclusion was reached by Egger *et al.*, 2009; Xu *et al.*, 2009).

MIC and MBC on functionalized AgNPs. The next step was to determine the MIC value of the functionalized AgNP@TEOS in liquid medium and it resulted at 122 μg/mL (Fig. 44). Similar values were found in literature: 100 μg/mL for *Bacillus* strain (Liong *et al.,* 2009) and 195 μg/mL for *S. aureus* (Gram+) (Xu *et al.*, 2009).

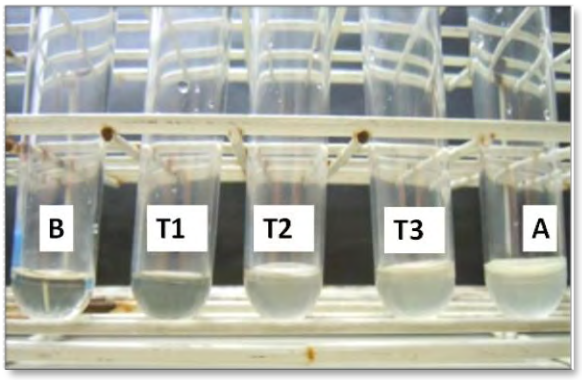

Figure 44. AgNPs@TEOS MIC test tubes. **B.** Negative control, NB and sterile H_2O. **A.** Positive control, *B. subtilis* (10^4 CFU/mL), NB and sterile H_2O. **T1**. *B. subtilis* (10^4 CFU/mL), NB and AgNP@TEOS 122 μg/mL. **T2**. *B. subtilis* (10^4 CFU/mL), NB and AgNP@TEOS 61 μg/mL. **T3**. *B. subtilis* (10^4 CFU/mL), NB and AgNP@TEOS 37 μg/mL.

These preliminary tests performed using functionalized nanoparticles on nutrient media (solid or liquid), evidenced that surface modified NPs retain biocidal activity. The next step was to evaluate the antimicrobial characteristics of the AgNPs grafted to the Serena stone surface.

Antibacterial activity on stone samples

It was first proposed an *ad hoc* experiment toward bacteria (*B. subtilis*) that implied cell deposition and recovery of viable cells by washing, briefly described as follows. A known number of viable cells are applied on a stone surface previously treated with NPs. After a proper period of time from deposition, bacteria are recovered by washing the stone specimen with saline solution, and dilutions of this washing solution are plated, incubated and colonies visually quantified. A similar experiment was performed recovering viable bacteria using contact plates. The antimicrobial characteristic of NP-treated stone samples were eventually assayed toward the growth a fungal strain (*A. versicolor*).

Cell deposition and recovery in solution

Preliminary tests. As long as this kind of experiment is based on the recollection of bacteria from the stone surface, it was necessary to perform some studies to evaluate how bacteria are retained by the stone porous structure. In particular, we were interested to know how many cells have to be inoculated on the stone surface and the lag time before recollecting them, with the aim to be able to appreciate significant differences in cell counts between test and control samples (*i.e.* NP treated and untreated specimens). The time interval from cell deposition to recollection is the period that AgNPs have on disposal to exert their antimicrobial activity.

A suspension of about 10^6 cells was laid on each stone sample and cells were recovered by washing after 1 min, 30 min and 4 h from deposition (interaction time in Table 5). Such short exposures (minutes) have been previously found long enough (even though dealing with different systems) to destabilize cell membrane of bacteria (Lok *et al*., 2006). As shown in Table 5, cells collected immediately after their deposition (1 min) constitute 64% of the inoculated ones; after 30 min from deposition the number of cells collected decreases more than 10 times, and after 4 h the value decreases by a factor of ~ 100. The amount of cells recovered after 30 min is well suited for antibacterial activity experiments. In fact, although 95% of cells results unrecoverable, 5% of the inoculated bacteria are still enough to count a reliable number of CFU and to appreciate differences up to two orders of magnitude

in cell viability (Bellissima *et al.*, 2013 a). It is important to highlight that to achieve a cell recovery useful for our aims, it was necessary to inoculate a very large number of bacteria on the stone surface, by far higher than what can be encountered in natural environment.

It was then investigated if, after 30 min from cell deposition, there was any difference in cell recovery from TEOS-treated or untreated samples. The same result was obtained (CFU % = 5.1 ± 0.1), indicating that TEOS does not interfere with CFU recovery and consequently does not have any antibacterial activity. TEOS treated samples were therefore used as blanks in all the following experiments.

Table 5. *B. subtilis* cell recovery by washing at different times after cell deposition on stone. Values are normalized for an inoculum of $5 \cdot 10^5$ cells/sample. All the experiments were held in duplicate and each washing solution was plated twice from two serial dilution.

	Cells Collected	
Interaction time [min]	**CFU [$\cdot 10^4$]**	**CFU [%]**
1	31.90 ± 0.84	63.8 ± 1.7
30	2.52 ± 0.17	5.0 ± 0.3
240	0.26 ± 0.089	0.5 ± 0.2

These preliminary tests were indicative of the fact that *B. subtilis* inoculum of about $5 \cdot 10^5$ CFU/sample and 30 min interaction time were the proper experimental conditions for our purpose.

Antibacterial activity. Serena stone specimens were treated with different amounts of functionalized AgNPs in the range 6-110 μg/sample (test samples) and the antimicrobial activity was evaluated by comparing CFU recovery from treated samples and the corresponding blanks (TEOS-treated specimens). The results are summarized in Table 6 (Bellissima *et al.*, 2013 a).

In all the experiments, the CFU counts from AgNP@TEOS-treated samples are significantly lower than the blank samples. The highest bacteria inhibition (80.6 %)

was obtained at AgNP concentration of 15 μg/sample; higher concentrations did not lead to any inhibition increase, with an antimicrobial effect around 68%.

The concentration of 6 μg/sample gave the lowest inhibition activity (54.6%). All the concentrations tested proved to be effective in diminishing cell viability of at least 50%, despite allowing NPs and bacteria to interact only for 30 min and despite using a very high concentration of bacteria.

Table 6. *B. subtilis* CFU recovery from stone samples treated with different concentration of AgNPs@TEOS (test samples) or treated only with TEOS (blank samples). The antimicrobial effect was evaluated comparing the number of cells collected from test and blank samples. Values are normalized for an inoculum of $5 \cdot 10^5$ cells/sample.

Concentration AgNP@TEOS [μg/sample]	**Cells collected CFU [$\cdot 10^4$]**		**Antimicrobial Effect [%]**
	AgNP@TEOS	**TEOS [a]**	
6	1.72 ± 0.25	3.79 ± 0.42	54.6 ± 8.3
15	0.32 ± 0.022	1.65 ± 0.11	80.6 ± 1.8
30	1.03 ± 0.067	3.38 ± 0.36	69.5 ± 3.8
60	2.34 ± 0.18	8.70 ± 0.29	73.1 ± 2.2
110	1.10 ± 0.17	2.77 ± 0.23	60.3 ±7.0

[a] For each concentration of AgNP@TEOS, the corresponding quantity of TEOS was used in the blank samples (TEOS).

The fact that the increase in concentration of AgNP@TEOS from 15 to 110 μg/sample only resulted in a slight decrease of the antimicrobial activity may appear in contrast with the growth inhibition results from the spot on spot assay, where an increase in NP concentration led to the enhancement of the antimicrobial activity. This could be partly due to the distribution in clusters of the AgNP@TEOS, which do not cover the stone surface in an uniform way, as observed by SEM analysis (Figg. 36-37).

It is also important to highlight that this cell deposition and recovery in solution assay is intrinsically different from the microbiological tests commonly used to evaluate antimicrobial activity, which generally involve a prolonged time of interaction between NPs and bacteria in a growth medium (solid or liquid). The method used, conversely, did not involve any growth of bacteria but only a recollection of the viable inoculated cells after a short interaction period with the cytotoxic NPs.

Cell deposition and recovery by contact plates

Preliminary tests. A different experimental approach was tested, and results were compared with those from the recovery method in solution. This method implied the use of contact plates both to recover cells from stone surface and to directly grow them. Results were visually evaluated. Preliminary tests were carried out to determine the proper amount of cells to be inoculated on the stone surface and the lag time from cell deposition to recollect a suitable amount of viable cells to give a countable number of colonies useful to evaluate AgNP antimicrobial effect. The stone specimens were not treated with NPs; the results are summarized in Table 7 and Figure 45.

Table 7. Stone samples inoculated either with $3.2 \cdot 10^4$ or $3.2 \cdot 10^3$ CFU/sample (*B. subtilis*). Bacterial cells were recovered using a NA contact plate after different interaction time.

	~10^4 CFU/sample		**~10^3** CFU/sample	
Interaction time [min]	**Cells collected (%)**	CFU	**Cells collected (%)**	CFU
1	//[a]	//[a]	9.8	315
15	1.49	476	1.3	41
30	0.85	272	0.59	19

[a] // indicates uncountable colonies

This method allows to recollect less bacterial cells than in the recovery in solution method. After 30 min from the deposition, 5% of the cells were recovered from blank samples using the recovery in solution method, whilst only 0.85% of the

inoculum was recovered through contact plates. That may be due to the fact that contact plates only sample cells from the very top of the surface of the stone specimens. Despite the low recovery percentage, 30 min application of about 10^4 CFU/sample was evaluated the best operative condition for this method, as the final cell counts allow to appreciate differences up to two orders of magnitude in cell viability between NP-treated and untreated samples.

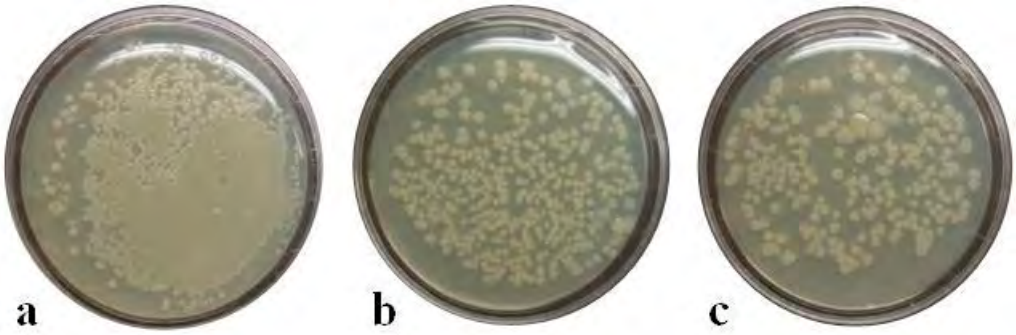

Figure 45. Contact NA plates applied on blank stone samples inoculated with ~10^4 CFU/sample after different times from cell deposition: **a**) 1 min, **b**) 15 min, **c**) 30 min.

Antibacterial activity. After these preliminary tests, stone specimens were treated with 27 μg/cm^2 AgNP@TEOS, the same concentration as in the 60 μg/sample specimen tested in the deposition and recovery in solution method. The reduction in cell viability due to the presence of AgNP@TEOS was 61.3% (Fig. 46), comparable to the 73.1% reduction obtained with the recovery in solution assay (Table 6). Even if the recovery by contact plate is simpler than the recovery in solution, that one still remains the method of choice to test the antimicrobial activity on stone surfaces, as it requires the use of smaller stone pieces (*i.e.* lower amount of NPs) and allows to recover viable cells also from underneath the surface, producing a better statistic.

In conclusion, by these two different cell recovery methods (in solution or by contact plates), it was verified that AgNPs@TEOS grafted to stone surface are effective in inhibiting bacterial cell viability, giving high percentages of antibacterial activity.

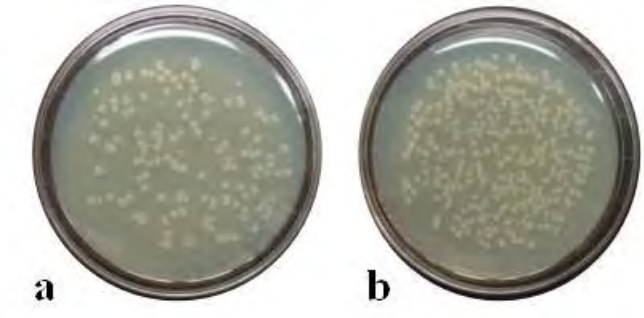

Figure 46. NA contact plates obtained from stone specimens treated with 27 μg/cm^2 AgNP@TEOS (**a**) and the corresponding blank (**b**).

Microbiological activity toward fungi. The next step of this study was to evaluate the antimicrobial activity of AgNPs@TEOS grafted to the stone surface also toward another kind of microorganism. Two fungal strains were chosen: *Aspergillus versicolor* (M2) and *Sarcinomyces petricola* (M4), both isolated from the statue "Il ratto delle Sabine", Piazza della Signoria, Florence. It was used a different experimental setup, based on the evaluation of fungal growth directly on the stone surface. Preliminary studies were performed to determine the proper amount of fungal spores to be inoculated on the stone specimen to have a visible growth in laboratory conditions. Stone samples were inoculated with about 10^4, 10^3 or 10^2 spores/sample and incubated for days at 30 °C at high humidity conditions. The growth was monitored with stereomicroscopic observations. Since *S. petricola* did not grow in such conditions, *A. versicolor* was the only fungal strain to be analyzed (Fig. 47).

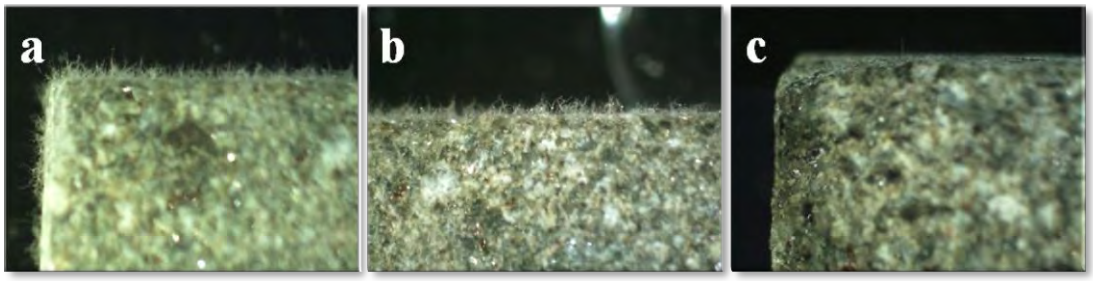

Figure 47. Stereomicroscope images (7 X) of Serena stone samples 7 days after the inoculum with 25μL of growth medium and different amounts of *A. versicolor* spores: ~10^4, 10^3, 10^2 spores/sample in panel **a**, **b** and **c,** respectively.

The intermediate spore dilution (~10^3 spores/sample) was considered the most appropriate to our purposes.

Stone specimens were treated with AgNP@TEOS at two different concentrations (200 μg/sample or 50 μg/sample) and inoculated with ~10^3 spores/sample. From the comparison of fungal growth on untreated (blank) and NP-treated samples, only a slight growth inhibition was noticeable in the 50 μg/sample specimen, whilst very good results were obtained from 200 μg/sample specimen, efficient in contrasting fungal growth (Fig. 48).

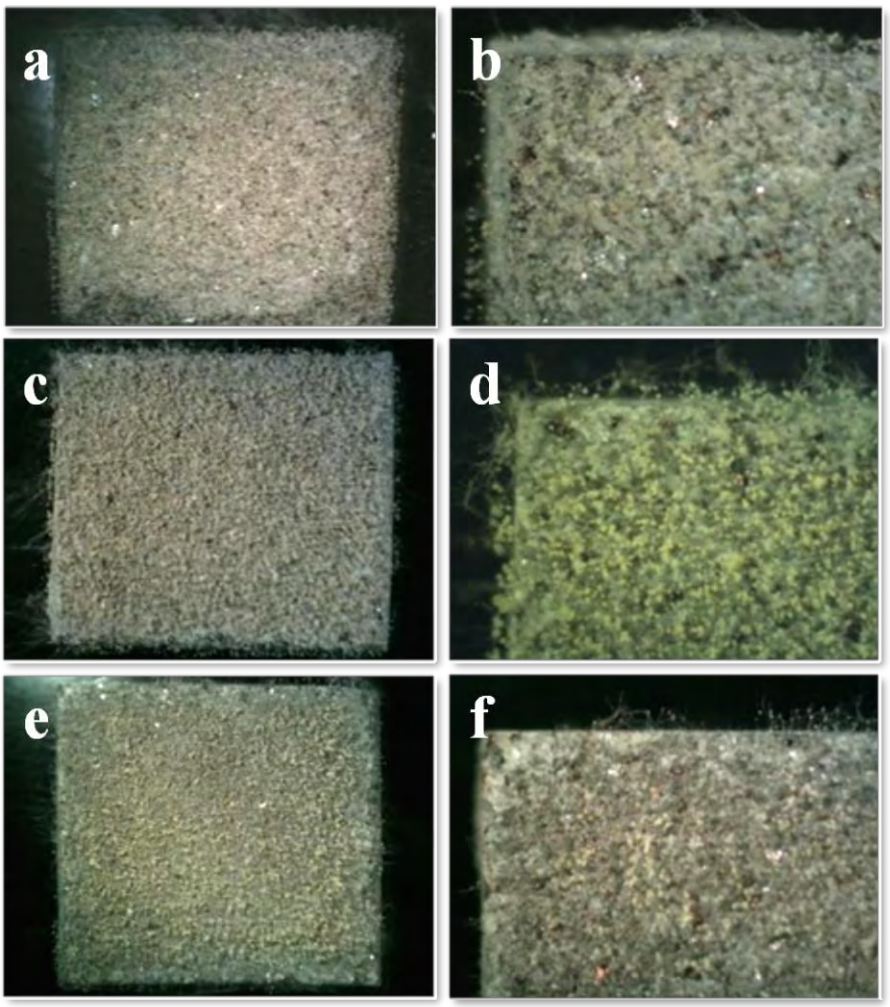

Figure 48. Stereomicroscopic images (7 X magnification on the left, 15 X magnification on the right) of Serena stone samples 4 days after the inoculum with *Aspergillus versicolor*. **a)** and **b)** images show the blank samples. **c)** and **d)** images show 50 μg/sample AgNP@TEOS specimens. **e)** and **f)** images show 200 μg/sample AgNP@TEOS specimens.

In conclusion, the microbiological tests performed on NP-treated stone surfaces resulted in very good microorganism viability inhibition results, both toward *B. subtilis* (bacterium) and *A. versicolor* (fungus). These results allow to think of the proposed nanoremedy as a valid alternative to treat stone surfaces in order to contrast their biodeterioration.

Chapter 5.
Conclusions

Modern conservation science is facing the challenge to guarantee that future generations have the opportunity to appreciate the cultural heritage patrimony we enjoy today. For this reason, scientific community and conservators are spending great efforts to implement appropriate treatments for the artworks to be preserved.

Lithic materials have being used for artistic expression since ancient times, from prehistoric stelae, historic monuments or statues. Such stone artworks are exposed to the action of chemical, physical and biological deterioration, each one contributing in the long-term to the decay of the artifact up to the loss of its original message. Careful studies on these potential deteriorating causes are required to ensure stone artworks the proper conservation.

In this thesis work the interest was focused on microbiological deterioration. Microbial colonization has a relevant impact on the conservation of stone-based artifacts with consequences ranging from esthetic changes to physical and chemical deterioration. The strategy we pursued to control detrimental biodeterioration effects was to prevent and reduce microorganism colonization through the design of a coating able to exert antimicrobial action on the exposed surfaces. Still, our scope was not to simulate a real case scenario, but only to demonstrate the antimicrobial activity exerted on lithic support by the proposed remedies.

In the present dissertation it was discussed the possibility to use two different kinds of cytotoxic nanoparticles, titanium dioxide (TiO_2 NPs) and silver nanoparticles (AgNPs), to inhibit bacteria colonization on the surface of lithic materials. These nano-remedies have a well recognized antimicrobial activity, and their use as preservative treatments against biocolonization is justified in view of a non-invasive application, long-lasting effect and compatibility with the substratum. The NPs were synthesized, characterized and surface modified. This last operation was necessary in order to graft the NPs to the lithic support. Alkoxysilanes were

chosen as the modifying agents, as long as their reactivity is known and their compatibility with the lithic substrate guaranteed.

In this thesis work, *B. subtilis* was used as the reference microorganism for the microbiological assays aimed at testing the biocidal efficacy of the proposed nano-remedies. *B. subtilis* is an heterotrophic spore-forming Gram+ bacterium frequently found on monumental stones. Some studies were also carried out toward a fungal strain, *Aspergillus versicolor*, a genus commonly found on stone degraded surfaces. The reference lithotype used was Serena stone, a sandstone very diffused in Italy, especially in Florentine buildings.

TiO_2 NPs. Titanium dioxide nanoparticles were synthesized in the anatase crystallographic phase through a known procedure (Liao *et al.*, 2009), and the effects on dimension and crystallinity induced by different synthetic solvent mixtures were studied. Lots of techniques were used to this purpose: SAXS, WAXD, TEM and XRD. All the NPs obtained were highly crystalline in the anatase form and no relevant variations of their size were induced by different solvent mixture used during the synthesis. IR-spectroscopy, TGA and HRTEM were used to study the methoxysilane functionalization of the NPs. These techniques evidenced that the grafting reaction to the NP surface took place efficiently, and HRTEM images clearly showed crystalline cores surrounded by an amorphous layer of silane. The adhesion of the NPs to the lithic support was studied by means of SEM technique. Serena stone was chosen as the reference lithic substratum, as long as when its surface was functionalized with the NPs, the nanoremedy was not diluted in the water flow after a washing treatment, remaining well anchored to the stone surface.

The mechanism that makes TiO_2 NPs extensively used for the degradation of organic compounds is the same on which it is based their antimicrobial activity, and involves the photoactivated production of reactive oxygen radical species by means of UV-light irradiation. In the direction to find out if the NP surface modification negatively interferes with the nanomaterial photo-characteristics, the synthesized nanosystems (functionalized of not) were preliminary tested toward the photocatalytic decomposition of an organic dye molecule. Since surface modification did not result to badly influence the photodegradation of the organic dye, the nanoremedies were further tested toward bacteria photodisinfection.

Prior to test NP efficacy on lithic support they were tested in nutrient media (either solid or liquid). These experiments were biased by the fact that UV-irradiation itself had a variable biocide effect on bacteria. It was nonetheless possible to demonstrate an effective role of TiO_2 NPs in increasing cell photodisinfection in NP irradiated batches (up to total bacteria killing). When Serena stone specimens were treated with the nanosystems and inoculated with *B. subtilis*, it was conversely not possible to appreciate any difference between the NP-treated and untreated samples or between UV-irradiated specimens and dark control.

Further investigations are planned in order to clarify the causes of the variable response of bacteria to UVA irradiation and the reasons why neither the photocatalytic disinfection (NP-mediated) nor the photochemical disinfection (only UV-mediated) were encountered irradiating bacteria inoculated stone surfaces.

AgNPs. Triangular nanoprisms were synthesized through a seed-based method (Aherne *et al.*, 2008) and they were surface modified by means of a common ethoxysilane derivative (TEOS) in order to confer the NPs the ability to be grafted to the lithic support. The NP adhesion to the surface was studied by means of SEM and AFM techniques, before and after the application of a stressing treatment aimed at simulating heavy rain conditions (washing treatment). The non-functionalized NPs did spread homogeneously on the stone surface but did not remain attached to the lithic support after the washing treatment. The functionalized NPs, conversely, arranged on the stone surface in clusters and they were not affected by the washing treatment, indicating that the grafting agent chosen was suitable to our scopes.

Classical microbiological methods on nutrient media (solid or liquid) were used to assay the surface functionalization effects on the antimicrobial activity of the NPs. As long as TEOS surface modification did not interfere with microbiocidal activity of AgNPs, an experimental setup was specifically tailored to test NP cytotoxic properties once grafted to the stone specimen. Cell deposition and recovery in solution assay was used to quantitatively evaluate the antibacterial activity of the NPs fixed on a lithic support. Bacteria viability was inhibited up to about 80% (6.7 $\mu g/cm^2$ AgNP@TEOS) with respect to the control sample (not NP-treated). That was a very good result, especially because the period of interaction between NPs and

bacteria was limited in time and bacteria concentration was higher than *in situ* conditions.

Good results in terms of inhibition of microorganism growth were obtained also dealing with fungal spores inoculated on AgNP@TEOS treated stone specimens, as about 89 μg/cm^2 AgNP@TEOS resulted in a drastic reduction of fungal growth over treated stone surface.

This dissertation proved that AgNPs functionalized with TEOS can adhere to Serena stone surface and act as effective nanoremedies to contrast microbial viability on treated stone specimens. The development of our research on the use of AgNPs as lithic surface antimicrobials implies the scale up of the experiments from laboratory conditions to natural environment and real case scenarios. In the prosecution of the work the proposed AgNPs@TEOS are going therefore to be applied as preservatives against microbial colonization for the *in situ* treatment of Serena stone Works of Art.

Annex.

Principal analytical techniques

In this chapter the principal and more complex characterization techniques used along this thesis work are outlined. First of all, the concepts underlying the scattering theory are briefly explained. Afterwards, it is reported an introduction to microscopy techniques, and more specifically two electron microscopy techniques (TEM and SEM) and a scanning probe microscopy (AFM) are described. The last paragraph is oriented to a brief introduction to the diffraction theory used in the XRD measurements.

Scattering techniques

A typical scattering experiment consists of a monochromatic beam that, through the interaction with the sample, is re-emitted in directions different from that of the incident beam (Fig. 49). The scattering centers in X-ray scattering experiments are the electron clouds. X-ray scattering is a suitable technique for studying structural features of colloidal matter. Small angle X-ray scattering is suited for probing distances in the range between 1 nm to 1 μm.

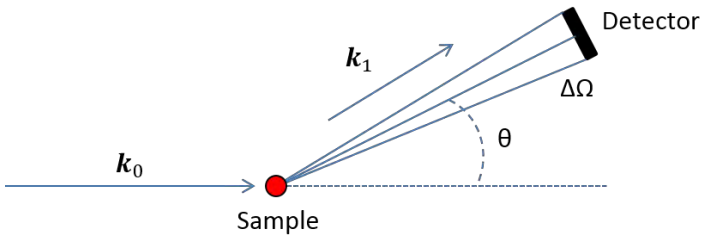

Figure 49. Typical scattering geometry. K_0 and k_1 respectively indicate incident and scattered wave vectors.

The scattering vector $\boldsymbol{Q}$ is the fundamental variable of the experiment and represents the difference between the wave vectors of incident and scattered radiation ($\boldsymbol{k_0}$ and $\boldsymbol{k_1}$ respectively).

$$\vec{Q} = \overrightarrow{k_0} - \overrightarrow{k_1}$$

Dealing with elastic scattering, the magnitude of the scattering vector is directly related to the scattering angle θ through the following relation:

$$|\vec{Q}| = \frac{4\pi n}{\lambda} \sin\theta$$

where λ is the wavelength and n the refractive index.

$\vec{Q}$ has the dimension of reciprocal length ($\dot{A}^{-1}$) and represents a measure of the spatial resolution of the scattering experiment. From the Bragg law, the distance (d) probed by the measurement at a given wave vector and wavelength results $d = {2\pi}/{Q}$.

Scattering experiments performed at different $\vec{Q}$ can be thought to give picture of the matter at different magnifications.

The waves scattered at a given angle by all the scattering centers interfere with each other to produce one point in the interference pattern, that is then transformed to reconstruct an image of all the correlations between the sample. It has to be considered that the waves scattered at the same scattering angle differ in path length, so that constructive and destructive interference occurs.

The scattering intensity is given by:

$$I(Q) \cong I_0 \, \Delta\Omega \, \eta \, T \, \frac{d\sigma(Q)}{d\Omega}$$

where I_0 is the incident flux, $\Delta\Omega$ is the solid angle subtended by the detector (whose efficiency is represented by η), T is the sample transmission and $d\sigma(Q)/d\Omega$

is the microscopic scattering cross section, that is related to the structure and interaction in the system over the *Q* range investigated.

The differential scattering cross section is given by:

$$\frac{d\sigma(Q)}{d\Omega} = N V^2 (\Delta\rho)^2 P(q)S(q) + bkg$$

where *N* is the concentration number of scattering particles, *V* is the volume of a scattering particle, $(\Delta\rho)^2$ is the contrast factor (the difference in scattering length between the particle and the surrounding), *P(Q)* is the form factor of the particle, *S(Q)* is the structure factor and *bkg* is the incoherent background signal.

The form factor is a function that describes how the scattering cross section is modulated by interference effects between radiation scattered by different parts of the same particle; the form factor is indeed related to the shape of the scattering particle. The structure factor can be neglected in diluted systems, as it describes the interference of scattering events from different particles, and contains information on their interactions.

Microscopy techniques

Brief introduction. The microscopes can be classified in three types: optical, charged particles or scanning probe. Optical microscopes use visible light and transparent lenses to see objects up to the micrometer size range. Charged particles microscopes use electrons or ions instead of light, electromagnetic or electrostatic lenses to focus the particles and their resolution gets up to tenths of nanometers. Scanning probe microscopes use a physical probe to scan the sample in contact or near-contact with it. They map forces and interactions between the probe and the sample to build up an image of the sample surface with atomic resolution.

The resolution of a microscopy technique, ρ, is defined as the distance between two details just separable one from the another. The following formula can be used to

calculate resolution of microscopes that use incoherent light or electron beam as probe:

$$\rho = {}^{0.61\lambda}/_{sen\alpha}$$

where λ is the wavelength of the beam and α the maximum angle between incident and deflected beam in the limit of the lens aberrations.

In the case of high-voltage accelerated electrons, their associated wavelength is

$$\lambda_{e^-} = {}^{1.23}/_{(accelerating\ voltage)^{1/2}}$$

Electron microscopy techniques

When electrons are accelerated up to high energy levels (kV) and focused on a specimen, a rich variety of interactions may take place (Fig. 50). Some electrons can be scattered elastically or inelastically (with precise directions if the specimen is crystalline); they can be reflected (backscattered); their impinging with the sample can produce Auger electrons; they can knock electrons from sample atoms, and such electrons escape as slow energy secondary electrons; they can induce atoms to emit X-rays or photons (cathodoluminescence); they can be transmitted.

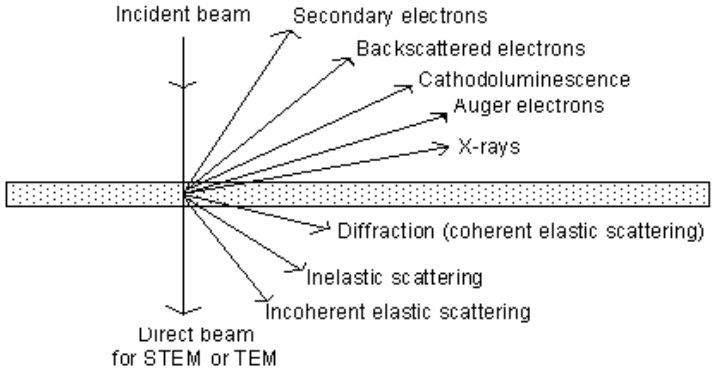

Figure 50. Possible interaction of the electron beam with the specimen.

Transmission electron microscopy (TEM)

The transmission electron microscope (TEM) can be compared to a slide show projector, in which the light source is an electron source, the lenses are magnetic and the projection screen is a fluorescent screen or an electronic imaging device (CCD camera). The microscope is fully enclosed to reduce interference from environmental sources, all the beam trajectory is under vacuum and the specimen have to be really thick to allow the beam to pass through it.

TEM instrument is constituted of four main components: an electron optical column, a vacuum system, the necessary electronics (lens supplies for focusing and deflecting the beam and the high voltage generator for the electron source), and a control software. Condenser lenses are used to focus the electron beam on the sample; objective lens is used to form the diffraction pattern in the back focal plane and the image of the sample in the image plane; intermediate lenses are required to magnify the image or the diffraction pattern on the screen. The power (focal length) of the magnetic lenses can be adjusted by changing the current through the lens coil. As the electrons pass through the thin specimen, the transmitted electron beam is collected, focused by an objective lens and a magnified real image of the specimen is projected onto the viewing device.

In a TEM experiment, the electrons are accelerated to very high voltage, hundreds of kV, and their associated wavelength is five orders of magnitude smaller than the light wavelength. That is not the only factor that makes TEM resolution really high, but also the fact that the convergence angle of the electron beam is about 0.5° (thanks to the use of magnetic lenses), instead of the 70° of the glass lenses used in optic microscopes. That allows for a resolution down to the Å order, that enables the imaging and structure determination at the atomic level.

There are two main imaging modes: bright and dark field. If the bright field mode is used, the crystalline parts in Bragg orientation appear dark and the amorphous or non-Bragg oriented parts appear bright. In the dark field mode, the incident beam is tilted and each of the diffracting phases can be differentiated by selecting one of the diffracted beams with an objective diaphragm. In the dark field mode the amorphous regions will appear dark.

HR-TEM. While in classical electron microscopies the image is carried by only one beam (diffracted or transmitted), high-resolution electron microscopy uses phase contrast resulting from the interference of several beams. In particular, high resolution transmission electron microscopy (HRTEM) differs from conventional TEM in that not only the transmitted beams or some of the forward scattered beams are used to create a diffraction contrast image, but both the transmitted and the scattered beams are used to create an interference image. It allows for direct imaging of the atomic structure of the sample relying on phase contrast. The direct imaging of the specimens is accomplished by allowing some of the diffraction images to overlay the bright field image, enhancing the contrast along the lattice lines.

The high performance of HRTEM microscope is due to the low spherical aberrations and high stability of several parameters, such as the high tension, lens currents or energy of the electron beam. HRTEM allows direct measurement of lattice parameters, inspection of individual defects and grain orientation.

SAED analysis. In the selected area electron diffraction (SAED), an aperture is used to define the area from which a diffraction pattern is formed in a TEM specimen. This method allows to obtain a diffraction pattern of small objects by focusing the electron beam up to a small spot size on a selected area of the surface. The resulting patterns contain information about the phases present (lattice spacing measurement) and the sample orientation.

The diffraction pattern is the result of the propagation of the electron wave through a crystal, and regular arrays of scattered intensities carry the information about the position of the scattering centers (atoms in the crystal). The spots of SAED become disks whose radii are the sources that provide the investigator with information about crystal symmetry, interplanar distances and the orientation to the beam path. This method is useful to confirm the identification of a phase.

The use of HRTEM images together with SAED patterns enable therefore to obtain a structural determination that is called “electron crystallography”. This determination is complementary to X-ray crystallography, as the strong interaction between electron and matter (thousands of times stronger than X-rays) allows for the structural determination with the precision of atomic positions.

Scanning Electron Microscopy (SEM)

SEM analysis can provide information on surface topography, crystalline structure, chemical composition and electrical behavior of the top of the specimen (~1 μm).

Similarly to TEM, scanning electron microscope is constituted of an electron optical column, a vacuum system, lenses and electronics and a control software. The column used is therefore shorter than in TEM, as SEM requires only lenses above the specimen and no lenses below it; the sample characteristics are not in fact analyzed through the projection onto a screen (TEM). Moreover, SEM sample chamber is larger than the TEM one, as this technique does not impose restriction on the sample size.

In a SEM analysis, an electron beam is emitted by an electron gun, focused by condenser lenses into a fine spot and deflected by scanning coils. Through the deflection of the beam in the x- and y-axes, the sample surface is scanned in a raster fashion over a rectangular area line by line. It is also possible not to sweep the electron beam across the surface but obtain a static analysis at one position.

When the electron beam interacts with the sample, it loses energy in the interaction volume (Fig. 51), whose size is dependent on the energy of the incident electrons. The energy exchange between the electron beam and the sample results in the reflection of high-energy electrons by elastic scattering (backscattered electrons, BSE), in the emission of low energy secondary electrons (SE) by inelastic scattering and in the emission of electromagnetic radiation (X-rays).

The intensities of the signal produced from the interaction with the specimen are registered and mapped as variations in brightness on the image display.

Secondary and backscattered electrons are the most commonly used signals for imaging a sample: SE are most valuable for showing morphology and topography, whilst BSE are most valuable for illustrating contrasts in composition in multiphase samples.

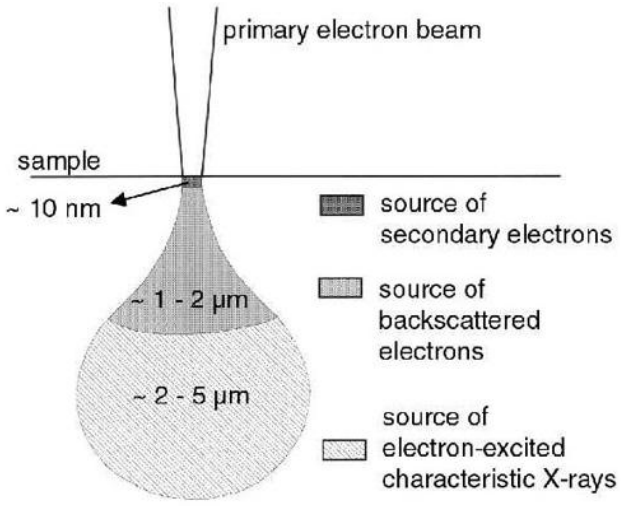

Figure 51. Different types of signals originated from different volumes of interaction. Secondary electron signals have the smallest interaction volume and potentially the highest resolution.

SE, according to their very low energy, can escape the sample and be detected only if they originate very close to the sample surface. For this reason, if SE are used to create an image, steep surfaces and edges tend to be brighter than flat surfaces, which appear dark. SE imaging have high spatial resolution and strong topographic contrast, so that images have a well-defined three-dimensional appearance. Conversely, BSE electrons are used for their strong atomic number contrast. For this reason they are useful at the presence of heavy elements, as they backscatter electrons more strongly than light elements, and appear brighter in the image. BSE are commonly used to detect contrasts between areas with different chemical compositions.

X-rays originate from a large volume of interaction and they are widely used for elemental microanalysis. X-ray energy corresponds to a difference between two electronic energy levels of the atom, as X-rays are emitted when the electron beam removes an inner shell electron from the sample and an higher-energy electron fills that shell releasing energy. Since the levels are quantified, X-ray energy spectrum represents the signature of the atom and allows for chemical analysis of the sample. X-rays can be detected through the energy dispersive spectrometry (EDS) system.

The increase in magnification in a SEM experiment is achieved by reducing the area scanned across the surface. The resolution of a SEM analysis depends on the reliability degree of the association of the signal to the position of the electron beam

at any time. To obtain sub-nanometer resolution at very low accelerating voltages, the use of a field emission electron gun is recommended (FEG-SEM), as it is capable of producing at these operative conditions high primary electron brightness and small spot size. Due to the very narrow electron beam, SEM micrographs have a large depth of field that yields the characteristic three-dimensional appearance of the surface structure of the sample.

The spatial resolution of the SEM experiment depends on the size of the electron spot and the size of the interaction volume. Because the spot size and the interaction volume are both large compared to the distances between atoms, SEM resolution is not high enough to image individual atoms. The resolution of single atoms is possible for electrons with shorter wavelength (*i.e.* higher energy), that is to say the ones used for TEM measurements.

Atomic Force Microscopy (AFM)

Atomic force microscopy belongs to the family of scanning probe microscopies (SPM), used to study surface properties of materials up to the atomic level. These techniques use a probe tip that measures changes in the surface characteristics as the tip scans over the sample surface. AFM apparatus is based on a laser radiation source, a cantilever, a tip and a position sensitive detector (Fig. 52).

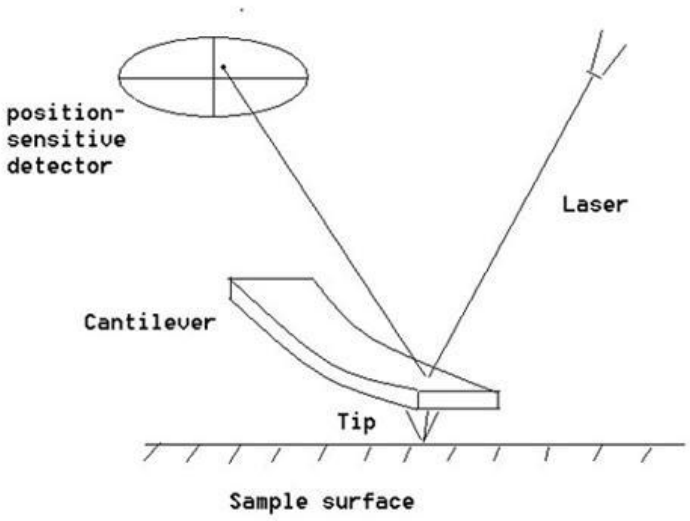

Figure 52. Schematic representation of an AFM apparatus.

The atomic force microscope relies on the forces between the tip and the sample. They are calculated by measuring the deflection of the cantilever through the simple Hook's law $F = -kz$, where F is the force, k is the stiffness of the lever and z the distance the lever is bent. The laser beam is reflected from the back of the reflective cantilever onto a position-sensitive four-segment photo-detector and the exact position of the probe tip is registered.

The most common operational modes for an AFM experiment are the contact mode, the non-contact mode and the tapping mode.

Using the contact mode, the tip is raster-scanned across the surface and it is deflected as it moves. If a constant force approach is used, the tip position is adjusted through a feedback circuit to maintain a lever constant deflection and these adjustments constitute the displayed data. If a variable-deflection approach is used, the deflection is measured without any adjustment.

In non-contact mode, a stiff cantilever is oscillated in the attractive regime (see Fig. 53), meaning that the tip is close to the sample but not touching it. The changes in the resonant frequency of the cantilever are measured.

In tapping mode AFM, a very stiff cantilever is oscillated closer to the sample than in non-contact mode. Part of the oscillation extends into the repulsive regime (see Fig. 53) so that the tip intermittently touches (taps) the surface.

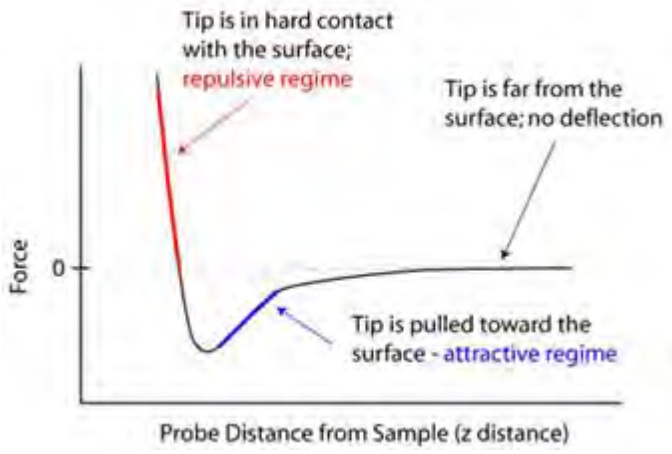

Figure 53. Schematic representation of the force between the probe and the surface as a function of the tip-sample distance.

X-ray Diffraction (XRD)

X-ray diffraction is a technique commonly used for the determination of the atomic and molecular structure of a crystal. The incoming X-rays are elastically diffracted in many specific directions and by measuring angles and intensities of these diffracted beams it is possible to obtain a three-dimensional picture of the electron density within a crystal. From this electron density, the mean positions of the atoms are determined.

This technique has its foundation in the Bragg model of diffraction (Fig. 54). The X-rays scattered from adjacent planes (at distance *d* one to the other) combine constructively when the angle θ between the crystallographic planes and the X-ray differ of an integer multiple *n* of the X-ray wavelength (λ). A given reflection is therefore associated with a set of evenly spaced sheets running through the crystal, usually passing through the centers of the atoms of the crystal lattice.

$$n\lambda = 2dsen\theta$$

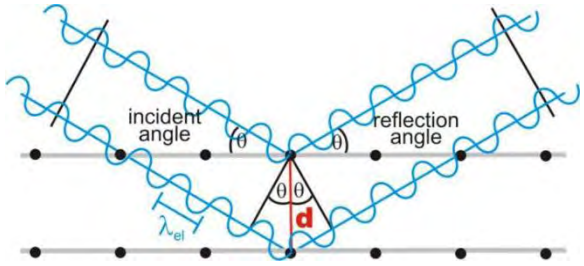

Figure 54. Schematic representation of the Bragg law of diffraction.

The X-rays are generated by a cathode ray tube, filtered to produce monochromatic radiation, collimated and directed toward the sample. The sample is scanned through a range of angles and all possible diffraction directions of the lattice should be attained due to the random orientation of the powdered material. The diffracted rays are then detected, processed and counted. A peak of intensity occurs when the interaction of the incident rays with the sample produces constructive interference, *i.e.* when Bragg's law conditions are satisfied. From the *d*-spacing it is possible to identify the crystallographic phase of the sample.

Bibliography

Aherne, D., Ledwith, D.M, Gara, M., Kelly, J.M., 2008. Optical properties and growth aspects of silver nanoprisms produced by a highly reproducible and rapid synthesis at room temperature. Advanced Functional Materials 18, 2005-2016.

Alakomi, H., Paananen, A., Suihko, M., Helander, I., Saarela, M., 2006. Weakening effect of cell permeabilizers on Gram-negative bacteria causing biodeterioration. Applied Environmental Microbiology 72, 4695-4703.

Allen, N. S., Edge, M., Verran, J., Caballero, L., Abrusci, C., Stratton, J., Maltby, J., Bygott, C., 2010. Photocatalytic surfaces: environmental benefits of Nanotitania. The Open Materials Science Journal 3, 6-27.

Anagnostopoulos, C. and Spizizen, J., 1961. Requirements for transformation in *Bacillus subtilis*. Journal of Bacteriology 61, 741-746.

Araujo, EA., Andrade, N., da Silva, JH., Dernardes, PC., de C. Teixeira, A., de Sa, JP., Fialho, JF., Fernandes, PE., 2012. Antimicrobial effects of Silver Nanoparticles against bacterial cells adhered to stainless steel surfaces. Journal of Food Protection 75, 701-705.

Baglioni, P., Giorgi, R., 2006. Soft and hard nanomaterials for restoration and conservation of cultural heritage. Soft Matter 2, 293-303.

Baglioni, P., Giorgi, R., Dei, L., 2009. Soft condensed matter for the conservation of cultural heritage. C.R. Chimie 12, 61-69.

Baker, C., Pradhan, A., Pakstis, L., Pochan Darrin J., Shah S. Ismat 2005. Synthesis and antibacterial properties of silver nanoparticles. Journal of Nanoscience and Nanotechnology 5, 244-249.

Barnes, R., Molina, R., Xu, J., Dobson, P., Thompson, I., 2013. Comparison of TiO_2 and ZnO nanoparticles for photocatalytic degradation of methylene blue and the correlated inactivation of gram-positive and gram-negative bacteria. Journal of Nanoparticle Research 15, 1432-1443.

Beaucage, G., 1995. Approximations leading to a Unified Exponential/Power-Law approach to Small-Angle Scattering. Journal of Applied Crystallography 28, 717-728.

Beaucage, G., 1996. Small-Angle Scattering from Polymeric Mass Fractals of Arbitrary Mass-Fractal Dimension. Journal of Applied Crystallography 29, 134-146.

Beaucage, G., Kammler, H. K., Pratsinis, S. E., 2004. Particle size distributions from small-angle scattering using global scattering functions. Journal of Applied Crystallography 37, 523-535.

Beaudet, L., Pitre, R., Robillard, L., Mercier, L., 2009. Structural perturbations in mesoporous silica microspheres prepared using cationic organosilanes. Chemistry of Materials 21, 5349-5357.

Belie, N., 2010. Microorganisms versus stony materials: a love–hate relationship. Materials and Structures 43, 1191–1202.

Bellissima, F., Bonini, M., Giorgi, R., Barresi, G., Mastromei, G., Perito, B., Baglioni, P., 2013 a. Antibacterial activity of silver nanoparticles grafted on stone surface. Environmental Science and Pollution Research DOI 10.1007/s11356-013-2215-7.

Bellissima, F., Carta, F., Innocenti, A., Scozzafava, A., Baglioni, P., Supuran, C.T., Berti, D., 2013 b. Structural Modulation of the Biological Activity of Gold nanoparticles functionalized with a Carbonic Anhydrase inhibitor. European Physical Journal E 36, 48-60.

Bonini, M., Bardi, U., Berti, D., Neto, C., Baglioni, P., 2002. A new way to prepare nanostructured materials: flame spraying of microemulsions. Journal of Physical Chemistry B 106, 6178-6183.

Bonini, M., Lenz, S., Giorgi, R., Baglioni, P., 2007. Nanomagnetic sponges for the cleaning of works of art. Langmuir 23, 8681-8685.

Brus, J., Kotlik, P., 1996. Consolidation of stone by mixtures of alkoxysilane and acrylic polymer. Studies in Conservation 41, 109-119.

Cappitelli, F., Zanardini, E., Sorlini, C., 2004. The biodetrioration of synthetic resins used in conservation. Macromolecular Bioscience 4, 399-406.

Carretti, E., Giorgi, R., Berti, D., Baglioni, P., 2007. Oil-in-water nanocontainers as low environmental impact clearing tools for works of art: two case studies. Langmuir 23, 6396-6403.

Chae, SY., Park, MK., Lee, SK., Kim, TY., Kim, SK., Lee, WI., 2003. Preparation of size-controlled TiO_2 nanoparticles and derivation of optically transparent photocatalytic films. Chemistry of Materials 15, 3326-3331.

Chaloupka, K, Malam, Y., Seifalian., A.M., 2010. Nanosilver as a new generation of nanoproduct in biomedical applications. Trends in Biotechnology 28, 580-588.

Chaudhari, G. N., Bende, A. M., Bodade, A. B., Patil, S. S., Sapkal, V. S., 2006. Structural and gas sensing properties of nanocrystalline TiO_2:WO_3-based hydrogen sensors. Sensors and Actuators B: Chemical 115, 297-302.

Chawengkijwanich, C., Hayata, Y., 2008. Development of TiO_2 powder-coated food packaging film and its ability to inactivate *E. coli* in *vitro* and in actual tests. International Journal of Food Microbiology 123, 288-292.

Che, S., Garcia-Bennett, A., Yokoi, T., Sakamoto, K., Kunieda, H., Terasaki, O., Tatsumi, T., 2003. A novel anionic surfactant templating route for synthesizing mesoporous silica with unique structure. Nature Materials 2, 801-805.

Chelazzi, D., Poggi, G., Jaidar, Y., Toccafondi, N., Giorgi, R., Baglioni, P., 2013. Hydroxide nanoparticles for cultural heritage. Consolidation and protection of wall paintings and carbonate materials. Journal of Colloid and Interface Science 392, 42-49.

Chen, J., Poon, C.-sun, 2009. Photocatalytic construction and building materials: From fundamentals to applications. Building and Environment 44, 1899-1906.

Chen, X., Mao, S. S., 2007. Titanium dioxide nanomaterials: synthesis, properties, modifications and applications. Chemical Reviews 107, 2891-2959.

Cheng, Q., Li, C., Pavlinek, V., Saha, P., Wang, H., 2006. Surface-modified antibacterial TiO_2/Ag^+ nanoparticles: preparation and properties. Applied Surface Science 252, 4154-4160.

Cheseddine, A., Morits, T., 1999. Nanostructuring titania: control over nanocrystal structure, size, shape and organization. European Journal of Inorganic Chemistry, 235-245.

Choi, O., Hu, Z., 2008. Size dependent and reactive oxygen species related nanosilver toxicity to nitrifying bacteria. Environmental Science & Technology 42, 4583-4588.

Coates, J., 2000. John Wiley & Sons Ltd, Chichester: Encyclopedia of Analytical Chemistry R.A. Meyers (Ed.), 10815-10837.

Costerton, J.W., Lewandowski, Z., Caldwell, D.E., Korber, D.R., Lappin-Scott, H.M., 1995. Microbial biofilms. Annual Review of Microbiology 49, 711-745.

Cozzoli, P. D., Comparelli, R., Fanizza, E., Curri, M. L., Agostiano, A., 2003. Photocatalytic activity of organic-capped anatase TiO_2 nanocrystals in homogeneous organic solutions. Materials Science and Engineering: C 23, 707–713.

De Leo, F., Iero, A., Zammit, G., Urzi, C.E., 2012. Chemoorganotrophic bacteria isolated from biodeteriorated surfaces in cave and catacombs. International journal of speleology 41, 125-136.

Dei, L., Mauro, M., Baglioni, P., Manganelli Del Fa, C., Fratini, F., 1999. Growth of crystal phases in porous media. Langmuir, 15, 8915-8922.

Ditaranto, N., Loperfido, S., Van der Werf, I., Mangone, A., Cioffi, N., Sabbatini, L., 2011. Synthesis and analytical characterization of copper-based nanocoatings for bioactive stone artworks treatment. Analytical and Bionalytical Chemistry 399, 473-481.

Domingues, J., Bonelli, N., Giorgi, R., Fratini, E., Gorel, F., Baglioni, P., 2013. Innovative Hydrogels Based on Semi-Interpenetrating p(HEMA)/PVP Networks for the Cleaning of Water-Sensitive Cultural Heritage Artifacts. Langmuir 29, 2746–2755.

Dong, C., Song, D., Cairney, J., Maddan, OL., He, G., Deng, Y., 2011. Antibacterial study of $Mg(OH)_2$ nanoplates. Material Research Bulletin 46, 576-582.

Duran, N., Marcato, P.D., De Souza, G.I.H., Alves, O.L., Esposito, E., 2007. Antibacterial effect of silver nanoparticles produced by fungal process on textile fabrics and their effluent treatment. J Biomed Nanotechnology 3, 203-208.

Duran, N., Marcato, PD., Conti, R., Alves, O.L., Costa, F., Marcelo, B., 2010. Potential use of silver nanoparticles on pathogenic bacteria, their toxicity and possible mechanisms of action. Journal Brazilian Chemical Society 21, 949-959.

Egger, S., Lehmann, R.P., Height, M.J., Loessner M.J., Schuppler, M., 2009. Antimicrobial properties of novel Silver-Silica nanocomposite material. Applied and Environmental Microbiology 75, 2973-2976.

El-Midany, A., Khallafb, M., El-Moftya, E., 2011. Characterization of silicone coating for archeological stone conservation. Surface and Interface Analysis 43, 1182–1188.

Faia, P. M., Furtado, C. S., Ferreira, A. J., 2004. Humidity sensing properties of a thick-film titania prepared by a slow spinning process. Sensors and Actuators B: Chemical 101, 183-190.

Faille, C., Jullien, C., Fontaine, F., Bellon-Fontaine, MN., Slomianny, C., Benezech, T., 2002. Adhesion of *Bacillus* spores and *Escherichia coli* cells to inert surfaces: role of surface hydrophobicity. Canadian Journal of Microbiology 48, 728-738.

Fajardo-Cavazos, P., Nicholson, W., *Bacillus* endospores isolated from granite: close molecular relationships to globally distributed *Bacillus* spp. from endolithic and extreme environments. Applied environmental microbiology 2006, 72, 2856-2863.

Falletta, E., Bonini, M., Fratini, E., Lo Nostro, A., Pesavento, G, Becheri, A., Lo Nostro, P., Canton, P., Baglioni, P., 2008. Clusters of poly(acrylates) and silver nanoparticles: structure and applications for antimicrobial fabrics. The Journal of Physical Chemistry C 112, 11758-11776.

Favaro, M., Mendichi, R., Ossola, F., Simon, S., Tomasin, P.,. Vigato, P., 2007. Evaluation of polymers for conservation treatments of outdoor exposed stone monuments. Part II: Photo-oxidative and salt-induced weathering of acrylicesilicone mixtures. Polymer Degradation and Stability 92, 335-351.

Feng, Q.L., Wu, J., Chen, G.Q., Cui, F.Z., Kim, T.N., Kim, J.O., 2000. A mechanistic study of the antibacterial effect of silver ions on *E. coli* and *S. aureus*. Journal of Biomedical Materials Research 52, 662-668.

Feynman, R., 1959. Lacture at the California Institute of Technology, December 29.

Finocchio, E., Macis, E., Raiteri, R., Busca, G., 2007. Adsorption of trimethoxysilane and of 3-Mercaptopropyltrimethoxysilane on silica and on silicon wafers from vapor phase: an IR study. Langmuir 23, 2505-2509.

Fonseca, AJ., Pina, F., Macedo, MF., Leal, N., Romanowska-Deskins, A., Liaz, L., Gomez-Bolea, A., Saiz-Jimenez, C., 2010. Anatase as an alternative application for preventing biodeterioration of mortars: evaluation and comparison with other biocides. International Biodeterioration and Biodegradation 64, 388-396.

Fu, G., Vary, P., Lin, CT., 2005. Anatase TiO_2 nanocomposites for antimicrobial coatings. Journal of Physical Chemistry B 109, 8889-8898.

Fujishima, A., 1999. TiO_2 photocatalysis: fundamentals and applications. 1st ed., Bkc: Tokyo.

Fujishima, A., Zhang, X., 2005. Titanium dioxide photocatalysis: present situation and future approaches. Comptes Rendus. Chimie 9, 750-760.

Gage, JP., Roberts, TM., Duffy, EJ., 2005. Susceptibility of *Pseudomonas aeruginosa* biofilm to UVA illumination over photocatalytic and non-photoatalytic surfaces. Biofilms, 2, 155-163.

Gao, Y., Masuda, Y., Seo, W.-S., Ohta, H., Koumoto, K., 2004. TiO_2 nanoparticles prepared using an aqueous peroxotitanate solution. Ceramics International 30, 1365-1368.

Gaylarde, C., Rodriguez, C., Navarro-Noya, Y., Ortega-Morales, O., 2012. Microbial biofilms on the sandstone monuments of the Angkor Wat Complex, Cambodia. Current microbiology 64, 85-92.

Gaylarde, C., Silva, M.R., Warsheid, T., 2003. Microbial impact on building materials: an overview. Materials and structures 36, 342-352.

Giorgi, R., Baglioni, M., Berti, D., Baglioni, P., 2010. New Methodologies for the Conservation of Cultural Heritage: Micellar Solutions, Microemulsions, and Hydroxide Nanoparticles. Accounts of chemical research 43, 695-704.

Giorgi, R., Bozzi, C., Dei, L., Gabbiani, C., Ninham, B., Baglioni, P., 2005. Soft and hard nanomaterials for the restoration and conservation of cultural heritage. Langmuir 21, 8495-8501.

Gong, P., Li, H., He, X., Wang, K., Hu, J., Tan, W., *et al*, 2007. Preparation and antibacterial activity og Fe_3O_4@Ag nanoparticles. Nanotechnology 18, 604-611.

Griffin, P.S., Indictor, N., Kloestler, R.J., 1991. The biodeterioration of stone: a review of deterioration mechanisms, conservation case histories and treatment. International Biodeterioration 28, 187-207.

Guiamet, P., Borrego, S., Lavin, P., Perdomo, I., de Saravia, S., 2011. Biofouling and biodeterioration in materials stored at the Historical Archive of the Museum of La Plata, Argentine and at the National Archive of the Republic of Cuba. Colloid and surfaces B 85, 229-234.

Guiamet, P., Crespod, M., Lavina, P., Poncee, B., Gaylardef, C., de Saravia, S., 2013. Biodeterioration of funeral sculptures in La Recoleta Cemetery, Buenos Aires, Argentina: pre- and post-intervention studies. Colloid and Surfaces B 101, 337-342.

Guiamet, P., Rosato, V., Gómez de Saraviae, S., Garcíaf, A., Moreno, D., 2012. Biofouling of crypts of historical and architectural interest at La Plata Cemetery (Argentina). Journal of Cultural Heritage 13, 339–344.

Guinier, A., Fournet, G., Walker, C. B., Yudowitch, K. L., 1995. Small Angle Scattering of X-Rays, Wiley: New York.

Gutarowska, B., Skora, J., Zduniak, K., Rembisz, D., 2012. Analysis of the sensitivity of microorganisms contaminating museums and archives to silver nanoparticles. International Biodeterioration and Biodegradation 68, 7-17.

Haenle, M., Fritsche, A., Zietz, C., Bader, R., Heidenau, F., Mittelmeier, W., Gollwitzer, H., 2011. An extended spectrum bactericidal titanium dioxide (TiO_2) coating for metallic implants: in vitro effectiveness against MRSA and mechanical properties. Journal of Materials Science: Materials in Medicine 22, 381-387.

Hagfeldt, A., Boschloo, G., Sun, L., Kloo, L., Pettersson, H., 2010. Dye-Sensitized Solar Cells. Chemical Reviews 110, 6595-6663.

Hajipour, M, Fromm, K., Ashkarran, A., de Aberasturi D., de Larramendi, I., Rojo, T., Serpooshan, V., Parak, W., Mahmoudi M., 2012. Antibacterial properties of nanoparticles. Trends in Biotechnology 30, 499-511.

Henriques, F., Charola, AE., rato, VM., Rodrigues, PF., 2007. Development of biocolonization resistant mortars: preliminary results. Restoration of building and monuments 13, 389-400.

Hu, X., Li, G., Yu, J. C. 2010. Design, Fabrication, and Modification of Nanostructured Semiconductor Materials for Environmental and Energy Applications. Langmuir 26, 3031-3039.

Huang, T. C., Toraya, H., Blanton, T. N., Wu, Y., 1993. X-ray powder diffraction analysis of silver behenate, a possible low-angle diffraction standard. Journal of Applied Crystallography 26, 180-184.

Huang, Z., Maness, P.-C., Blake, D. M., Wolfrum, E. J., Smolinski, S. L., Jacoby, W. A., 2000. Bactericidal mode of titanium dioxide photocatalysis. Journal of Photochemistry and Photobiology A: Chemistry 130, 163-170.

Hueck, H., 1965. The biodeterioration of materials as part of hylobiology. Mater Org 1, 5-34.

Ilavsky, J., Jemian, P. R., 2009. *Irena*: tool suite for modeling and analysis of small-angle scattering. Journal of Applied Crystallography 42, 347-353.

Iuchi, K.-ichiro, Ohko, Y., Tatsuma, T., Fujishima, A., 2004. Cathode-separated TiO_2 photocatalysts applicable to a photochromic device responsive to backside illumination. Chemistry of Materials 16, 1165-1167.

Kakinoki, K., Yamane, K., Teraoka, R., Otsuka, M., Matsuda, Y. 2004. Effect of relative humidity on the photocatalytic activity of titanium dioxide and photostability of famotidine. Journal of Pharmaceutical Sciences 93, 582-589.

Kangwansupamonkon, W., Lauruengtana, V., Surassmo, S., Ruktanonchai, U., 2009. Antibacterial effect of apatite-coated titanium dioxide for textiles aplication. Nanomedicine 5, 240-249.

Karunakaran, C., Abiramasundari, G., Gomathisankar, P., Manikandan, G., Anandi, V., 2010. Cu-doped TiO2 nanoparticles for photocatalytic disinfection of bacteria under visible light. Journal of Colloid and Interface Science 352, 68-74.

Kato, K., Tsuzuki, A., Taoda, H., Torii, Y., Kato, T., Butsugan, Y. 1994. Crystal structures of TiO_2 thin coatings prepared from the alkoxide solution via the dip-coating technique affecting the photocatalytic decomposition of aqueous acetic acid. Journal of Materials Science 29, 5911-5915.

Khamova, T., Shilova, O., Vlasov, D., Ryabusheva, Y., Mikhal'chuk, V., Ivanov, V., Frank-Kamenetskaya, O., Marugin, A., Dolmatov, V., 2012. Bioactive coatings based on nanodiamond-modified epoxy siloxane sols for stone materials. Inorganic Materials 48, 702–708.

Kim, J.S., Kuk, E., Yu, K.N., Kim, J.H., Park, S.J., Lee, H.J., Kim, S.H., Park, Y.K., Hwang, C.Y., Lee, Y.S., Jeong, D.H., Cho, M.H., 2007. Antimicrobial effects of silver nanoparticles. Nanomedicine: Nanotechnology, Biology and Medicine 3, 95-101.

Kim, YH., Lee, DK., Cha, HG., Kim, CW., Kang YS., 2007. Synthesis and Characterization of antibacterial Ag-SiO_2 nanocomposite. The Journal of Physical Chemistry C 111, 3629-3635.

Knetsch, M.L.W., Koole, L.H., 2011. New strategies in the development of antimicrobial coatings: the example of increasing usage of silver and silver nanoparticles. Polymers 3, 340-366.

Kobayashi, Y., Katakami, H., Mine, E., Nagao, D., Konno, M., Liz-Marzan, L.M., 2005. Silica coating of silver nanoparticles using a modified Stober method. Journal of Colloid and Interface Science 283, 392-396.

Lake, J. A. 1967. An iterative method of slit-correcting small angle X-ray data. Acta Crystallographica 23, 191-194.

Le, Y., Hou, P., Wand, J., Chen, J.F., 2010. Controlled release active antimicrobial corrosion coatings with Ag/SiO_2 core-shell nanoparticles. Materials Chemistry and Physics 120, 351–355.

Lewis, F.J., May, E., Daley, B., Bravery, A.F., 1987. The role of heterotrophic bacteria in the decay of sandstone from ancient monuments. In: Morton, L.G.H. (Ed.), The Biodeterioration of Constructional Materials, The Biodeterioration Society, Pieston, Occasional Publication No. 3, pp. 45-53.

Li, B., Logan, BE., 2005. The impact of ultraviolet light on bacterial adhesion to glass and metal oxide-coated surface. Colloids and Surfaces B 41, 153-161.

Liao, J., Shi, L., Yuan, S., Zhao, Y., Fang, J., 2009. Solvothermal synthesis of TiO_2 nanocrystal colloids from peroxotitanate complex solution and their photocatalytic activities. Journal of Physical Chemistry C 113, 18778-18783.

Lien, C.-F., Lin, Y.-F., Lin, Y.-S., Chen, M.-T., Lin, J.-L., 2005. FTIR Study of Adsorption and Surface Reactions of $N(CH_3)_3$ on TiO_2. The Journal of Physical Chemistry B 109, 10962-10968.

Lin, C., Li, C., 2013. Inactivation of microorganisms on the photocatalytic surfaces in air. Aerosol Science and Technology 37, 939-946.

Lin, H.-M., Keng, C.-H., Tung, C.-Y., 1997. Gas-sensing properties of nanocrystalline TiO_2. Nanostructured Materials 9, 747-750.

Liong, M., France, B., Bradley, K.A., Zink, J.I., 2009. Antimicrobial activity of silver nanocrystals encapsulated in mesoporous silica nanoparticles. Advanced Materials 21, 1684-1689.

Lok, C-N., Ho, C-M., Chen, R., He, Q-Y., Yu, W-Y., Sun, H., Tam, P.K-H., Chiu, J-F., Che, C-M., 2006. Proteomic analysis of the mode of antibacterial action of silver nanoparticles. Journal of proteome research 5, 916-924.

Lopez, D., Vlamakis, H., Kolter, R., 2010. Biofilms. Cold Spring Harb Perspect Biol 2, 1-11.

Lu, ZX., Zhou, L., Zhang, ZL., Shi, WL., XIe, ZX., Xie, HY., Pang, DW., Shen, P., 2003. Cell damage induced by photocatalysis of TiO_2 thin films. Langmuir 19, 8765-8768.

Macedo, M.F., Miller, A.Z., Dionisio, A., Saiz-Jimenez, C., 2009. Biodiversity of cyanobacteria and green algae on monuments in the Mediterranean basin: an overview. Microbiology 144, 3476-3490.

Magoldi, M., Nugari, M., Altieri, A., Lonati, G., 2000. Fassina V (ed) Proceedings of the ninth international congress on deterioration and conservation of stone, Elsevier, Amsterdam, The Netherlands 2, 225–233.

Maness, PC., Smolinski, S., Blake, DM., Huang, Z., Wolfrum, EJ., Jacoby, WA., 1999. Bactericidal activity of photocatalytic TiO2 reaction: toward an understanding of its killing mechanism. Applied and Environmental Microbiology 65, 4094.

Mariani, S., Ermini, M. L., Scarano, S., Bellissima, F., Bonini, M., Berti, D., Minunni, M., 2013. Improving surface plasmon resonance imaging of DNA by creating new gold and silver based surface nanostructures. Microchimica Acta 180, 1093-1099.

Martínez-Castañón, G.A., Niño-Martínez, N., Martínez-Gutierrez, F., Martínez-Mendoza, J.R., Ruiz, F., 2008. Synthesis and antibacterial activity of silver nanoparticles with different sizes. Journal of Nanoparticle Research 10, 1343-8.

Martinez-Gutierrez, F., Olive, P.L., Banuelos, A., Orrantia, E., Nino, N., Morales Sanchez, E., Ruiz, F., Bach, H., Av-Gay, Y., 2010. Synthesis, characterization, and evaluation of antimicrobial and cytotoxic effect of silver and titanium nanoparticles. Nanomedicine 6, 681-688.

Matsunaga, T., Tomoda, R., Nakajima, T, Wake, H., 1985. Photoelectrochemical sterilization of microbial cells by semiconductor powders. FEMS Microbiology Letters, 29, 211-214.

McNamara, C.J., Mitchell, R., 2005. Microbial deterioration of organic stones. Frontiers in Ecology and the Environment 3, 445-451.

Miller, A., Sanmartin, P., Pereira-Pardo, L., Dionisio, A., Saiz-Jimez, C., Macedo, M., Prieto, B., 2012. Bioreceptivity on building stones: a review. Science of Total Environment 426, 1-12.

Miller, AM., Laiz, L., Dionisio, A., Macedo, MF., Saiz-Jimenez, C. 2009. Growth of phototrophic biofilms from limestone monuments under laboratory conditions. International Biodeterioration and Biodegradation 63, 860-867.

Mills, A., Wang, J., 1999. Photobleaching of methylene blue sensitized by TiO_2: an ambiguous system? Journal of Photochemistry and Photobiology A, 127, 123-124.

Montis, C., Milani, S., Berti, D., Baglioni, P., 2012. Complexes of nucleolipid liposomes with single-stranded and double-stranded nucleic acids. Journal of Colloid and Interface Science 373, 57-68.

Morones, J.R., Elechiguerra J.L., Camacho, A., Holt, K., Kouri, J.B., Ramires, J.T., Yacaman, M.J., 2005. The bactericidal effect of silver nanoparticles. Nanotechnology 16, 2346-2353.

Mosquera, M, de los Santos, D., Montes, A., Valdez-Castro L., 2008. New Nanomaterials for Consolidating Stone. Langmuir 24, 2772-2778.

Murphy, W. F., Zerbetto, F., Duncan, J. L., McKean, D. C., 1993. Vibrational spectrum and harmonic force field of trimethylamin. The Journal of Physical Chemistry 97, 581-595.

Narayanan, K., Sakthivel, N,. 2010. Biological synthesis of metal nanoparticles by microbes. Advances in Colloid and Interface Science 156, 1-13.

Nascimbene, J., Salvadori, O., 2008. Lichen recolonization on restored calcareous statues of three venetian villas. International Biodeterioration and Biodegradation 62, 313-318.

Neouze, M.-A., Schubert, U., 2008. Surface modification and functionalization of metal and metal oxide nanoparticles by organic ligands. Monatshefte für Chemie 139, 183-195.

Niitsoo, O., Couzis, A., 2011. Facile synthesis of silver core-silica composite nanoparticles. Journal of Colloid and Interface Science 354, 887-890.

Ortega-Morales, B., Gaylarde, C., Englert, G., Gaylarde, M., 2005. Analysis of salt-containing biofilms on limestone buildings of the Mayan culture at Edzna, Mexico. Geomicrobiology Journal 22, 261-268.

Ortega-Morales, O., Guezennec, J., Hernandez-Duque, G., Gaylarde, C. C., Gaylarde, P. M., 2000. Phototrophic biofilms on ancient Mayan buildings in Yucatan, Mexico. Current Microbiology 40, 81-85.

Ozawa, T., Iwasaki, M., Tada, H., Akita, T., Tanaka, K., Ito, S., 2005. Low-temperature synthesis of anatase–brookite composite nanocrystals: the junction effect on photocatalytic activity. Journal of Colloid and Interface Science 281, 510-513.

Ozy, F., Guden, M., Uzel, A., Karaboz, I., Akil, O., Bulut, H., 2010. Antimicrobial activity of TiO_2-coated orthodontic ceramic brackets against *Streptococcus mutans* and *Candida albicans*. Biotechnology and Bioprocesses Engineering 15, 680-685.

Page, K., Palgrave, R.G., Parkin, I., Wilson, M., Savin, S.L.P., Chadwick, A.V., 2007. Titania and silver-titania composite films on glass-potent antimicrobial coatings. Journal of Materials Chemistry 17, 95-104.

Pal, S., Tak, Y.K., Song, J.M., 2007. Does the antibacterial activity of silver nanoparticles depend on the shape of the nanoparticle? A study of the Gram-negative bacterium *E. coli*. Applied and Environmental Microbiology 73, 1712-1720.

Palmer, R., Siebert, J., Hirsch, P., 1991. Biomass and organic acids in sandstone of a weathering building: production by bacterial and fungal isolates. Microbial Ecology 21, 253-266.

Panacek, A., Kvitek L., Prucek, R., Kolar, M., Vecerova, R., Pizurova, N., Sharma, V.K., Nevecna, T., Zboril, R., 2006. Silver colloid nanoparticles: Synthesis, characterization, and their antibacterial activity. Journal of Physical Chemistry B 110, 16248-16253.

Papida, S., Murphy, W., May, E., 2000. Enhancement of physical weathering of building stones by microbial populations. International Biodeterioration and Biodegradation 46, 305-317.Paz, Y., 2010. Application of TiO_2 photocatalysis for air treatment: Patents' overview. Applied Catalysis B: Environmental 99, 448-460.

Pinna, D., Lega, A.M., Mazzotti, V., 2009. Monitoring and maintenance of ceramic objects in outdoor environment: aspects of biological deterioration for some Faenza monuments. Akros 21, 18-25

Pinna, D., Salvadori, B., Galeotti, M., 2012. Monitoring the performance of innovative and traditional biocides mixed with consolidants and water-repellents for the prevention of biological growth on stone. Science of the Total Environment 423, 132-141.

Poggi, G., Giorgi, R., Toccafondi, N., Katzur, V., Baglioni, P., 2010. Hydroxide Nanoparticles for Deacidification and Concomitant Inhibition of Iron-Gall Ink Corrosion of Paper. Langmuir 26,19084-19090.

Polo, A., Diamanti, MV., Bjarnsholt, T., Hoiby, N., Villa, F., Pedeferri, MP., Cappitelli, F., 2011. Effects of photoactivated Titanium Dioxide nanopowders and

coating on planktonic and biofilm growth of *Pseudomonas aueruginosa*. Photochemistry and Photobiology, 87, 1387-1394.

Raccomandazioni NorMal, 1993. AA VV Raccomandazioni NorMal 43/93, Misure colorimetriche strumentali I superfici opache, Roma CNR-ICR.

Rai, M., Yadav, A., Gade, A., 2009. Silver nanoparticles as a new generation of antimicrobials. Biotechnology Advances 27, 76-83.

Rajagopal, GS., Maruthamuthu, S., Mohanan, S., Palaniswamy, N., 2006. Biocidal effects of photocatalytic semiconductor TiO2. Colloids and Surfaces B, 51, 107-111.

Ramirez, AM., De Belie, N., 2009. Evaluation of the algaecidal activity of titanium dioxide on autoclaved aerated concrete. Journal of advanced oxidation technologies, 12, 1-5

Reicha, F., Sarhan,A., Abdel-Hamid, M., El-Sherbiny, I., 2012. Preparation of silver nanoparticles in the presence of chitosan by electrochemical method. Carbohydrate Polymers 89, 236-244.

Ridi, F., Fratini, E., Alfani, R., Baglioni, P., 2013. Influence of acrylic superplasticizer and cellulose-ether on the kinetics of tricalcium silicate hydration reaction. Journal of Colloid and Interface Science 395, 68-74.

Rincon, AG., Pulgarin, C., 2003. Photocatalytical inactivation of E. coli: effect of (continuous-intermitent) light intensity and of (suspended-fixed) TiO_2 concentration. Applied Catalysis, 44, 263-284.

Rodrıguez, J. A., ernandez-Sanchez, C., Domınguez, C., Hernandez, S., Berencen, Y., 2012. Bulk silica-based luminescent materials by sol-gel processing of non-conventional precursors. Applied Physics Letters 101, 171908.

Romero, D., Aguilar, C., Losick, R., Kolter, R., 2010. Amyloid fibers provide structural integrity to *Bacillus subtilis* BIOFILMS. Proc Natl Acad Sci 107: 2230–2234.

Rueda, D. R., Garc a-Guti r rez, M. C., oga les, A., Capit n, M. J., zquerra, T. A., Labrador, A., raga, ., Beltr n, D., Juanhuix, J., Herranz, J. F., Bordas, J., 2006. Versatile wide angle diffraction setup for simultaneous wide and small angle X-ray scattering measurements with synchrotron radiation. Review of Scientific Instruments 77, 033904.

Ruffolo, S., La Russa, M., Malagodi, M., Rossi, C., Palermo, A., Crisci, G., 2010. ZnO and $ZnTiO_3$ nanopowders for antimicrobial stone coating. Applied Physics A 100, 829-834.

Sabzi, M., Mirabedini, S. M., Zohuriaan-Mehr, J., Atai, M., 2009. Surface modification of TiO_2 nano-particles with silane coupling agent and investigation of its effect on the properties of polyurethane composite coating. Progress in Organic Coatings 65, 222–228.

Saito, T., Iwase, T., Morioka, TJ., 1992. Mode of photocatalytic bacteriacidal action of powdered semiconductor TiO2 on mutans streptococci. Journal of Photochemistry and Photobiology B, 14, 369-379.

Sand, W., 2001. Microbial corrosion and its inhibition. In:Rehm HJ (ed) Biotechnology. Vol 10. Wiley-VCH VerlagGmbH, D-69469 Weinheim, Germany, pp 183–190

Sandrolini, F., Franzoni, E., Pigino, B., 2012. Ethyl silicate for surface treatment of concrete – Part I: Pozzolanic effect of ethyl silicate. Cement & Concrete Composites 34, 306–312.

Sawicka, M., Storoniak, P., Skurski, P., Blazejowski, J., Rak, J., 2006. TG-FTIR, DSC and quantum chemical studies of the thermal decomposition of quaternary methylammonium halides. Chemical Physics 324, 425–437.

Scheerer, S., Ortega-Morales, O., Gaylarde, C., 2009. Microbial deterioration of stone monuments-an update overview. Advances in Applied Microbiology 66, 97-139.

Schmidt, H., Menning, M., Naß, R., 1994. Sol–Gel processing and application, ed. Y. A. Attia, Plenum Press, New York, 185–186.

Schreurs, WJ., Rosenberg, H., 1982. Effect of silver ions on transport and retention of phosphate by *Escherichia coli*. Journal of Bacteriology 152, 7-13.

Shah, S., Nag, M., Kalagara, T., Singh, S., Manorama, S., 2008. Silver on PEG-PU-TiO_2 polymer nanocomposite films: an excellent system for antibacterial applications. Chemistry of Materials 20, 2455-2460.

Sharma, K., Verna, K., 2011. Fungal involvement in biodeterioration of ancient monuments: problem and prospects. Journal of Phytology 15-17.

Sharma, VK., Yngard, RA., Lin, Y, 2009. Silver nanoparticles: green synthesis and their antimicrobial activities. Advances in colloid and interface science 145, 83-96.

Siddiquey, I. A., Ukaji, E., Furusawa, T., Sato, M., Suzuki, N., 2007. The effects of organic surface treatment by methacryloxypropyltrimethoxysilane on the photostability of TiO_2. Materials Chemistry and Physics, 105, 162–168.

Silver, S., 2003. Bacterial silver resistance: molecular biology and uses and misuses of silver compounds. FEMS Microbiology reviews 27, 341- 353.

Simonovicova, A., Godyova, M., Sevc, J., 2004. Airborne and soil microfungi as contaminants of stone in a hypogean cemetery. International Biodeterioration & Biodegradation 54, 7 – 11.

Sintubin, L., Verstraete, W., Boon, N., 2012. Biologically produced nanosilver: current state and future perspectives. Biotechnology and Bioengineering 109, 2422-2436.

Sondi, I., Salopek-Sondi, B., 2004. Silver nanoparticles as antimicrobial agent: a case study on *E. coli* as a model for Gram-negative bacteria. Journal of Colloid and Interface Science 275, 177-182

Song, Y. Y., Hildebrand, H., Schmuki, P., 2010. Optimized monolayer grafting of 3-aminopropyltriethoxysilane onto amorphous, anatase and rutile TiO_2. Surface Science 604, 346–353.

Stassi, A., Zanardini, F., Cappitelli, F., Schiraldi A., Sorlini, C., 1998. Calorimetric investigations on the metabolism of *Bacillus* strains isolated from artistic stoneworks. Annals of Microbiology and Enzymology 48, 111-120.

Stöber, W., Fink, A., Bohn, E., 1968. Controlled growth of monodisperse silica spheres in the micron size range. Journal of Colloid and Interface Science 26, 62-69.

Sunada, K., Kikuchi, Y., Hashimoto, K., Fujishima, A., 1998. Bactericidal and detoxification effects of TiO_2 thin film photocatalysts. Environmental Science and Technology 32, 726-728.

Swetha, S., Santhosh, SM., Balakrishna, G., 2010. Enhanced bactericidal activity of modified titania in sunlight against *Pseudomonas aeruginosa*, a water-borne Pathogen. Photochemistry and Photobiology 86, 1127-1134.

Taniguchi, N., 1974. On the basic concept of nanotechnology. Proc. Intl. Conf. Prod. Eng Tokyo, *Part II*, Japan Society of Precision Engineering.

Tian, G., Fu, H., Jing, L., Tian, C. 2009. Synthesis and photocatalytic activity of stable nanocrystalline TiO_2 with high crystallinity and large surface area. Journal of Hazardous Materials 161, 1122-1130.

Tomaselli L., 2003. Biodeterioration processes on inorganic substrata. Coalition 6, 5-9.

Tretiach, M., Crisafulli, P., Imai, N., Kashiwadani, H., Moon, KH., Wada, H., Salvadori, O., 2007. Effcacy of a biocide tested on selected lichens substrata and its effects on their substrata. International Biodeterioration and Biodegradation 59, 44-54.

Ukaji, E., Furusawa, T., Sato, M., Suzuki, N., 2007. The effect of surface modification with silane coupling agent on suppressing the photo-catalytic activity of fine TiO_2 particles as inorganic UV filter. Applied Surface Science 254, 563-569.

Urzì, C., De Leo, F., Bruno, L., Albertano, P., 2010. Microbial Diversity in Paleolithic Caves: A Study Case on the Phototrophic Biofilms of the Cave of Bats (Zuheros,Spain). Microbial Ecology 60, 116-129.

Urzi, C., Realini, M., 1998. Color changes of oto' s calcareous sandstone as related to its colonization by microorganisms. International Biodeterioration Biodegradation 42, 45-54.

Vayssieres, L., 2009. On solar hydrogen & nanotechnology, John Wiley & Sons (Asia): Singapore ,Hoboken NJ.

Villa, F., Giacomucci, L., Polo, A., Principi, P., Toniolo, L., Levi, M., Turri, S., Cappitelli, F., 2009. N-vanillylnonanamide tested as a non-toxic antifoulant, applied to surfaces in a polyurethane coating. Biotechnology Letters 31, 1407-1413.

Vohra, M.S., Malik, A.A., Al-suwaiyan, M.S., Bukari, A.A., 2009. TiO_2-assisted photocatalytic removal of phenol: effect of co-pollutants. International Journal of Applied Environmental Sciences 4, 33-45.

Wang, H., Lu, G., Zhang, J., Zheng, D., 2013. Multifunctional nanocomposites for paper conservation. Studies in Conservation 58, 23-29.

Warren, B. E., 1969. X-ray diffraction. Addison-Wesley, Reading, MA, 251-275.

Warscheid, T., Braams, J., 2000. Biodeterioration of stone: a review. International Biodeterioration Biodegradation 46, 343-368.

Wessel, DP., 2003. The use of metallic oxides in control of biological growth on outdoor monuments. Art, biology and conservation: biodeterioration of works of art. Ed. RJ Koestler, VH Koestler, AE Charola, FE Nieto-Fernandez, New York: The Metropolitan Museum of Art, 536-551.

Wheeler, G., Schein. A., Shearer, G., Blackwel, S., 1992. Preserving our heritage in stone, Analytical Chemistry 6, 347-356.

Xu, J., Li, L., Yan, Y., Wang, H., Wang, X., Fu, X., Li, G., 2008. Synthesis and photoluminescence of well-dispersible anatase TiO_2 nanoparticles. Journal of Colloid and Interface Science 318, 29-34.

Xu, K., Wang, J-X., Kang, X-L., Chen, J-F., 2009. Fabrication of antibacterial monodispersed Ag-SiO_2 core-shell nanoparticles with high concentration. Materials Letters 63, 31-33.

Xu, R, Wang, DS, Zhang, JT, Li, YD, 2006. Shape-dependent catalytic activity of silver nanoparticles for the oxidation of styrene. Chemical Asian Journal 1, 888-893.

Yang, F., Liu, Y., Zhu, Y., Long, S., Zuo, G., Wang, C., Guo, F., Zhang, B., Jiang, S., 2012. Conservation of weathered historic sandstone with biomimetic apatite. Chinese Science Bulletin 57, 2171-2176.

Yao, N., Yeung, K.L., 2011. Investigation of the performance of TiO_2 photocatalytic coatings. Chemical Engineering Journal 167, 13-21.

Yeung, KL., Leung, WK., Yao, N., Cao, S, 2009. Reactivity and antimicrobial properties of nanostructured titanium dioxide. Catalysis today 143, 218-224.

Yu, J., Wang, J., Zhang, J., He, Z., Liu, Z., Ai, X., 2007. Characterization and photoactivity of TiO_2 sols prepared with triethylamine. Materials letters 61, 4984-4988.

Zacarias, SM., Vaccari, MC., Alfano, OM., Irazoqui, HA., Imoberdorf, GE., 2010. Effect of the radiation flux on the photocatalytic inactivation of spores of *Bacillus subtilis*. Journal of Photochemistry and Photobiology A 214, 171-180.

Zarraga, R., Alvarez-Gasca, D., Cervantes, J., 2002. Solvent effect on TEOS film formation in the sandstone consolidation process. Silicon Chemistry 1, 397-402.

Zeitler, V. A., Brown, C. A., 1957. The Infrared spectra of some Ti-O-Si, Ti-O-Ti and Si-O-Si compounds. The Journal of Physical Chemistry 61, 1174-1177.

Zendri, E., Biscontin, G., Nardini, I., Riato, S., 2007. Characterization and reactivity of silicatic consolidants. Construction and Building Materials 21, 1098-1106.

Zhao, W., Ma, W., Chen, C., Zhao, J., Shuai, Z. 2004. Efficient degradation of toxic organic pollutants with $Ni_2O_3/TiO_{2-x}B_x$ under visible irradiation. Journal of American Chemical Society 126, 4782-4783.

List of publications

Publications

Bellissima, F., Bonini, M., Giorgi, R., Barresi, G., Mastromei, G., Perito, B., Baglioni, P., 2013. Antibacterial activity of silver nanoparticles grafted on stone surface. Environmental Science and Pollution Research, DOI 10.1007/s11356-013-2215-7.

Mariani, S., Ermini, M. L., Scarano, S., **Bellissima**, F., Bonini, M., Berti, D., Minunni, M., 2013. Improving surface plasmon resonance imaging of DNA by creating new gold and silver based surface nanostructures. Microchimica Acta 180, 1093-1099.

Bellissima, F., Carta, F., Innocenti, A., Scozzafava, A., Baglioni, P., Supuran, C.T., Berti, D., 2013. Structural modulation of the biological activity of gold nanoparticles functionalized with a Carbonic Anhydrase inhibitor. European Physical Journal E 36, 48-60.

Proceedings

VIII Congresso Nazionale CSGI, 28/06-01/07/2010, Chianciano Terme. Nanosystems for the control of biodeterioration of manufactured lithoic materials. Poster.

XXXIX Convegno Nazionale di Chimica-Fisica della Società Chimica Italiana, 20-24 September 2010, Stresa, Italy. 10° Sigma Aldrich Young Chemists Symposium, 18-20 October 2010, Pesaro, Italy. Gold nanoparticles coated with a carbonic anhydrase inhibitor; size and functionalization control. Poster.

XIV Congresso Nazionale di Chimica dell'Ambiente e dei Beni Culturali, 2-5 June 2013, Rimini, Italy. Antibacterial activity of silver nanoparticles grafted on stone surface. Oral presentation performed by Dr. Rodorico Giorgi.

Ringraziamenti

Il mio primo ringraziamento è rivolto al Prof. Piero Baglioni per l'opportunità che mi ha dato di lavorare ad un progetto nuovo e stimolante, per l'aiuto che mi ha fornito in questi anni con i suoi consigli e per la fiducia che ha voluto riporre in me. Ringrazio inoltre:

il Dott. Rodorico Giorgi per aver seguito in tutti i suoi sviluppi questo lavoro di tesi, per aver creduto in me anche nei momenti di maggiore difficoltà e per avermi introdotto nel mondo tanto complesso quanto affascinante della conservazione dei beni culturali;

il Dott. Massimo Bonini per aver saputo indirizzarmi con grande competenza nel mondo delle nanoparticelle e per avermi trasmesso l'entusiasmo per la ricerca;

la Dott.ssa Brunella Perito che ha avuto la pazienza di insegnarmi i rudimenti della microbiologia e mi ha fornito gli strumenti necessari per lavorare in un ambito per me assolutamente nuovo;

il Prof. Giorgio Mastromei che mi ha accolto nei suoi laboratori e sostenuto con i suoi consigli;

il Dott. Emiliano Fratini, la Dott.ssa Francesca Ridi, la Dott. Patrizia Canton, la Dott.ssa Nicole Bonelli ed il Dott. Francesco Rugi per la collaborazione nell'acquisizione di alcuni dati presentati in questa tesi e per il prezioso contributo nell'interpretarli.

Ringrazio la ex-laureanda (ormai Dottoressa) Giovanna Barresi per avermi dato l'opportunità di imparare insegnando, e per aver collaborato con me all'ottenimento di alcuni dei risultati microbiologici discussi nella tesi. Grazie inoltre a Cristina Indorato che ha reso più facile, grazie al suo supporto tecnico, il mio lavoro nei laboratori di microbiologia.

Ringrazio la Dott. Debora Berti per avermi saputo affascinare durante la tesi di laurea con il mondo delle nanoparticelle e per aver condiviso con me la gioia legata alla mia prima pubblicazione scientifica.

Grazie alle mie amiche Claudia ed lis a ("chimichesse" anche loro), con cui ho trascorso bei momenti di studio e di svago.

Il ringraziamento più caloroso va a tutta la mia famiglia, per avermi sempre spronato a credere in me, anche di fronte a sfide che io stessa dubitavo di riuscire a vincere. Grazie per avermi sempre dato la sicurezza di non essere sola, mai.

Ed infine grazie a Valerio, per essermi stato sempre così vicino pur vivendo così lontani e per avermi sempre sostenuto.

Environ Sci Pollut Res
DOI 10.1007/s11356-013-2215-7

Antibacterial activity of silver nanoparticles grafted on stone surface

F. Bellissima · M. Bonini · R. Giorgi · P. Baglioni · G. Barresi · G. Mastromei · B. Perito

Received: 4 July 2013 / Accepted: 2 October 2013

Abstract Microbial colonization has a relevant impact on the deterioration of stone materials with consequences ranging from esthetic to physical and chemical changes. Avoiding microbial growth on cultural stones therefore represents a crucial aspect for their long-term conservation. The antimicrobial properties of silver nanoparticles (AgNPs) have been extensively investigated in recent years, showing that they could be successfully applied as bactericidal coatings on surfaces of different materials. In this work, we investigated the ability of AgNPs grafted to Serena stone surfaces to inhibit bacterial viability. A silane derivative, which is commonly used for stone consolidation, and *Bacillus subtilis* were chosen as the grafting agent and the target bacterium, respectively. Results show that functionalized AgNPs bind to stone surface exhibiting a cluster disposition that is not affected by washing treatments. The antibacterial tests on stone samples revealed a 50 to 80 % reduction in cell viability, with the most effective AgNP concentration of 6.7 μg/cm^2. To our knowledge, this is the first report on antimicrobial activity of AgNPs applied to a stone surface. The results suggest that AgNPs could be successfully used in the inhibition of microbial colonization of stone artworks.

Responsible editor: Gerald Thouand

Electronic supplementary material The online version of this article (doi:10.1007/s11356-013-2215-7) contains supplementary material, which is available to authorized users.

F. Bellissima · M. Bonini · R. Giorgi · P. Baglioni (✉)
Department of Chemistry "Ugo Schiff" and CSGI, University of Florence, 50019 Sesto Fiorentino, Florence, Italy
e-mail: piero.baglioni@unifi.it

G. Barresi · G. Mastromei · B. Perito
Department of Biology, University of Florence, 50019 Sesto Fiorentino, Florence, Italy

Published online: 23 October 2013

Keywords Silver nanoparticles · Conservation of cultural heritage · Stone biodeterioration · *Bacillus subtilis* · Antibacterial activity

Introduction

Microbial colonization has a relevant impact on the conservation of stone materials with consequences ranging from esthetic changes to physical and chemical deterioration of the stone itself. Biodeterioration processes are the result of complex activities and interactions of the microbial community that is present on stone surfaces in the predominant form of biofilms. Deterioration mechanisms include acidolysis, accumulation of organic nutrients, discoloration, changes in the porosity, thermal–hydric alterations, vapor diffusion changes, and mobilization of ions (Gaylard et al. 2003; McNamara and Mitchell 2005; Scheerer et al. 2009; Warscheid and Braams 2000). Bacteria are extensively involved in biofilm formation, and heterotrophic bacteria can also establish on stones as primary colonizers without the pioneering participation of autotrophic organisms (Warscheid and Braams 2000). Gram-positive bacteria are the most recurrent chemoorganotrophic bacteria. Among them, organisms of the *Bacillus* and *Bacillus*-related genera have been frequently identified on monumental stones, both through culture and molecular biology techniques (McNamara and Mitchell 2005; Sheerer et al. 2009). *Bacillus* is able to withstand extreme environmental conditions because of its spore-forming ability (Fajardo-Cavazos and Nicholson 2006). Its potential degrading activity, taking place through the production of acids and surfactants, has been demonstrated through laboratory experiments (Stassi et al. 1998). *Bacillus* bacteria were also found in association to mineral precipitates of white fluffy biofilm, covering deteriorated surfaces of caves and catacombs, and they may actively participate to the precipitation of mineral phases (De Leo et al. 2012).

Avoiding the formation and growth of biofilms on stone surfaces of high cultural interest represents a crucial aspect for their long-term conservation as well as for their esthetic aspect. A recent study (Pinna et al. 2012) has evaluated the effectiveness of mixtures of consolidants, water-repellents, and copper nanoparticles (NPs) in preventing biological growth, and yielded good results also as a preservative treatment against recolonization after conservation treatment.

Silver ions are known as one of most toxic heavy metal ions to microorganisms, having a relevant activity against a broad range of bacteria, fungi, and viruses (Kim et al. 2007; Morones et al. 2005). Silver-based antimicrobials present excellent properties such as thermal and chemical stability, health and environmental safety, and low toxicity to human cells. These features make silver-based materials suitable for a variety of applications (Rai et al. 2009), including those where they are exposed to a broad range of temperature, irradiation, and humidity. Both the release of silver ions and the nanoparticle characteristics play a key role in the antimicrobial activity of silver nanoparticles (AgNPs) (Lok et al. 2007; Pal et al. 2007; Panacek et al. 2006). AgNP bactericidal activity includes: (1) the direct interaction with cell membranes, affecting the transport through the membrane itself and causing perforations (Sondi and Solopek-Sondi 2004); (2) the accumulation of reactive oxygen species (ROS) at the surface of the particles (Choi and Hu 2008); and (3) silver ion's interaction with DNA or sulphidryl groups of vital enzymes, which lead to cell death (Lok et al. 2006; Rai et al. 2009). The synergy between these mechanisms makes the resistance of microorganism to silver not frequent (Silver 2003).

Silver-containing materials are exploited to prevent bacterial colonization both in medical and nonmedical applications (Chaloupka et al. 2010). In some of these cases, AgNPs have been successfully applied as coatings on different materials (Knetsch and Koole 2011; Falletta et al. 2008). To the best of our knowledge, little is known about the application of AgNPs to protect stone artworks from biodeterioration. To this aim, we investigated the antibacterial properties of stone samples whose surface was treated with functionalized silver nanoparticles in laboratory conditions. *Serena* stone was chosen as the substrate since it is a much diffused stone in Italy, especially in Tuscany. A silane derivative was used as the grafting agent to take advantage of its chemical reactivity toward stones; moreover, it is known that silane functionalization of AgNPs does not hinder their antimicrobial activity (Egger et al. 2009; Xu et al. 2009). *Bacillus subtilis* was used as the reference bacterium, as it is very frequently identified on cultural heritage materials. Moreover, *Bacillus* is a Gram-positive bacterium and, due to their thicker cell wall, Gram-positive cells usually result to be more tolerant and resistant to silver compounds than Gram-negative bacteria (Feng et al. 2000; Jung et al. 2008).

Materials and methods

Nanoparticle synthesis

Silver nanoparticles were synthesized according to a seed-based procedure (Aherne et al. 2008) that results in the formation of triangular nanoprisms. Silver nanoprisms were preferred over any other nanostructures because of their high antimicrobial activity (Pal et al. 2007).

The synthesis was performed in water at room temperature, so that it could be easily scaled up to produce at reasonable costs the necessary amount of nanoparticles to treat large artifacts. Silver seeds were prepared combining 5 mL of aqueous trisodium citrate (2.5 mM), 0.250 mL of aqueous poly(sodium styrenesulphonate) (500 mg/L), and 0.3 mL of aqueous sodium borohydride solution (freshly prepared, 10 mM), followed by the addition of 5 mL of aqueous silver nitrate solution (0.5 mM, added at a rate of 2 mL/min under stirring). Nanoprism growth was achieved by combining 150 mL of water, 2.25 mL of aqueous ascorbic acid solution (10 mM), and 3.6 mL of seed solution, followed by the addition of 90 mL aqueous silver nitrate solution (0.5 mM) at a rate of 1 mL/min under stirring (AgNP dispersions at different stages of the synthesis are shown in Fig. SI-1 in the Supporting Information). After the synthesis, 15 mL of aqueous trisodium citrate solution (25 mM) were added to stabilize the dispersion and avoid aggregation and precipitation of nanoprisms.

Nanoparticle functionalization

In order to chemically graft the nanoparticles to the stone surface, pristine silver nanoprisms were functionalized through the condensation of a silane precursor on the surface of AgNPs using dimethylamine (DMA; Sigma Aldrich) as a catalyst (Kobayashi et al. 2005; Niitsoo and Couzis 2011). We used tetraethylorthosilicate (TEOS; Merck, AgNP/TEOS 20:1 *w*/*w*) as a grafting agent in order to coat AgNPs with a monolayer of silane molecules. To reduce the amount of water during the condensation of TEOS on the surface of nanoprisms, the pristine aqueous AgNP dispersion was concentrated to a volume of <200 μL using centrifugal concentrators Vivaspin 20 (Sartorius Vivascience MWCO, 3,000 Da, 20 mL) and Amicon 500 (Merck Millipore, Amicon Ultra, 0.5 mL) and diluted to the final reaction volume with 2-propanol (2-propanol/aqueous solution of AgNP 4:1 *v*/*v*). Under stirring conditions, DMA (Aldrich, purum, final concentration of 0.4 M) and TEOS (Merck, synthesis grade, 2-propanol solution) were added. Functionalized nanoparticles (AgNP@TEOS) were resuspended by sonication before their use.

Stone surface characterization

Serena stone samples (1.5×1.5×0.3 cm^3) caved from quarry in Firenzuola, Italy, 5–10 % open porosity, were used (Dei et al. 1999). AgNPs (either TEOS-functionalized or not) were applied on stone specimens by dropping 50 μL of the dispersion and allowing the samples to dry under a laboratory hood. Stone surface was characterized by means of scanning electron microscopy (SEM), atomic force microscopy (AFM), and colorimetric measurements. All the measurements were carried out on fully dried surfaces, i.e., typically 24 h after sample preparation.

SEM experiments were carried out with a field emission gun (FEG)-SEM, model ΣIGMA by Carl Zeiss, working with an 8-kV acceleration potential. Images were acquired by collecting backscattered electrons (BSE) to highlight the differences between high atomic weight (silver) and light elements (calcium) and by collecting secondary electrons with an in-lens detector, when working at high magnifications.

AFM images were collected using a Park XE-100 microscope in noncontact mode (SSS-NCHR probes, nominal resonant frequency of 330 kHz, radius of curvature <5 nm). Stone specimens treated only with the corresponding amount of TEOS solution (without NPs) were used as reference samples.

Color changes induced by the presence of AgNPs were evaluated by means of colorimetric measurements. The light reflected by the sample (1 mm^2 spot) was collected by means of a fiber-optic cable (FRP series) and recorded with a high sensitivity CCD camera. Colorimetric data were collected using standard illuminant C and standard observer CIE 1931 (2°) in a λ range of 400–700 nm and with a 0°/0° geometry, operating conditions being derived from UNI NORMAL 43/93 recommendations (Raccomandazioni NorMal 1993). Stone specimens were analyzed in two different regions, three measurements being taken for each region. The colorimetric coordinates L^*, a^*, b^* were averaged out to obtain a single value for each specimen. The resultant chromatic change (ΔE) was determined through the equation:

$$\Delta E = \sqrt{\Delta L^{*2} + \Delta a^{*2} + \Delta b^{*2}}$$

Δ indicating the difference between the coordinates of the treated and untreated samples.

Bacterial strain and growth conditions

Bacterial cultures of *B. subtilis* strain 168 (Anagnostopoulos and Spizizen 1961) were prepared in 100-mL flasks by inoculating a single bacterial colony into Nutrient Broth (NB; Oxoid) medium. The culture was aerobically incubated on a rotary shaker at 30 °C and 120 rpm for 18 h. To determine the viable count of the *B. subtilis* culture, the microbial suspension was serially diluted and 100 μL of each dilution were spread on Nutrient Agar (NA; Oxoid) plates. Colony formant units (CFU) were counted after 24 h of incubation at 37 °C. In such growth conditions, the viable count of the starting culture was about 10^8 CFU/mL.

Zone of inhibition "spot on spot" technique

Antibacterial activity of AgNPs on solid medium was assessed by evaluating the presence of growth inhibition zones. Ten microliters of nanoparticle dispersion were spotted on NA plates and allowed to dry under aspiration hood. Afterwards, 20-μL spots (containing about 10^3 cells) were placed over the same spot, so that the area covered by the cells was larger than the nanoparticle spot. Plates were incubated for 24 h at 37 °C, and the inhibition activity was visually evaluated.

Antimicrobial activity on stone by cell deposition and recovery assay

Serena stone samples (1.5×1.5 cm^2) were treated with 50 μL of AgNP@TEOS dispersions at different concentrations and allowed to dry overnight. Each test sample was placed in a Petri dish (∅ 5 cm), and the surface was treated with 50 μL of 10^{-1} dilution of an overnight *B. subtilis* culture. After 30 min, 10 mL of a saline solution (0.85 % NaCl) was added and the Petri dish was shaken during 30 min (the sample was turned upside down after 15 min). One milliliter of this "washing solution" was withdrawn (twice for each sample) and diluted 10 and 100 times with saline solution. To enumerate the viable bacteria recovered from the stone samples, 0.1 mL of undiluted and diluted solutions were plated on NA, incubated at 37 °C for 24 h and visually counted. Stone samples treated with the corresponding amount of TEOS solution were used as reference and treated in the same way. Two replicates, with at least three repetitions each, were performed for each concentration of AgNPs, and the same was done for the corresponding references. The whole method is sketched in Fig. 1.

The reduction in cell viability due to AgNPs was evaluated by comparing final microbial counts (FMC) of AgNP@TEOS-treated and TEOS-treated samples (Ozy et al. 2010; Page et al. 2007):

$$\text{Antimicrobial effect}\% = \frac{\text{FMC(untreated)} - \text{FMC(treated)}}{\text{FMC(untreated)}} * 100$$

Results

Nanoparticle characterization

The shape and size of the obtained nanoparticles were assessed by FEG-SEM. Results are reported in Fig. 2, where the prismatic shape of particles is shown.

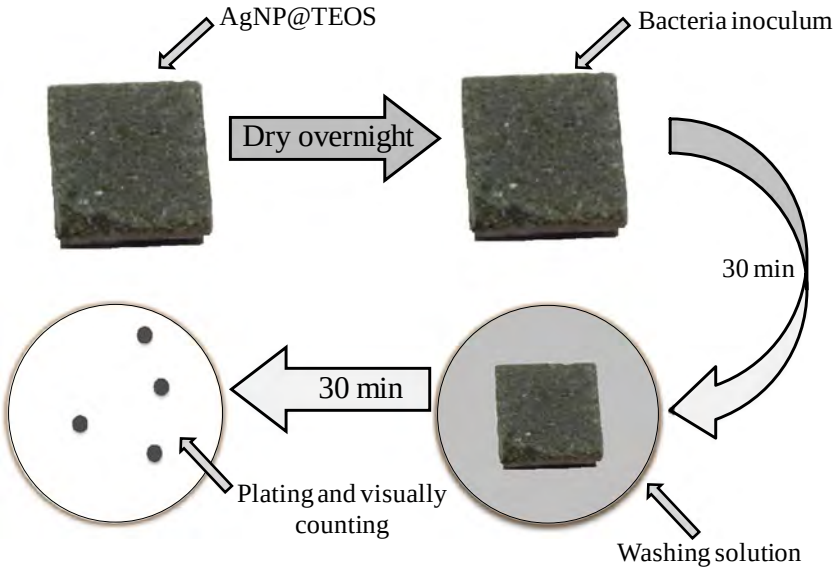

Fig. 1 Schematic representation of the different steps of cell deposition and recovery method

Stone surface characterization

SEM analysis provides insights about the distribution and the adhesion of AgNPs on the stone surface. In order to assess the resistance of nanoparticle grafting, samples were subjected to a water jet at 7 mL/s for 30 min (Yao and Yeung 2011). Images in Figs. 3 and 4 display representative regions of AgNPs and AgNP@TEOS-treated samples, before and after washing.

Pristine nanoparticles (Fig. 3) are quite homogeneously spread over the stone surface, while functionalized AgNPs (Fig. 4) tend to form micrometer-sized clusters. Through the analysis of several SEM images (about 50) acquired moving frame by frame along parallel lines, it was estimated an average AgNP@TEOS cluster-to-cluster distance of about 150 μm.

Results suggest that clusters are formed during the functionalization of AgNPs. Nevertheless, the adhesion of AgNPs to the stone surface is allowed by the presence of unreacted ethoxyl groups on the surface of clusters that are still able to react with the hydroxyl groups present on the stone. When pristine AgNPs are applied to stones, they homogeneously spread over the surface, but they display poor adhesion as they could be removed through a washing treatment (Fig. 3). This is not the case when AgNPs were previously functionalized with TEOS, highlighting the strong interaction between AgNPs and the stone surface (Fig. 4).

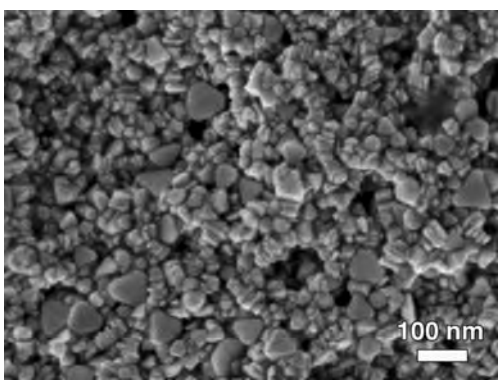

Fig. 2 FEG-SEM micrograph of AgNPs. The edge length is about 70 nm, thickness is about 5 nm

SEM images at higher magnifications (Fig. 5) show the details of the disposition of the nanoparticles (pristine or functionalized) on the stone surface.

The stone surface was also analyzed by means of AFM microscopy. Due to the presence of large cracks and voids on the surface of *Serena* stone surfaces, images were acquired over selected regions where no micrometric irregularities were detected with the aid of the optical microscope equipping the AFM (see Fig. SI-2 in the Supporting Information). A representative AFM image of the reference sample (i.e., after the treatment with TEOS, but without AgNPs) is shown in Fig. 6a. The surface displays the typical aspect of a freshly cut stone slab. No evidence of silica structures resulting from TEOS condensation could be detected, suggesting that the amount of TEOS added (which is the same present in the case of AgNPs@TEOS) is not sufficient to cover the surface and that the application conditions do not take to the formation of silica nanospheres.

Figure 6b shows an AFM image of the *Serena* stone surface after functionalization with AgNP@TEOS and washing treatment. Consistently with SEM, results show the presence of clusters, highlighting that the AgNPs retain their triangular shape also after TEOS functionalization.

Colorimetric measurements reveal that grafting nanoparticles to the stone surface does not produce any significant change in the chromatic aspect of the specimens, even using

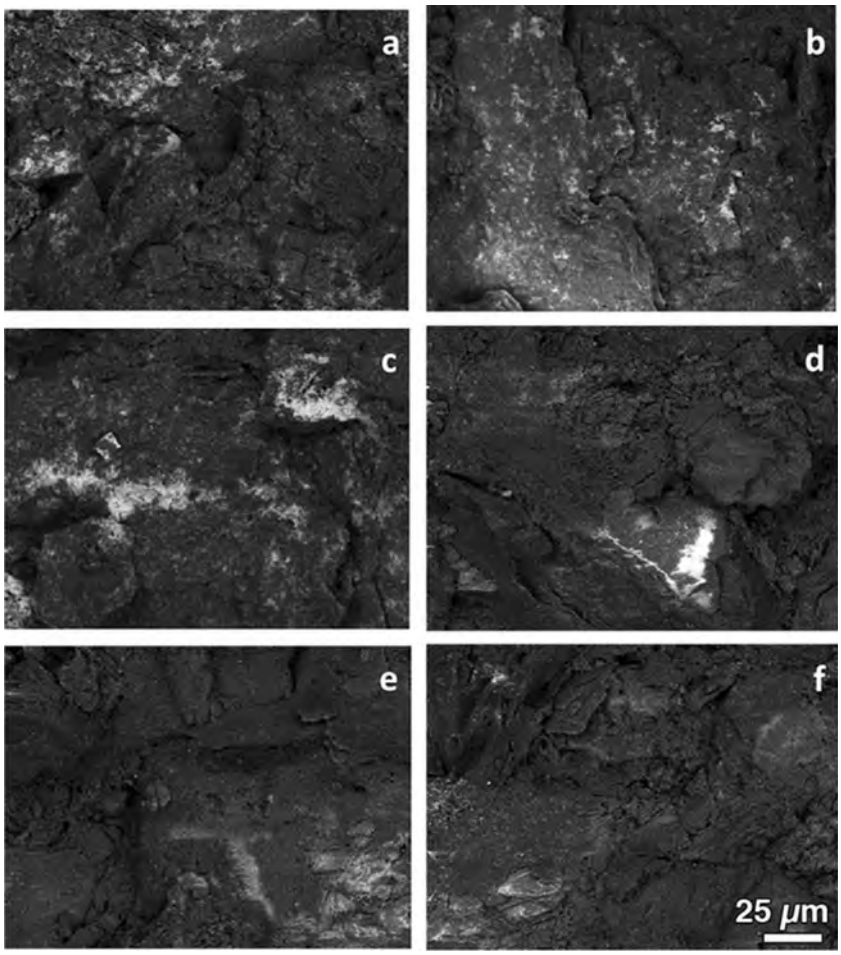

Fig. 3 SEM images acquired in BSE mode of stone surface treated with pristine AgNPs before (**a**–**c**) and after (**d**–**f**) washing with 7 mL/s water for 30 min. All the images are collected at 15 kX magnification

the highest concentration of AgNP@TEOS tested in the microbiological assays (ΔE=0.5 for sample treated with 110 μg/sample).

Antimicrobial activity

We evaluated the growth inhibition properties of TEOS-functionalized and pristine AgNPs against *B. subtilis* by the "spot on spot" method on solid nutrient medium. In order to assess the minimum amount of AgNPs (i.e., Ag weight) showing an effective antimicrobial activity, spots with different concentration of AgNPs were tested. Results show that 5 μg do not inhibit bacterial growth; 35 μg are only partially effective, while 70 μg fully inhibit bacterial growth (Table 1). There is no difference in antimicrobial activity between pristine and functionalized nanoparticles, indicating that functionalization does not affect nanoparticle toxicity.

It was therefore possible to assay the antimicrobial action of AgNP@TEOS grafted to the stone surface. An ad hoc experiment was set up to this purpose, comparing the viable bacteria recovered from silver-treated and untreated stone samples. Bacteria suspensions were deposited over the stone surface, and cell recovery was performed through washing. Preliminary tests were carried out to evaluate the *B. subtilis* CFU recovery from *Serena* stone at different times from bacteria deposition. A suspension of about 5×10^5 cells was laid over each stone sample. Cells were recovered by washing 1 min, 30 min, and 4 h after deposition (corresponding to the interaction times given in Table 2). As shown in Table 2, cells collected immediately after their deposition (1 min) constituted the 64 % of the inoculated amount; after 30 min of incubation the applied bacterial suspension was absorbed onto the stone surface, and the number of collected cells decreased by one order of magnitude, while after 4 h, the value decreased by two orders of magnitude. The amount of cells collected after 30 min is well suited for antibacterial activity experiments: in fact, although 95 % of cells result unrecoverable, 5 % of the inoculated bacteria is still enough to count a reliable number of CFU and to appreciate differences up to two orders of magnitude.

TEOS-treated samples were also investigated, showing that the number of cells recovered after 30 min was nearly identical (CFU %=5.1±0.1) to that obtained with pristine AgNPs, clearly indicating that TEOS does not interfere with CFU recovery. These conditions (both in terms of inoculum and interaction time) were then used to test the *B. subtilis* CFU

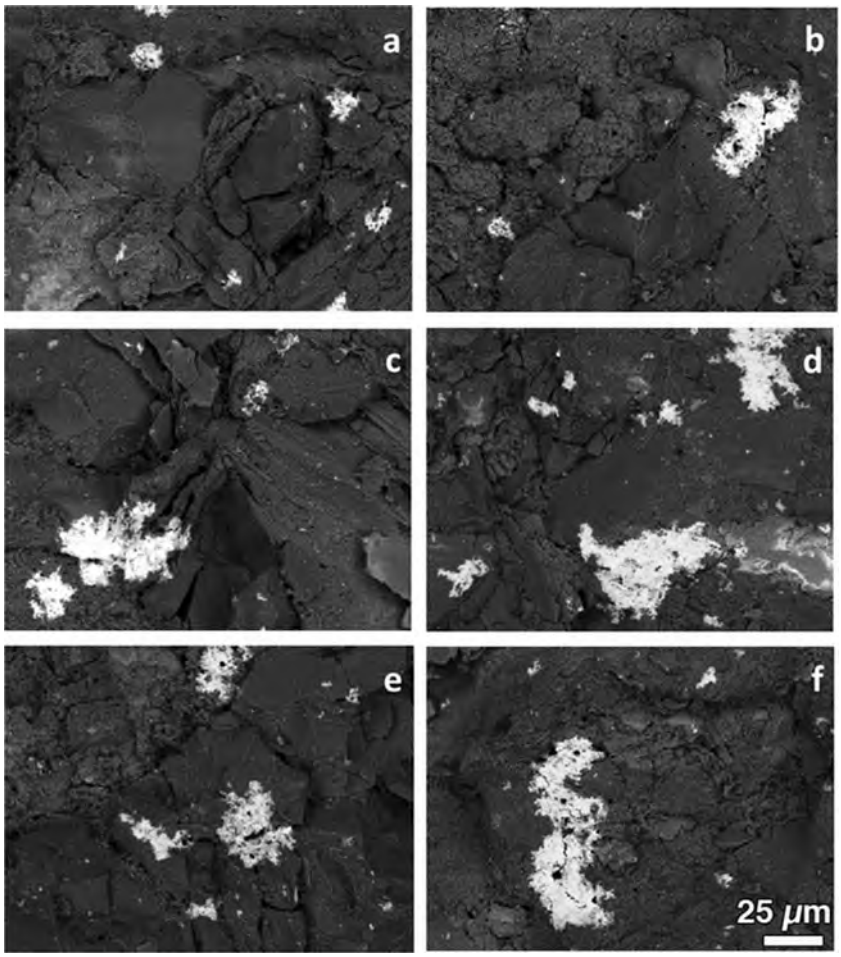

Fig. 4 SEM images acquired in BSE mode of stone surface treated with functionalized AgNPs before (**a**–**c**) and after (**d**–**f**) washing with 7 mL/s water for 30 min. All the images are collected at 1.5 kX magnification

recovery from AgNP@TEOS-treated samples. TEOS-treated samples were used as reference.

Results of the experiments carried out using AgNP@TEOS in the range of 6–110 μg/sample are reported in Table 3. In all the experiments, the CFU counts from silver-treated samples were always significantly lower than the ones from the reference.

The maximum bacteria inhibition (80.6 %) was obtained with a nanoparticle concentration of 15 μg/sample; higher concentrations did not lead to any increase, with an antimicrobial effect around 68 %. On the other hand, the concentration of 6 μg/sample gave the lowest inhibition activity (54.6 %).

Discussion

In this work, we investigated the use of TEOS-functionalized silver nanoparticles grafted to stone surfaces to inhibit bacterial viability. We used *Serena* stone as the substrate because it is a sandstone very commonly used in Works of Art, especially in architectural elements located outdoors and subjected to biocolonization. The grafting agent (TEOS) was chosen as it is commonly used for consolidation treatments of stones (Mosquera et al. 2008).

The first step involved the surface characterization of *Serena* stone after the application of nanoparticles. Microscopy results

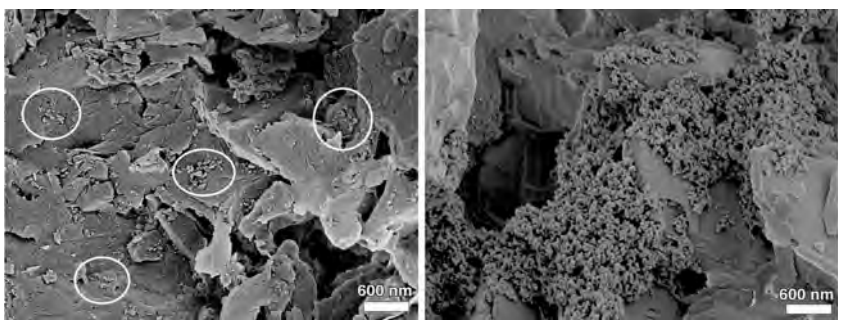

Fig. 5 SEM images of unwashed pristine NPs (*left image*) and functionalized NPs (*right image*) on *Serena* stone surface (50 kX magnification). The circles highlight groups of NPs

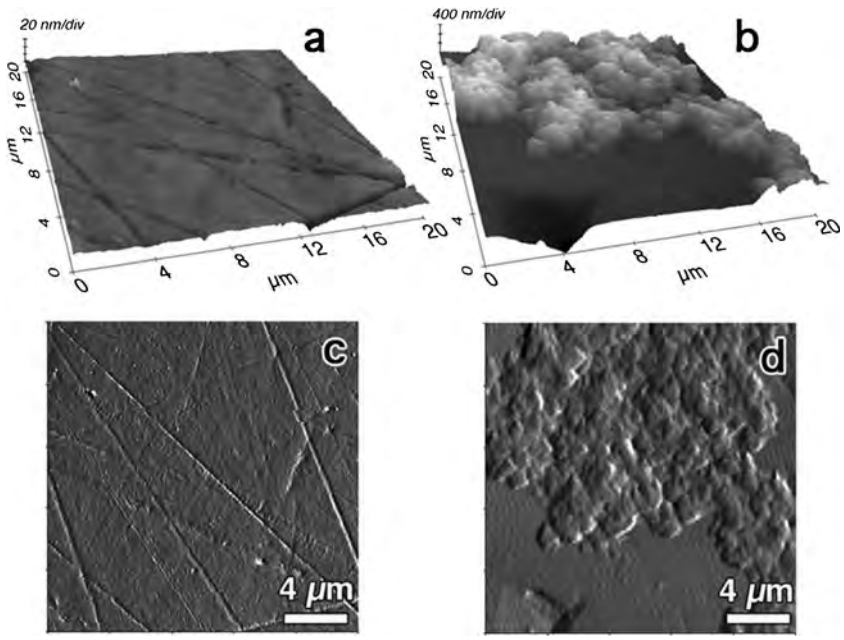

Fig. 6 AFM results (**a**, **b** 3D topographies; **c**, **d** corresponding error images) of the surfaces after washing of a stone sample treated with TEOS (**a**, **c**) and with AgNPs@TEOS (**b**, **d**)

showed that pristine nanoparticles are arranged in a much more uniform manner than functionalized ones, which conversely tend to dispose as clusters over the surface. This is reasonably due to the fact that the hydrolysis of TEOS functions is not confined to the formation of Si–O–Si bridges between one AgNP and the stone surface but could also take place between AgNPs, taking to the formation of clusters. Results also show that the treatment of the stone surface with AgNP@TEOS is resistant to washing treatments, conversely to what happens when pristine AgNPs are used.

Colorimetric measurements reveal no significant color changes of stone surface after treatment, validating the possible use of silver nanostructures for inhibition of the microbial growth on Works of Art made of *Serena* stone. In the case of the maximum amount of AgNP@TEOS applied on stone (110 μg/sample), ΔE results at 0.5, below the limit value of $\Delta E<2$ above which the human eye can appreciate a chromatic difference.

To evaluate the antimicrobial properties of AgNP@TEOS in standard microbiological culture experiments as well as after grafting on stones, *B. subtilis* was used as the target microorganism. It belongs to a very common genus frequently isolated from stone monuments, and, being a Gram-positive bacterium, it is also acknowledged to have a much higher resistance to antimicrobial silver compounds (Egger et al. 2009; Rai et al. 2009). In particular, the well-known laboratory strain 168 was used to test the AgNP@TEOS antibacterial effectiveness in laboratory conditions.

To understand if AgNP functionalization is effective against antibacterial activity, preliminary microbiological tests were carried out using a spot on spot technique on solid growth medium, comparing the inhibition activity of pristine and functionalized AgNP. This test allowed to overcome the usual problems met when more conventional microbiological methods are used: (1) 2-propanol, present in the AgNP@TEOS solution, inhibits the growth of *B. subtilis* vegetative cells, as well as spores, both in liquid and in solid medium, when applied after plating cell or spore suspensions and (2) AgNPs, either naked or functionalized, do not diffuse from disks to medium in the classical agar diffusion test. No inhibition differences were observed between pristine and functionalized AgNPs, the amount of nanoparticles needed

Table 1 Results of the spot on spot method. Chloramphenicol (Cmf) and TEOS solution were used as positive and negative control, respectively

	Cmf (μg)	TEOS [a]	AgNPs (μg)[b]			AgNP@TEOS (μg)[b]		
Sample	5		5	35	70	5	35	70
Growth	−	+	+	±	−	+	±	−

+ indicates bacteria growth, − indicates complete growth inhibition

[a] The quantity of TEOS used was the same of the 70 μg AgNP@TEOS sample

[b] Calculated as the total Ag content

Table 2 *B. subtilis* cell recovery by washing at different times after their deposition on stone. Values are normalized for an inoculum of about $5 \cdot 10^5$ cells/sample

	Cells collected[a]	
Interaction time [min]	CFU [$\cdot 10^4$]	CFU [%]
1	31.90±0.84	63.8±1.7
30	2.52±0.17	5.0±0.3
240	0.26±0.089	0.5±0.2

[a] The values are mean standard deviations for measurements obtained from two independent stone samples with at least three repetitions each

Table 3 *B. subtilis* CFU recovery from stone samples treated with different concentration of AgNP@TEOS or TEOS only (reference). The antimicrobial effect is evaluated comparing the number of cells collected from silver-treated and reference samples. Values are normalized for an inoculum of about $5 \cdot 10^5$ cells/sample

Concentration AgNP@TEOS [μg/sample]	Cells collected CFU [$\cdot 10^4$]		Antimicrobial Effect [%]
	AgNP@TEOS	TEOS[a]	
6	1.72±0.25	3.79±0.42	54.6±8.3
15	0.32±0.022	1.65±0.11	80.6±1.8
30	1.03±0.067	3.38±0.36	69.5±3.8
60	2.34±0.18	8.70±0.29	73.1±2.2
110	1.10±0.17	2.77±0.23	60.3±7.0

[a] For each concentration of AgNP@TEOS, the corresponding quantity of TEOS was used in the reference samples (TEOS)

to fully inhibit the bacterial growth being 70 μg in both cases. Results indicate that functionalization with TEOS does not alter the AgNP antimicrobial characteristics, as previously observed (Egger et al. 2009; Xu et al. 2009), and suggests that antimicrobial properties are very promising also in the case of functionalized nanoparticles.

The antimicrobial activity of the AgNP@TEOS was tested on stone specimens. A quantitative assay was set up to quantify the viability of bacteria: a known number of viable bacterial cells were applied over previously treated stone samples; cells were recovered by washing, and dilutions of the washing solution were plated and evaluated. Preliminary experiments were carried out to assess the proper amount of *B. subtilis* to be inoculated on the stone surface and the proper interaction time in order to recollect enough microorganisms for viability count. We found the inoculum of about $5 \cdot 10^5$ CFU and 30 min interaction time as the most suitable experimental conditions to our purpose. In these conditions, bacterial cell's recovery from untreated stone samples or from specimens treated with different amounts of TEOS is the same, indicating that TEOS does not interfere with CFU recovery and, consequently, does not have any antibacterial activity.

Samples were then treated with different amounts of functionalized AgNPs, and the antimicrobial activity was evaluated by comparing CFU recovery from treated sample and the corresponding reference (TEOS-treated). All tested concentrations proved to be effective in decreasing cell viability of at least 50 % despite the use of an interaction time of only 30 min and a very high concentration of bacteria, not likely to be found in in situ conditions.

The most effective AgNP@TEOS concentration is 15 μg/sample, a lower concentration (6 μg/sample) results less effective, while the increase of up to 110 μg/sample results in a slight decrease of the antimicrobial activity.

In contrast with the growth inhibition results from the spot on spot assay, the increase in NP concentration do not lead to the enhancement of antimicrobial activity. This could be partly due to the distribution in clusters of the AgNP@TEOS which do not homogeneously cover the stone surface, as observed by SEM analysis (Fig. 4). It is important to highlight, however, that the cell deposition and recovery assay on stone is intrinsically different from the common microbiological tests used to evaluate antimicrobial activity, which generally involve a longer interaction time between AgNPs and bacteria in a growth medium, either solid or liquid.

Conclusions

It was investigated in this study the possibility to use functionalized silver nanoparticles grafted to *Serena* stone surface as novel antimicrobials. Microscopic investigations show that TEOS, used as grafting agent, binds the NPs to the surface in a cluster disposition and does not change their morphology and dimensions. Moreover, microbiological tests prove that functionalization does not modify the antibacterial activity of the AgNPs toward the reference bacterium *B. subtilis*. The antibacterial assay performed on stone samples reveals an effectiveness ranging from 50 to 80 % in reducing cell viability, with the most effective AgNP@TEOS concentration of 6.7 μg/cm^2. In our knowledge, this is the first report where antimicrobial activity of silver NPs applied on a stone surface is demonstrated. These preliminary results obtained in laboratory conditions are encouraging for further studies, aiming at using the proposed nano-remedy for in situ treatment of Works of Art made of *Serena* stone to discourage bacteria colonization of the surface.

Acknowledgments CSGI and Ministry for Education and Research (MIUR, PRIN2009-2009P2WEAT) are gratefully acknowledged for financial support. M.B. thanks the EU for financial support under the Marie Curie Actions - European Reintegration Grants (FP7-PEOPLE-2009-RG, Project number: 249319, SUPRACRYST). The authors also thank dr. Nicole Bonelli, CSGI, for the assistance with colorimetric measurements.

References

Aherne D, Ledwith DM, Gara M, Kelly JM (2008) Optical properties and growth aspects of silver nanoprisms produced by a highly reproducible and rapid synthesis at room temperature. Adv Funct Mater 18: 2005–2016

Anagnostopoulos C, Spizizen J (1961) Requirements for transformation in *Bacillus subtilis*. J Bacteriol 61:741–746

Chaloupka K, Malam Y, Seifalian AM (2010) Nanosilver as a new generation of nanoproduct in biomedical applications. Trends Biotechnol 28:580–588

Choi O, Hu Z (2008) Size dependent and reactive oxygen species related nanosilver toxicity to nitrifying bacteria. Environ Sci Technol 42: 4583–4588

De Leo F, Iero A, Zammit G, Urzi CE (2012) Chemoorganotrophic bacteria isolated from biodeteriorated surfaces in cave and catacombs. Int J Speleol 41:125–136

Dei L, Mauro M, Baglioni P, Manganelli Del Fa C, Fratini F (1999) Growth of crystal phases in porous media. Langmuir 15:8915–8922

Egger S, Lehmann RP, Height MJ, Loessner MJ, Schuppler M (2009) Antimicrobial properties of novel silver-silica nanocomposite material. Appl Environ Microbiol 75:2973–2976

Fajardo-Cavazos P, Nicholson W (2006) *Bacillus* endospores isolated from granite: close molecular relationships to globally distributed *Bacillus* spp. from endolithic and extreme environments. Appl Environ Microbiol 72:2856–2863

Falletta E, Bonini M, Fratini E, Lo Nostro A, Pesavento G, Becheri A, Lo Nostro P, Canton P, Baglioni P (2008) Clusters of poly(acrylates) and silver nanoparticles: structure and applications for antimicrobial fabrics. J Phys Chem C 112:11758–11776

Feng QL, Wu J, Chen GQ, Cui FZ, Kim TN, Kim JO (2000) A mechanistic study of the antibacterial effect of silver ions on *E. coli* and *S. aureus*. J Biomed Mater Res 52:662–668

Gaylarde C, Silva MR, Warscheid T (2003) Microbial impact on building materials: an overview. Mater Struct 36:342–352

Jung WK, Koo HC, Kim KW, Shin S, Kim SH, Park YH (2008) Antibacterial activity and mechanism of action of the silver ion in *S. aureus* and *E. coli*. Appl Environ Microbiol 74:2171–2178

Kim JS, Kuk E, Yu KN, Kim JH, Park SJ, Lee HJ, Kim SH, Park YK, Hwang CY, Lee YS, Jeong DH, Cho MH (2007) Antimicrobial effects of silver nanoparticles. Nanomed Nanotechnol Biol Med 3:95–101

Knetsch MLW, Koole LH (2011) New strategies in the development of antimicrobial coatings: the example of increasing usage of silver and silver nanoparticles. Polymers 3:340–366

Kobayashi Y, Katakami H, Mine E, Nagao D, Konno M, Liz-Marzan LM (2005) Silica coating of silver nanoparticles using a modified Stöber method. J Colloid Interface Sci 283:392–396

Lok CN, Ho CM, Chen R, He QY, Yu WY, Sun H, Tam PKH, Chiu JF, Che CM (2007) Silver nanoparticles: partial oxidation and antibacterial activities. JBIC J Biol Inorg Chem 12:527–534

Lok CN, Ho CM, Chen R, He QY, Yu WY, Sun H, Tam PKH, Chiu JF, Che CM (2006) Proteomic analysis of the mode of antibacterial action of silver nanoparticles. J Proteome Res 5:916–924

McNamara C, Mitchell R (2005) Microbial deterioration of historic stone. Front Ecol Environ 3:445–451

Morones JR, Elechiguerra JL, Camacho A, Holt K, Kouri JB, Ramires JT, Yacaman MJ (2005) The bactericidal effect of silver nanoparticles. Nanotechnology 16:2346–2353

Mosquera MJ, Santos DM D l, Montes A, Valdez-Castro L (2008) New nanomaterials for consolidating stone. Langmuir 24:2772–2778

Niitsoo O, Couzis A (2011) Facile synthesis of silver core-silica composite nanoparticles. J Colloid Interface Sci 354:887–890

Ozy F, Guden M, Uzel A, Karaboz I, Akil O, Bulut H (2010) Antimicrobial activity of TiO_2-coated orthodontic ceramic brackets against *Streptococcus mutans* anc *Candida albicans*. Biotechnol Bioprocess Eng 15:680–685

Page K, Palgrave RG, Parkin I, Wilson M, Savin SLP, Chadwick AV (2007) Titania and silver-titania composite films on glass-potent antimicrobial coatings. J Mater Chem 17:95–104

Pal S, Tak YK, Song JM (2007) Does the antibacterial activity of silver nanoparticles depend on the shape of the nanoparticle? A study of the Gram-negative bacterium *E. coli*. Appl Environ Microbiol 73: 1712–1720

Panacek A, Kvitek L, Prucek R, Kolar M, Vecerova R, Pizurova N, Sharma VK, Nevecna T, Zboril R (2006) Silver colloid nanoparticles: synthesis, characterization, and their antibacterial activity. J Phys Chem B 110:16248–16253

Pinna D, Salvadori B, Galeotti M (2012) Monitoring the performance of innovative and traditional biocides mixed with consolidants and water-repellents for the prevention of biological growth on stone. Sci Total Environ 423:132–141

Raccomandazioni NorMal (1993) AA VV Raccomandazioni NorMal 43/93, Misure colorimetriche strumentali I superfici opache. CNR-ICR, Roma

Rai M, Yadav A, Gade A (2009) Silver nanoparticles as a new generation of antimicrobials. Biotechnol Adv 27:76–83

Scheerer S, Ortega-Morales O, Gaylarde C (2009) Microbial deterioration of stone monuments—an update overview. Adv Appl Microbiol 66:97–139

Silver S (2003) Bacterial silver resistance: molecular biology and uses and misuses of silver compounds. FEMS Microbiol Rev 27:341–353

Sondi I, Salopek-Sondi B (2004) Silver nanoparticles as antimicrobial agent: a case study on *E. coli* as a model for Gram-negative bacteria. J Colloid Interface Sci 275:177–182

Stassi A, Zanardini F, Cappitelli F, Schiraldi A, Sorlini C (1998) Calorimetric investigations on the metabolism of *Bacillus* strains isolated from artistic stoneworks. Ann Microb (Milan) 48:111–120

Warscheid T, Braams J (2000) Biodeterioration of stone: a review. International Biodeterioreation Biodegrad 46:343–368

Xu K, Wang JX, Kang XL, Chen JF (2009) Fabrication of antibacterial monodispersed Ag-SiO_2 core-shell nanoparticles with high concentration. Mater Lett 63:31–33

Yao N, Yeung KL (2011) Investigation of the performance of TiO_2 photocatalytic coatings. Chem Eng J 167:13–21

Microchim Acta (2013) 180:1093–1099
DOI 10.1007/s00604-013-1023-6

ORIGINAL PAPER

Improving surface plasmon resonance imaging of DNA by creating new gold and silver based surface nanostructures

Stefano Mariani · Maria Laura Ermini · Simona Scarano · Francesca Bellissima · Massimo Bonini · Debora Berti · Maria Minunni

Received: 25 February 2013 / Accepted: 31 May 2013 / Published online: 28 June 2013

Abstract The use of nanoparticles (NPs) can substantially improve the analytical performance of surface plasmon resonance imaging (SPRi) in general, and in DNA sensing in particular. In this work, we report on the modification of the gold surface of commercial biochips with gold nanospheres, silica-coated gold nanoshells, and silver nanoprisms, respectively. The NPs were tethered onto the surface of the chip and functionalized with a DNA probe. The effects of tethering conditions and varying nanostructures on the SPRi signals were evaluated via hybridization assays. The results showed that coupling between planar surface plasmons and electric fields, generated by localized surface plasmons of the NPs, is mandatory for signal enhancement. Silver nanoprisms gave the best results in improving the signal change at a target DNA concentration of <50 nM by +50 % (compared to a conventional SPRi chip). The limit of detection for the target DNA was 0.5 nM which is 5 times less than in conventional SPRi.

Keywords Nanoparticles · Surface nanostructuring · Analytical performances · DNA sensors · Optical sensors · Surface plasmon resonance imaging

Electronic supplementary material The online version of this article (doi:10.1007/s00604-013-1023-6) contains supplementary material, which is available to authorized users.

S. Mariani · M. L. Ermini · S. Scarano · F. Bellissima · M. Bonini (✉) · D. Berti · M. Minunni (✉)
Department of Chemistry "Ugo Schiff" and CSGI, University of Florence, Via della Lastruccia 3, 50019 Sesto Fiorentino, FI, Italy
e-mail: massimo.bonini@unifi.it
e-mail: maria.minunni@unifi.it

Introduction

Biosensors are innovative analytical devices based on the close integration between a biological receptor and a transducer. The bioreceptor is immobilized on the surface of the transducer and it is responsible for the selectivity of the system. The receptor recognizes the analyte in solution and binds it, generating an event sensed by the transducer. Different receptors coupled to a variety of transduction principles are available. Among receptors, we can distinguish between enzymes, leading to catalytic sensors, and receptors based on affinity interactions. Antigen-antibody reactions (immunoreactions), nucleic acids binding (DNA and/or RNA), aptamers and their ligands, lead all to Affinity-Based Biosensors (ABBs). About the detection of the event, transduction can be electrochemical, gravimetric, optical, thermometric, etc. Therefore, different combinations among receptors and transduction principles result in a wide variety of possible analytical applications [1–4].

Since 20 years Surface Plasmon Resonance (SPR) has been applied to a variety of problems related to biochemistry, molecular biology, drug development, and analytical chemistry [5, 6]. Conventional SPR and its most recent advancement, SPR-imaging (SPRi), are more and more exploited for advanced applications aiming at fast, label-free, real-time multiplexed analysis of bio-interactions for clinical diagnostic as well as anti-doping analysis, where high sample throughput and fast analysis time are mandatory [7]. In particular, SPRi technique results to be a suitable asset for developing versatile DNA affinity biosensors [8, 9]: in fact, as we recently reported [10], SPRi has been used in a variety of affinity systems, including DNA/DNA, DNA-binding protein, DNA and RNA aptamers/protein, antibody-antigen

and carbohydrate/protein interactions. SPRi can eventually contribute to support membrane related studies [11].

Among the analytical challenges behind SPR biosensing, increased sensitivity is of crucial importance. Recently, some authors have reported interesting improved detection limits by using catalytic activity of enzymes [12]. Alternatively, improved analytical performances in SPR based-sensing are obtained when using nanoparticles to enhance SPR signal [13–16]. Metallic Nanoparticles (NPs) are nanoscale materials that possess optical and electronic properties opening new perspectives in the strategies for detections of biomolecules such as DNA, RNA, and proteins. Different approaches have been pursued to obtain higher sensitivity in optical SPR-based sensing. Most of them deal with nanostructures incorporated within sandwich-like assays, using NPs as mass enhancers or to obtain plasmon coupling. Interesting advances on the use of functionalized Au NPs in DNA biosensing strategies have been recently summarized [17]. Particular attention has been devoted to ultra-sensitive DNA detection, aiming at DNA sequence detection directly in genomic, unamplified samples, bypassing Polymerase Chain Reaction (PCR). Behind this work, excellent reviews that have given comprehensive summaries of updated processes involving DNA sensors and DNA microarrays have been also published [18–22]. Quantum dots were also used in SPRi immunosensors [23].

More recently, applications of SPRi-based sensing have been reported for the detection of target sequences in real samples of genomic DNA from plants and human blood, in sandwiched gold NPs-based assays [24]. NPs were coated with streptavidin and further modified with biotinylated probes. In particular, a marker sequence of transgenosis was detected in genomic DNA samples carrying different amounts of genetically modified (GM) sequences (Roundup Ready soybean, RR) [25]. The same assay scheme was used for the detection of single nucleotide polymorphism (SNP), meaning the difference in one nucleotide, in samples from human genomic DNA extracted from lymphocytes to detect a mutation present in the globin gene, involved in thalassemia [26].

Our group has recently explored the possibility to use NPs for improving analytical performances of SPRi-based sensing.

In particular in this work, different nanostructures were introduced in a SPRi biochip to be used in DNA sensing. In particular gold nanoparticles, silica-coated Au nanoshells and silver nanoprisms were synthesized and immobilized on gold surfaces and the efficiency in the amplification of the analytical signal was evaluated in a DNA biosensor.

First, NPs were synthesized and then covalently linked via dithiols on the gold chip surface, which could provide a simple and reliable platform for immobilization [27], and finally nanostructured surfaces were functionalized with thiolated-DNA probes. The nanostructured surfaces have been characterized by scanning electron microscopy (SEM) and atomic force microscopy (AFM). Finally, hybridization experiments between the immobilized probe and its specific complementary target sequence in solution were performed and the relative sensor performances were evaluated, with the final aim of finding the best NP structure for improving the analytical performances of the sensor, mainly in terms of sensitivity.

Experimental

Immobilization

Immobilization Solution (IS) was a water solution 1 M KH_2PO_4 (pH 3.8). Hybridization Solution (HS) was a water solution of 300 mM NaCl, 20 mM Na_2HPO_4, 0.1 mM EDTA, 0.05 % TWEEN®20 (Polyethylene glycol sorbitan monolaurate), pH 7.4. Solutions were prepared in MilliQ water. Reagents were purchased from Sigma Aldrich (www.sigmaaldrich.com/, Milan, Italy). All synthetic oligonucleotides were purchased from Eurofins MWG Operon (www.eurofinsgenomics.eu/, Germany). Nucleotide sequences were: TProbe (Testing Probe) 5′ HS-(CH2)6-GTGGTGTCACAGGAAGAGATT 3′ and the complementary TTarget (Testing Target) 5′ AATCTCTTCCTGTGACACCAC 3′. The TProbe sequence at its 3′ end maps the rs1045642 single nucleotide polymorphism (position 87138645 of the chromosome 7 on human ABCB1 gene), a variation in human genome related to the incidence of many diseases [28, 29] and drug resistance [30, 31].

An unspecific sequence was used as negative control: 5′ HS-(CH2)6-GAGGGCGATGCCACCTAC 3′. The TTarget was removed from the hybrid with immobilized TProbe using a regeneration solution (RS) consisting in 100 mM HCl in MillQ water.

Nanoparticles (NPs)

Silver nanoprisms: trisodium citrate (>99 %), poly(sodium styrene sulfonate), sodium tetrahydridoborate (>99 %) and silver nitrate (>99 %) were purchased from Sigma Aldrich (www.sigmaaldrich.com/, Milan, Italy). Solutions were prepared in milliQ water. Silica-coated Au nanoshells: ammonium hydroxide (30 %) and sodium hydroxide pellets (>98 %) were from PanreacQuimica (www.panreac.com/, Spain). Tetraethylorthosilicate (TEOS) (>99 %), ethanol ultrapure p.a., milliQ water 18.2 MW/cm, tetrachloroauric acid (>99.9 %), tetrakis(hydroxymethyl)phosphonium chloride (THPC, 80 % solution in water), (3-Aminopropyl) trimethoxysilane ATPS (97 %), hydrochloric acid (37 %), formaldehyde (37 % w/w) were all from Sigma Aldrich-

Fluka (www.sigmaaldrich.com/, Milan, Italy). Pentane (96 %) was from Riedel de Haen (www.riedeldehaen.com/, Milan, Italy), potassium carbonate p.a. was from Merck (www.merck.it/, Darmstadt, Germany). Gold nanoparticles: tetrachloroauric acid (>99,9 %) and trisodium citrate dehydrate (>99 %) were purchased from Sigma Aldrich-Fluka, (www.sigmaaldrich.com/, Milan, Italy). All solutions were prepared in MilliQ water.

Thiols and dithiols: 11-mercapto-1-undecanol (MU), 6-mercapto-1-hexanol (MCH), 1,8 Octanedithiol (ODT) and 1,4-Benzenedimethanethiol (BDMT) were purchased from Sigma (www.sigmaaldrich.com/, Milan, Italy).

Thiols and dithiols

11-mercapto-1-undecanol (MU), 6-mercapto-1-hexanol (MCH), 1,8 Octanedithiol (ODT) and 1,4-Benzenedimethanethiol (BDMT) were purchased from Sigma (www.sigmaaldrich.com/, Milan, Italy).

SPRi setup

SPRi-Lab^{+} instrument was from GenOptics-Horiba Scientific (www.horiba.com/, USA). The opto-mechanical part of the instrument consisted in a light source emitting at 635 nm. Biochip were housed in a cell integrated with a fluidic system (PEEK tubing, Restek Corporation, www.restek.com/, 1/16″ OD×001″ ID) equipped with a Rheodyne valve (50 μL loop volume) and the continuous flow of HS was generated by a peristaltic pump (Miniplus 3, Gilson Inc., www.gilson.com/, USA) using accurate tubing from Elkay Laboratory Products (www.elkaylabs.com/, UK) orange/black, 0.015 cc·min^{-1}.

NPs synthesis

Three different types of nanoparticles were synthesized: gold nanospheres, gold nanoshells and silver nanoprisms. Gold nanospheres were synthesized according to the Turkevich method [32]. Gold nanoshells have been grown on silica spheres [33]. Silver nanoprisms were synthesized with a seed-based method [34]. Details about the synthesis of the nanostructures are given in the Online Resource, together with respective UV–vis absorption spectra.

NPs and surface characterization

All nanoparticles suspensions were characterized by UV–vis spectrophotometry using a Perkin Elmer Lambda 900 (www.perkinelmer.com/). Gold nanospheres were 15 nm in diameter, the total diameter of the nanoshells were 150 nm and silver nanoprisms side was 40 nm. Nanostructured gold surfaces of SPRi biochips were characterized by SEM (Scanning Electron Microscope) and AFM (Atomic Force Microscope). Scanning electron microscopy experiments were carried out with a ZEISS Sigma FEG-SEM (www.zeiss.it/). Atomic force microscopy images were collected by means of a PSIA XE-100 (www.parkafm.com/) microscope in non-contact mode (NCHR probes, radius of curvature <10 nm).

Chip surface nanostructuring

NPs were immobilized onto the gold surface of SPRi biochips through a dithiol linker. To this aim, two different dithiols were tested 1,8-Octanedithiol (ODT) and 1,4-Benzenedimethanethiol (BDMT). Dithiols immobilization was carried out by applying a pre-punched PDMS mask to obtain a removable micro-welled (1 mm in diameter) support for the deposition of dithiols (concentration: 1 mM in MilliQ water, 0.8 μL/micro-well). After the deposition of the drops, the chip was placed into a moist chamber to which vacuum was applied for about 20 min to eliminate air bubbles from micro-wells and left into the moist chamber for 20 h, avoiding the drying of the immobilization solution. Finally, drops in micro-wells were aspired with micro-syringe and micro-wells were washed with MilliQ water. Control spots, where the unspecific sequence was immobilized, and blanks (bare gold) were also prepared on the biochip.

Nanoparticles suspensions were eluted in MilliQ water to a certain density ensuring the total coverage of the spot area (1 mm in diameter each). NPs were also alternatively diluted in 20%vol/vol ethanol or 5 % vol/vol ammonium hydroxide water solutions (pH~10). After that, silver nanoprisms, gold-silica core-shell NPs and gold nanospheres were covalently immobilized on the gold chip by depositing 0.8 μL onto different dithiolated micro-wells.

DNA probe immobilization on nanostructured SPRi biochips

Thiolated DNA probes (TProbe) were immobilized onto nanostructured surfaces, exploiting the affinity of sulphur for gold and silver. A 10 μM TProbe solution was prepared in IS and 0.8 μL were deposited in each micro-well and let react in the moist chamber for 20 h. Finally, after the removal of the PDMS mask, the prism was immersed in a Passivation Solution PS (1 μM 11-mercapto-1-undecanol, MU, and 1 μM 6-mercapto-1-hexanol, MCH, in MilliQ water) for 20 h to passivate the rest of the gold surface. Finally, the chip surface was rinsed with MilliQ water and housed in the instrument cell.

SPRi measurements on nanostructured surfaces

Calibration curves were obtained by injecting 100 μL of the complementary TTarget in HS, within the range of concentration 5 nM–250 nM. The immobilized TProbe was then

regenerated from the hybridized TTarget after each measurement by RS solution for 30 s. All measurement cycles were performed at fixed angle of incident light (maximum slope of reflectivity curve), and the variation of intensity of reflected light due to the target interaction was monitored as SPRi signal.

Results and discussion

In this work commercially available SPRi biochips were modified with different nanostructures and tested for their potential use in enhancing the sensitivity of a SPRi-based DNA biosensor. The basic idea was to functionalize the gold layer of biochips with NPs through the covalent linking offered by dithiols. To this aim, the most suitable dithiol was selected and the nanostructures obtained with different NPs were studied. DNA sequences were immobilized on the obtained three nanostructured chip surfaces and the hybridization reactions with the complementary target sequence were evaluated by SPRi sensing. The rationale of this approach was based on the occurrence of two phenomena: i.e. the increase of the surface area available for sensing (due to the functionalization of the chip surface with nanostructures) and the electronic properties of the nanostructured surface. The nanostructuring of a flat surface, such as the one of the chip, carries to an increase of the surface area that could enhance the amount of immobilized DNA. At the same time, the presence of structures on top of the chip gold surface could result in non-optimized instrumental conditions, which are eventually re-established by adjusting the source-gold surface impinging angle. On the other hand, the sensitivity of SPRi biosensor could take advantage of the coupling between the planar surface plasmons and electric fields generated by localized surface plasmons. Recently, this approach has been successfully exploited in the functionalization with noble metal NPs of the interacting surface of a gold SPRi biochip [35].

Nevertheless, many aspects are still to be optimized when introducing nanostructure onto the surface of commercial biochips. For this reason we decided to investigate the effect of the plasmon resonance wavelength of the nanostructures in relation to that of the chip gold surface, especially in terms of improvement performance. To this aim, the gold surface was therefore functionalized with three different nanostructures.

Silver nanoprisms were selected because of their surface plasmon resonance peak at 633 nm, almost matching the wavelength of the instrumental light source (635 nm).

On the other hand, the resonance of the plasmon of the gold nanospheres (Absmax=528 nm) is well separated from the resonance of the chip surface, while gold nanoshells (Absmax=588 nm) were selected as an intermediate case.

Nanostructuring procedures were optimized in terms of the best dithiol and solutions to be used to immobilize the NPs, i.e. MilliQ water, ethanolic, or ammonia solution. Nanostructured surfaces were compared to bare gold surface in terms of stability under HS flow and of the reflectivity curves.

In order to choose the best linker for the NPs, two different dithiols, BDMT and ODT, were tested. After NPs immobilization, reflectivity curves relative to different dithiol/NP combinations were compared. Nanostructures built on ODT dithiol did not show significant shifts in the resonance angle, contrary to BDMT. Shift observed in presence of BDMT points toward the coupling between planar surface plasmons and electric fields generated by localized surface plasmons of NPs, so BDMT was chosen as the best linker to be used for NPs immobilization.

Gold nanospheres and silica-coated Au nanoshells were successfully deposited by simply adding their water dispersions on top of the BDMT layer. The nanostructured biochip surface resulted stable under HS flow: in fact, no change in the plasmonic curves was recorded by the real-time CCD image of the spots after 48 h of continuous flow of HS (data shown in the Online Resource). This is consistent with the high affinity between sulphur and gold.

Nanostructuring with water dispersions of silver nanoprisms reflected the lower affinity between silver and sulphur, resulting damaged after 8 h of exposure to HS. Then, to perform successfully and steady a surface nanostructuring with silver nanoprisms, 5 % of ammonium hydroxide was added to aqueous dispersion of NPs (optimizations and data were shown in Online Resource). The success of optimization could be explained by the dithiol deprotonation in presence of ammonia solution that could promote the covalent binding with nanoprisms.

Among the studied nanostructures, nanostructuring with silver nanoprisms displayed the largest shift (0.51°, see Table in Online Resource), highlighting the coupling between the plasmon resonances of NPs and chip. These results showed that the position of the plasmon resonance peak of nanoparticles represented a useful parameter when designing a nanostructured biochip for SPRi.

The nanostructured SPRi biochip surfaces were investigated by SEM (Scanning Electron Microscopy) and AFM (Atomic Force Microscopy). In Fig. 1, the images relative to the three different nanostructured spots are reported, together with bare gold spots as reference.

Gold nanospheres and silica-coated Au nanoshells appeared irregularly distributed on the dithiolated surface, forming large aggregates which could take to a loss of sensitivity of the SPRi biochip, possibly because of the distance from the sensing surface (due to aggregate thickness) and/or because the irregular distribution of the DNA probe immobilization, affecting the hybridization of the complementary TTarget. On the other hand, a homogeneous coverage was obtained with silver nanoprisms on dithiolated

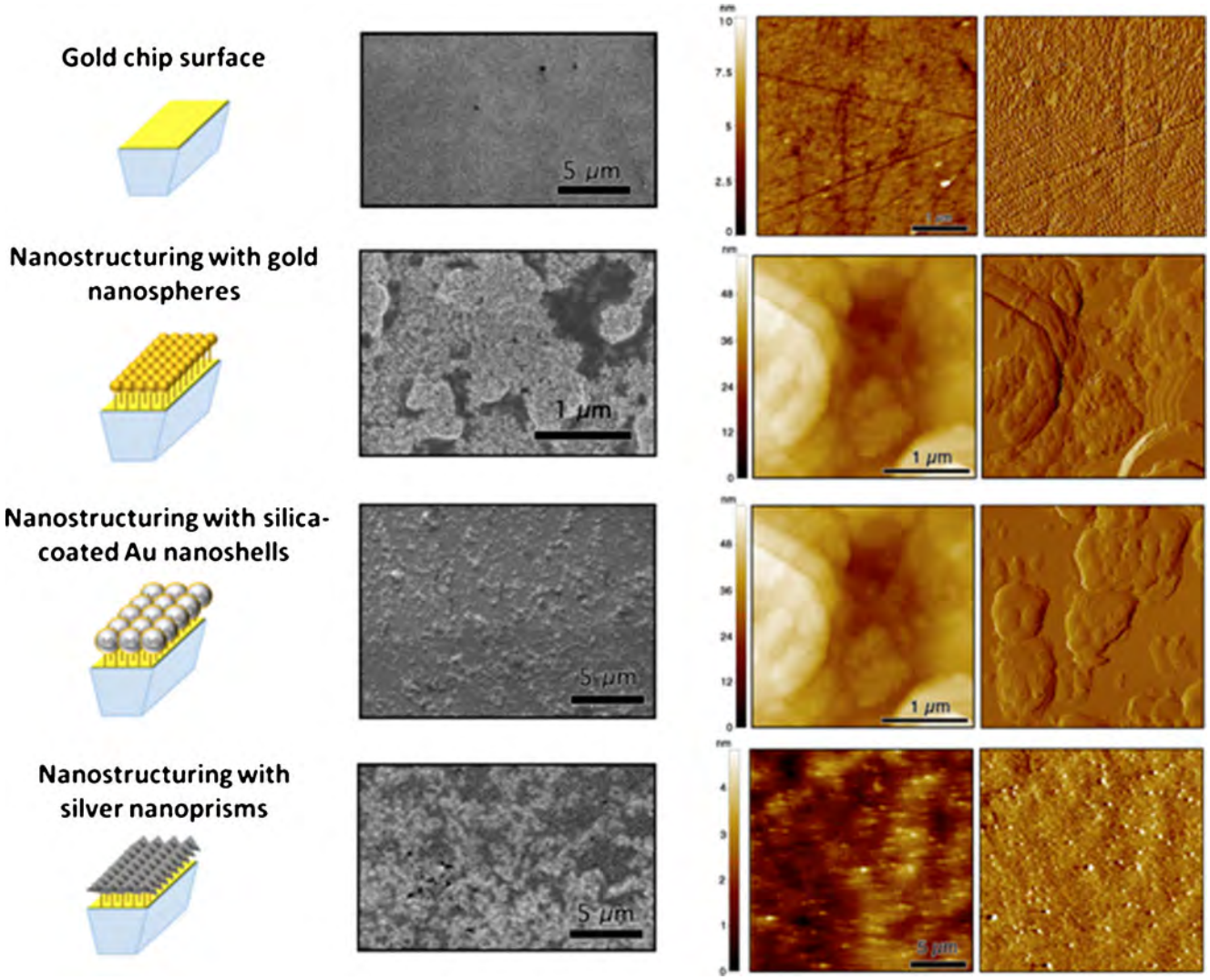

Fig. 1 Schematic representations of chip surfaces (*left*) together with SEM (*center*) and topography and error AFM images (*right*) of the nanostructured surfaces. SEM images were taken with a Zeiss Sigma FEG-SEM (www.zeiss.it/). AFM height and error images were taken with a PSIA XE-100 microscope (www.parkafm.com/)

surface. The platelet-like shape of nanoprisms and their reduced thickness was of great help in the formation of a homogeneous and thin coating, which from a structural point of view, made nanoprisms the best candidate among the tested nanostructures in the design of highly sensitive SPRi biochips.

Once covalently bound to the chip surface, nanostructures were functionalized by coupling the thiolated TProbe on their surface. The effect of the different nanostructures was evaluated through the study of hybridization signals obtained by injecting the complementary TTarget onto nanostructured spots modified with TProbe, compared with those obtained from the same TProbe directly bound to the unmodified gold biochip surface. Signal intensities of the observed interactions were evaluated at different TTarget concentrations for the all three nanostructures. Negative control oligonucleotides solution was also assayed giving no significant signal. The results are summarized in Fig. 2.

Both gold nanospheres and silica-coated Au nanoshells caused a loss of sensitivity of the system. In particular, nanoshells produced the strongest decrease on SPRi hybridation signals, probably because of the large distance between the probe and the sensing surface. Nanoshells were characterized by a diameter of about 150 nm, making the biochip surface insensitive (from the plasmonic point of view) to the hybridization taking place on the surface of the nanoshells. In the case of gold nanospheres, their size should not represent a problem, as long as a monolayer (or few layers) of NPs is deposited onto the chip surface. Unfortunately, as highlighted by the microscopy results, large aggregates were present on the surface, indicating that an accurate control of the deposition step is a prerequisite for the

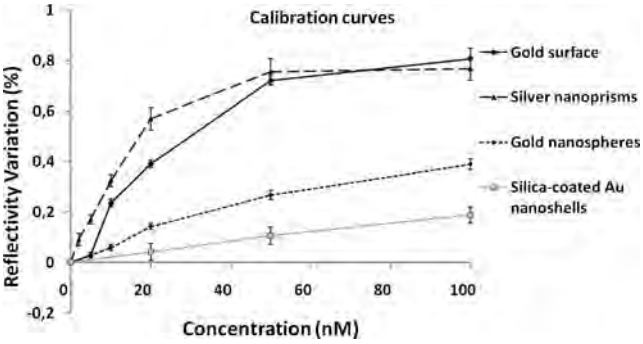

Fig. 2 Reflectivity variation for different concentrations of DNA target recorded from DNA probes immobilized on different functionalized surfaces

preparation of an efficient system. Finally, silver nanoprisms showed a significant improvement over the conventional approach for target concentrations lower than 50 nM (see Fig. 2): in fact, an enhancement up to 50 % in SPRi signals was recorded at 20 nM (see Fig. 3).

A calibration curve on silver nanoprisms nanostructure, in the linear dynamic range between 20 nM (LOL, limit of linearity) and 0.5 nM (LOD, limit of detection), was eventually obtained and reported in the Online Resource. LOD was 5 times smaller than that of nucleic acid biosensor based on conventional SPR imaging (2.5 nM) [8].

The increased sensitivity could be explained by the analysis of the reflectivity curves (reflectivity vs. angle of incident light, reported in the Online Resource) of TProbe directly bound on gold and the corresponding tethered on the silver nanostructure.

In the case under study, the nanostructure produced a sharper reflectivity curve than the control spot one (probe on bare gold). As a consequence, for the same interaction on the sensing surface, variations of the resonance angle, corresponded to a greater variation of intensity of reflected light. To further analyze the increase in sensitivity obtained

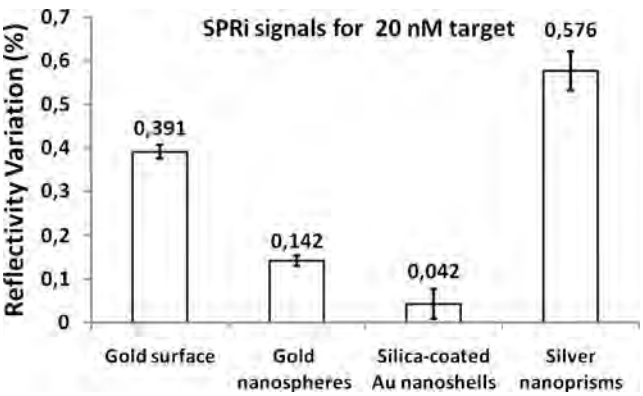

Fig. 3 Reflectivity variation percent for 20 nM DNA target, recorded from DNA probes immobilized on different functionalized surfaces

with silver nanostructures, one could eventually evaluate the first derivate in the inflection point of reflectivity curves, which corresponds to the measuring angle (inflection angle), both for bare gold and nanostructured surfaces. In particular, the fitting was achieved using a polynomial interpolation of the reflectivity curves which provided an excellent coefficient of determination (0.999) for both reflectivity curves. As results the first derivate in inflection angle of the silver nanostructured surface was 6.5 % greater than the one of bare gold surface. As consequence, for the same variations of angle in the neighborhood of the inflection angles, the variations of intensity of reflected light are greater for nanostructured surface respect to bare gold surface, explaining the increased sensitivity for the nanostructured DNA sensors.

Finally, the biosensor resulted to be usable with an excellent reproducibility (CV% <10) within the first 10 measurements cycles (TProbe-TTarget interaction and hybrid denaturation by TProbe regeneration with RS).

Conclusion

The surface of a commercial SPRi biochip was functionalized with nanostructures differing in terms of composition, dimension, and shape, but all showing a surface plasmon resonance peak in the visible range. Then, nanostructured surfaces were functionalized with DNA probe and the hybridization reaction between the immobilized probe and the complementary target DNA in solution was studied. A significant improvement of the SPRi sensitivity (below 50 nM target concentrations) and a decrease of LOD to 0.5 nM (5 times less than conventional SPRi one) was achieved, when silver nanoprisms were employed in gold surface nanostructure. These results showed that the morphology of the nanostructured coating, the tethering conditions and the electronic properties of the nanostructures were key factors in the engineering of nanostructured SPRi, showing that coupling between surface plasmon resonances of substrate and nanostructure was an effective approach to SPRi signal enhancement. Further enhancement of the analytical performances could be achieved by optimizing these aspects. This would allow a more sensitive label free direct detection of DNA, possibly bypassing DNA amplification, i.e. the PCR step, and reducing time and cost of DNA analysis. Therefore, nanostructured SPR biochips could be employed as platform for the study of DNA defects (i.e. point mutations, deletions and insertions), relevant in diagnostics and pharmacogenomics, through the development of fast, label free and ultrasensitive assays.

Acknowledgments This work was supported by CSGI and MIUR. M.B. acknowledges the EU for financial support (FP7-PEOPLE-2009-RG, project SUPRACRYST). COSTTD1003 Action is also acknowledged.

References

1. Iliuk AB, Hu L, Tao WA (2011) Aptamer in bioanalytical applications. Anal Chem 83(4440):4452. doi:10.1021/ac201057w
2. Kimmel DW, LeBlanc G, Meschievitz ME, Cliffel DE (2012) Electrochemical sensors and biosensors. Anal Chem 84:685–707. doi:10.1021/ac202878q
3. Paleček E, Bartošík M (2012) Electrochemistry of nucleic acids. Chem Rev 112:3427–3481. doi:10.1021/cr200303p
4. Marx KA (2003) Quartz crystal microbalance: a useful tool for studying thin polymer films and complex biomolecular systems at the solution-surface interface. Biomacromolecules 4:1099–1120. doi:10.1021/bm020116i
5. Homola J (2003) Present and future of surface plasmon resonance biosensors. Anal Bioanal Chem 377:528–539. doi:10.1007/s00216-003-2101-0
6. Homola J (2008) Surface plasmon resonance sensors for detection of chemical and biological species. Chem Rev 108:462–493. doi:10.1021/cr068107d
7. Scarano S, Ermini ML, Spiriti MM, Mascini M, Bogani P, Minunni M (2011) Simultaneous detection of transgenic DNA by surface plasmon resonance imaging with potential application to gene doping detection. Anal Chem 83:6245–6253. doi:10.1021/ac200877m
8. D'Agata R, Spoto G (2013) Surface plasmon resonance imaging for nucleic acid detection. Anal Bioanal Chem 405(2–3):573–584. doi:10.1007/s00216-012-6563-9
9. Sípová H, Homola J (2013) Surface plasmon resonance sensing of nucleic acids: a review. Anal Chim Acta 773:9–23. doi:10.1016/j.aca.2012.12.040.
10. Scarano S, Mascini M, Turner APF, Minunni M (2010) Surface plasmon resonance imaging for affinity-based biosensors. Biosens Bioelectron 25:957–966. doi:10.1016/j.bios.2009.08.039
11. Wang Z, Wilkop T, Han JH, Dong Y, Linman MJ, Cheng Q (2008) Development of air-stable, supported membrane arrays with photolithography for study of phosphoinositide-protein interactions using surface plasmon resonance imaging (2008). Anal Chem 80:6397–6404. doi:10.1021/ac800845w
12. Zhou WJ, Chen Y, Corn RM (2011) Ultrasensitive microarray detection of short RNA sequences with enzymatically modified nanoparticles and SPR imaging measurements. Anal Chem 83:3897–3902. doi:10.1021/ac200422u
13. Lee HJ, Wark AW, Corn RM (2006) Creating advanced multifunctional biosensors with surface enzymatic transformations. Langmuir 22:5241–5250. doi:10.1021/la060223o
14. Manera MG, Spadavecchia J, Tautino A, Rella A (2010) Colloidal Au-enhanced surface plasmon resonance imaging: application in a DNA hybridization process. J Opt 12(3):035003. doi:10.1088/2040-8978/12/3/035003
15. Chen H, Liu F, Koh K, Lee J, Ye Z, Yin T, Sun L (2013) Sensitive detection of tuberculosis using nanoparticle-enhanced surface plasmon resonance. Microchim Acta. doi:10.1007/s00604-013-0943-5
16. Spadavecchia J, Barras A, Lyskawa J, Woisel P, Laure W, Pradier CM, Boukherroub R, Szunerits S (2013) A novel approach for plasmonic based DNA sensing: amplification of the wavelength shift and simultaneous detection of the plasmon modes of gold nanostructures. Anal Chem 85(6):3288–3296. doi:10.1021/ac3036316
17. Zanoli LM, D'Agata R, Spoto G (2011) Functionalized gold nanoparticles for ultrasensitive DNA detection. Anal Bioanal Chem 402:1759–1771. doi:10.1007/s00216-011-5318-3
18. Rosi NL, Mirkin CA (2005) Nanostructures in biodiagnostics. Chem Rev 105:1547–1562. doi:10.1021/cr030067f
19. Sassolas A, Leca-Bouvier BD, Blum LJ (2008) DNA biosensors and microarrays. Chem Rev 108:109–139. doi:10.1021/cr0684467
20. Cosnier S, Mailley P (2008) Recent advances in DNA sensors. Analyst 133:984–991. doi:10.1039/b803083a
21. Song S, Qin Y, He Y, Huang Q, Fan C, Chen HY (2010) Functional nanoprobes for ultrasensitive detection of biomolecules. Chem Soc Rev 39:4234–4243. doi:10.1039/C000682N
22. Teles FRR, Fonseca LP (2008) Trends in DNA biosensors. Talanta 77:606–623. doi:10.1016/j.talanta.2008.07.024
23. Malic L, Sandros MG, Tabrizian M (2011) Designed biointerface using near-infrared quantum dots for ultrasensitive surface plasmon resonance imaging biosensors. Anal Chem 83:5222–5229. doi:10.1021/ac200465m
24. Spoto G, Minunni M (2012) Surface plasmon resonance imaging: what next? J Phys Chem Lett 3:2682–2691. doi:10.1021/jz301053n
25. D'Agata R, Corradini R, Ferretti C, Zanoli L, Gatti M, Marchelli R, Spoto G (2010) Ultrasensitive detection of non-amplified genomic DNA by nanoparticle-enhanced surface plasmon resonance imaging. Biosens Bioelectron 25:2095–2100. doi:10.1016/j.bios.2010.02.008
26. D'Agata R, Breveglieri G, Zanoli LM, Borgatti M, Spoto G, Gambari R (2011) Direct detection of point mutations in nonamplified human genomic DNA. Anal Chem 83:8711–8717. doi:10.1021/ac2021932
27. Chen H, Lee J, Kang NL, Koh K, Lee J (2011) A surface plasmon resonance study on the optical properties of gold nanoparticles on thin gold films. Microchim Acta 172:489–494. doi:10.1007/s00604-011-0550-2
28. Wang J, Wang B, Bi J, Li K, Di J (2012) MDR1 gene C3435T polymorphism and cancer risk: a meta-analysis of 34 case–control studies. J Canc Res Clin Oncol 138:979–989. doi:10.1007/s00432-012-1171-9
29. Campa D, Sainz J, Pardini B, Vodickova L, Naccarati A, Rudolph A, Novotny J, Försti A, Buch S, von Schönfels W, Schafmayer C, Völzke H, Hoffmeister M, Frank B, Barale R, Hemminki K, Hampe J, Chang-Claude J, Brenner H, Vodicka P, Canzian F (2012) A comprehensive investigation on common polymorphisms in the MDR1/ABCB1 transporter gene and susceptibility to colorectal cancer. PLoS One 7(3):e32784. doi:10.1371/journal.pone.0032784
30. Sharma V, Kaul S, Al-Hazzani A, Prabha TS, Rao PPKM, Dadheech S, Jyothy A, Munshi AJ (2012) Association of C3435T multi drug resistance gene-1 polymorphism with aspirin resistance in ischemic stroke and its subtypes. Neurol Sci 315:72–76. doi:10.1016/j.jns.2011.11.027
31. Drain S, Flannely L, Drake MB, Kettle P, Orr N, Bjourson AJ, Catherwood MA, Alexander HD (2011) Multidrug resistance gene expression and ABCB1 SNPs in plasma cell myeloma. Leuk Res 35:1457–1463
32. Turkevich J, Stevenson PC, Hillier J (1951) A study of the nucleation and growth processes in the synthesis of colloidal gold. Disc Faraday Soc 11:55–75. doi:10.1039/DF9511100055
33. Rasch MR, Sokolov KV, Korgel BA (2009) Limitations on the optical tunability of small diameter gold nanoshells. Langmuir 25:11777–11785. doi:10.1021/la901249j
34. Aherne D, Ledwith DM, Gara M, Kelly JM (2008) Optical properties and growth aspects of silver nanoprisms produced by a highly reproducible and rapid synthesis at room temperature. Adv Funct Mater 18:2005–2016. doi:10.1002/adfm.200800233
35. Jung J, Na K, Lee J, Kim KW, Hyun J (2009) Enhanced surface plasmon resonance by Au nanoparticles immobilized on a dielectric SiO2 layer on a gold surface. Anal Chim Acta 651:91–97

Eur. Phys. J. E (2013) **36**: 48
DOI 10.1140/epje/i2013-13048-5

THE EUROPEAN PHYSICAL JOURNAL E

Regular Article

Structural modulation of the biological activity of gold nanoparticles functionalized with a carbonic anhydrase inhibitor

Francesca Bellissima, Fabrizio Carta, Alessio Innocenti, Andrea Scozzafava, Piero Baglioni, Claudiu T. Supuran, and Debora Berti[a]

Department of Chemistry and CSGI, University of Florence, Sesto Fiorentino, Florence, 50019 Italy

Received 24 September 2012 and Received in final form 31 January 2013
Published online: 17 May 2013 –

Abstract. Gold nanoparticles (AuNPs) have gained attention for their potential and application in different fields, *e.g.* nanomedicine. This study explores the surface functionalization of AuNP with inhibitors of carbonic anhydrases (CAs, EC 4.2.1.1). Some CA transmembrane isoforms have been recognized as therapeutic targets for the treatment of hypoxic tumors. Embedding a CA inhibitory function onto a nanosized unit has been proved to enable selective targeting of transmembrane isoforms. We report the preparation in aqueous media, the characterization and CA inhibition tests of AuNPs coated with a sulfonamide (SA) derivative, already known for its inhibitory activity toward CAs. The physico-chemical characterization of SA-coated AuNPs was performed with a combination of scattering and spectroscopic techniques. We detect a threshold effect of the SA concentration on the final hydrodynamic and core sizes of the capped nanoparticles and on their stability over aggregation. These modified nanoparticles were assayed for inhibition of some CA transmembrane isoforms (CA IX and XII) as well as of two cytosolic isoforms (CA I and II), and show interesting inhibitory efficiency in the submicromolar range and some selectivity for transmembrane isoforms.

List of abbreviations

AuNP:	gold nanoparticles
CA:	carbonic anhydrase
SA:	sulfonamide
CAI:	carbonic anhydrase inhibitor
DMSO:	dimethylsulfoxide
DLS:	dynamic light scattering
SAXS:	small angle X-ray scattering
ATR-FTIR:	attenuated total reflection Fourier-transformed infrared spectroscopy
Na_3Ct:	trisodium citrate dihydrate
ICP-AES:	inductively coupled plasma-atomic emission spectroscopy
TGA:	thermogravimetric analysis
SLD:	scattering length density
TEM:	transmission electron microscopy
SPR:	surface plasmon resonance
DLVO:	Derjaguin, Landau, Verwey, Overbeek

[a] e-mail: debora.berti@unifi.it

1 Introduction

Inorganic nanoparticles, such as gold nanoparticles (AuNPs) [1,2], find widespread application in a variety of different fields, spanning from chemistry, physics and electronics to biology, medicine, bioanalytic and materials science [3–5]. Their potential in the biomedical field has received growing attention over the past years, due to the unique electronic and optical properties together with simple available preparation methods, versatility for bioconjugation and biocompatibility. In order to obtain useful systems for biomedical applications, the possibility of engineering nanoparticles with the desired chemical function is gaining an ever-increasing relevance for targeted drug delivery or cancer diagnostic and therapy [6–12].

In this work we present the preparation and characterization of novel gold nanoparticles functionalized with a sulfonamide ligand that acts as inhibitor of carbonic anhydrase (CA).

Carbonic anhydrases are ubiquitous zinc enzymes that catalyze the simple physiological interconversion between carbon dioxide and bicarbonate ion [13]. Human CA IX is a transmembrane extracellular isoform, overexpressed in some cancer tissues, that could constitute a novel target for the anticancer therapy, being not found in appreciable amounts in healthy tissues [14]. This enzyme is a multidomain protein [15] with the CA subdomain sit-

uated outside the cell and possessing a very high CO_2 hydrase catalytic activity, making it a key player in the regulation of tumor *p*H [14–21]. CA IX expression is strongly increased in many types of solid tumors, such as gliomas/ependymomas, mesotheliomas, papillary/follicular carcinomas, as well as carcinomas of the bladder, uterine cervix, kidneys, esophagus, lungs, head and neck, breast, brain, vulva, and squamous/basal cell carcinomas, among others [14,22]. Furthermore, such hypoxic tumors do not generally respond to the classic chemo- and radiotherapy [14,22].

For these reasons, CA IX has recently been shown to be a target for imaging and treatment of hypoxic tumors. *In vivo* experiments showed that silencing of CA IX alone leads to a 40% reduction in xenograft tumor volume [21]. Silencing of both CA IX and CA XII gave an impressive 85% reduction of tumor growth. Thus, hypoxia-induced CA IX and CA XII are major tumor prosurvival *p*H-regulating enzymes, and their targeting (*i.e.*, inhibition) holds potential for the design of anticancer drugs with a novel mechanism of action. The *in vivo* proof of concept that sulfonamide CA IX inhibitors may indeed show antitumor effects, has been published by Neri's group [20].

The present study was inspired by a previous work by some of us [23] in which a selective CA IX inhibitor was developed, consisting of gold nanoparticles coated with a lipoic acid tailed sulfonamide (SA); sulfonamides were already tested to be CA-inhibitors (CAI). 3 nm AuNPs were synthesized [23], which showed excellent inhibitory activity against CA IX, and were less inhibitory against CA I and II. We thus decided to investigate in more details the design of nanoscale CAIs with controllable size and functionalization as compared to the NPs studied earlier, possibly with simpler and greener synthetic routes. Our main interest was to correlate the NPs properties with the enzyme inhibitory activity. In the earlier contribution [23], CAI coated nanoparticles were obtained by a single step reduction of chloroaurate with sodium borohydride in DMSO in the presence of the lipoic-acid–sulfonamide conjugate. The black precipitate formed was collected and dried to obtain a powdered material. Those nanoparticles showed excellent CA IX inhibitory properties and selectivity over the cytosolic isoforms.

Biomedical applications require a good dispersibility and stability in aqueous media with respect to aggregation of the particles, so that their chemico-physical characteristics are well defined, reproducible and correlated to their structural and functional properties.

Some research groups have reported about stable water re-dispersible AuNPs functionalized by thiolated poly(ethylene glycol) [24,25] or by thiolalkylated oligo (ethylene glycol) [26], but more often the redispersion of dry nanoparticles is a challenging task.

In order to devise alternative routes and prevent possible drawbacks related to redispersion of the powdered nanoparticles, we have extended the previous study focusing our attention towards a one-pot preparation of an aqueous dispersion of AuNPs coated with the CAI derivative, with the desired size and functional properties.

Wet synthesis methods for AuNPs [27] (either organic or water-based), involve nucleation and growth within confined nanoreactors, such as microemulsions [28], or in the presence of a stabilizer that can adsorb onto the nanoparticles [29,30] or covalently bind to their surface [31]. The stabilizer, through its solubility, steric or charge properties, controls the growth of the nanoparticles, prevents the clusters from aggregation and provides tailored properties through specific functional groups [32].

In the classic aqueous synthesis proposed by Turkevich more than fifty years ago (citrate method) [33], the nanoclusters are stabilized by a layer of citrate anions, which is generally exchanged with a suitable ligand for the final application of the dispersion; a post-synthetic step is then usually required. The common procedure to coat the nanoparticles with the desired functional moiety is called "ligand exchange" [34], and the original stabilizer shell is replaced, partially or completely, by another ligand with an end functional or coupling moiety. Usually, the ligands are anchored to AuNP through a thiol function, as this group shows the highest affinity for gold, that results in a strong Au-S bond [35].

Our synthetic strategy was a modification of the classic citrate method [33,36]. In the proposed approach, citrate is simultaneously the reducing agent of the gold salt and of the lipoic acid dithiolanic ring of the CAI. A similarly modified citrate method has been reported in order to obtain mercapto-stabilized gold nanoparticles [37].

We have studied the effect of the variation of the reagent ratios on the nanoparticles size and then we have further investigated the stability of the SA-capped nanoparticles at increasing salt concentrations, proving that SA initial concentration is directly related to the stability of the nanoparticles.

The structural characterization has been performed with a combination of scattering techniques, in order to analyze the particles in solution rather than in the dry state. Dynamic Light Scattering (DLS) was used to determine the hydrodynamic radius of the nanoparticles synthesized at variable SA concentrations, while Small Angle X-ray Scattering (SAXS) was used to characterize the gold core radius. The core size was also studied by UV-visibile measurements. Attenuated Total Reflection Fourier Transformed Infrared Spectroscopy (ATR-FTIR) was employed to confirm the immobilization of SA over the nanoparticles surface, and the surface charge was investigated measuring its ζ-potential.

We finally assayed SA-capped gold nanoparticles solutions as CA inhibitor using a Stopped Flow apparatus, and compared the results for CA I, CA II (cytosolic forms), CA IX and CA XII (transmembrane forms).

2 Experimental section

2.1 Materials

$HAuCl_4 \cdot 3H_2O$, (±)-α–lipoic acid, 4-aminoethylbenzene sulfonamide, DMA, EDCI HCl, DMAP, DMSO, ethanol, acetonitrile were purchased from Sigma-Aldrich. Celite

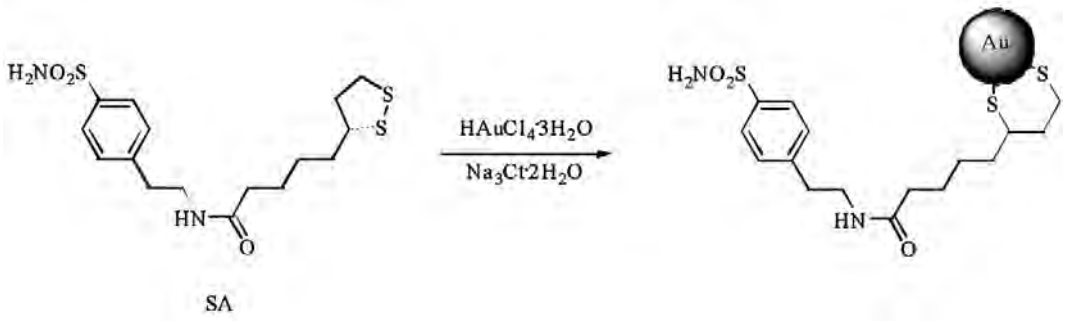

Scheme 1. Synthesis of colloidal solution of AuNP coated with sulfonamide CAI.

545® was supplied from Merk. Trisodium citrate dihydrate ($Na_3Ct \cdot 2H_2O$) and sodium chloride were provided from Fluka. All reagents were used as obtained. All glassware was cleaned prior to use with alcoholic potassium hydroxide. Water was purified with a Millipore system (resistivity 18 MΩ · cm).

All reactions involving air- or moisture-sensitive compounds were performed under a nitrogen atmosphere using dried glassware and syringes techniques to transfer solutions. Flash chromatography purifications were performed on Merck Silica gel 60 (230-400 mesh ASTM) as the stationary phase and eluting with 10% MeOH in DCM.

2.2 Synthesis

2.2.1 Sulfonamide synthesis

The lipoic acid tailed sulfonamide (SA) was synthesized according to the reported procedure [23]. In brief, to a solution of 300 mg of (±)-α–lipoic acid (1.5 mmol, 1 eq.) in 2.5 ml of anhydrous DMA 300 mg of 4-aminoethylbenzene sulfonamide (1.5 mmol, 1 eq.), 287 mg of EDCI (1.5 mmol, 1 eq.) and 183 mg of DMAP (1.5 mmol, 1 eq.) were added. The mixture was stirred under nitrogen atmosphere until the starting materials were consumed and then diluted with slush water (20 ml) and filtered on Celite 545® pad. The filtrate was extracted with ethyl acetate (3 × 20 ml) and the combined organic layers dried over Na_2SO_4, filtered and concentrated under vacuum to obtain a solid residue which was purified by silica gel column chromatography eluting with 10% MeOH in DCM.

2.2.2 Gold nanoparticles synthesis

Gold nanoparticles were prepared by a modified citrate-reduction method (Scheme 1).

To a boiling and refluxing solution of 19 ml of 0.63 mM tetrachloroauric acid in a 100 cm^3 round bottom flask was added a boiling solution of 0.5 ml of either 2.4 mM (Sample *0.06 mM SA*), 4.8 mM (Sample *0.12 mM SA*) or 9.6 mM (Sample *0.24 mM SA*) sulfonamide in methanol along with 0.5 ml aqueous solution of 91.2 mM trisodium citrate (Na_3Ct). The citrate-to-gold ratio was kept constant, while the molar concentration of sulfonamide was varied in order to understand the role of that parameter on the structural characteristics of the gold functionalized clusters (table 1). The resulting solutions were kept refluxing under vigorous stirring for 25 min.

These values (reported in table 1) refer to the samples most intensively characterized from a physico-chemical point of view and whose inhibitory activity toward the CA isoforms was tested. However, other reagents concentrations or reaction conditions were analyzed (see the Results and discussion section).

To purify the colloidal solutions from the free citrate excess, sulfonamide or unreduced chloroaurate ions, the samples were dialyzed (24 h, molecular weight cutoff of the dialysis membranes 12 kDa) and then ultrafiltered under vacuum with a Millipore Amicon apparatus (cell model 8003, Cat. No. 5125, Millipore corporation, membrane of regenerated cellulose, 10 kDa NMWL, Cat. No. 13612), halving twice the solution volume and then restoring the initial concentrations with MilliQ water. After the purification procedure, the *p*H of the solutions was 5.9.

The same procedure was employed to concentrate the dispersions, this time just halving their volume.

2.3 Techniques

2.3.1 Dynamic light scattering (DLS)

DLS experiments were carried out on a Brookhaven Instrument apparatus, New York, USA (BI 9000AT correlator card and BI 200 SM goniometer).

The signal was detected by an EMI 9863B/350 photomultiplier. The light source was the doubled frequency of a Coherent Innova diode pumped Nd:YAG laser, (λ = 532 nm, 20 mW). The laser long-term power stability was 0.5%. Self-beating detection was recorded using decahydronaphthalene (thermostated by a water circulating system) as index matching liquid. Measurements have been performed at 25 °C on 0.5 mL samples previously transferred into cylindrical Hellma scattering cells.

The time autocorrelation functions of the intensity of the scattered light were measured at 90°; the data are plotted in terms of $\beta^2 g_1(q,t)$ related to the normalized

intensity autocorrelation function through the Siegert relationship

$$g_2(q,t) = 1 + \beta^2 \left| g_1(q,t) \right|^2 , \quad (1)$$

where β is a spatial coherence factor dependent on the geometry of the detection system [38].

Data analysis has been performed according to standard procedures. In order to obtain a distribution $w(\Gamma)$ of decay rates, a constrained regularization method, CONTIN, developed by Provencher [39], was used to invert the experimental data. A statistical parameter "probability to reject", R, is calculated for each $w(\Gamma)$ generated by CONTIN. The preferred solution is usually the one characterized by the R value closest to 0.5.

The translational diffusion coefficients, D_t, have been determined from the decay rates, Γ, through the relation $\Gamma = D_t \cdot q^2$ which is valid for diffusive modes. The diffusion coefficients provide access to the hydrodynamic correlation lengths R_H for isotropic particles through the Stokes-Einstein relationship

$$D_t = \frac{k_B T}{6\pi\eta_S R_H} , \quad (2)$$

where η_S is the solvent viscosity and k_B the Boltzmann constant.

The AuNP dispersions were filtered through a 200 nm pore-size filter to avoid interference from dust.

2.3.2 Small Angle X-ray Scattering (SAXS)

SAXS measurements were carried out using two different instruments. The samples where no NaCl was added were analyzed with a HECUS SWAX apparatus (Kratky camera) equipped with a position-sensitive detector (OED 50 M) containing 1024 channels of width 54 μm. CuK_α radiation of wavelength 1.542 Å was produced by a X-ray generator (Seifert ID-3003), operating at a maximum power of 2 kW. A 10 μm thick nickel filter was used to remove CuK_β. The volume between the sample and the detector was kept under vacuum ($P < 1$ mBar) during measurements to minimize scattering from air. Samples were transferred into 1 mm quartz capillary and then sealed with an epoxide glue. Measurements were done at 25 °C and temperature was controlled by a Peltier element, with an accuracy of ±0.1 °C. All scattering curves were acquired between 0.01 and 0.5 Å^{-1} and the data were corrected for the solvent contribution and slit desmeared by a linear method.

SAXS measurements of the samples treated with NaCl were taken using a S3-MICRO SAXS/WAXS INSTRUMENT (HECUS GmbH, Graz, Austria), which consists of a GeniX microfocus X-ray sealed CuK_a source (Xenocs, Grenoble, France) power 50 W, which provides a detector focused X-ray beam with $k = 0.1542$ nm CuK_a line. The instrument is equipped with two one-dimensional (1D) position-sensitive detectors (HECUS 1DPSD- 50 M system); each detector is 50 mm long (spatial resolution 54 lm/channel, 1024 channels) and covers the SAXS Q-range ($0.003 < Q < 0.6$ Å^{-1}) and the WAXS Q-range ($1.2 < Q < 1.9$ Å^{-1}). The temperature was controlled by means of a Peltier TCCS-3 Hecus [38].

In SAXS experiments, the measured intensity of the radiation, $I(Q)$, scattered by a collection of uniform particle is given by [40]

$$I(Q) = A \cdot \phi \cdot P(Q) \cdot S(Q) + I_{\text{bkg}}, \quad (3)$$

where A is the amplitude accounting for the instrumental factors, ϕ is the particle volume fraction, $P(Q)$ is the particles form factor, $S(Q)$ is the interparticle structure factor accounting for the interparticle correlations, I_{bkg} is the incoherent background and Q is the scattering vector. Due to the dilution of the system, the influence of the interparticle structure factor can be neglected ($S(Q) \approx 1$).

The fitting model used for the analysis of the SAXS was based on the assumption of polydisperse spherical nanoparticles [39] with a core described by a Schultz distribution of radii and a constant scattering length density (SLD) [41–43]

$$f(R) = \left[\frac{z+1}{R_{\text{avg}}}\right]^{z+1} R^z \exp\left[-\frac{z+1}{R_{\text{avg}}}R\right] \frac{1}{\Gamma(z+1)} , \quad (4)$$

with R_{avg} being the mean sphere radius and z the parameter related to the width of the sistribution. In particular, the polidispersity index $\rho = \frac{\sigma_R}{R_{\text{avg}}}$ is related to z by means of the equation

$$\rho = \frac{1}{(z+1)^{1/2}} . \quad (5)$$

Because of the higher electronic density in the gold core with respect to the organic layer, no contribution of the shell has been taken into account in the fitting procedure (Scheme 2). The only variable parameters are the radius and its polidispersity, along with a pre-multiplicative factor.

2.3.3 UV-visible spectroscopy

The optical properties of the colloidal solutions were monitored on a Cary 100 Bio Varian. The samples were measured in a 1 cm Hellma quartz cuvette.

2.3.4 Inductively coupled plasma-optical emission spectrometry (ICP-OES)

A VARIAN 720 OES inductively coupled plasma optical emission spectrometer was used for the determination of gold and sulfur content (ppm) in the solution before and after purification procedure. The samples were diluted 20 times in nitric acid solution, pH = 1.5. Calibration curves of standard gold solutions were used. The ICP-AES was programmed to detect Au (208.207; 242.794; 267.594 nm) and to give the average value of the obtained results. An internal standard of Ge 1 ppm (209.426 nm) was used to correct from matrix effects.

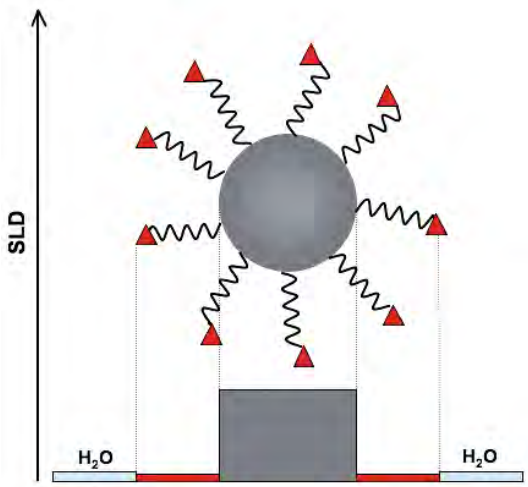

Scheme 2. Scattering length density (SLD) profiles of the functionalized gold nanoparticle. Au SLD is $1.23 \cdot 10^{-4}$ Å^{-2}, solvent (water) SLD is $9.46 \cdot 10^{-6}$ Å^{-2}, lipoic acid-tailed sulfonamide SLD is $8.56 \cdot 10^{-6}$ Å^{-2}.

2.3.5 ζ-potential

The ζ-potential of the samples was performed on a BI ZetaPlus, Zeta Potential Analyser (Brookhaven Instruments Corporation, Holtsville, NY). Zeta potentials (ζ) were obtained from the electrophoretic mobility (u) using the Helmholtz-Smoluchowski equation

$$\zeta = \frac{\eta}{\varepsilon} u, \tag{6}$$

with η being the viscosity of the medium and ε the dielectric permittivity of the dispersing medium. This equation is valid in the limit $\kappa \cdot R \gg 1$, with κ^{-1} the Debye length and R_h the hydrodynamic radius of the particles. These assumption was validated using R_h from DLS measurements and κ from the relation $\kappa^{-1} = (\varepsilon K_B T)^{1/2} (2e^2 I N_A)^{-1/2}$, with K_B the Boltzmann constant, e the electron charge, I the ionic strength and N_A the Avogadro constant [38,44].

2.3.6 TGA

Thermogravimetric analysis (TGA) profiles of $\sim$ 0.5 mg of accurately weighted sulfonamide or citrate-capped gold nanoparticles powders were recorded on a SDT Q600 apparatus (TA instrument, Milan, Italy) between 25 and 450 °C, with a rate of 10 °C/min and under nitrogen flux (100 ml/min). Nanoparticle powders were obtained by freeze-drying the solutions that were first dialyzed for 24 h against MilliQ water and then concentrated by Amicon Millipore apparatus.

2.3.7 ATR-FTIR

Fourier-transformed infrared spectra were collected operating in attenuated total reflectance mode with a Nexus 870 spectrophotometer (Thermo Nicolet, Paris) equipped with a MCT-A detector. Spectra were obtained with 32 scans at 4 cm^{-1} resolution. Gold nanoparticles solutions were dialyzed for 24 h against MilliQ water, to eliminate the excess of reagents, concentrated and then freeze-dried to obtain a solid residue.

2.3.8 CA inhibition assay

A SX.18MV-R Applied Photophysics stopped-flow instrument was used for assaying the CA catalysed CO_2 hydration activity. 0.2 mM Phenol Red was used as indicator (pH 6.8–8.4), working at the absorbance maximum of 557 nm. During the tests, a saturated CO_2 solution (17 mM at 20 °C) was used.

Stock solutions of the enzyme (1 μM for CA I and CA II, 0.1 μM for CA IX and CA XII) were prepared in MilliQ water. Stock solutions of the inhibitor (gold concentration in the range 10^{-4}–10^{-8} M) were prepared in buffer (HEPES 0.01 M, Trizma Hydrochloride 0.01 M, Na_2SO_4 0.1 M, pH 7.5). Inhibitor (CAI) and enzyme (E) solutions were preincubated together for 2 h prior to assay, in order to allow the formation of the E–CAI complex [45]. K_I's were calculated by the Prusoff-Cheng equation as reported earlier [23].

3 Results and discussion

3.1 SA-coated gold nanoparticles

The preparation and characterization of CAI-coated gold nanoparticles is performed with a one-pot reaction, adapted from the Turkevich-Frens method [33,36], where citrate acts as the reducing agent of both the noble cation and of the precursor of the capping molecule. We also tested an alternative route consisting in a post-synthetic ligand exchange on the previously formed citrate gold nanoclusters, but, as the agent (SA) was added to the otherwise stable nanoparticles dispersion, extended aggregation and precipitation invariably occurred.

Several Au^{3+}/SA ratios have been tested, while the reducing agent concentration was held constant (table 1).

During the course of the reaction, the solution color varied differently depending on the amount of SA. The sample *0.06 mM SA* turned dark grey 1 min after the addition of the reducing agent and then turned to dark red; the sample *0.12 mM SA* turned to dark violet (after $\sim$ 4 min) and ruby red afterwards; the sample *0.24 mM SA* turned to a pale pink solution (after $\sim$ 10 min) that got lightly stronger with time, but never ruby red; the sample without SA turned immediately grey with a powder-like appearance, and within 4 min it assumed a ruby red color [46].

After 25 min refluxing, the solutions were allowed to cool at room temperature and purified from excess free citrate, sulfonamide or unreduced chloroaurate ions (see the Experimental section). The colloidal dispersions of nanoparticles were then stable for several months (fig. 1).

Table 1. Concentration (mM) of the reagents in the reaction mixture. The molar ratio between citrate and gold cations is held fixed at 3.8.

Sample [SA]	$[Au^{3+}]$	$[Na_3Ct]$	[SA]	$[Au^{3+}]/[SA]$
0.06	0.6	2.28	0.06	10
0.12	0.6	2.28	0.12	5
0.24	0.6	2.28	0.24	2.5
Without SA	0.6	2.28	/	/

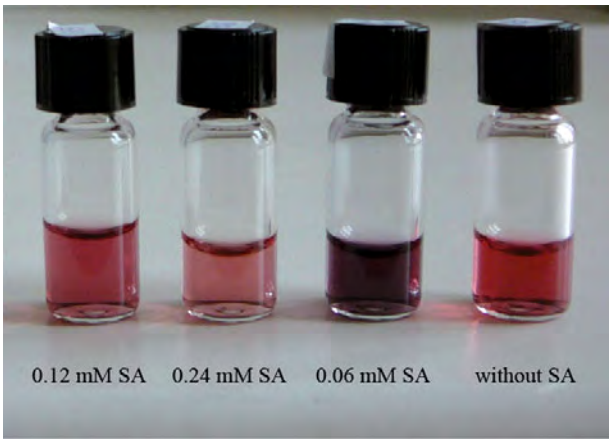

Fig. 1. Photograph of the colloidal dispersions prepared by adding different mole fractions of sulfonamide capping agent (SA).

From ICP-OES measurements we detected a loss of gold around 10% resulting from the purification procedure, while if the reaction mixture was allowed to reach room temperature just after the color change, the gold loss ranged between 14 and 25%, depending on the sample. Therefore, keeping the solutions to reflux for 25 min after the color change gave a higher and reproducible yield in nanoparticles.

In order to have a more direct proof of the successful conjugation of SA to gold nanoparticles, an ATR-FTIR analysis was conducted (fig. 2).

The bands at 1334 and 1157 cm^{-1} are respectively indicative of asymmetric and symmetric S–O stretching vibrations [13]. The very sharp peaks at 1623 and 1542 cm^{-1} in the neat sulfonamide spectrum are respectively characteristic of C=O stretching from the amide group and of the aromatic ring [47]. These same peaks appear as shoulders in the band centered at 1590 cm^{-1} in the SA functionalized nanoparticles. The peaks at 1080 and 1035 cm^{-1} are indicative of the lipoic acid tailed sulfonamide, being also present in the neat SA spectrum. The peak at 1590 cm^{-1}, without any shoulder, is indicative of the C=O vibrations of the citrate. The band at 1713 cm^{-1} can be assigned to a C=O stretching vibration of citric acid [48]. The *p*H of the nanoparticles dispersions is in fact 5.9 and the pKa_3 for citric acid is 6.4. This means that in these solutions citrate is only dibasic and that we can thus detect the shifted signal of

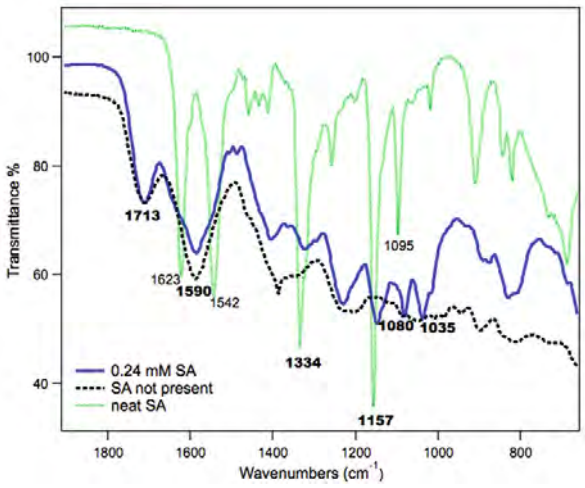

Fig. 2. ATR-FTIR spectra of the sulfonamide-capped nanoparticles (0.24 mM SA), of the citrate-stabilized nanoparticles (SA not present) and of neat SA. Spectra were recorded on powdered samples.

the residual protonated carboxylic group of the molecule. Furthermore, these results confirm that the nanoparticles are not completely saturated with the new ligand molecule, but that some residual citrate co-covers their surface, helping to stabilize the nanoparticles themselves.

The surface coverage (γ) of the nanoparticles by SA has been established through a thermogravimetric analysis (TGA). The weight loss has been monitored as a function of temperature, from room conditions up to 450 °C. The sulfonamide derivative thermally decomposes at high temperatures; first the amide bond breaks releasing the molecular portion not anchored to the gold surface, then the lipoic acid linker decomposes. However, several factors limit the reliability of such measurements, as a comparison with the behavior of the neat SA highlights: at the maximum temperature, only 74% (w/w) of SA is decomposed. Moreover, the simultaneous decomposition of citrate alters the final weight losses. From an approximate calculation, the weight loss of adsorbed sulfonamide in sample *0.24 mM SA* is 12.6%. From that weight loss it was determined $\gamma \cong 0.1$ (eq. (7)), so that the gold surface atoms-to-SA ratio is in the range 9-10 [49]

$$\chi_{\text{organic}} = [4\pi(R_{\text{core}} - R_{\text{Au}})^2(\rho_{\text{HCP}})(MW_{\text{SA}})\gamma]/ [4\pi(R_{\text{core}} - R_{\text{Au}})^2(\rho_{\text{HCP}})(MW_{\text{SA}})\gamma + 4/3\pi R^3_{\text{core}}(\rho_{\text{Au}})(AW_{\text{Au}})], \quad (7)$$

where χ_{organic} is the mass fraction of sulfonamide ligand in the cluster, R_{Au} the crystallographic radius of a gold atom (0.145 nm), R_{core} the core radius of the nanoparticles (from SAXS results), ρ_{HCP} the number density of surface atoms (13.89 atoms/nm^2, assuming hexagonal cd-lose packing), MW_{SA} the sulfonamide ligand molecular weight, γ the coverage (SA-to-surface Au atoms ratio), ρ_{Au} the atom density of bulk gold (58.01 atoms/nm^2) and AW_{Au} the gold atomic weight. However, the extent of the approximations does not allow to find a trend in the de-

gree of functionalization when SA/Au ratio is varied. For these reasons, the values from TGA should be regarde as purely indicative.

3.2 Characterization of AuNPs at different SA concentrations

It is well established that particle size, shape and stability display a strong dependence on the concentration of the precursors, their rate and order of addition as well as the stirring over the reaction course [36]. In our case, if the citrate-to-gold ratio is set at 15.0 (instead of 3.8) precipitation readily occurs. Conversely, when sulfonamide is present even in modest percentages (citrate-to-SA ratio set at 130) the resulting solution presents extended aggregation but no precipitation. This is an indication that SA effectively binds to gold surface even in the presence of a large citrate excess, and plays a central role in stabilizing the nanoparticles preventing them from major aggregation.

All the samples described within this paper are referred to an initial concentration of 0.6 mM gold salt and to a citrate-to-gold ratio set at 3.8 (table 1), unless otherwise stated; these conditions result in the lowest particle size and better stability of citrate stabilized nanoparticles [29,50], in the absence of SA. To assess the effect of the ligand presence on the size and functional properties of the nanoparticles, we have varied the initial concentration of the SA ligand precursor (table 1).

As already mentioned, Na_3Ct simultaneously reduces the gold salt and the ligand precursor. Following the reduction step, one can expect a competition between citrate physisorption and SA binding to the nanoparticle core. The resulting size and degree of functionalization will be the result of these events.

Dynamic light scattering (DLS) is the technique of choice to determine the hydrodynamic radius of the nanoparticles, that is the radius of the sphere with an identical diffusion coefficient as the scattering objects. In our case, assuming a globular metallic core and a radially isotropic distribution of the coating layer, we detect the characteristic size of the core plus the ligand shell with bound ions and the hydration sphere.

Figure 3 shows the autocorrelation function decays of the scattering intensity of the colloidal solutions for different SA concentrations; the decays are directly connected to the center-of-mass diffusion of the nanoparticles. For the highest SA mole fraction, the autocorrelation function is characterized by the slowest decay rate, while faster decay times are detected in presence of lower amounts of SA (very slight differences are appreciable between *0.06 mM* and *0.12 mM SA*). The fastest overall decay is obtained when SA is not present in the reaction mixture.

The distribution of decay rates obtained from the Laplace inversion method CONTIN (see the Experimental Section) yields a hydrodynamic radii distribution centered at 14 nm for the nanoparticles synthesized without SA, at 20–25 nm for the colloidal solutions *0.06 mM SA* and *0.12 mM SA* and 31 nm for *0.24 mM SA*; these hydrodynamic

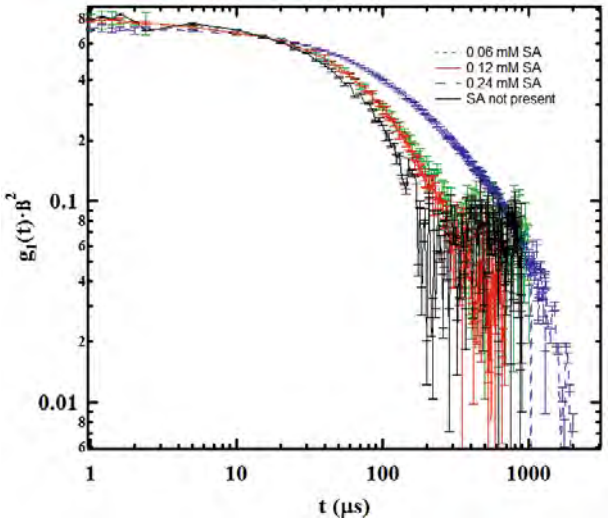

Fig. 3. DLS curves obtained for AuNP dispersions as a function of different initial SA concentrations in the reaction mixture, while keeping constant all the other parameters. The error bars indicate the variance over five different measurements.

radii are composed of the core radius and the length of the organic shell.

The resulting size of the citrate-coated nanoparticles, *i.e.* the reference sample, is in agreement with the data reported in the literature for similar reaction conditions [29].

The presence of the functional organic ligand generally increases the hydrodynamic sizes, and among SA containing samples, we observed a threshold effect for the particles size that depends on the SA concentration. The trend in the hydrodynamic radii can imply a higher degree of functionalization in the presence of increasing amounts of organic ligand, which is bulkier than citrate anions. Moreover, corresponding to *0.24 mM SA* concentration, a closer packing of the chemisorbed units onto the gold nanoparticles surface can alter the ligand conformation and the hydrodynamic thickness around the metallic core, the hydrodynamic shell being composed not only by SA or citrate but also by the dispersing solvent (water).

Appreciable deviations from the previously determined hydrodynamic sizes cannot be found with modest variation of both the initial concentration of citrate and the Au/SA ratio (fig. 4). This implies that in our experimental conditions the main structural parameter in determining the final size of the nanoparticles is the Au/SA ratio. Moreover, this finding points out that the proposed synthetic procedure is not affected by minor variations of the initial reagents concentrations up to a threshold value. This experimental reproducibility and tunability is of outmost importance for the correlation of the targeting and inhibition efficiency with structural parameters.

However, DLS is not suited to distinguish between the contribution of the Au core and of the organic shell and, based on these data, we cannot exclude that different SA amounts can determine different growth pathways for gold nuclei.

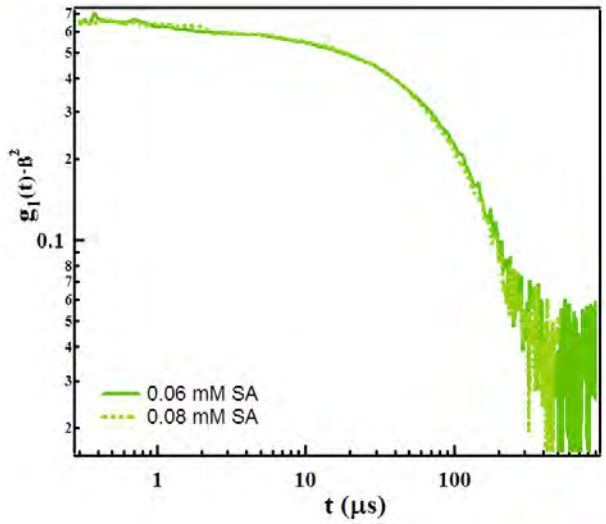

Fig. 4. DLS curves of nanoparticles solutions prepared with different initial reagent conditions. Sample *0.06 mM SA*: 0.6 mM Au^{3+}, 2.28 mM Na_3Ct, 0.06 mM SA. Sample *0.08 mM SA*: 0.6 mM Au^{3+}, 1.92 mM Na_3Ct, 0.08 mM SA.

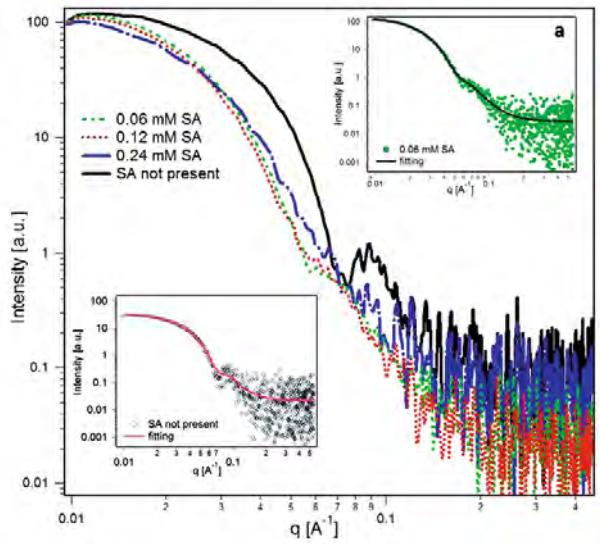

Fig. 5. SAXS curves of the AuNPs capped with different amounts of sulfonamide (*0.06, 0.12, 0.24 mM SA*) and of citrate-stabilized AuNPs (*SA not present*). a) Schultz fit of the scattering intensity of a functionalized sample (*0.06 mM SA*) b) Schultz fit of the scattering intensity of the citrate-stabilized nanoparticles. The data have been arbitrarily normalized to 100 for the $q \to 0$ limit. The fitting parameters are the NP mean radius and the polydispersity index while the SLD for the core and the shell were held constant.

In order to determine the size of the metal core of the nanoparticles, we performed Small Angle X-Ray scattering (fig. 5). SAXS is a powerful tool to investigate functionalized AuNP core size because, as we indicated in the Experimental section (Scheme 2), gold nanoparticles have in fact favourable scattering length density profile, since all the scattering intensity can be assumed to be due to the gold core.

SAXS is preferred to Transmission Electron Microscopy (TEM) because it provides the dimensions of the particles in solution and a better statistic over the whole sample, while TEM gives information on the sizes of the dried specimens and may therefore introduce artifacts on the evaluation of real sizes.

The experimental data have been fitted with a model of polydisperse spheres with a Schultz distribution of the radii and constant SLDs. The agreement between experimental and calculated curves is good, as shown in fig. 5. A definite trend emerges from SAXS results: nanoparticles having citrate physisorbed on their surface have a smaller core size (radius = 5.7 nm) and a smaller polydispersity ($\sim$ 16%) than the nanoparticles that have SA adsorbed on the surface. SAXS data also show that the variation of the amount of sulfonamide from *0.06 mM* to *0.12 mM* does not affect appreciably neither the core size of SA coated AuNPs (7.5 nm) nor their polydispersity ($\sim$ 20%). Conversely, at *0.24 mM* SA concentration the coated nanoparticles have smaller radius (6.3 nm) and larger polydispersity (29%).

Comparing SAXS results with the DLS data, it is clear that for the lowest SA concentrations both the metallic cores and the shells are identical in size, while in the *0.24 mM* sample the higher hydrodynamic size can be entirely attributed to the ligand shell, as the gold core is smaller. The presence of SA increases the width of the size distribution, which might indicate a shift from a diffusion-controlled growth to a surface-controlled growth process for the nanoparticles, which generally results in higher polydispersity [51,52].

These results are partially unexpected, since one could suppose that the core radius would be larger in the absence of the SA capping agent, which should in principle inhibit particle growth while promoting an enlargement of the size distribution. The SA precursor, reduced by citrate, was in fact supposed to chemically bind to the particle in the early stages of its growth, thus stabilizing and inhibiting the cluster from increasing in size [53,54]. In line with this argument, the highest is the concentration of the organic ligand in the reaction mixture the smaller is the core radius of the particles.

The experimental data prove that this hypothesis is in our case wrong, and that some other mechanisms should prevail in the synthetic step since the core of the citrate-stabilized particles is smaller than the sulfonamide-capped core. However, the sulfonamide amount in the reaction plays a critical role in the size of the core when it reaches a specific concentration. At *0.24 mM SA*, the core size is smaller than at *0.06* and *0.12 mM SA* and, as seen from DLS results, the shell thickness around the core is larger.

On the basis of these results we can suppose that, in a first stage, gold reduction leads to NPs stabilized both by citrate and SA. When the organic ligand is also present, gold nanoparticles can grow further up to a SA threshold concentration. This would explain the fact that citrate stabilized nanoparticles are smaller and less polydisperse than the sulfonamide stabilized ones; this hypothesis needs corroboration from a kinetic study aimed at distin-

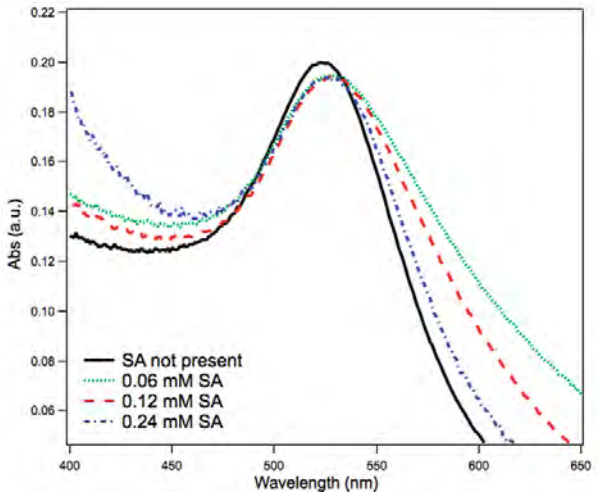

Fig. 6. Absorbance spectra of all the samples in the visible region.

guishing the different stages, possibly performed with a reducing agent different from citrate, which also acts as stabilizer.

The SAXS data suggest that in the case of *0.06 mM SA* and *0.12 mM SA* the ligand concentration could be below the threshold concentration, where the core size starts to be affected in terms of growth inhibition.

In order to have a different and complementary insight on the metal core, we have performed an UV-Visible spectrophotometric analysis. That technique is widely used since the absorption bands wavelengths are related to the diameter of the metal cluster. At nanometer length scales, the conducting electrons (plasma) are characterized by a collective oscillation frequency known as Surface Plasmon Resonance frequency (SPR). The nanoparticles absorption stems from the coherent plasma oscillations induced by the interaction with a resonating electromagnetic radiation [55,56].

The position of that absorption band is affected by many different factors, such as size of the metal core, dielectric properties of the medium, interactions on the particle surface, surface charge, functionalization, aggregation degree or interparticle distance [57]. We are therefore not interested in deriving quantitative values of the core radii from these kinds of measurements but only to make some comparative considerations. Figure 6 shows the UV-visible spectra of the nanoparticles colloidal solutions prepared with different amounts of sulfonamide. All samples show an absorption peak around 520-530 nm, which is typical of gold SPR band [50].

The SPR absorbance peak of the citrate-stabilized nanoparticles is at 523 nm. When SA is present in the reaction mixture the plasmon absorption band red-shifts to 527 nm, regardless of the amount of SA introduced, and the width of the band increases, due to alteration of the local dielctric constant around the particle and to the presence of adsorbate material which can give rise to so-called chemical interface damping [55].

In this size range, a red-shift of the SPR is a consequence of an increase in the radius size [55]. From these measurements we do not appreciate the smaller core size of the *0.24 mM SA* sample with respect to the *0.06* and *0.24 mM SA* samples because the absorption band is affected by other factors. Even if no quantitative data about the size of the NP can be derived form these measurements, UV spectra support the previous SAXS finding that the reaction performed without introducing the organic ligand in the mixture leads to smaller clusters than in presence of SA.

To obtain some information on the AuNP surface charge, we have performed ζ-potential measurements. The particles exhibit largely negative potentials (ζ-potential -45 and -60 mV), as both the ligand [58] and the citrate are negatively charged at *p*H 5.9. It is not possible to see a definite trend in the surface charge when the sulfonamide concentration is increased, as the differences between the samples lie in the experimental uncertaintity. Therefore, these results account for the high stability of the dispersions with respect to aggregation; the repulsive Coulombian interaction between the ligand coatings makes them stable for months.

It is important to stress that an overall negative surface charge is a prerequisite for the nanostructured CA inhibitor to interact with its enzymatic target [13].

To monitor the extent of such electrostatic stabilization, even in connection to the degree of functionalization, we have gradually increased the solution ionic strength, to overcome the repulsion barrier that ultimately prevents the approach corresponding to the attractive well which would cause irreversible agglomeration [59], as the classical DLVO theory predicts. This stability toward aggregation is a fundamental property of AuNP dispersions in perspective of their applicative potential. CAI-capped nanoparticles would in fact be used in physiological conditions, where they would be subject to a relevant saline concentration for which a structural study in neat water might underestimate the extent of aggregation.

In order to detect a critical salt molar concentration above which an alteration in the structural characteristics of the nanoparticles occur, we have added increasing amounts of sodium chloride to the as-prepared solutions and monitored the change of their properties by DLS, SAXS and UV-Visible spectrophotometry.

Figure 7 shows the decay of autocorrelation functions of the nanoparticle solutions at different NaCl concentrations. From the Laplace inversion of the experimental data by a CONTIN algorithm, it results that the sample *0.06 mM SA* doubles its hydrodynamic radius when salt concentration reaches 30–40 mM; the sample *0.12 mM SA* doubles its size at 40 mM NaCl; the sample *0.24 mM SA* needs 70 mM NaCl to halve its diffusion coefficient.

Both *0.06 mM SA* and *0.12 mM SA* samples present precipitation at 85 mM salt concentration. This is not the case for the *0.24 mM SA* solution (precipitation is evident at 110 mM NaCl). Conversely, adding sodium chloride to the solution of nanoparticles only stabilized by citrate results in prompt precipitation already at 10 mM

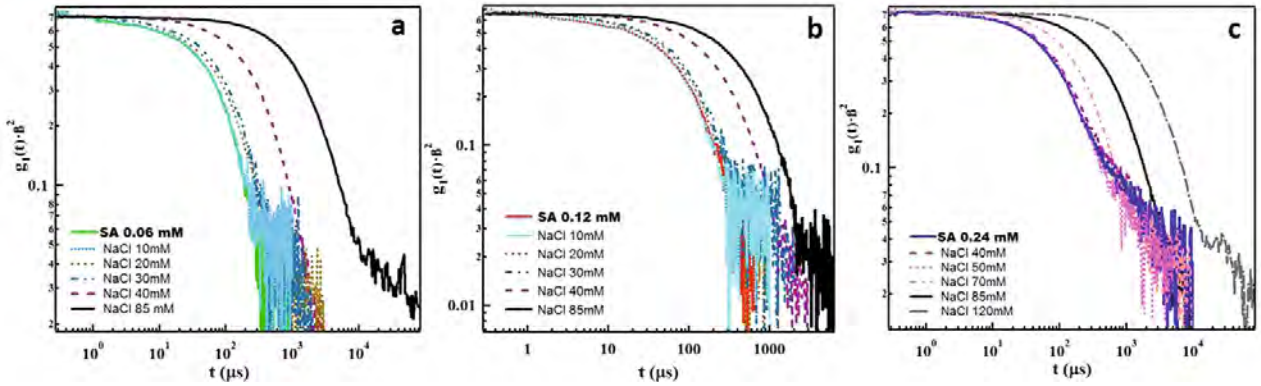

Fig. 7. Autocorrelation function profiles for samples *0.06 mM SA* (a), *0.12 mM SA* (b) and *0.24 mM SA* (c) as a function of NaCl concentration in solution.

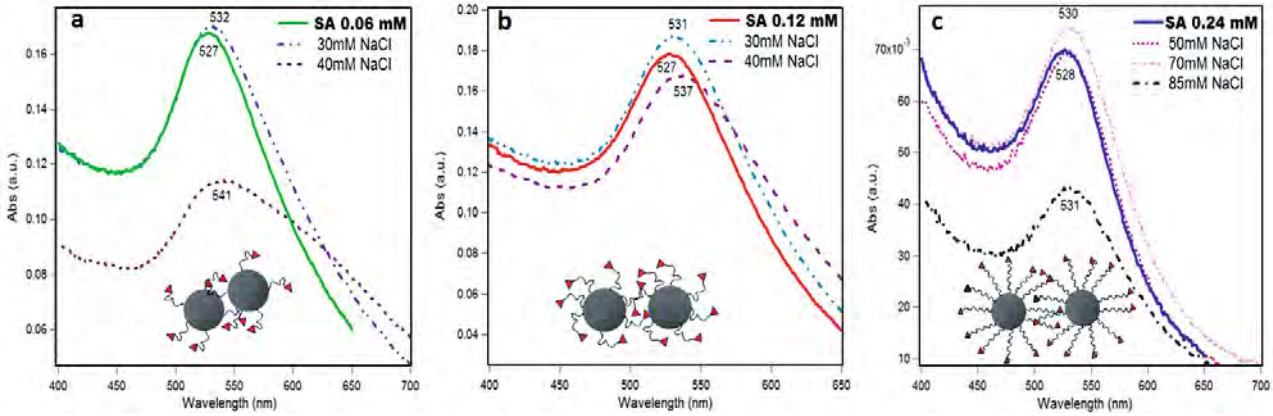

Fig. 8. UV-visible spectra of the sulfonamide-capped nanoparticles (a: *0.06 mM SA*, b: *0.12 mM SA* and c: *0.24 mM SA*) at different NaCl concentrations in solution. The cartoons schematically show all the results obtained from the different experiments, also including the hypothesized contact interaction between two primary nanoparticles as a function of their degree of functionalization.

salt concentration. The onset of precipitation at such low NaCl concentration in the non-modified nanoparticles is really informative about the fact that the SA presence results in a more efficient stabilization of the particles themselves. The same conclusion can be indirectly reached from careful observation of the behavior during the purification steps after the particles synthesis. The particles stabilized only by citrate physisorption on their surfaces cannot be purified with the Amicon Millipore apparatus, as precipitation readily occurs.

These DLS data are very interesting because the correlation with the sulfonamide content is straightforward: the sample where SA is not present is the most instable to the increase of the ionic strength, and among the SA-stabilized nanoparticles, the higher the mole ratio, the higher the ionic strength required to double the hydrodynamic size. In other words, the more SA is present, the more protected are the coated nanoparticles from aggregation and precipitation. Moreover, these results are perfectly in agreement with DLS data of the as-prepared solutions, as it is confirmed that sample *0.24 mM SA* (whose hydrodynamic radius is the largest) is the most functionalized, hence stabilized, sample.

Figure 8 shows the UV-visible spectra recorded at representative salt concentration for each sample, *i.e.* around the value when the detected hydrodynamic radius is doubled with respect to the as-prepared samples. We do notice a red shift in the plasmon band of the solutions, indicative of a contact aggregation of the primary particles. This shift is particularly evident for the sample *0.06 mM SA*, while is difficultly detectable for the *0.24 mM SA* sample. Again, this finding can be a direct consequence of the samples different degrees of functionalization, which in the case of *0.24 mM SA* might be too high to allow the particles to approach at the interaction distance (see the inset cartoons in fig. 8).

SAXS measurements confirm that in presence of NaCl a contact aggregation occurs, since the scattering intensity profiles differ in the low-q part and superimpose for high-q values, where the structure of the primary particles determines the scattering pattern (fig. 9).

To summarize, the ensemble of the experimental results gathered is consistent with the conclusion that the functionalized gold nanoparticles have two different core sizes in dependence on the concentration of the organic ligand: its presence produces larger particle cores with re-

Table 2. CA inhibition data (K_I values, μM) of the nanoparticles toward different CA isoforms: CA I, CA II (cytosolic isoforms) and CA IX, CA XII (transmembrane isoforms). The inhibition assay was performed at different concentration of SA without any addition of NaCl. K_I's were calculated as reported earlier [23].

	K_I (μM)			
Sample [SA]	hCA I	hCA II	hCA IX	hCA XII
0.06	$0.16 \pm 5\%$	$0.17 \pm 3\%$	$0.08 \pm 4\%$	$0.04 \pm 7\%$
0.12	$0.17 \pm 8\%$	$0.25 \pm 6\%$	$0.04 \pm 5\%$	$0.03 \pm 4\%$
0.24	$0.24 \pm 8\%$	$0.18 \pm 8\%$	$0.02 \pm 7\%$	$0.13 \pm 7\%$
SA [23]	0.21	0.23	0.04	/
AuNP 3 nm [23]	32	31.6	29.5	/

Table 3. CA inhibition data (K_I values, μM) of the nanoparticles toward different CA isoforms: CA I, CA II (cytosolic isoforms) and CA IX, CA XII (transmembrane isoforms). The inhibition assay was performed at different concentration of SA in presence of the corresponding subcritical amount of NaCl. K_I's were calculated as reported earlier [23].

	K_I (μM)			
Sample [SA]–[NaCl]	hCA I	hCA II	hCA IX	hCA XII
0.06–40 mM	$0.16 \pm 4\%$	$0.21 \pm 6\%$	$0.25 \pm 6\%$	$0.04 \pm 5\%$
0.12–40 mM	$0.43 \pm 5\%$	$0.22 \pm 4\%$	$0.07 \pm 5\%$	$0.14 \pm 6\%$
0.24–70 mM	$0.07 \pm 7\%$	$0.14 \pm 8\%$	$0.02 \pm 5\%$	$0.13 \pm 8\%$

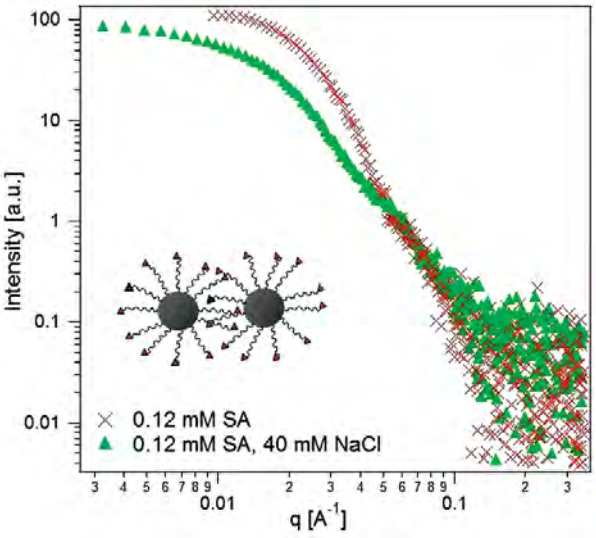

Fig. 9. SAXS curves of sample *0.12 mM SA* in the presence or not of NaCl (40 mM). The inset cartoon schematically represents the contact aggregation between two primary particles. The data have been arbitrarily normalized to 100 for the $q \to 0$ limit. The low-q cutoffs of the two curves are different, because the spectra have been collected with two different instruments (see Experimental section).

spect to the citrate-only case, but, once above a threshold amount lying between *0.12 mM* and *0.24 mM*, the core size starts to decrease.

Furthermore, these nanoparticles have different hydrodynamic sizes in dependence on their degree of functionalization. AuNP with the smallest core radii have the largest hydrodynamic radius (*0.24 mM SA*) and this is not due to increased hydration or citrate effects, but is rather ascribable to a closer layer of strongly bound ligand on gold surface.

Finally, the degree of surface modification also correlates with the stability of the nanoparticles over aggregation, as the sample with the thickest layer of the organic ligand is the most stable when the ionic strength of the dispersion is increased.

3.3 Inhibition tests

Stopped-flow measurements were performed in order to assay the inhibitory activity of the functional nanoparticles toward different CA isoforms, such as CA I, II, IX and XII, all of which are drug targets or off-targets [13, 14]. The initial rates of the CA-catalyzed interconversion between CO_2 and HCO_3^- were monitored following pH change, which leads to a variation of the absorption spectrum ($\lambda_{max} = 557$ nm) of an acid-base indicator (Phenol red) [45]. The final results are the IC_{50} values (molarity of inhibitor producing a 50% decrease of the enzyme activity), expressed as K_I (as reported earlier [23]) and summarized in table 2 and table 3, respectively for the case in which no NaCl or subcritical amount of NaCl was added. These data are referred to the overall gold concentration; gold nanoparticles concentration is $\sim 10^5$ times lower than the gold one, since the aggregation number is typically around 10^5, as estimated from the density of gold (19.3 g cm^{-3}), with the crude assumption that all particles are spherical with a diameter of 14.8 nm (from SAXS measurements) and using the gold concentration resulting from the ICP-AES analysis [60,61].

These results suggest that the proposed one-pot synthetic procedure leads to CAI-capped nanoparticles that

retain the SA high efficiency toward enzyme inhibition, in the nanomolar range, even at high ionic strength (table 3). In particular, the samples appear to be effective CA IX and CA XII inhibitors (K_I's $\sim 0.05\,\mu$M) and moderate CA I and CA II inhibitors (K_I's $\sim 0.20\,\mu$M), in similar way to what already assayed in a previous work [23]. Comparing these data to the ones obtained from 3 nm pristine nanoparticles [23] we can also asses that the inhibition observed is due only to the interaction of the sulfonamide moiety with the enzyme, ruling out any AuNP's aspecific effects. We cannot though observe a definite trend of inhibition as a function of SA coverage percentage of the AuNPs.

We do expect these systems to achieve the desired selectivity toward the transmembrane isoforms (CA IX and CA XII) due to the impermeability of the cell membrane to such negatively charged and functionalized nanoparticles. Anionic constructs, in fact, bind less efficiently to cell surfaces than neutral or cationic ones. Furthermore, the uptake of the gold nanoparticles is commonly mediated by the absorption of serum proteins on their surfaces [62–65]; it is reasonable to assume that, because of the nanoparticles are capped with strongly bound ligands, both the absorption of serum proteins on their surfaces and the intracellular uptake would be limited [64].

4 Conclusions

We reported the one-pot preparation and characterization of aqueous dispersions of CAI-coated gold nanoparticles by a modified citrate synthesis method. The colloidal solutions are stable for months and their chemicophysical characteristics are reproducible. Introducing different concentrations of the capping organic sulfonamide ligand (SA) in the reaction mixture, we have detected a threshold effect and a corresponding variation in the hydrodynamic and core radii of the functionalized nanoparticles. Interestingly, a larger amount of SA leads to smaller core size and larger hydrodynamic size; this could be a consequence of the supposed core growth inhibition played by SA and of a closer packing of the capping agent onto the nanoparticle surface, respectively.

By addition of increasing amounts of NaCl to the solutions, we have detected that to the highest SA concentration corresponds the highest nanoparticles stabilization over aggregation, and that would account for a different degree of functionalization of the AuNPs. Even if citrate provides a residual coverage of the gold nanoparticles, sulfonamide plays the major role in the stabilization *versus* the ionic strength increase, since citrate-stabilized nanoparticles precipitate at very low NaCl concentration.

We assayed these systems as CA inhibitors of two cytosolic (CA I, CA II) and two intermembrane (CA IX, CA XII) isoforms of the enzyme. The K_I values are very promising both in the case of absence or presence of a critical amount of NaCl, as the SA-modified nanoparticles show high efficiency toward enzyme inhibition and some selectivity for inhibiting the transmembrane over cytosolic isoforms. These results are encouraging both for *in vitro* testing and for *in vivo* applications. The negative surface charge density, along with size properties and the SA modification of the surface would limit the intracellular receptor-mediated endocytosis, enabling the nanoparticles to specifically target the transmembrane isoforms.

We acknowledge financial support from FIRB ITALNANONET (RBPR05JH2P) and PRIN 2010-2011 (B11J12002450001). We would like to thank Francesco Rugi for the ICP-AES measurements, Dr. Massimo Bonini and Dr. Emiliano Fratini for fruitful discussions. This work was also financed by an EU project of the 7th FP (Metoxia) to CTS.

References

1. M.C. Daniel, D. Astruc, Chem. Rev. **104**, 293 (2004).
2. C.M. Niemeyer, Angew. Chem. Int. Ed. **40**, 4128 (2001).
3. S. Nappini, T. Al Kayal, D. Berti, B. Norden, P. Baglioni, J. Phys. Chem. Lett. **2**, 713 (2011).
4. S. Nappini, M. Bonini, F.B. Bombelli, F. Pineider, C. Sangregorio, P. Baglioni, B. Norden, Soft Matter **7**, 1025 (2011).
5. S. Nappini, F.B. Bombelli, M. Bonini, B. Norden, P. Baglioni, Soft Matter **6**, 154 (2010).
6. E.C. Dreaden, S.C. Mwakwari, Q.H. Sodji, A.K. Oyelere, M.A. El-Sayed, Bioconjugate Chem. **20**, 2247 (2009).
7. R.A. Sperling, P. Rivera Gil, F. Zhang, M. Zanella, W.J. Parak, Chem. Soc. Rev. **37**, 1896 (2008).
8. E. Boisselier, D. Astruc, Chem. Soc. Rev. **38**, 1759 (2009).
9. N. Wangoo, K.K. Bhasin, S.K. Mehta, C.R. Suri, J. Colloid Interface Sci. **323**, 247 (2008).
10. N.R. Panyala, E.M. Pena-Mendez, J. Havel, J. Appl. Biomed. **7**, 75 (2009).
11. M.C. Bowman, T.E. Ballard, C.J. Ackerson, D.L. Feldheim, D.M. Margolis, C. Melander, J. Am. Chem. Soc. **130**, 6896 (2008).
12. J. Nam, N. Won, H. Jin, H. Chung, S. Kim, J. Am. Chem. Soc. **131**, 13639 (2009).
13. C.T. Supuran, A. Scozzafava, Bioorgan. Med. Chem. **15**, 4336 (2007).
14. C.T. Supuran, Nat. Rev. Drug Discov. **7**, 168 (2008).
15. V. Alterio, M. Hilvo, A. Di Fiore, C.T. Supuran, P. Pan, S. Parkkila, A. Scaloni, J. Pastorek, S. Pastorekova, C. Pedone, A. Scozzafava, S.M. Monti, G. De Simone, Proc. Natl. Acad. Sci. U.S.A. **106**, 16233 (2009).
16. O. Ozensoy, G. De Simone, C.T. Supuran, Curr. Med. Chem. **17**, 1516 (2010).
17. G. De Simone, C.T. Supuran, Biochim. Biophys. Acta **1804**, 404 (2010).
18. E. Svastova, A. Hulikova, M. Rafajova, M. Zat'ovicova, A. Gibadulinova, A. Casini, A. Cecchi, A. Scozzafava, C.T. Supuran, J. Pastorek, FEBS Lett. **577**, 439 (2004).
19. O. Swietach, A. Hulikova, R.D. Vaughan-Jones, A.L. Harris, Oncogene **29**, 6509 (2010).
20. J.K.J. Ahlskog, C.E. Dumelin, S. Trussel, J. Marlind, D. Neri, Bioorg. Med. Chem. Lett. **19**, 4851 (2009).
21. J. Chiche, K. Ilc, J. Laferriere, E. Trottier, F. Dayan, N.M. Mazure, M.C. Brahimi-Horn, J. Pouyssegur, Cancer Res. **69**, 358 (2009).
22. A. Thiry, J.M. Dogn, B. Masereel, C.T. Supuran, Trends Pharmacol. Sci. **27**, 566 (2006).

23. M. Stiti, A. Cecchi, M. Rami, M. Abdaoui, V. Barragan-Montero, A. Scozzafava, Y. Guari, J.Y. Winum, C.T. Supuran, J. Am. Chem. Soc. **130**, 16130 (2008).
24. W.P. Wuelfing, S.M. Gross, D.T. Miles, R.W. Murray, J. Am. Chem. Soc. **120**, 12696 (1998).
25. E.E. Foos, A.W. Snow, M.E. Twigg, M.G. Ancona, Chem. Mater **14**, 2401 (2002).
26. A.G. Kanaras, F.S. Kamounah, K. Schaumburg, C.J. Kiely, M. Brust, Chem. Commun. **20**, 2294 (2002).
27. B.L. Cushing, V.L. Kolesnichenko, C.J. O'Connor, Chem. Rev. **104**, 3893 (2004).
28. M. Bonini, U. Bardi, D. Berti, C. Neto, P. Baglioni, J. Phys. Chem. B **106**, 6178 (2002).
29. S. Kumar, K.S. Gandhi, R. Kumar, Ind. Eng. Chem. Res. **46**, 3128 (2007).
30. E. Falletta, F. Ridi, E. Fratini, C. Vannucci, P. Canton, S. Bianchi, C. Valter, P. Baglioni, J. Colloid Interface Sci. **357**, 88 (2011).
31. M. Brust, M. Walker, D. Bethell, D.J. Schiffrin, R. Whyman, J. Chem. Soc. Chem. Commun. **7**, 801 (1994).
32. D. Philip, Spectrochim. Acta A **71**, 80 (2008).
33. J. Turkevich, P.C. Stevenson, J. Hillier, Discuss. Faraday Soc. **11**, 55 (1951).
34. R.A. Sperling, W.J. Parak, Philos. Trans. R. Soc. A **368**, 1333 (2010).
35. J.C. Love, L.A. Estroff, J.K. Kriebel, R.G. Nuzzo, G.M. Whitesides, Chem. Rev. **105**, 1103 (2005).
36. G. Frens, Nature: Phys. Sci. **241**, 20 (1973).
37. T. Yonezawa, T. Kunitake, Colloid Surf. A **149**, 193 (1999).
38. C. Montis, S. Milani, D. Berti, P. Baglioni, J. Colloid Interface Sci. **373**, 57 (2012).
39. S.W. Provencher, Comput. Phys. Commun. **27**, 213 (1982).
40. A. Guinier, G. Fournet, *Small Angle Scattering of X-Rays* (John Wiley, New York, 1955).
41. G.V. Schultz, J. Phys. Chem. B **43**, 25 (1935).
42. P.J. Hayter J.B., Mol. Phys. **42**, 109 (1981).
43. M. Kotlarchyk, R.B. Stephens, J.S. Huang, J. Phys. Chem. **92**, 1533 (1988).
44. R.J. Hunter, *Zeta Potential in Colloid Science. Principles and Applications* (Academic Press, New York, 1981).
45. R.G. Khalifah, J. Biol. Chem. **246**, 2561 (1971).
46. B.K. Pong, H.I. Elim, J.X. Chong, W. Ji, B.L. Trout, J.Y. Lee, J. Phys. Chem. C **111**, 6281 (2007).
47. C.T. Supuran, F. Mincione, A. Scozzafava, F. Briganti, G. Mincione, M.A. Ilies, Eur. J. Med. Chem. **33**, 247 (1998).
48. Y. Sahoo, A. Goodarzi, M.T. Swihart, T.Y. Ohulchanskyy, N. Kaur, E.P. Furlani, P.N. Prasad, J. Phys. Chem. B **109**, 3879 (2005).
49. R. Terrill, T. Postlethwaite, C. Chen, C. Poon, A. Terzis, A. Chen, J. Hutchison, M. Clark, G. Wignall, J. Londono, R. Superfine, M. Falvo, C. Johnson, E. Samulski, R. Murray, J. Am. Chem. Soc. **117**, 12537 (1995).
50. J. Kimling, M. Maier, B. Okenve, V. Kotaidis, H. Ballot, A. Plech, J. Phys. Chem. B **110**, 15700 (2006).
51. Y.P.M. Williams R., F.S. Stofko, J. Colloid Interface Sci. **106**, 388 (1985).
52. A.E. Nielsen, *Kinetic of Precipitation* (Mac Millan, New York, 1964).
53. M.J. Hostetler, J.E. Wingate, C.J. Zhong, J.E. Harris, R.W. Vachet, M.R. Clark, J.D. Londono, S.J. Green, J.J. Stokes, G.D. Wignall, G.L. Glish, M.D. Porter, N.D. Evans, R.W. Murray, Langmuir **14**, 17 (1998).
54. C.J. Ackerson, P.D. Jadzinsky, R.D. Kornberg, J. Am. Chem. Soc. **127**, 6550 (2005).
55. S. Link, M.A. El-Sayed, J. Phys. Chem. B **103**, 8410 (1999).
56. L.M. Liz-Marzan, Langmuir **22**, 32 (2006).
57. V. Amendola, M. Meneghetti, J. Phys. Chem. C **113**, 4277 (2009).
58. Z.M. Qiang, C. Adams, Water Res. **38**, 2874 (2004).
59. T. Laaksonen, P. Ahonen, C. Johans, K. Kontturi, Chem.Phys.Chem. **7**, 2143 (2006).
60. X.O. Liu, M. Atwater, J.H. Wang, Q. Huo, Colloid Surf. B **58**, 3 (2007).
61. Y.J. Gu, J.P. Cheng, C.C. Lin, Y.W. Lam, S.H. Cheng, W.T. Wong, Toxicol. Appl. Pharm. **237**, 196 (2009).
62. A. Verma, F. Stellacci, Small **6**, 12 (2010).
63. A. Verma, O. Uzun, Y.H. Hu, Y. Hu, H.S. Han, N. Watson, S.L. Chen, D.J. Irvine, F. Stellacci, Nat. Mater **7**, 588 (2008).
64. B.D. Chithrani, A.A. Ghazani, W.C.W. Chan, Nano Lett. **6**, 662 (2006).
65. B.D. Chithrani, J. Stewart, C. Allen, D.A. Jaffray, Nanomed. Nanotechnol. **5**, 118 (2009).

Tutor: Prof. Piero Baglioni

Co- tutor: Dr.ssa Brunella Perito

Coordinatore: Prof. Piero Baglioni